Crystallographic Determination of Wild Type, Mutant and Substrate-Analogue Inhibited Structures of Bacterial Members of a Family of Superoxide Dismutases

by

Simon Hardie Oakley

Submitted as part of the requirements for the degree of

Doctor of Philosophy

Institute of Fundamental Sciences, Chemistry

Massey University, New Zealand

2009

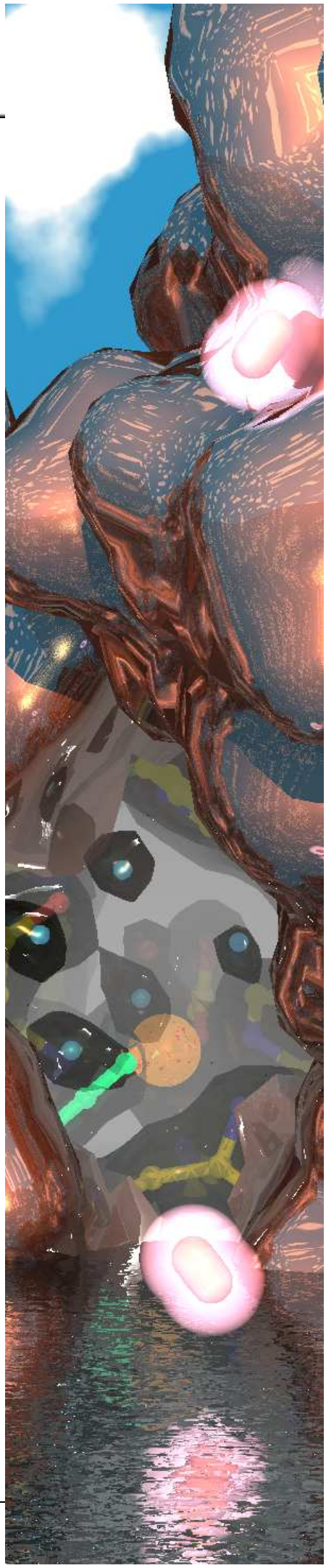

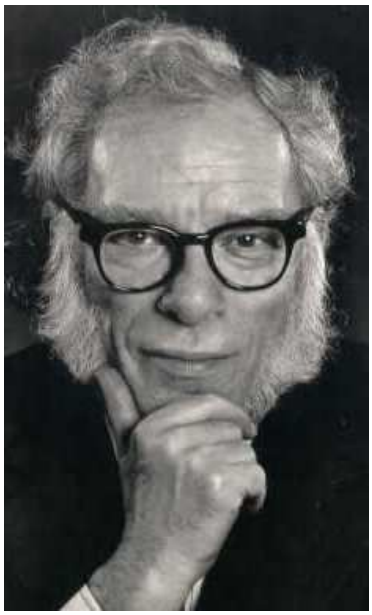

"Part of the inhumanity of the computer is that, once it is competently programmed and working smoothly, it is completely honest."

Isaac Asimov (1920-92), author,

inventor of the word “robotics”.

0.1 Abstract

Crystallographic Determination of Wild Type, Mutant and Substrate-Analogue Inhibited Structures of Bacterial Members of a Family of Superoxide Dismutases

The iron and manganese superoxide dismutases are a family of metallo-enzymes with highly conserved protein folds, active sites and dimer interfaces. They catalyse the elimination of the cytotoxic free radical superoxide to molecular oxygen and hydrogen peroxide by alternate reduction then oxidation of the active-site with the concomitant transfer of protons from the solvent. There are many key aspects of enzymatic function that lack a structural explanation.

The focus of this study is on three crystal structures. The iron-substituted manganese superoxide dismutase from *Escherichia coli* complexed with azide, a substrate-mimicking inhibitor, was solved to 2.2 Å. This "wrong" metal form shows a binding pattern seen previously in the manganese superoxide dismutase from *Thermus thermophilus.* Wild-type manganese specific superoxide dismutase from the extremophile *Deinococcus radiodurans* was solved to 2.0 Å and has an active site reminiscent of other solved manganese superoxide dismutases despite a lack of product inhibition. The azide-inhibited manganese superoxide dismutase from *Deinococcus radiodurans* was determined to a resolution of 2.0 Å and showed binding of azide, and by inference superoxide, different to that seen in *Thermus thermophilus,* but reminiscent of that seen in azide-inhibited iron superoxide dismutases. These results indicate that the azide ion, and by inference superoxide, bind to the metal centre of manganese superoxide dismutases in two modes, and transition between the two modes may be entropy dependent.

These structures, integrated with knowledge from other structures, known biochemistry and various spectra, provide insight into catalytic function. An outer-sphere mechanism of proton transfer that does not rely on through-peptide proton uptake is proposed and compared to a previously proposed inner-sphere mechanism. This is based on the observation that a water molecule moves into the active site of the manganese superoxide dismutase from *Deinococcus radiodurans* upon azide binding, providing a Grötthus pathway for rapid proton transfer to the active site from the bulk solvent.

Also presented in this study are the partially refined structures of four point mutants (S82T, L83M, L133V, and M164L/L166V) of the manganese superoxide dismutase from *Escherichia coli* all solved to roughly 2 Å resolution, designed to investigate product inhibition which varies across species.

0.2 Acknowledgements

Acknowledgement pages generally read like a mix between an Oscar acceptance speech and a shopping list, so here goes. There are many people who contributed to my time at Massey University both professionally and social. Therefore to quote the bard, “brevity is the sole of wit” I apologise to all those not named specifically in my efforts to be both laconic and pretentious.

Firstly, would like to acknowledge my supervisor Geoff for his support, encouragement and vast knowledge on all things chemical, X-ray, and crystal.

Secondly, the post-docs; my co supervisor Bryan for answering questions about various computer software and crystallography, and Jim, whose brief foray into protein crystallography from chemistry was very fruitful.

Thirdly, Gill, Trev, and the other members of the X-lab past and present for providing lab space, office space, computing, stolen pens, interesting talks, moral encouragement, cakes, parties, beer, wine, gossip *et cetera*. These were all gladly accepted but not always reciprocated.

Penultimately, I would like to thank my various flat-mates and friends over my time in Palmerston North who put up with my bad jokes and stories over the past few years.

Lastly, but most importantly, I would like to thank my family for their long-distance encouragement and support.

-Simon

0.3 Table of contents

0.4 List of figures

Colour images occur on the following pages

5,15,22,24,26,27,31,70,72,75,76,77,79,80,81,82,82,83,84,87,88,90,91,91,92,93,100,105
,

107,128,129,132,138,139,139,140,143,145,147,151,154,155,156,158,159,162,163,209,

209,211,211,212,213,227,228.

0.5 List of equations

0.6 List of tables

0.7 Abbreviations

α helix	secondary structure element of proteins
ATP	adenosine-5'-triphosphate
β-sheet	secondary structure element of proteins
CD	circular dichroism
DNA	2’-deoxyribonucleic acid
$E^{o'}$	standard reduction potential at pH 7
EPR	electron paramagnetic resonance
HFEPR	high-magnetic field electron paramagnetic resonance
HPLC	high pressure liquid chromatography
K	kelvin, temperature scale
k_{cat}	the maximum number of enzymatic reactions catalysed per second
K_m	Michaelis constant, approximate substrate concentration, where enzyme activity is half the maximum
L	Litre, measure of volume
LB	Luria broth, media for bacterial growth
M	moles/litre, a measure of concentration
MCD	magnetic circular dichroism
MR	molecular replacement
MIR	multiple isomorphous replacement
mRNA	messenger RNA
mV	millivolt, a thousandth of a volt

NAD(P)H	nicotinamide adenine dinucleotide (phosphate) –reduced form
NCS	non-crystallographic symmetry
NMR	nuclear magnetic resonance
PCR	polymerase chain reaction
PDB	protein data bank
pH	activity of the hydrogen ion, measure of acidity, where $pH = -\log a_{H+}$
p*K*	disassociation constant of a proton or a hydroxide, defined as $pK = -\log K$
redox	reduction/oxidation
R_{free}	set of reflections, excluded from refinement and (electron) density calculations
RMS	root-mean-square, measure of the magnitude of a varying quantity. As RMS deviation, measure of scatter of values about a target value. Relevant to geometric parameters in protein structures.
RNA	ribonucleic acid
ROS	reactive oxygen species, including O_2^-, H_2O_2, O_2NO^- (peroxynitrate), OCl^- (hypochlorite)
RPM	revolutions per minute
SIR	single isomorphous replacement
SOD	superoxide dismutase
SD	standard deviation
TLS	translation-libration-screw

μL	microlitre, measure of volume
UV	ultra violet
V	volt, potential difference across a conductor

0.8 Naming conventions of superoxide dismutases.

Throughout the literature concerning superoxide dismutases different naming conventions have been used for both genes and proteins. Some known names are Cu,ZnSOD, Cu-Zn superoxide dismutase, FeSOD, MnSOD, SOD, SOD-1, SOD-2, SOD-3, SOD-4, SODF, SODS, copper-zinc superoxide dismutase, cuprein, cytocuprein, erythrocuprein, ferrisuperoxide dismutase, hemocuprein, hepatocuprein, superoxidase dismutase, superoxide dismutase I, superoxide dismutase II, *et cetera.*

The most common abbreviations of superoxide dismutase are "SOD" pertaining to protein and "sod" for dealing with genes, but some have used "SD". Superoxide dismutase activity has been detected in a number of polypeptides and subsequently potential superoxide dismutase activity has been inferred for many genes. Many organisms have multiple superoxide dismutases and a variety of naming schemes have been used.

sodA, sodB, sodC…	alphabetically based.
sod1, sod2, sod3…	numerically based.
sodA, sod1..	italicised to indicate gene.
sodM, sodF, sodN…	where the letter refers to the obligate metal cofactor Mn, Fe, Ni.

In this thesis a functional and hierarchical nomenclature will be used to describe the enzyme function, the obligate metal cofactor, oxidation state, the species of origin, inhibitors and mutation. Throughout this work "SOD" will used as an abbreviation for superoxide dismutase. Members will be identified first by the element symbol, then abbreviation, for example "NiSOD" for a nickel-specific superoxide dismutase. Hierarchical naming systems have been used in several papers: the system used here is an extension, albeit with minor modifications, of that used by Vance and Miller (Vance & Miller, 1998b).

1. There are at present three major families of superoxide dismutases: nickel dependent (NiSOD), those which require both copper and zinc (Cu/ZnSOD), and the third family that are active with either manganese (MnSOD) or iron

(FeSOD). The abbreviations of “MnSOD” and “FeSOD” are treated as words beginning with vowels; e.g. “FeSOD” should be pronounced “eff-ee-sod” rather than as “i-arn-sod” and should be prefixed by the indefinite object, “an”, rather than “a”.

2. If it is unknown or ambiguous whether a superoxide dismutase is active with manganese or iron it is designated “Fe/MnSOD”. There are some members that have significant activity with both iron and manganese and these are commonly termed “cambialistic” These are referred to as “camb-Fe/MnSOD”, and hence the manganese-only form of a cambialistic enzyme would be “camb-MnSOD”.

3. If the redox state of the active-site metal is known it is denoted as a superscript of the elemental symbol. For example, “camb-Fe^{3+}SOD” and “camb-Fe^{2+}SOD” denote two different oxidation states of the iron in a cambialistic enzyme.

4. It is possible to generate superoxide dismutases with incorrect metal ions substituted for the preferred metals. The preferred metal is indicated immediately adjacent to the SOD expression, preceded by the metal that has been substituted, separated by a hyphen. For example, “Mn-FeSOD” represents an iron superoxide dismutase in which active-site iron is replaced with manganese.

5. By default the enzyme is assumed to have the native sequence. If increased clarity is required, then the prefix “WT” will be used as an abbreviation for “wild type”. If the protein has a point mutation it will be indicated by a prefix. The prefix will be the single letter code of the native sequence, followed by the residue number and the single letter code of the mutant. For example “Y34F-MnSOD” represents a mutation of a tyrosine to a phenyalanine at position 34 in an MnSOD. This is in contrast to the non-mutated native or “WT-MnSOD”.

6. The species of origin is indicated by an italicised expression between the indication of mutation and the metal designation. The basis of the italicised expression may either be the common or the scientific name. For example, “Y34F-*Ec*-MnSOD” and “Y34F-*mito*-MnSOD” represent the same point

mutation of the *Escherichia coli* and the human mitochondrial manganese superoxide dismutases respectively.

7. Superoxide dismutases interact with a number of small-molecule inhibitors to form stable complexes; this is indicated by the chemical name (and charge) of the inhibitor, written after the "SOD" expression. The azide-inhibited form of the cattle Cu/Zn superoxide dismutase would be indicated as "*bovine*-Cu/ZnSOD-N_3^-".

8. Other experimental techniques and variables can be included into this naming convention. These will be introduced after any description of inhibitors. For example "RT" is used to abbreviate for room temperature and "110 K" for an experiment at cryo-conditions of 110 K. For example, there exist spectral studies for Y34F-*Ec*-MnSOD-N_3^- at ambient and cryogenic conditions designated "Y34F-*Ec*-MnSOD-N_3^--RT" and "Y34F-*Ec*-MnSOD-N_3^--110 K" respectively.

9. This nomenclature lends itself to the identification of individual atoms within a structure. This follows the hierarchy of protein name, underscore, chain identifier (italicised), underscore, one-letter amino acid code, residue number, underscore, and atom name. Atom names are capitalised forms, following the naming conventions of the protein data bank (Berman *et al.*, 2000). This makes distinguishing atoms that are closely located spatially unambiguous. The expressions "*Ec*-MnSOD_*A*_D146_OD1" and "*Ec*-MnSOD_*A*_D146_OD2" distinguishes between two atoms of the same amino-acid side chain. If there is a known PDB code for a protein, then this can be substituted for the protein name, for example "1VEW_*A*_D146_OD1".

10. If an atom or side chain in a crystal structure has split or multiple conformations then this will be indicated by a subscript after the atom name. For example, individual atoms within the two conformations of lysine 29 in the A chain of Y174F-*Ec*-MnSOD are described as "1IXB_*A*_K29_NZ_A" and "1IXB_*A*_K29_NZ_B"

11. The naming of water molecules will follow the hierarchy of protein name, underscore, an italicised chain number (if present), underscore, “WAT” followed by the number of the water, for example 1EN5_WAT72.

The naming and abbreviation of amino acids generally follow IUPAC conventions for the use of trivial names, three-letter system and one-letter system (Cornish-Bowden, 1984). The naming and use of elements and chemicals will follow IUPAC conventions, but some trivial names will also be used.

1 The prehistory and history of the superoxide dismutase protein families

1.1 Background on oxygen, oxygen toxicity and identification of superoxide

Who actually discovered molecular oxygen is of debate. The Englishman Joseph Priestley, who is widely regarded as the discoverer of oxygen, performed his experiments in 1774 and published his findings in 1775. The Swede Carl Wilhelm Scheele had produced oxygen in 1772 but he did not publish until 1777. The novel gas was largely investigated by Antoine Lavoisier, “the father of modern chemistry”, whose results published in 1778 identified the nature and chemical properties of oxygen. Lavoisier’s work, which was started in 1774, introduced quantitative measurement into the discipline of chemistry. He was greatly aided by his wife, whose engravings are still illuminating today; refer to Figure 1-1 (Lavoisier & Lavoisier, 1789).

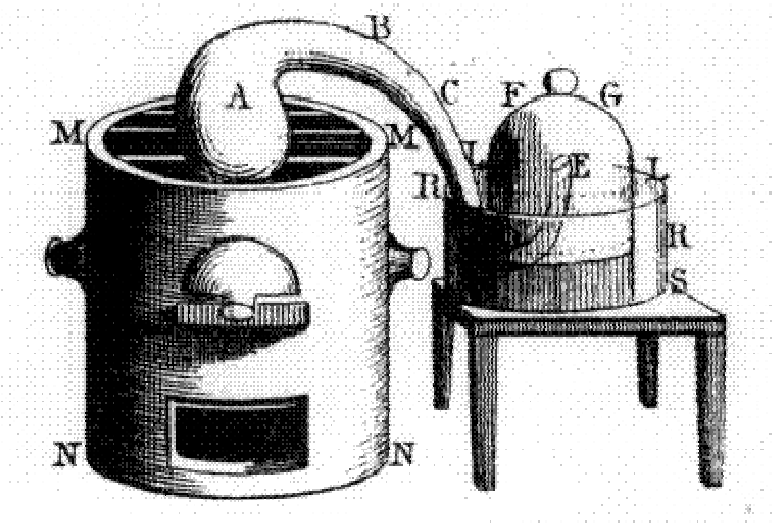

Figure 1-1. Apparatus used by Lavoisier in his early experiments with oxygen.

Figure 1-1. This apparatus was used to disprove the phlogiston theory. Lavoisier introduced quantification into his experiments and was then able to demonstrate conservation of mass, leading to the field of modern chemistry. Taken from *Traité élémentaire de chimie* (Lavoisier & Lavoisier, 1789).

Lavoisier also identified some of the central roles of oxygen in biology, as he correctly identified respiration as a form of combustion. Subsequent experiments showed that animals in high oxygen environments had altered physiologies, including death from lung congestion. This showed that high concentrations of oxygen could be toxic, but a mechanism of oxygen toxicity would be largely unknown for nearly 200 years. In the intervening years oxygen toxicity was investigated by physiologists such as Paul Bert who showed that an animal in 4 atmospheres of oxygen exhibited similar pathologies to

animals in 20 atmospheres of air (Bert, 1878) indicating that toxic affects were derived from oxygen alone and not from pressure. Most of the toxic effects of oxygen were seen in the lungs but other tissues were also affected (Smith, 1899).

Interest in hyperbaric pressures and oxygen toxicity was renewed by World War Two, mainly due to the treatment of deep-sea diving and submariner mishaps in hyperbaric chambers. It was also recognised that hyperbaric treatment led to positive outcomes in a variety of conditions. Subsequently, during the 1950's there was a proliferation of hyperbaric chambers into clinical settings. There was also a concurrent increase in the amount of fundamental research into oxygen toxicity as well as in the number of reviews (Haugaard, 1968).

The primary mechanism of oxygen toxicity was identified by biochemists McCord and Fridovich in their seminal work (McCord & Fridovich, 1969). Superoxide was detected within biological systems and specific superoxide dismutase (SOD) activity was defined for the metallo-protein erythrocuprein (at the time thought to be involved in copper storage) from bovine erythrocytes. The second metal co-factor, zinc, was not identified until later when the enzyme was further characterised (Keele *et al.*, 1971) as a copper/zinc SOD (Cu/ZnSOD). The wide distribution of SOD activity was also identified early (McCord *et al.*, 1971), with only obligate anaerobes lacking mechanisms for elimination of superoxide. The study of superoxide and other free radicals has gone on to influence most fields of biosciences. Before this, superoxide was a molecule of limited interest to chemists and of little interest to biologists.

1.2 Early biochemistry and structures

Identification of a specific activity and identification of an enzyme responsible led to a rapid expansion of the field. A second distinct family of proteins with SOD activity but different molecular weight and metal specificity was rapidly identified when a manganese SOD (MnSOD) was identified in *Escherichia coli* (Keele *et al.*, 1970) with an iron SOD (FeSOD) following shortly thereafter (Yost & Fridovich, 1973). Based on similarities in amino-acid composition and molecular weight it was suspected that MnSOD and FeSOD were related evolutionarily, but not related to the Cu/ZnSOD family.

During the 1970's a large number of SODs from a wide variety of species was identified and characterised biochemically, pathologically, physiologically and spectroscopically. Crystallographic investigations of Cu/ZnSODs began in earnest

during the 1970's with reports of crystals of bovine Cu/ZnSOD (Richardson *et al.*, 1972) followed closely by a medium-resolution crystal structure (Thomas *et al.*, 1974).

Structural studies of the Fe/MnSOD lagged behind. Crystals were reported for an FeSOD from *Pseudomonas ovalis* (Yamakura *et al.*, 1976) preceding the structural solution (Ringe *et al.*, 1983), which showed definitively that the FeSOD protein fold was distinct from the Cu/ZnSOD peptide fold. The solution of a crystal structure of an MnSOD from *Thermus thermophilus* (Stallings *et al.*, 1984) showed the same overall fold as that seen in FeSOD as well as a conserved active-site structure indicating that FeSODs and MnSODs are related and derived from a common ancestor. The advent of high-resolution structural knowledge identified important residues and influenced proposed enzymatic mechanisms. This in turn led SOD research to be more directed as proposed mechanisms and hypotheses could now be investigated.

The rapid development and expansion of genetic techniques in the 1980's and 1990's had drastic effects on the SOD field. Improvements in gene sequencing meant that more definitive assignment of amino-acid side chains could be made in already solved structures such as the FeSOD from *E. coli.* This structure (Stallings *et al.*, 1983) was improved with sequence information (Carlioz *et al.*, 1988). Sequence information has generally improved the quality of the model derived from X-ray data, especially for the FeSOD from *Pseudomonas ovalis* (Stoddard, Howell *et al.*, 1990). Knowledge of gene sequence also makes it easier to identify and clone novel homologous members of a protein family. The generation of recombinant plasmids allowed the rapid generation of native, recombinant and mutant proteins in expression strains for biochemical and structural studies.

There have also been concurrent improvements in computing speeds, instrumentation, programs, X-ray sources and X-ray crystallographic techniques that have drastically decreased the time required to solve the structure of a diffracting crystal. This has led to an exponential increase in the number of structures being solved annually.

As SODs are metallo-enzymes with transition-metal ions at their active sites, spectroscopic disciplines and techniques that take advantage of this can be readily used. This has been the case since the initial discovery of the first Cu/ZnSOD where UV-visible and electron paramagnetic resonance (EPR) spectroscopies were used to make inferences about structure (McCord & Fridovich, 1969). Since the 1960's, new

spectroscopic techniques have been developed and existing techniques used to investigate SODs have also increased in sensitivity and accuracy.

In 1996 a nickel-dependent superoxide dismutase (NiSOD) was identified from several *Streptomyces* species. This NiSOD shared no sequence homology to either the Cu/ZnSOD or Fe/MnSOD protein families (Youn *et al.*, 1996). The NiSODs have an extremely limited distribution within *Streptomyces* and cyanobacteria, in sharp contrast to the more ubiquitous distribution of other SODs. This may be due in part to the recent identification of the protein family but is likely to be a realistic phenomenon. The crystal structure of NiSOD (Wuerges *et al.*, 2004) showed a novel fold with a unique active-site architecture. There is a limited knowledge base for the NiSOD family; this is due to its recent identification and its limited distribution. The lack of a eukaryote homologue means that there will be limited interest in NiSOD from medical and plant biologists. A comparison of all three families is given in Figure 1-2.

Figure 1-2. In all three representations, alpha helices are shown as blue cylinders, smoothed beta sheets as yellow arrows, unsmoothed loops as grey coils and metal co-factors of the active site as spheres. From comparative examination of the three distinct folds it is apparent that these folds are derived from unique ancestors.

The uppermost stereo-pair shows the structure of a Cu/ZnSOD, derived from the atomic coordinates of the oxidised bovine enzyme (2SOD), with the copper ion depicted as a cyan sphere and the zinc ion as an orange sphere. The dominant feature of the Cu/ZnSOD is a flattened cylinder of a Greek key beta-barrel.

The central stereo-pair shows the structure of a member of the Fe/MnSOD family, the *E. coli* FeSOD (1ISA), with the metal cofactor shown as a magenta sphere. Fe/MnSODs are made up of two sub-domains that enclose the active site; the N-terminal domain located on the left side of the image is dominated by two large helices and the carboxy-terminal is made up of three anti-parallel strands and associated short helices.

The lowermost stereo-pair shows the fold of the recently solved NiSOD, from atomic coordinates 1T6U, with the magenta sphere showing the position of the bound Ni ion. The NiSOD is made up of four helices in an up-and-down bundle with the N-terminal loop contributing to the active-site structure.

Image was generated using pymol (http://www.pymol.org/).

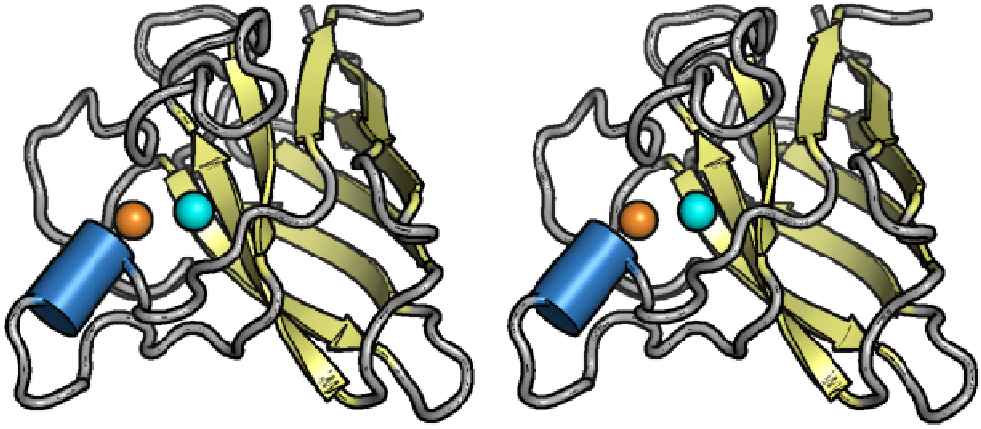

Cu/ZnSOD ↑

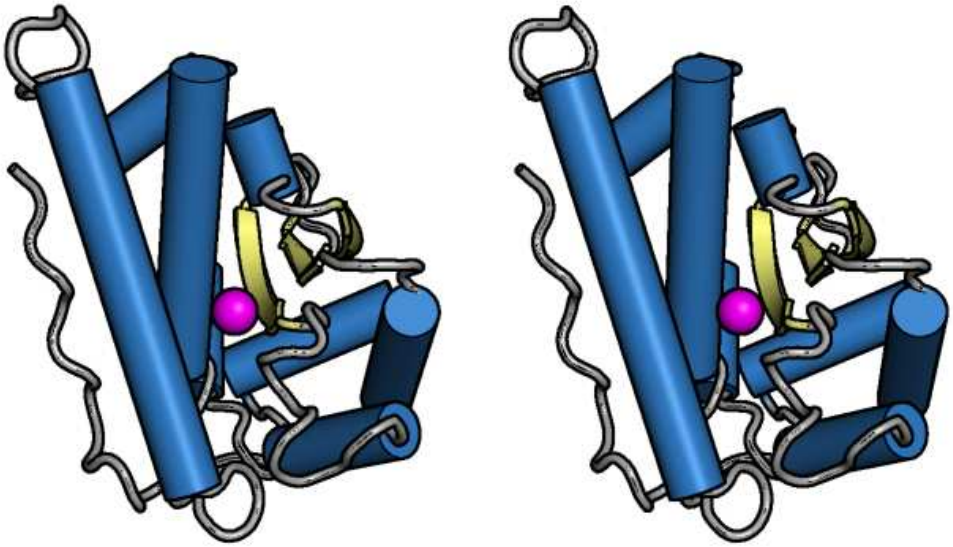

Fe/MnSOD ↑

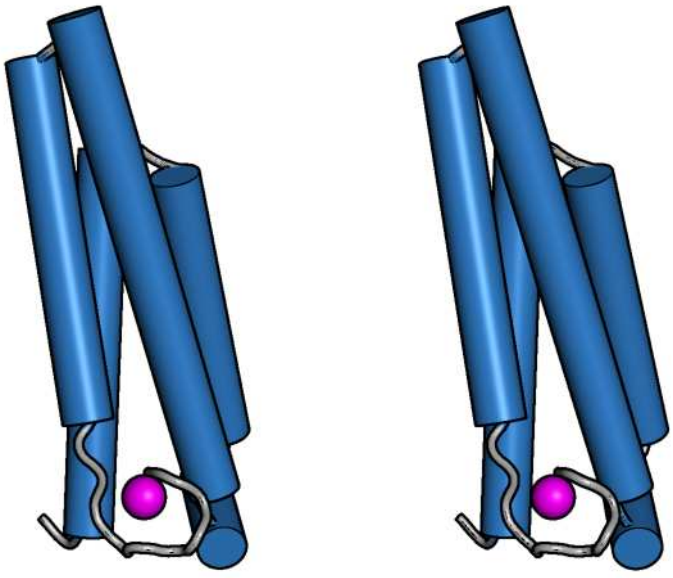

NiSOD ↑

Figure 1-2. Wall-eyed stereo-diagrams of the tertiary structure of the three superoxide dismutase protein folds.

1.3 Roles of superoxide and SODs

In eukaryotes oxygen is required as the ultimate electron acceptor of oxidative phosphorylation, the process by which the majority of ATP is generated in the mitochondria. Incomplete reduction of oxygen generates the majority of superoxide within cells, with some estimates that about 2% of electrons entering the electron-transport chain end up as superoxide (Chance *et al.*, 1979). In higher animals the metabolism of oxygen is controlled by regulating blood flow and the number of red blood cells within the blood. The resulting levels of superoxide are tightly controlled resulting in redox homeostasis. When oxygen supplies to tissues are altered, by conditions such as cancers or ischemia/reperfusion injury, the redox state of tissues is perturbed. A lack of oxygen creates a reducing environment within tissues that favours superoxide formation. In particular, if reperfusion occurs, there is a burst of free-radicals generated after oxygen enters the reduced tissue, which cause additional damage.

1.4 Medical importance

Genetic polymorphisms of human mitochondrial MnSOD have been linked to increased incidence of drug-induced liver injury (Huang *et al.*, 2007), although the mechanisms of drug metabolism are unknown. Polymorphisms of Cu/ZnSOD may lead to impaired lung function (Dahl *et al.*, 2008). Familial amyotrophic lateral sclerosis (ALS), commonly known as Lou Gehrig's disease, is strongly associated with misfolding of the Cu/ZnSOD protein (de Aguilar *et al.*, 2007). More than 100 mutations have been reported. Loss of Cu/ZnSOD function leads to a progressive degradation of motor neurons.

A loss of SOD activity was identified in many cancers, as reviewed (Oberley & Buettner, 1979), indicating that there is a strong linkage between tumour malignancy and redox state. It was originally thought that superoxide was simply a harmful metabolic by-product of oxygen metabolism (Fridovich, 1978), but now superoxide has been shown to be a critical molecule in cellular signalling and cellular survival (Baas & Berk, 1995).

Another major source of superoxide in humans is the inducible NADPH oxidase (Baas & Berk, 1995), which is primarily associated with phagocytosis by neutrophils in the innate and adaptive immune system (Curnutte & Babior, 1974). The active enzyme, which is membrane-bound and is made up of six subunits generates superoxide by transferring electrons from NADPH to molecular oxygen. In phagocytosis this leads to high levels in the phagosome of superoxide, hydrogen peroxide and other ROS,

especially OCl^- (hypochlorite), which can then breakdown engulfed particles or pathogens. Some bacteria have evolved to exist within neutrophils. For instance, *Mycobacterium tuberculosis* can persist within macrophages for decades. The *Mycobacterium* contains a translocase to transport FeSOD to the phagosome; when the translocase is deleted *Mycobacterium tuberculosis* loses infectivity (Rigel & Braunstein, 2008).

More recently, NADPH-derived superoxide has been seen as a signalling molecule in the cardiovascular system (Li & Shah, 2004). The identification of dual roles for superoxide as a free radical and as a signalling molecule has lead to resurgence of interest in SODs. It is hoped that the study of superoxide and SODs will lead to better treatments of a variety of human diseases. There are also other, more fundamental, reasons to investigate SODs.

1.5 Catalytic turnover, catalytically perfect enzymes

The SOD enzymes are amongst the fastest known, with k_{cat}/K_m values often reported in the order of 10^8 to 10^9 M^{-1} s^{-1}, meaning that the enzyme catalysis is approaching the diffusion limits of the substrate. This puts them into the important class of proteins termed "catalytically perfect" or "kinetically perfect", implying that nearly every molecule of substrate that interacts with the enzyme is catalysed. This class of enzymes raises questions related to the speed of catalysis. How are substrates directed to active sites? Why is catalysis at the active site so rapid? How do end-products leave the active site so quickly? Are there mechanisms to prevent leaving end-products interacting with incoming substrates? Why are not all enzymes this fast?

The "catalytically perfect" SOD activity has not only evolved once, but three times for each of the SOD folds. The carbonic anhydrases are another example of "catalytically perfect" enzymes that have evolved from different ancestors. The study of these enzymes will hopefully identify the common traits of perfect enzymes, which, in turn, could lead to designer proteins.

During periods of high catalytic turnover by SODs there are mechanistic constraints that should be considered. There are constant changes in the oxidation state and hence the net charge of the active site. The substrates, negatively charged superoxide ions and positively charged protons, must be steered towards the active site. As well, the end products, uncharged oxygen and hydrogen peroxide, must be steered away from the active site. These events must be well coordinated to prevent an impasse at the active

site. This is particularly true of the Fe/MnSODs, which have a buried active-site 15 Å away from the bulk solvent, as will be described in more detail shortly.

1.6 Prevalent theories as to how enzymes promote catalysis

These "catalytically perfect" enzymes are of interest to theoreticians interested in enzyme function and catalysis as they approach optimum efficiency. In classical kinetics catalysts work by lowering energy barriers to transition states, thereby facilitating the movement of reactants into products. As such, there are several theories as to how enzymes catalyse the formation of products. These theories are not mutually exclusive of one another.

1. One of the theories proposed in the early days of structural biology, but still widely believed, is that enzymes stabilise the transition state of a reaction (Pauling, 1948). In this scheme reactant(s) will bind with low affinity and the enzyme promotes the formation of a high-affinity transition complex(es), which break down into product(s) that bind with lower affinity. Thus, chemicals that mimic the transition state complex(es) can bind at the active site of an enzyme and are potent inhibitors of substrates. Experiments using the kinetic isotope effect are critical of this theory.

2. A related view is that rather than the active site of the enzyme stabilising the transition state, the reactant(s) are destabilised by the active site, promoting movement of reactant(s) into transition state(s) that, in turn, give rise to product(s) (Jencks, 1975). This hypothesis is energetically similar to transition-state mechanism but implies a different physical mechanism, whereby the substrate is forced into a higher energy conformation suitable for catalysis.

3. A third view is that the active sites of enzymes alter the solvation of reactant(s) and transition state(s), thereby promoting reactions that would not be favoured in aqueous solution (Warshel, 1978). Thus the active site of an enzyme increases the likelihood that a reaction will occur.

4. A fourth scheme is that an enzyme stabilizes reactant(s) in positions, termed near-attack conformations, such that thermal fluctuations are enough to overcome energy barriers that prevent formation of transition state(s) and product(s) (Lau & Bruice, 1998). In this scheme fluctuations in the near attack conformations are essentially random but the likelihood of correct arrangement

followed by catalysis is increased by the enzyme. In this scheme the protein component has an essential “wobble” that drives catalysis.

5. The fifth scheme is an extension of the fourth, in that, changes in reaction coordinate are dynamically coupled to ordered protein motion (Antoniou *et al.*, 2002), rather than random thermal fluctuations. In this scheme pre-catalytic conformations of reactant(s) are ordered by the protein conformation, then as catalysis occurs protein-reactant(s) move through a somewhat ordered series of transition steps to form product(s). In this scheme the essential “wobble” of the protein is not random but ordered or concerted.

The first three schemes listed above focus on the local environment of active site, while the latter two are influenced by thermodynamic considerations of the entire protein.

1.7 Evolution of SODs

When speculating about the evolutionary origins of SODs (or any bio molecule), most speculations are inferred from modern species and assumptions about the past derived from knowledge of the fossil record, geology, and chemistry. Evolution acts on individual proteins as well as on whole organisms, although on much longer time scales. The Oparin-Haldane theory of the 1920’s and 1930’s postulated that the atmosphere and, more importantly, the oceans of primitive Earth were anaerobic when life first evolved. Refer to (Fry, 2006) for historical perspective on this theory. Over time oxygen levels rose as primitive life-forms evolved photosynthesis, which ultimately oxidises water into oxygen. It was at this time that the first SODs probably evolved to deal with oxygen by-products, such as superoxide, within cells. However, the majority of molecular oxygen would diffuse away into the reducing environs to oxidise free iron and sulfur. At this point superoxide dismutase activity may have been a non-specific activity.

As ambient oxygen levels rose this increased the likelihood that cells would encounter oxygen and therefore superoxide. This led to an “oxygen catastrophe”, which occurred about 2.2-2.5 billion years ago (Kasting, 1993). This, in turn, may have led to a “snowball Earth”, leading to evolutionary bottlenecks, for which oxygen tolerance would be required to survive. At this time there would have been strong pressure to increase specific SOD activity (Kirschvink *et al.*, 2000).

Later oxygen-dependent oxidative phosphorylation evolved, which generates significant levels of superoxide as a by-product during ATP production. Any heritable factor that

promoted the dismutation of superoxide would have conferred a strong selective advantage. The development of an oxidative metabolism, with increased ATP production, would have been impossible without an efficient SOD.

It is impossible to tell which of the three SOD families evolved first, in which sort of organism and in what sort of local environment. The three different SOD families may have arisen to take advantage of whichever ions were most abundant in the local environment. Some information on the ancestors and phylogeny of SODs can be inferred from modern examples but there are some limitations to this. The current situation is listed below:

1. At present there are three known families of SODs but in the distant past there may have been additional bio-molecules with superoxide dismutase activity that have gone extinct.

2. The modern forms of SODs may be different from ancestral forms.

3. It is also difficult to know whether a SOD present in the genome of an organism is the result of evolution of an ancestral form or the result of horizontal gene transfer.

4. The modern SODs may represent a recent radiation event.

5. There are many organisms that have more than one SOD present in their genomes making it difficult to determine which if any SOD was present in ancestor species.

6. Information and conclusions about one SOD family may not be relevant to other SOD families.

7. The expression of SODs is not constant in time and space.

8. Post-transcriptional control modulates levels and types of SODs in organisms that contain more than one SOD.

1.7.1 Extinct SODs

Superoxide dismutase activity may have evolved more than the three times represented by the three recognised SOD folds seen today, especially since evolution has been punctuated by a series of major mass extinctions (Raup, 1986). There may have been other unique protein folds that exhibited SOD activity that are now extinct. It may have

been possible for non-peptidyl bio-molecules, such as RNA-based ribozymes that coordinate redox-active metal ions, to achieve reasonable SOD activity. It is widely believed that the primitive life that existed before oxygenic photosynthesis was RNA-based (Gilbert, 1986), with RNA fulfilling the information storage role of DNA and the catalytic role of peptides.

The catalytic dismutation of superoxide has been mimicked by a number of small molecules (Beyer & Fridovich, 1990, Salvemini *et al.*, 1999, Reddan *et al.*, 2003) that bind transition metals. Presently small-molecule SOD mimics, with appreciable activity, are being investigated for therapeutic roles (Orrell, 2006). Similar complexes may have existed in early life-forms. However, peptide-based catalysis is generally several orders of magnitude more efficient.

1.7.2 Direct evolution

The protein-folding pathways that lead to mature folds may be the most conserved unit of heredity and slowest to change. The SODs that are seen today are the result of over a billion years worth of evolution, and they may be radically different from the primordial enzymes. There is variation in rates of evolution between protein families. The SODs are likely to be slowly evolving, as they are constrained by requirements of metal-binding and catalytic turnover. Within the Fe/MnSOD family, the most divergent members retain greater than 30% identity.

It is difficult to speculate whether the primordial SODs arose from other pre-existing protein families or from random sequence. The NiSODs have the smallest fold, ~100 residues, made up of four helices in a four-helical up-and-down bundle. The Cu/ZnSOD fold, which is slightly larger at ~150 residues, is often categorised as being immunoglobulin-like (Richardson *et al.*, 1976). The Fe/MnSODs have the largest fold, at ~200 residues, which is made up of two domains, a helical domain and a mixed helical-sheet domain. The lineage is unclear for all SODs.

1.7.3 Horizontal transfer

The horizontal transfer of genetic material from one organism to another is a rarer event than the vertical transfer of genetic material to descendants, but this may have occurred with SOD genes as they confer a strong selective advantage. If horizontal transfer has occurred then the phylogeny and origins of a SOD may be indistinct. Horizontal transfer occurs readily in bacteria. There is evidence of a recent horizontal transfer of an FeSOD from bacteria to the protist *Entamoeba histolytica* based on un-rooted phylogenetic trees

(Smith *et al.*, 1992). Subsequently, FeSODs from protists do not appear in many published phylogenetic trees, possibly because they will cluster with bacteria.

The organelles of modern eukaryotes, chloroplasts and mitochondria, are believed to be derived from bacterial symbionts that have fused genomes with a primitive eukaryote host (Dyall *et al.*, 2004). The eukaryote SODs, in particular the organelle-specific SODs, may have descended from either the host or the symbiont.

1.7.4 Recent radiation

The time scale for SOD evolution is long, in the order of billions of years. It is difficult to tell if the radiation of Cu/ZnSOD and Fe/MnSOD into all orders of life is a relatively recent evolutionary event or an ancient event. Many have constructed cladograms based on DNA and protein sequence for all three SOD families to investigate phylogenetic relationships. Cladograms have been constructed for the Cu/ZnSODs (Livesay *et al.*, 2003), Fe/MnSODs (Fink & Scandalios, 2002, Schäfer & Kardinahl, 2003), NiSODs (Dupont *et al.*, 2008) and multiple families (Landis & Tower, 2005, Smith & Doolittle, 1992, Zelko *et al.*, 2002). It is difficult to determine when the branch points occurred relative to major evolutionary events such as the rise of molecular oxygen or the separation of eukaryotes and prokaryotes (Kirschvink *et al.*, 2000).

1.7.5 Multiple SODs

It may be advantageous for organisms to have multiple SODs as this may allow variable control of redox potentials or take advantage of whichever metal cofactor is most prevalent in the environment. Humans have an MnSOD, a dimeric Cu/ZnSOD and a tetrameric Cu/ZnSOD (Oury *et al.*, 1996), targeted to the mitochondria, cytoplasm, and extracellular space respectively. It appears that there are multiple SOD isozymes in plants (Rodríguez-Serrano *et al.*, 2007, Kukavica *et al.*, 2005). It is difficult to establish which of the SODs entered a genome first and which arrived most recently.

1.7.6 Transferring information between SOD families

There will be some commonalities between the SOD families that are due to convergent evolution and being subjected to similar selective pressures. However, conclusions drawn from the evolution of one SOD family may not be directly transferred to another SOD family. As the three SOD families have distinct origins, each with unique structure, each SOD family should be treated uniquely.

1.7.7 Differences in SOD expression

For many organisms, SOD expression, and hence redox state of cells, is tightly controlled. There can be changes in SOD expression brought about by changes in the environment and stage of life cycle, and as a result of disease and aging. For instance, *Escherichia coli* has an Fe-specific SOD (*Ec*-FeSOD) that is constitutively expressed and an Mn-specific SOD (*Ec*-MnSOD) that is expressed as a result of oxidative stress (Schiavone & Hassan, 1988). There are also variations in the spatial expression of SODs. There are SODs that are exported from cells, are membrane associated, are located in the cytoplasm and, in eukaryotes, are subject to organelle-specific expression and/or location. Conclusions and inferences drawn from one SOD in one unique environment may not be relevant to related SODs in divergent environments.

1.7.8 Post-transcriptional control of SODs

As well as tightly controlling the transcription of SOD genes, many eukaryotic organisms also increase the number of SODs produced with splice variation (Shao *et al.*, 2007, Fink & Scandalios, 2002). As well as altering the amino-acid sequence of peptides, splice variation may affect mRNA stability. There has been little investigation into how splice variations affect catalytic activity of SODs.

Many of these limitations listed above can apply to the evolution of any modern enzyme. There is much in common between a palaeontologist and an evolutionary enzymologist, as both have to make suppositions about the past based on limited information that is available in the present.

1.8 Oligomers

The selective pressures to evolve and then maintain oligomers are likely to be multi-factorial but likely involve control of conformational freedom (Hammes-Schiffer & Benkovic, 2006), structural stabilisation (Jaenicke, 1991) and substrate specificity (Griffin *et al.*, 2008). All three families of SODs are known to form oligomers. The Cu/ZnSODs are known to be functional as monomers, dimers and tetramers. For the Fe/MnSODs monomers are inactive and members absolutely require dimerisation for activity. In addition, some members of this family also go on to form tetramers, discussed more in section 2.4. The recently identified NiSODs have been detected as functional hexamers but it is unclear if monomers have activity.

1.9 Convergent evolution with convergent mechanism

The Cu/Zn, Fe/Mn and Ni families of superoxide dismutases are examples of convergent evolution as they perform the same enzymatic function but have evolved from unique ancestors. This is apparent from the comparative examination of the protein folds (refer to Figure 1-2) as well as the active sites (refer to Figure 1-3). This is analogous to the catalytic triads of serine and cysteine peptidases, which perform the same or similar chemistry but have evolved from different protein folds (Barrett & Rawlings, 2001). All three SOD families require metal cations at the active site for activity as the metal cations more readily undergo redox chemistry than polypeptides. But overall, the catalysis occurs with a similar mechanism: refer to Equation 1 and Equation 2, producing the same end products, oxygen and hydrogen peroxide, and not for example oxygen and water.

Figure 1-3. All three images are a combination of ball-and-stick to show the important active-site residues and ribbon representation to show secondary structure. The bonding between transition metal ion co-factors and active-site side chains and solvent molecules is shown as dashed lines. The active sites of the three SOD families are unrelated, but all have basic residues coordinating active-site molecules and nearby solvent molecules.

The top image was generated from the submitted atomic coordinates 2SOD and shows the active site of a Cu/ZnSOD. The cartoon representation of eight residues, that obscure the active site, has been omitted for clarity. The Cu^{2+} ion is coordinated by four histidines, one of which is also a ligand for the Zn^{2+} along with two other histidines and an aspartate. The fifth ligand of the Cu^{2+} ion is a solvent molecule, which dissociates when the metallo-enzyme is reduced to Cu^{+}. It is believed that a conserved arginine has a role in catalytic turnover.

The central image, derived from 1ISA, shows the Fe coordinated to three histidines, an aspartate and a solvent molecule stabilised by a hydrogen bond to a glutamine. Coordination occurs in a trigonal-bipyramidal arrangement. A well conserved tyrosine that has roles during catalytic turnover is also shown.

The bottom image of the active site of an NiSOD is derived from the coordinates 1T6U. Shown is the Ni^{2+} coordinated to two cysteines, a histidine and the N terminus of the peptide. Also shown is a nearby tyrosine that is expected to have similar roles to the conserved tyrosine of Fe/MnSODs. Here and elsewhere carbon atoms are shown in yellow, oygen in red, nitrogen in blue and sulfur in gold.

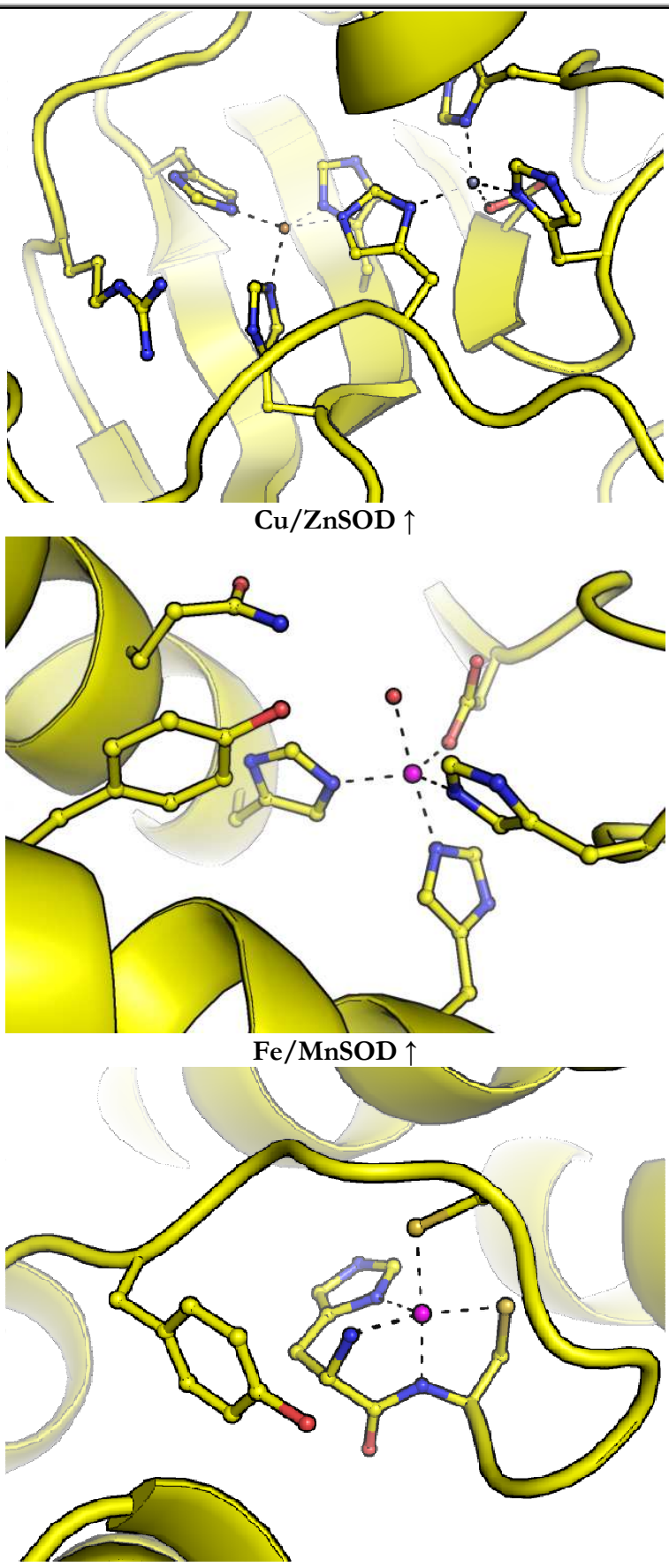

Figure 1-3. Comparison of the active sites of the three superoxide dismutase families.

$$(SOD\text{-}M^{+}) + O_2^{-} + H^{+} \rightarrow (SOD\text{-}M)\text{-}H^{+} + O_2$$

Equation 1

$$(SOD\text{-}M)\text{-}H^{+} + O_2^{-} + H^{+} \rightarrow (SOD\text{-}M^{+}) + H_2O_2$$

Equation 2

M is the transition-metal ion(s) characteristic of each SOD family. These cations are found in trace amounts in the environment. During catalytic turnover, active-site cations are alternately reduced by superoxide then oxidised by superoxide. In Cu/ZnSODs the active-site copper cycles between Cu^{2+} and Cu^{+}. FeSODs cycle between Fe^{3+} and Fe^{2+}, and MnSODs between Mn^{3+} and Mn^{2+}. For NiSODs the active site alternates between Ni^{3+} and Ni^{2+}. All three SOD families appear also to couple the uptake of a proton to the reduction of the metal ion. The location of proton binding is unknown for each family and is difficult to determine experimentally.

The evolution of classical SOD activity requires four things to occur: a protein with some structural elements evolves, the protein develops affinity for a redox-active metal ion, weak superoxide dismutase activity occurs and then random mutation improves specific activity. The early ancestor of SOD proteins probably had very low specific activity and may simply have been involved in metal storage and bioaccumulation. The ultimate selective pressure that caused convergent evolution in SODs is the superoxide molecule, which is invariant. This negatively charged free radical will lose an electron to a transition-metal cation in its oxidised state, such as those bound at the active site of SODs, forming molecular oxygen and, on the other hand, superoxide will readily couple the gain of an electron from the reduced transition-metal cation to proton uptake forming hydrogen peroxide.

There are suggested reaction schemes for each of the three SOD families and for the roles played by side chains close to the active site. These include proposed hydrogen-bonding partners for transition states and potential sources of protons. These schemes are based largely on the native structures, structures with small-molecule inhibitors, coordination chemistry, and spectroscopy.

The NiSODs are the least studied SOD family, with the narrowest distribution, so there is little known about internal variation in this group. Within the Cu/ZnSOD and Fe/MnSOD there are measureable differences in catalytic turnover, post-translational modifications, pH dependence, quaternary structure, thermal stability and inhibition by small molecules. Some of this variation can be explained by point mutations, other

variation will be the result of insertions and deletions into peptide sequences. At present the variations seen in structure and function of Cu/ZnSOD and Fe/MnSOD can not be accurately predicted from sequence alone.

2 The Fe/MnSOD family

Our research interest is primarily in the Fe/MnSOD family, which through minor variations in amino-acid sequence achieves a wide variation in metal specificity, catalytic activity, inhibitor specificity and oligimerisation patterns. All the members of this family contain the same basic protein fold, derived from a common ancestor, and have a highly conserved active-site structure and dimer interface. At present many of these observed functional differences lack a structure-based explanation. In contrast to many protein folds, for example the TIM barrel $(\beta\alpha)_8$ fold, the Mn/FeSOD fold is associated, so far, only with enymes showing superoxide dismutase activity.

There is pronounced variation by individual members within this protein family as to how much catalytic turnover each of the metal cofactors, Fe and Mn, elicits. There are members that are highly metal specific; there are also "promiscuous" members that are catalytically active with either metal ion, which are termed cambialistic. The two most well characterised MnSODs are from *E. coli* (*Ec*-MnSOD) and the human mitochondrial variant (*mito*-MnSOD), while the most well studied FeSOD is from *E. coli* (*Ec*-FeSOD). The most studied example of a cambialistic SOD is from *Propionibacterium shermanii* (*Psherm*-camb-Fe/MnSOD). All of these enzymes are well characterised biochemically and spectroscopically and have had their native structures solved as well as the structures of various point mutants.

2.1 Genomic era

The rapid increase in the number of known genomes has meant that there is now a multitude of known Fe/MnSOD sequences available. The annotation of these genes has been a largely computer-automated process, based on similarities to known genes rather than on direct measurement of biochemical assays. The limitations of automated annotation have been commented on for bacteria (Stothard & Wishart, 2006) and for higher organisms (Brent, 2008, Birney *et al.*, 2007).

There may be SODs that are biologically active with Mn that have been misclassified as FeSODs on the basis of sequence similarity. The reciprocal may also be true for FeSODs that have been categorised as MnSODs. Cambialistic enzymes are harder to identify than metal-specific SODs, and they are likely to be misclassified as MnSODs or FeSODs. There may also be pseudo-genes, which code for inactive proteins that have been annotated as functional genes. Pseudo genes are likely to arise from gene duplications and subsequent loss of function. Errors made during automated annotation

will only be identified during functional assays where activity is tested with each metal cofactor. Some efforts have been made to improve the annotation of MnSODs and FeSODs (Wintjens *et al.*, 2008). However, once metal-specific activity has been definitively determined biochemically, automated annotation can be superseded.

2.2 Macromolecular structure and contribution to active-site architecture

The structure of the monomer of Fe/MnSOD is highly conserved, made up of two domains that both contribute side chains to the active site; refer to the central image of Figure 1-2. The N-terminal domain is α-helical and dominated by two long helices each of which contributes a metal-binding histidine to the active site. The C-terminal domain features a motif of three strands of β-sheet surrounded by a number of short helices. Directly following the third strand of the β-sheet, there is a highly conserved loop structure. This contributes the third metal-binding histidine and the aspartate ligand. Other residues of this conserved loop contribute to the dimer interface. The active site is buried between the two domains and stabilised by an extensive network of hydrogen bonds from residues in both domains, and across the dimer interface, as described in more detail below.

As noted earlier, all three SOD families form oligomers, with a stoichiometry of one active site per monomer. The formation of the Fe/MnSOD dimer is absolutely required for full enzymatic activity and all structures of Fe/MnSODs that have been solved feature a common dimeric unit. Apo forms of Fe/MnSODs, which have been generated by using chelating agents, have subsequently crystallised as dimers. This indicates that the metal binding is not absolutely required for monomer stability and dimer formation. Apo forms of metal-specific Fe/MnSODs that have been reconstituted with incorrect cations also form stable dimers (Edwards, Whittaker *et al.*, 1998).

2.3 Dimer interface

Residues from one monomer stabilise the active site of their dimer partner, as shown in Figure 2-1. Of particular interest is a conserved glutamate, residue number 170 in the *Ec*-MnSOD numbering, which protrudes into the active site of the neighbouring monomer and makes a hydrogen bond with an active-site histidine, residue number 171 in *Ec*-MnSOD. The structure of the dimer interface is highly conserved, including several conserved water molecules.

The conserved dimer interface and the histidine-glutamate bridge suggest a possible communication pathway between the two active sites. Point mutants of the glutamate

residue disrupt dimerisation and abolish metal-specific activity (Whittaker & Whittaker, 1998). It is plausible that there are allosteric effects across the dimer interface of Fe/MnSODs. The binding of substrates (or products) in one monomer may influence the structure and dynamics of the active site of the other monomer. Cooperative behaviour may explain, in part, why the catalytic turnover is so high in Fe/MnSODs. Detection of monomer-to-monomer communication is difficult to detect in intact Fe/MnSODs as acquiring unambiguous information from individual monomers of a dimer pair is experimentally formidable.

Another intersubunit hydrogen bond that has been investigated by using a point-mutation approach is between His30 and Tyr174 in *Ec*-MnSOD. The mutants H30A-*Ec*-MnSOD, H30N-*Ec*-MnSOD and Y174F-*Ec*-MnSOD have lowered specific activities that are 30%, 38% and 41% respectively of the wild-type (Edwards *et al.*, 2001b).

All of the Fe/MnSODs that have been solved by X-ray crystallography are slightly asymmetric, with minor differences between one monomer and other within the asymmetric unit. The asymmetric nature of the Fe/MnSODs is usually manifested as differences in solvent structure, alternate rotamers and asymmetries in temperature factor distribution. For example, the structure of *Ec*-Fe^{2+}SOD (Lah *et al.*, 1995) crystallised as a dimer in the asymmetric unit with pronounced differences in water structure between the A and B subunits close to their active sites. The asymmetric crystal structures seen may represent asymmetry seen in the biological unit *in vivo*, but may be the result of different local environments due to different crystal contacts within the crystal.

Another consequence of a conserved dimer interface between the FeSODs and the MnSODs is the appearance of hybrid SODs with one half of the obligate dimer being an FeSOD and the other an MnSOD. This occurs in *E. coli* where there is co-expression of *Ec*-FeSOD and *Ec*-MnSOD and a hybrid (*Ec*-hybridSOD) can be detected (Dougherty *et al.*, 1978). The hybrid could be separated from *Ec*-FeSOD and *Ec*-MnSOD by isoelectric focussing and differential centrifuging. The *Ec*-hybridSOD was moderately stable; however, after several months it had converted to dimer *Ec*-FeSOD and *Ec*-MnSOD. The hybrid has activity and an inhibitor profile that is a mixture between *Ec*-FeSOD and *Ec*-MnSOD (Clare *et al.*, 1984), although this research was hampered by the inability to perform iron-specific reconstitution experiments without denaturing the enzyme.

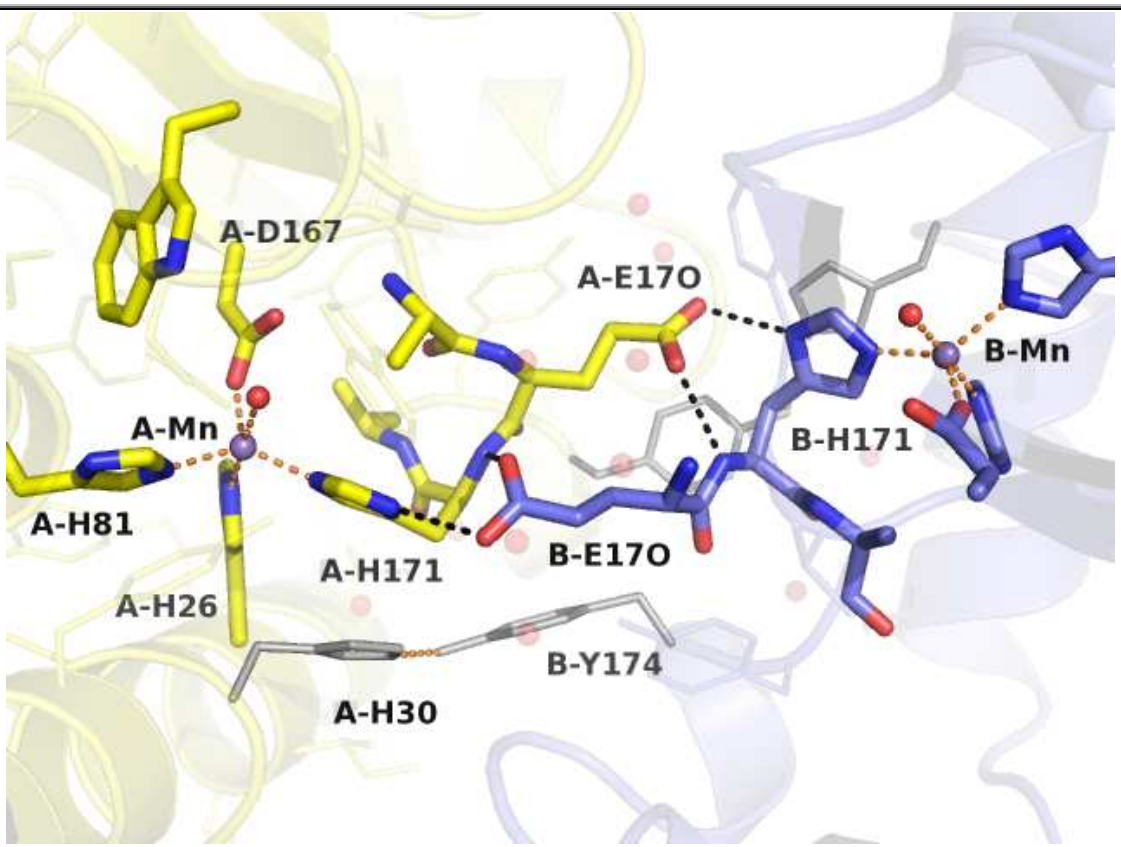

Figure 2-1. Dimer interface of *Ec*-MnSOD showing contributions to the active site by the dimer partner.

Figure 2-1. Active-site and dimer-interface residues are shown in stick representations; other residues are shown as transparent sticks and transparent cartoon. Solvent molecules that line the dimer interface are shown as transparent red spheres. The colour of carbon atoms in the A chain is yellow, and in the B chain is slate. Nitrogen atoms are shown in blue, oxygen in red, and active-site manganese ions in purple. The active-site Mn of chain A is coordinated by four residues *A*_His26, *A*_His81, *A*_His171, *A*_Asp167 and a solvent molecule. An adjacent residue *A*_Glu170 protrudes into the active site of the neighbouring B monomer and makes two hydrogen bonds with *B*_His171, one with the main chain and the other with the side chain. The reciprocal arrangement with *B*_Glu170 protruding into active site of the A monomer also exists, hydrogen bonding with *A*_His171. The dual glutamate-histidine bridge links the two active sites. The hydrogen bond between *A*_His30 and *B*_Tyr174 is shown as an orange dashed line. Both residues are depicted as thin grey sticks and are labelled. The reciprocal hydrogen-bond residues, *B*_His30 and *A*_Tyr174, are also shown as grey sticks but are partially obscured by the active site of the B chain. The image was generated using pymol, which is unable to produce italics.

2.4 Differences in quaternary structure

After dimerisation some members of the Fe/MnSOD family go on to form tetramers and some do not. In contrast to the dimerisation pattern, which is highly conserved, the patterns seen in tetramerisation are divergent (Wagner *et al.*, 1993); refer to Figure 2-2. The tetramer interfaces are located away from the active site and residues involved in

dimer formation. Tetramers are mainly formed by interactions across the N-terminal domains, but are different for each tetramer type.

There may be functional consequences to forming tetramers. The formation of a tetramer will reduce the dynamic freedom of the individual monomers, which in turn may limit the conformational freedom at the active site. A consequence of tetramer formation is that the relative amount of peptide surface that is buried increases, and less of the monomer interacts with solvent. In solution, a tetramer of Fe/MnSOD will have twice the positively charged active sites relative to the dimer and hence this may have consequences in the electrostatic steering of superoxide towards active sites. Formation of dimers, and tetramers in some cases, may simply be a way to provide thermal stability to the mature fold and/or prevent degradation by proteases. Human mitochondrial MnSOD (*mito*-MnSOD) forms a stable tetramer that has a half life of 3 years at 37°C. The polymorphic variant mutant I58T-*mito*-MnSOD disrupts the tetramer interface and has a half life reduced to 3 hours (Borgstahl *et al.*, 1996). On the other hand, when MnSODs and FeSODs are co-expressed, tetramers may have evolved to limit the existence of hybrid SODs.

There are selective pressures to evolve and maintain tetramers in some organisms, contrasted to other organisms where selective pressures maintain the dimer form. The different patterns of tetramerisation are most likely an example of convergent evolution where SODs have evolved different tetramer interfaces.

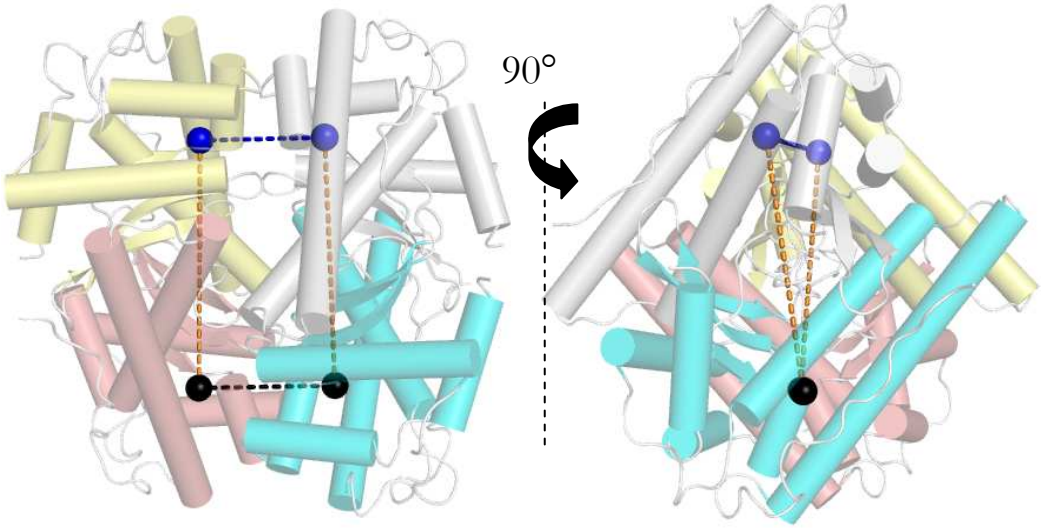

Methanobacterium thermoautotrophicum

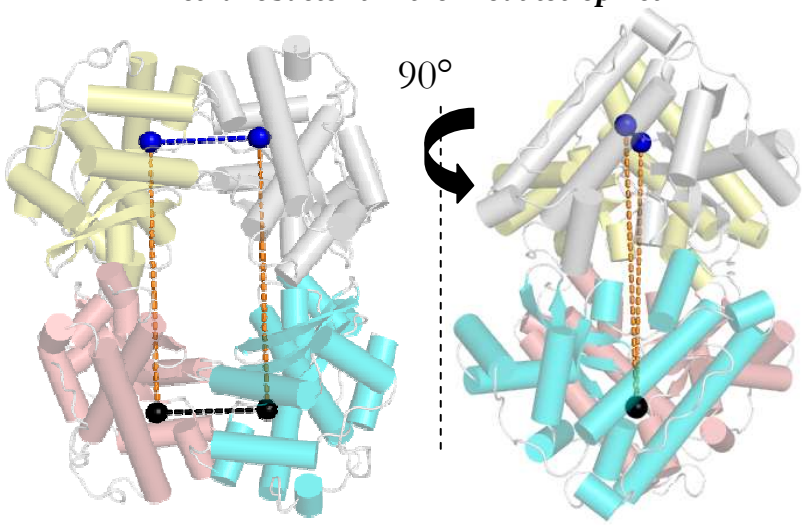

Thermus thermophilus

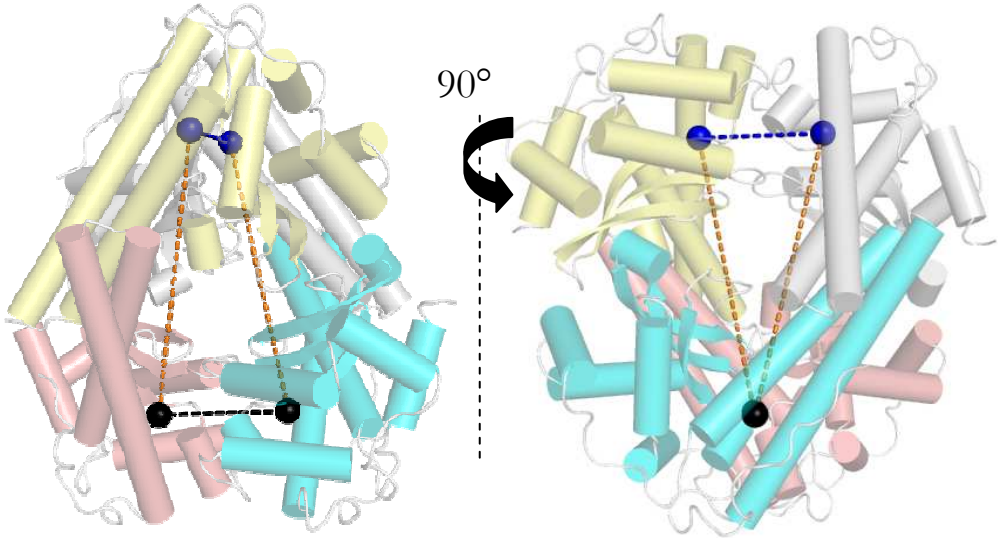

***Homo sapiens* mitochondrial**

Figure 2-2. Differences in tetramer formation amongst the Fe/MnSODs.

Figure 2-2**.** Three different tetramers types are depicted, all orientated with respect to the lower obligate dimer pair. In this dimer, one chain is coloured salmon and the other cyan. The black spheres depict active-site metal ions and the two active-site metal ions are joined by dashed black lines. In the second dimer pair, secondary structure elements are coloured yellow and grey, with active-site metal ions shown as blue spheres and joined by a blue dashed line. Orange dashed lines show the distance from one active-site metal to the closest metal centre across the tetramer interface. Right-hand images show the same tetramers rotated 90° with respect to the black dashed line. The topmost pair of images is derived from the FeSOD from *Methanobacterium thermoautotrophicum* (1MA1), the middle pair depicts the MnSOD from *Thermus thermophilus* (3MDS), and the lower pair shows the *Homo sapiens* mitochondrial MnSOD (1NOJ).

In all three structures the dimer interface is conserved. The distance between metal centres (the black and blue dashed lines) is highly conserved, with distances ranging from 18.1 Å to 18.3 Å. This is in contrast to the variable distances of the tetramer interface (the orange lines), which are 33.2 Å, 45.3 Å and 41.0 Å for the top, middle, and lower images respectively. There are also differences in orientation of the tetramers. The tetramer interface of *mito*-MnSOD is tetrahedrally twisted with respect to the *Methano*-FeSOD and *Thermus*-MnSOD. In both *Methano*-FeSOD and *Thermus*-MnSOD the four metal ions roughly form a plane with metal ions at the vertices. There are also differences in the extent of the tetramer interface; the tetramer interface of the *Methano*-FeSOD (top) contains a larger buried surface than the *Thermus*-MnSOD (middle) or *mito*-MnSOD.

2.5 Solvent-access funnel to the Fe/MnSODs

Along with high conservation of the active site and dimer structure, the solvent-access funnel is also highly conserved. Therefore, the way substrates, products and inhibitors enter and leave the active site is also conserved. In particular, there is a well defined narrow “gate” between the solvent and the metal-containing active site; refer to Figure 2-3. This gate is made up by four atoms (*Ec*-MnSOD numbering), three of which are contributed by the A monomer, *A*_His30_ND1, *A*_Tyr34_OH, and *A*_Trp169_CZ. The fourth atom, *B*_Glu170_OE2, is contributed by the B subunit. The narrow nature of this gate means that only small inhibitors, which are two or three atoms long, can enter the active site and interact with the metal centre, whereas larger negatively charged inhibitors, such as thiocyanate or sulfate, are weak inhibitors (Bull & Fee, 1985). The separation of active-site metal and its ligands from the bulk solvent is confined to Fe/MnSODs and is not seen in Cu/ZnSODs or NiSODs.

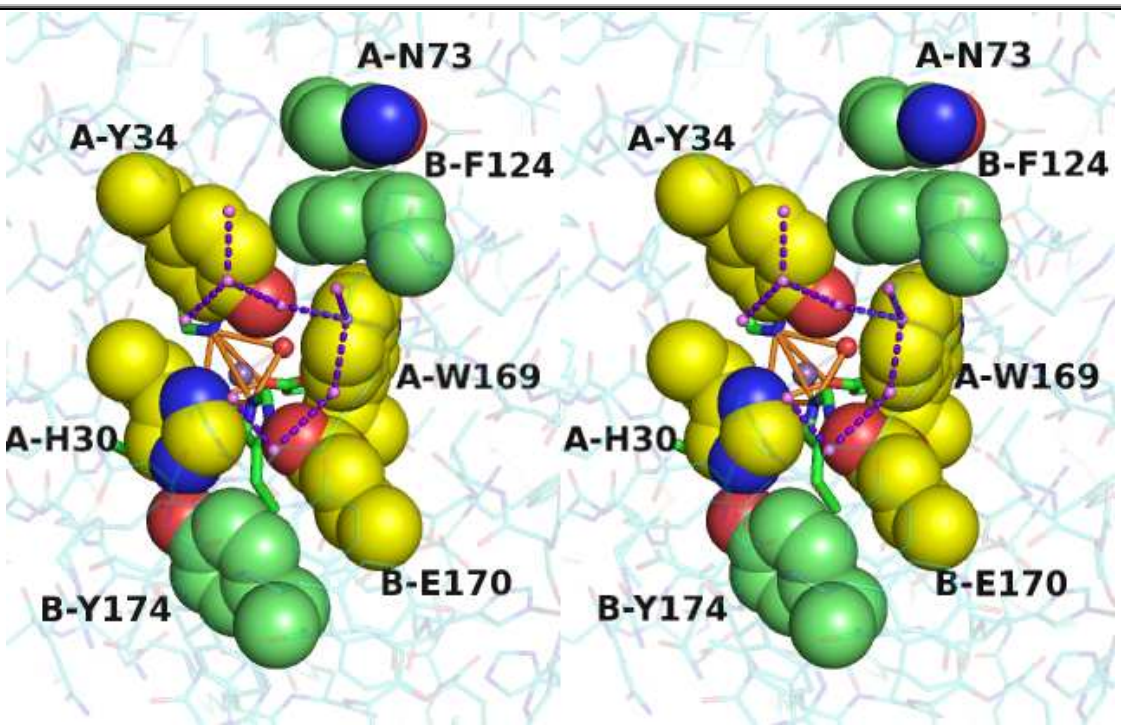

Figure 2-3. Wall-eyed stereo-diagram of the gating residues of the solvent-access funnel from *Ec*-MnSOD.

Figure 2-3**.** The aspect shown here is looking down the solvent funnel towards the trigonal-bipyramid of the active site (of *Ec*-MnSOD, derived from coordinates 1VEW). The solvent-access funnel is made up from both members of the dimer pair, A and B. It is believed that substrates, inhibitors and products enter and leave the active site by passing through the small "gate" between the active site and the solvent. The side chains of the four gating residues, *A*_His30, *A*_Tyr34, *A*_Trp169 and *B*_Glu170, are shown as space-filling spheres with nitrogen atoms coloured blue, oxygen red and carbon yellow. Three other important residues, *B*_Tyr174, *B*_Phe124 and *A*_Asn73, are shown as space-filling spheres with carbon atoms coloured green. There is a stabilising inter-dimer hydrogen bond between *B*_Tyr174_OH and *A*_His30_NE2. The position of the conserved active-site tyrosine is influenced by a hydrophobic interaction between *A*_Tyr34_CE1 and *B*_Phe124_CZ. The hydrophobic residue *B*_Phe124 contributes to the dimer interface by protruding into a cavity between *A*_Tyr34 and *A*_Asn73. The trigonal-bipyramidal coordination of the penta-coordinate active site is shown as solid orange lines. The manganese cofactor is shown as a purple sphere, coordinated solvent is shown as a red sphere and active-site residues are shown as sticks. However, the active-site is partially obscured by gating residues. Water molecules that line the solvent-access funnel are shown as small pink spheres, linked by purple dashed lines that represent hydrogen bonds.

Another conserved motif that is seen in the solvent-access funnel of Fe/MnSODs is the presence of positively charged residues, such as lysine and arginine. These residues are believed to electrostatically steer the negatively charged superoxide ion towards the active site. Mutating lysine to non-polar residues (Gabbianelli *et al.*, 1997) or chemically modifying these residues (Benovic *et al.*, 1983) reduces catalytic activity in

Psherm-camb-Fe/MnSOD. There are comparable residues in Cu/ZnSODs and NiSODs (Wuerges *et al.*, 2004). These charged groups, as well as the overall positive charge at the active-site, make the solvent-access funnel of Fe/MnSODs an extremely positive local environment; refer to Figure 2-4.

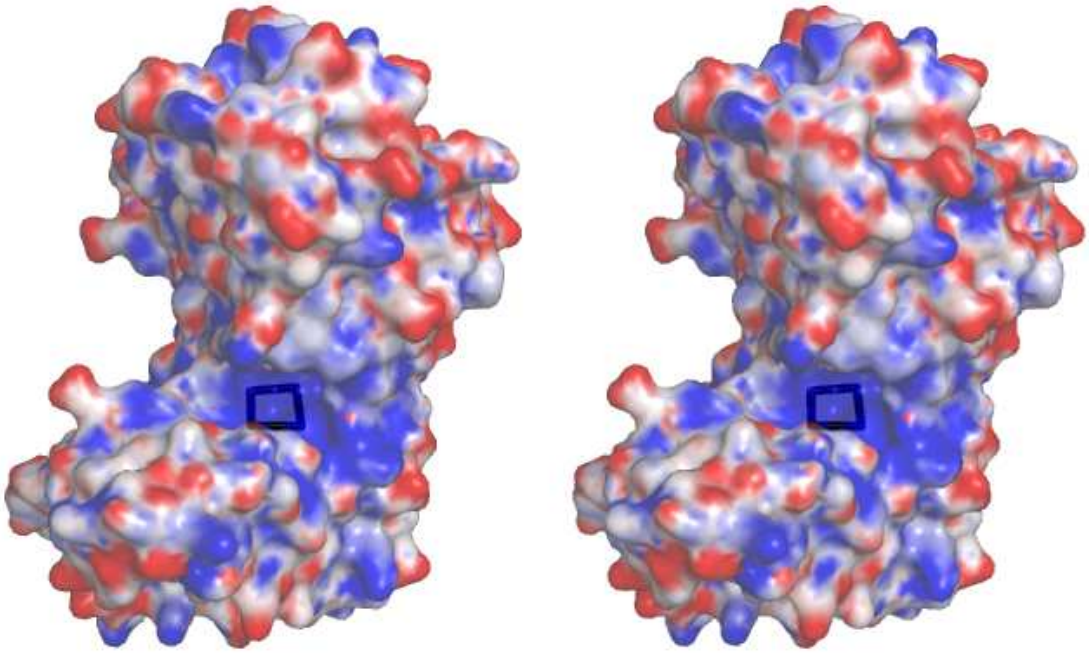

Figure 2-4. Wall-eyed stereo-diagram showing the solvent-accessible surface of *Ec*-FeSOD coloured by electrostatic potential.

Figure 2-4**.** The solvent-accessible surface is shown as a slightly transparent surface. The surface is coloured from negative (-15 kT/e), neutral, positive (15 kT/e) as red to white to blue respectively. The four atoms of the "gate" between the buried active site and the solvent are shown as the corners of the black rhomboid. The "gate" is located at the bottom of a positively charged pocket, while the rest of the surface displays a more variable range of charge distribution. The negatively charged superoxide free radical is drawn into the positively charged pocket, passes through the gate and then enters the active-site for dismutation. This representation is derived from the coordinate set 1ISA, with electrostatic potential generated by APBS (Baker *et al.*, 2001). The atoms that make up the gate for *Ec*-FeSOD are 1ISA_*A*_H31_ND1, 1ISA_*A*_Y34_OH, 1ISA_*A*_W158_CZ3 and 1ISA_*B*_E159_OE2.

2.6 Fe/MnSOD knowledge derived from spectroscopy, structures and biochemistry

The four protein ligands that bind the metal ion in Fe/MnSODs are universally conserved and form the first coordination shell. The fifth ligand is a solvent-derived molecule. The identity of the fifth ligand has been ascribed as either a water molecule or an hydroxide ion (Lawrence & Sawyer, 1979) depending on pH. It is now widely believed that at physiological pH ranges when the active-site metal ion is oxidised, the

coordinated molecule is an hydroxide. Upon the reduction of the active-site metal, either during catalysis or artificially manipulated, there is an associated uptake of a proton into the active site which is widely believed to convert the bound hydroxide to a water molecule.

The coordination of the metal ion at the active site of Fe/MnSODs is always at least penta-coordinate and sometimes hexa-coordinate. A sixth solvent-derived ligand has been observed in MnSODs with various spectroscopic (Whittaker & Whittaker, 1996) and crystallographic techniques (Borgstahl *et al.*, 2000, Schmidt, 1999) and is most likely to be a second hydroxide ion. This sixth ligand is more prevalent at high pH and at cryogenic conditions. The sixth ligand binds in a position that is the likely binding place of superoxide and small-molecule inhibitors such as azide, and hence explains why the catalytic turnover of Fe/MnSODs decreases in alkaline conditions (Maliekal *et al.*, 2002), as the coordinated hydroxide is a competitive inhibitor to superoxide at the active site.

2.7 Second shell and third shell of residues

Further out from the first shell of absolutely conserved amino acids and coordinated solvent molecules is a highly, but not absolutely, conserved second coordination shell that is linked to the first shell through covalent bonds, hydrophobic interactions, and an extensive hydrogen-bonding network. Point differences in the second coordination shell have been proposed as the reason for variations in metal specificity, pH dependence, inhibitor effects, *et cetera*. However, the second coordination shell also contains residues that are involved in the dimer interface and solvent-access funnel. Many of these residues are likely to have dual roles, both interacting with substrates as well as maintaining the overall fold structure and the structure of the active site. The residues of interest can be investigated by the generation of specific point mutants and measuring changes in activity, function and structure.

2.8 Wrong metal forms

In addition to the hybrid SODs mentioned in section 2.3, “wrong” metal forms also exist. It is possible to reconstitute Fe-specific SODs with manganese, abbreviated to Mn-FeSOD, and Mn-specific SODs with iron, here abbreviated to Fe-MnSOD (Clare *et al.*, 1984). *In vitro,* this is generally done with chelating agents to remove active-site metal ions with subsequent reconstitution with the “wrong” metal ion. The Mn-FeSODs

and Fe-MnSODs generally have less than 5% the activity of native FeSODs (Yamakura & Suzuki, 1980) and MnSODs (Ose & Fridovich, 1979), respectively.

The situation is more complex *in vivo*, where three forms of *Ec*-MnSOD have been isolated by HPLC from a uniform culture of *E. coli*: wild-type, completely iron-substituted, and a mixed form (Fe at one active site of the obligate dimer and Mn at the other) (Beyer & Fridovich, 1991), here abbreviated to WT-*Ec*-MnSOD, *Ec*-Fe-MnSOD and *Ec*-Mn/Fe-MnSOD respectively. The specific activity of WT-*Ec*-MnSOD was the highest, *Ec*-Fe-MnSOD retained 3% of the specific activity of WT-*Ec*-MnSOD and *Ec*-Mn/Fe-MnSOD retained 45% of the WT activity.

Perhaps the most intriguing information taken from the separation and isolation of WT-*Ec*-MnSOD, *Ec*-Fe-MnSOD and *Ec*-Mn/Fe-MnSOD is that they could be separated at all. The wrong metal forms had altered isoelectric points and were able to be separated using chromatography. A change of one atomic number of the bound cation at one active site of the dimer pair alters how the enzyme interacts with the environment.

The metal specificity in some Fe/MnSODs is in stark contrast to the cambialistic SODs, which have appreciable activity with either Fe or Mn (Meier *et al.*, 1982). This leads to perhaps the most important question about the Fe/MnSOD family. How do the Fe/MnSODs achieve such variations in metal specificity by minor variations in primary amino-acid sequence while first-shell residues are absolutely conserved?

2.9 Metal specificity amongst Fe/MnSODs

Metal selectivity is thought to be determined by differences within the second coordination shell influencing the active site. The Fe/MnSOD family is derived from a common ancestor, but all members are obligate metallo-enzymes. The active-site architecture is highly conserved among Fe-specific, Mn-specific, and cambialistic Fe/MnSODs. A detailed hypothesis as to which residues are important for metal specificity is lacking, but several groups have investigated this property through point mutation approaches (Yamakura *et al.*, 2003) or sequence analysis (Wintjens *et al.*, 2008).

At present theories of how proteins fold and then interact with metal co-factors are extremely limited (Wilson *et al.*, 2004). The Fe/MnSODs generally fold in a local environment that is crowded with a wide variety of charged and uncharged organic and inorganic molecules and successfully incorporate the correct co-factor, but metal-ion

selection is thought to be determined by kinetic rather than thermodynamic processes as well as by metal bioavailability (Mizuno *et al.*, 2004).

The selective pressures that drive changes in metal specificity over time are unknown. The mutation event(s) required to change an MnSOD into an FeSOD or *vice versa* is (are) unknown. It is difficult to know whether an individual SOD has changed metal specificity recently, in the distant past, or at all. There are three possible scenarios for the evolution of the Fe/MnSOD family: the ancestor was Mn-specific, the ancestor was Fe-specific or the ancestor was cambialistic. As the Fe/MnSOD family most likely evolved in primordial oceans, where there are trace amounts of Fe and Mn, it is likely that the ancestor of the Fe/MnSOD had some enzymatic activity with both metals.

2.10 Metal specificity as a method of control

The other aspect of metal specificity is metal selectivity. When metal-specific Fe/MnSODs are expressed in environs where both metal ions are present, then they preferentially bind the correct metal (Clare *et al.*, 1984) other metallo-proteins lack the ability to discriminate between metal ions (Tottey *et al.*, 2008). When Fe-specific and Mn-specific SODs are reconstituted with the "wrong" metal cofactor, they are stable and long lived but there is usually a significant drop of activity. In most environments both Fe and Mn are present so there will always be a small pool of inactive enzyme. When the homeostatic balance between metal ions and their target proteins is perturbed then "wrong" metal forms become more important.

With the evolution of cellular organelles in eukaryotes, the availability of metal ions in the cytoplasm differs from that within organelles. This may be why some eukaryotes have an extracellular FeSOD and an MnSOD targeted to the mitochondria where there is virtually no free iron. The majority of mitochondrial Fe is tightly regulated and associated with Fe-S clusters and haem groups in the electron-transport chain, whereas there are fewer roles for Mn in mitochondria. In a low Fe environment there would be a selective advantage to having an Mn-specific SOD. The situation is more complicated in plants where there are many organelle-specific Fe/MnSODs, and these enzymes are less well characterised. For instance, in maize, in addition to at least four Cu/ZnSODs (Fink & Scandalios, 2002) there are at least (Tardat & Touati, 1991) four Fe/MnSOD genes, which have differing patterns and locations of expression including an embryo-specific variant (Zhu & Scandalios, 1993).

In humans the tight regulation of iron metabolism means that there are very low levels of free iron in solution, which limits bacterial growth. In the facultative gut anaerobe *E. coli* there is an FeSOD that is constitutively expressed and an MnSOD that is transiently expressed as a result of oxidative stress; this may be due to limitations in free iron concentration (Tardat & Touati, 1991).

2.11 Serious alterations to hydrogen-bonding networks

Mutations of residues in the second coordination shell critically impair enzyme function as well as disrupting the hydrogen-bonding network. Perhaps the most discussed hydrogen-bonding pattern in Fe/MnSODs links the conserved tyrosine of the solvent-access funnel to the metal-binding aspartate *via* a coordinated solvent and a glutamine (or histidine). An overlay of this hydrogen-bonding pattern is shown in Figure 2-5, for *Ec*-MnSOD, *Ec*-FeSOD and *Psherm*-camb-FeSOD. In *Ec*-MnSOD this pathway involves four atoms, Y34_OH to Q146_NE2 (of the second αβ domain), Q146_NE2 to the coordinated solvent and the coordinated solvent to D167_OD1 of a first shell residue. In *Ec*-FeSOD the pathway is similar, linking Y34_OH to Q69_NE2 (of the first α domain) to the coordinated solvent and to the D156_OD1 of a first-shell residue. In *Psherm*-camb-FeSOD, the equivalent pathway links Y35_OH to H146_NE2 to the coordinated solvent via H146_CE1, and finally to the D161_OD1. The second member of this pathway (glutamine or histidine) is variable in residue type and primary-sequence position.

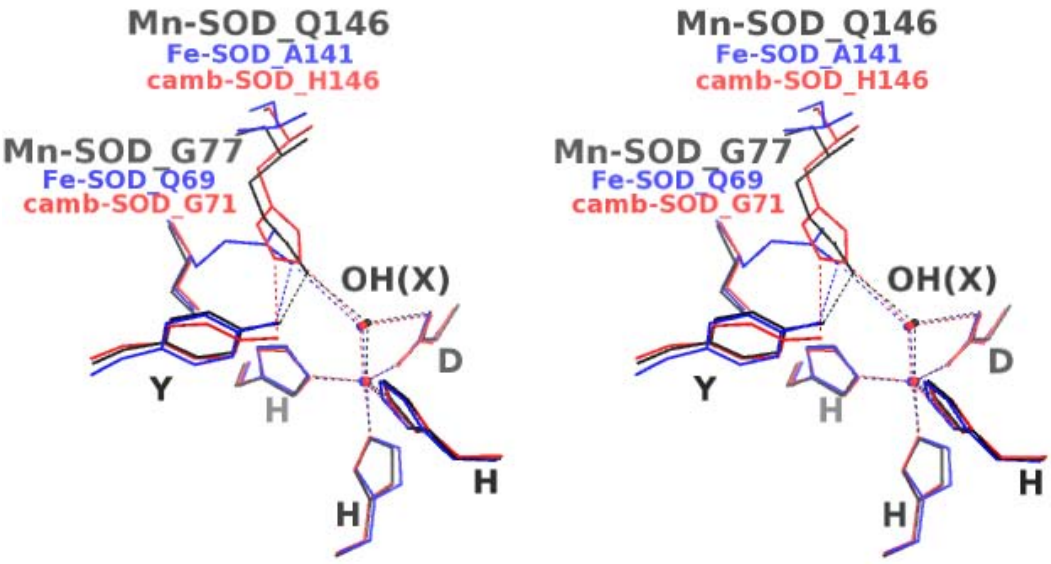

Figure 2-5. Wall-eyed stereo-diagram of a conserved hydrogen-bonding motif that links the metal-coordinated solvent molecule to the tyrosine within the solvent-access channel.

Figure 2-5. The figure was generated by overlaying the alpha carbon atoms of the three metal-binding histidines and aspartate residues labelled H and D respectively. Three structures are shown as lines, the black lines show *Ec*-MnSOD (1VEW), the red lines show *Psherm*-camb-FeSOD (1AR5) and the blue lines show *Ec*-FeSOD (1ISA). The fifth ligand, derived from solvent and labelled OH(X) and may either be a water or an hydroxide ion, is stabilised by a hydrogen bond to the OD1 of the active-site aspartate residue. The atom OH(X) forms a second hydrogen bond to a residue that is variable between *Ec*-MnSOD, *Psherm*-camb-FeSOD and *Ec*-FeSOD; these residues in turn hydrogen bond to the OH of the conserved tyrosine. In *Ec*-MnSOD the hydrogen bond is supplied by Q146_NE2 from a conserved loop; in *Psherm*-camb-FeSOD the equivalent atom is H146_NE2 in the deposited structure 1AR5. In reality, an alternate rotamer conformation of H146 may occur, in which case the hydrogen bond donor is H146_CE1. In both *Ec*-MnSOD and *Psherm*-camb-FeSOD the buttressing partner is a glycine (numbered 77 and 71 respectively) on a conserved helix. In contrast in *Ec*-FeSOD the equivalent residue is a glutamine that contributes the hydrogen bonding atom, Q69_NE2, into the active-site and is buttressed against A141. There are differences in the lengths of hydrogen bonds, and differences in the angles between bonds, where Q69_NE2 of *Ec*-FeSOD is less optimally placed for hydrogen bonding compared to Q146_NE2 of *Ec*-MnSOD and H146 of *Psherm*-camb-FeSOD.

Mutating the conserved Gln146 in *Ec*-MnSOD has greater effects on activity and on the hydrogen-bonding network than mutations that affect the conserved tyrosine. In the mutant Q146E-*Ec*-MnSOD, activity has been abolished, whereas Q146L-*Ec*-MnSOD and Q146H-*Ec*-MnSOD mutants have 5-10% of wild-type activity and show altered optical absorption spectra. Of this series of mutants, Q146H-*Ec*-MnSOD most closely resembles FeSODs, as there is some activity of Q146H-*Ec*-Fe-MnSOD at pH 7.8. When pH is lowered to 6.5, activity of Q146H-*Ec*-Fe-MnSOD is greater than that of Q146H-*Ec*-MnSOD (Edwards *et al.*, 2001a). The Q146L and Q146H mutants of *Ec*-MnSOD have altered orientations of the Tyr34, Trp128 and the coordinated solvent-derived fifth ligand.

A series of similar point mutants of the equivalent glutamine residue has been performed for the human mitochondrial form of MnSOD (Lévêque *et al.*, 2000). The mutant Q143H-*mito*-MnSOD had a 150-fold decrease in activity. The mutant Q143A-*mito*-MnSOD had a 250-fold decrease in activity. In the crystal structure of Q143A-*mito*-MnSOD, water molecules had moved into vacant positions where the residue Q143 would lie, providing a possible pathway for protons to reach the coordinated solvent-derived ligand. This conserved glutamine may have roles other than proton

transfer, such as stabilising the active site. Other mutants have even less activity: Q143V-*mito*-MnSOD, Q143N-*mito*-MnSOD and Q143E-*mito*-MnSOD.

The equivalent hydrogen-bonding pathway has been investigated in *Ec*-FeSOD. The conserved Gln69 is thought to be a hydrogen bond donor to the fifth ligand, the coordinated solvent-derived molecule. The mutants Q69H-*Ec*-FeSOD (hydrogen-bond donor and acceptor) and Q69E-*Ec*-FeSOD (hydrogen bond acceptor) have lowered activity and lower Fe content. The active sites of Q69H-*Ec*-FeSOD and Q69E-*Ec*-FeSOD are generally similar to the WT with minor changes in side-chain orientations (Yikilmaz *et al.*, 2007, Yikilmaz *et al.*, 2006), although the metal content of these mutants was not controlled.

2.12 Tyrosine of the solvent-access funnel

There have been several point-mutation studies of the tyrosine at the base of the solvent-access funnel. The most common approach is to mutate to a phenyalanine, such as Y34F-*Ec*-MnSOD which lowered the activity to 85% of the wild-type enzyme and the more "drastic" Y34A-*Ec*-MnSOD mutant that surprisingly retained full activity. In the crystal structure of these mutants (Edwards *et al.*, 2001a), or the human equivalent *mito*-Y34F-MnSOD (Guan *et al.*, 1998), the hydrogen bonding pattern is altered and water molecules move into the active site, to fulfil the role of WT-*Ec*-MnSOD_Y34_OH. These indicate that the solvent-access funnel tyrosine is not absolutely required for proton uptake into the active site of MnSODs and for catalytic turnover of superoxide. Also, mutants of Tyr34 have increased affinity for the inhibitors azide and fluoride (Tabares *et al.*, 2007, Whittaker & Whittaker, 1997a), and altered optical and EPR spectra, perhaps indicating that in WT-*Ec*-MnSOD the role of Tyr34 may be to isolate the active site from bulk solvent.

Mutations of this conserved tyrosine do not affect enzyme activity in MnSODs, but drastically decrease FeSOD activity. For instance, an equivalent mutation in the Fe-specific SOD (Y34F-*Ec*-FeSOD) decreases the activity to 40% of that for the WT-*Ec*-FeSOD (Miller *et al.*, 2005, Hunter *et al.*, 1997), a greater decrease than observed in *Ec*-MnSOD. This indicates that the role of the solvent-access funnel tyrosine is slightly different between FeSODs and MnSODs.

The selection pressure to maintain the conserved solvent-access funnel tyrosine in SODs is likely to be multifactorial. There is strong indication that this residue has structural roles in stabilising second-shell residues and that it is involved in "gating" of

the active sites to preferentially accept superoxide in favour of other negatively charged small molecules. In an *in vivo* situation where the enzyme will be exposed to a barrage of negatively charged by-products of metabolism, the tyrosine with its terminal OH moiety will provide an energy barrier that separates the positively charged active site from the cytoplasm, favouring the selection of superoxide over other larger negatively charged molecules.

The conserved tyrosine may also have roles in the passage of protons into the active site, as two protons are provided to the nascent peroxo ion in the second half-reaction. The tyrosine is close to both the solvent and the active site, and at physiological pH ranges tyrosine is protonated, making it a likely candidate for direct proton donation to the active site and subsequent re-protonation by bulk solvent. On the other hand, the tyrosine may be indirectly indicated in proton donation.

Similar work has been performed by introducing point mutations into first and second coordination shells of human mitochondrial MnSOD (*mito*-MnSOD), generally with little effect on the protein structure, but with great effects on the enzyme activity, for example W161F-*mito*-MnSOD (Cabelli *et al.*, 1999).

2.13 Product inhibition in MnSODs

At low concentrations of superoxide, MnSODs act at near diffusion-controlled limits. However, at higher concentrations of superoxide all MnSODs are subject to product inhibition by a relatively long-lived chemical species (Bull *et al.*, 1991), which saturate the enzyme, preventing dismutation of superoxide. Product inhibition has not been detected in the FeSODs (Bull & Fee, 1985). The exact chemical nature of the catalytic dead-end in MnSOD is unknown, but most evidence supports that it is a peroxo species (or a hydroperoxo) that is bound side-on (Carrasco *et al.*, 2007) to the catalytic site manganese, blocking the flow of superoxide ions and protons to the metal and its environs. Over time the by-product breaks down by first-order kinetics to leave the native enzyme. The human form of MnSOD is extremely prone to product inhibition, whereas bacterial forms are able to function in levels of superoxide that would saturate the human form. The Y34F-*mito*-MnSOD mutant suffers increased product inhibition (Guan *et al.*, 1998), indicating that product inhibition is influenced by the peptide component.

In humans, and other higher organisms, during normal metabolism, oxygen concentrations are tightly controlled and hence superoxide flux is well below saturating

levels and product inhibition is largely unimportant. Product inhibition becomes important in disease states when oxygen supply is disrupted and superoxide levels are increased.

2.14 Differences in inhibition by small-molecule inhibitors

It had been suggested by Bull and Fee (1985), before structural information became available, that there is an anion-binding pocket where weak inhibitors such as SCN^- and ClO_4^- could bind and that this binding was affected by a protonated group. Stronger inhibitors such as azide and fluoride (as well as substrate superoxide) could pass on to the active site. With the advent of detailed structures, this cavity is likely to be the substrate-access funnel and the protonated residue, the conserved tyrosine.

The interactions between small-molecule inhibitors and Fe/MnSODs are stable and long-lived. Inhibited enzymes have been investigated using spectroscopy and structural techniques, which have resulted in several solved structures. The most effective inhibitors of Fe/MnSODs are small, usually less than three atoms, negatively charged and interact with the bound cation. Inhibitors have to be small to enter the active site and get past the "gate" between the solvent-access funnel and the buried active site described in section 2.12. The most well studied inhibitors are azide and fluoride (Slykhouse & Fee, 1976). Negatively charged, but larger, inhibitors such as ClO_4^- and SCN^- have been shown to be weak inhibitors of *Ec*-FeSOD (Bull & Fee, 1985). This is in stark contrast to the Cu/ZnSOD and NiSOD families whose active sites are located close to the solvent and are able to be inhibited by larger negative ions such as SCN^-, Cl^- and SO_4^{2-}.

Azide (N_3^-) has been used often to investigate Fe/MnSODs, as it is an analogue for superoxide, being of similar size as well as having similar front-end orbitals. However, once associated with the metal centre it does not break down and it is able to persist long enough to facilitate structural and spectroscopic examinations.

Azide inhibits MnSODs, FeSODs and cambSODs. However, there are some differences in how azide interacts with the FeSODs compared to the MnSODs. At ambient temperatures and physiological pH ranges, N_3^- coordinates to the active site Fe of Fe^{3+}SODs, although less effectively than fluoride (Miller *et al.*, 2005). However, at similar pH and temperature ranges, N_3^- does not coordinate to the Mn centre of Mn^{3+}SODs, but it does interact. When temperature is lowered to cryogenic ranges, N_3^- does coordinate to the active-site metal (Whittaker & Whittaker, 1996). The transition

from room temperature Mn^{3+}SOD-N_3^--RT to an Mn^{3+}SOD-N_3^--cryo species has been assigned as a transition from outer-sphere to hexa-coordinate inner-sphere complex by using resonance Raman, CD and MCD spectroscopies (Jackson *et al.*, 2004). A similar approach has been used to study this transition using high magnetic-field electron paramagnetic resonance (HFEPR) (Tabares *et al.*, 2006). In *Psherm*-camb-Fe/MnSOD azide inhibition is dependent on the metal bound, with the *Psherm*-camb-FeSOD being more readily inhibited than *Psherm*-camb-MnSOD (Meier *et al.*, 1998). The crystal structure of *Psherm*-camb-FeSOD-N_3^- (Schmidt *et al.*, 1998) showed an azide orientation reminiscent of *Ec*-FeSODs-N_3^- (Lah *et al.*, 1995) and not *Pso*-FeSODs-N_3^- (Stoddard, Ringe *et al.*, 1990).

Fluoride has also been used as an inhibitor of Fe/MnSODs. It binds at the sixth ligand position of *Ec*-Fe^{2+}SOD and *Ec*-Fe^{3+}SOD in a pH-dependent manner (Miller *et al.*, 2005) and may also be able to displace the fifth ligand (Slykhouse & Fee, 1976). Fluoride is also an inhibitor of camb-FeSOD, and has been seen in crystal structures (Schmidt, 1999). Fluoride has also been used as an inhibitor of Mn^{2+}SODs, and shows a temperature-dependent transition similar to azide (Tabares *et al.*, 2006).

Nitric oxide has been used as an inhibitor of *Ec*-Fe^{2+}SOD and forms a six-coordinate adduct in a manner that may be analogous to the second half-reaction. In contrast, azide does not bind to the reduced form (Jackson *et al.*, 2003).

Although technically a product of the reaction, it was found that H_2O_2 selectively inhibits the FeSODs and not MnSODs (Asada *et al.*, 1975). In the past, differences in inhibition by H_2O_2 had been used to discriminate FeSODs from MnSODs (Kirby *et al.*, 1980, Clare *et al.*, 1984). However an FeSOD from *Methanobacterium thermoautotrophicum* that is resistant to H_2O_2 was identified a few years later(Takao *et al.*, 1991). This inhibition of FeSODs results from the chemical modification of the enzyme by H_2O_2 while in MnSODs H_2O_2 acts as a competitive inhibitor.

2.15 SODs with very low affinity for azide

There are some FeSODs that have very low affinity for azide and decreased susceptibility to hydrogen peroxide, which is a pattern more reminiscent of MnSODs. There are differences in the residues surrounding the conserved solvent-access funnel tyrosine that have been proposed to confer azide resistance. In the thermophile *Methanobacterium thermoautotrophicum*, the FeSOD (*Methano*-FeSOD) has an extremely low affinity for azide (Takao *et al.*, 1991). The conserved tyrosine protrudes

into the substrate-access funnel and is more tightly constrained against a tryptophan; see structure 1MA1 in the protein data bank (Berman *et al.*, 2000). This would make dynamic motion of this tyrosine difficult, and prevent the entry of azide into the active site.

In the human mitochondrial form of MnSOD, mutating a histidine (equivalent to His30 in *Ec*-MnSOD), which sits opposite the conserved tyrosine, to a valine decreases the enzyme's affinity for inhibitors. There is also a significant loss of activity. The mutant residue sticks into the solvent-access channel, blocking off access to the active site, and also makes close contacts to the tyrosine (Hearn *et al.*, 2004, Hearn *et al.*, 2003).

2.16 General trends amongst FeSODs compared to MnSODs

A lot of the information comparing FeSODs and MnSODs is derived from the well characterised *E. coli* variants for which large amounts of correctly folded protein can easily be produced and isolated without the use of expression tags. However, translating information from *E. coli* variants to other Fe/MnSODs should be done with appropriate caution.

Generally, the FeSODs are; inhibited by azide, resistant to product inhibition and prone to inactivating chemical modification by hydrogen peroxide. Meanwhile, the MnSODs are; more resistant to azide, susceptible to product inhibition and not chemically modified by hydrogen peroxide. Generally the FeSODs suffer a greater loss of activity than MnSODs when the conserved solvent-funnel tyrosine is replaced by phenylalanine.

2.17 Current hypotheses for differences between FeSODs and MnSODs

All the information required to form a correctly folded biologically active SOD that goes on to form quaternary structure and acquire the correct metal ion is contained within the primary amino-acid sequence. There will be some interplay between the unfolded polypeptide and the environment while it is being translated and folded. The primary amino-acid sequence codes for variations in tetramerisation, metal specificity, pH dependence, inhibitor specificity, hydrogen-bonding patterns and product inhibition. Delineating what differences in primary amino-acid sequence determine one characteristic, such as metal selectivity, is difficult.

Some attempts to understand metal specifity have been made by introducing minimal amino-acid substitutions to generate an MnSOD from an FeSOD and vice versa. For instance the somewhat Mn-preferring cambialistic Fe/MnSOD from *Porphyromonas*

gingivalis (*Pg*-MnSOD) has had its FeSOD activity increased (and its MnSOD activity decreased) by mutating the buried glycine distant to the active site to a threonine (Yamakura *et al.*, 2003). It was subsequently found that the HFEPR spectra of *Pg*-G155T-MnSOD was reminiscent of *Ec*-Mn-FeSOD and distinct from *Ec*-MnSOD, *Pg*-WT-MnSOD, and the manganese form of the cambialistic SOD from *Rhodobacter capsulatus* (Un *et al.*, 2004). This indicates that the protein component of the metallo-enzyme can alter the properties of the active-site metal.

2.18 Tuning redox potential

One school of thought on the matter of metal specificity is that the protein is involved in the fine tuning of the redox potential of the metal ion (Vance & Miller, 1998b, a, Bull & Fee, 1985, Vance & Miller, 2001). Since the $E^{o'}$(reduction potential) of Mn compounds are approximately 500 mV higher than those of equivalent Fe compounds (Stein *et al.*, 1979) it has been proposed that the protein fold of Mn-specific SODs tends to depress the redox potential of MnSOD to a value close to FeSODs in order for the enzyme to react with superoxide with favourable ΔG for both reduction and oxidation steps.

Mutations of important second-shell residues that decrease the correct metal-specific catalytic activity have been shown to have altered reductive potential (Yikilmaz *et al.*, 2006). The mutant Q69E-*Ec*-FeSOD had an E_m (mid-point potential derived from cyclovoltammetric measurements) 660 mV higher than that of WT and showed virtually no activity, whereas Q69H-*Ec*-FeSOD had a slightly increased E_m relative to WT (increase of 220 mV) and retained partial activity. A mechanism that links these mutations to changes in redox state has been investigated but remains unknown (Yikilmaz *et al.*, 2007).

2.19 pH dependences are different between the FeSODs and the MnSODs

During normal catalytic turnover, the active site must take up two protons and thus the activity of the Fe/MnSOD family is dependent on pH at high pH ranges. At low pH ranges, the active site can readily take up a proton upon reduction (Bull & Fee, 1985). At high pH levels, the activity of both FeSODs and MnSODs is decreased relative to the physiological pH ranges. It was shown that the overall K_m of *Ec*-FeSOD was independent of pH below pH 8.0 but above this pH range K_m increases in a pH-dependent manner (Bull & Fee, 1985). Above pH 10 for every pH unit increase there is a tenfold increase in K_m. Similar results were seen in *Ec*-MnSOD (Miller *et al.*, 2003). At neutral ranges, both protons and hydroxide ions are able to bind to or around the

active site. There is a number of pH-dependent events associated with protonation/deprotonation and association/disassociation of hydroxide ions at the active site, which may differ between MnSODs and FeSODs, as summarised by Maliekal and co-workers (Maliekal *et al.*, 2002). There are differences in pH dependence of spectroscopic properties between the FeSODs and MnSODs, the most notable difference being a difference of one pH unit for the mid-range p*K* of Mn^{2+}SOD compared to Fe^{2+}SOD. This may merely be a consequence of tuning of redox potentials for the FeSODs and MnSODs.

The location of the proton taken up at the active site upon reduction in Fe^{3+}SODs (Bull & Fee, 1985) and Mn^{3+}SODs (Miller *et al.*, 2003) is unknown. However, it is unlikely to be the solvent-access funnel tyrosine, as shown by NMR experiments (Miller *et al.*, 2003). It is widely believed that the fifth ligand, the coordinated solvent molecule that is ascribed as an hydroxide in both FeSODs and MnSODs, is one of the proton acceptors.

There is a marked difference between Fe^{3+}SODs and Mn^{3+}SODs when it comes to pH dependence (Maliekal *et al.*, 2002). In *Ec*-Fe^{3+}SOD the coordination number changes from five to six when moving from pH 7 to pH 10 as shown by X-ray absorption spectroscopy (Tierney *et al.*, 1995). There is a widely observed p*K* for *Ec*-Fe^{3+}SOD at 8.5 (Bull & Fee, 1985, Tierney *et al.*, 1995, Miller *et al.*, 2003), which is interpreted as an hydroxide ion coordinating to the active-site metal ion as the sixth ligand rather than deprotonation of a residue in the solvent-access funnel (Miller *et al.*, 2003); refer to Figure 2-6. However, once reduced, *Ec*-Fe^{2+}SOD undergoes a pH-dependent transition with a similar mid-point p*K* of 8.4, which is believed to be the deprotonation of the conserved tyrosine.

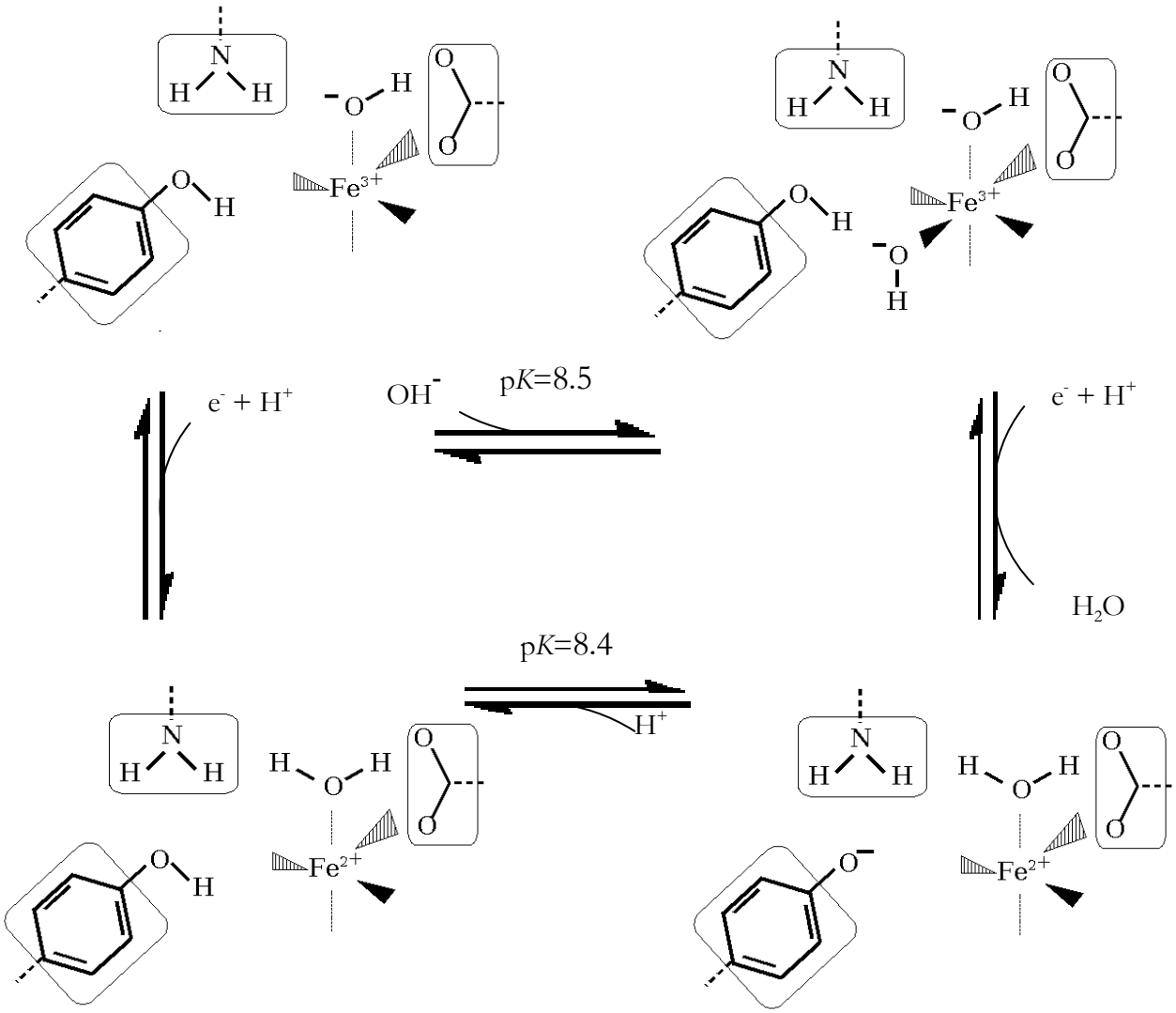

Figure 2-6. Redox- and pH-dependent changes in active-site structure of FeSOD.

Figure 2-6**.** At physiological pH range, the oxidised form of the metallo-enzyme has a penta-coordinate Fe^{3+} cofactor, which binds to an hydroxide ion. The hydroxide ion is stabilised by interactions with two hydrogen-bonding partners, the metal-ligating aspartate and a nearby glutamine. Upon reduction of the active-site metal ion, a proton is also taken up converting the coordinated hydroxide to a water molecule. Both the oxidised and reduced forms undergo pH-linked transitions with p*K* of ~8.5. In the oxidised form this is associated with hydroxide entering the active site and in the reduced form this is associated with the de-protonation of the conserved tyrosine. At high pH, active-site metal-ion reduction is associated with the uptake of a proton and the loss of a water molecule. This mechanism is based on various p*K* determinations from several sources (Bull & Fee, 1985, Tierney *et al.*, 1995, Sorkin *et al.*, 1997, Sorkin & Miller, 1997).

There is also marked pH dependence in MnSODs with the p*K* of oxidised Mn^{3+}SOD being 8.5 (Miller *et al.*, 2003, Maliekal *et al.*, 2002, Whittaker & Whittaker, 1997a). There are currently two hypotheses concerning the nature of this pH-dependent event. Some believe that this corresponds to the deprotonation of the solvent-access funnel tyrosine in MnSODs (Jackson *et al.*, 2002, Guan *et al.*, 1998, Maliekal *et al.*, 2002); refer to Figure 2-7. The alternate, but slightly older, hypothesis is that this p*K* is due to an hydroxide ion associating with the active-site Mn (Whittaker & Whittaker, 1997a, Borgstahl *et al.*, 2000), similar to FeSODs. The higher p*K* of 10.3 shows pH dependence in Mn^{2+}SOD (Maliekal *et al.*, 2002, Whittaker & Whittaker, 1997a), where HFEPR shows a transition (Tabares *et al.*, 2006), indicating that the pH-dependent transitions are altered, but not eliminated, by changes in redox state, unlike the FeSODs where the p*K* are comparable for both oxidised and reduced states.

Both of these hypotheses are based on *Ec*-MnSOD and rely on interpretation of spectroscopic and structural data. Tyrosine deprotonation is mainly supported by ^{13}C NMR of labelled tyrosines (Miller *et al.*, 2003, Maliekal *et al.*, 2002). The most compelling evidence for hydroxide association is the existence at low temperature of a hexa-coordinate structure for *Ec*-MnSOD (Borgstahl *et al.*, 2000).

Complementary to this is research done on the pH dependence of the binding of a sixth ligand to the Fe form of the cambialistic SOD from *Propionibacterium shermanii* (Meier *et al.*, 1998). The structure has been solved at four different pH including some above and below the pH where coordination changes from five to six (Schmidt, 1999). The occupancy of the sixth ligand, a hydroxide, increases as pH increases and is mimicked by the binding of the small-molecule inhibitor fluoride, which binds with partial occupancy in neutral pH ranges.

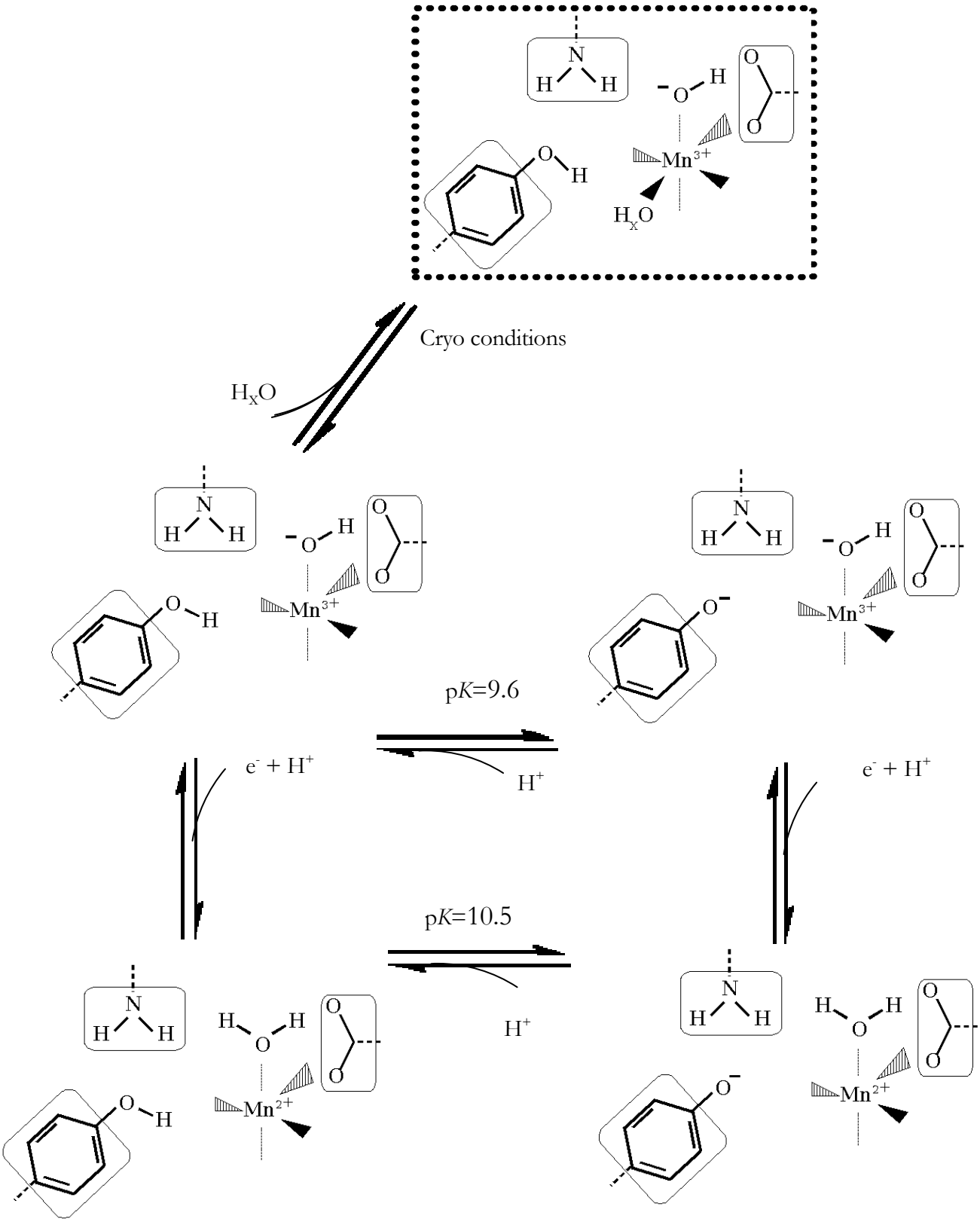

Figure 2-7. Temperature-, redox- and pH-dependent changes in active-site structure of MnSOD.

Figure 2-7. At low physiological pH ranges, the oxidised form of MnSOD contains a penta-coordinated Mn^{3+} ion that has a coordinated hydroxide that is stabilised by hydrogen bonds to the metal ligand aspartate and to a glutamine. At these pH ranges, the nearby tyrosine is protonated. In the oxidised form of the metallo-enzyme, the deprotonation of the tyrosine occurs with a p*K* of 9.6. Upon reduction, a proton is taken up by the coordinated hydroxide converting it to a water molecule. In the reduced form of MnSOD, the deprotonation of the conserved tyrosine occurs with a p*K* of 10.5. Under cryogenic conditions there is a transition to a hexa-coordinate state where H_XO (a water or hydroxide ion), binds to the Mn^{3+}.

2.20 Metal-substituted Fe/MnSODs with altered p*K*

With metal substitution there are shifts in the p*K* values indicating that the metal ion has some effect on the local environment of the active site. When comparing FeSOD and Mn-FeSOD, it is easy to draw parallels between their apparent pH dependencies. However, the p*K* associated with anion binding is different, being 6.7 in Mn-FeSOD. This value is 2 orders of magnitude lower than in FeSOD or MnSOD, and occurs without a large change in EPR signal. A second p*K* seen in Mn-FeSOD at pH 8.5 is associated with a large change in EPR signal (assumed to be associated with the deprotonation of Tyr34). The separation of p*K* associated with anion binding and changes in EPR signals seen in the wrong-metal form may be the key to why the *Ec*-Fe-MnSOD is inactive at physiological pH (Vance & Miller, 1998a), as the sixth coordinated ligand, an hydroxide ion, is not eliminated from the active site, thereby preventing activity. In native FeSOD the coordination of the hydroxide occurs at a higher pH close to the point where the conserved tyrosine loses a proton and the enzyme loses activity.

2.21 Unresolved issues in the structure and function of the Fe/MnSOD family

As shown in the preceding text there has been a large body of research about the Fe/MnSOD family of proteins that links observations to theories on how the Fe/MnSODs function. Some facts are taken to be “gospel truth”, some facts are widely believed, others have multiple explanations and some have at present no viable explanation. Some of the facts about Fe/MnSODs that are universally accepted and well supported experimentally are listed below.

1. Fe/MnSODs are distinct from the Cu/ZnSODs and the NiSODs while catalysing the same reaction. The Fe/MnSODs are a distinct family, with a common fold and a common active-site structure.

2. There are members of the Fe/MnSOD family that are metal specific, some that are metal preferring and others that are cambialistic.

3. Metal ion is required for full activity.

4. The Fe/MnSODs are active as dimers; there are no active monomers. Some members further associate into tetramers.

5. The Fe/MnSODs are descended from a common ancestor. This is evident from the conserved protein fold and active-site structure.

6. Catalysis occurs at the active-site metal ion.

7. Various spectra, such as NMR, are perturbed by changes in pH, temperature and small-molecule inhibitors.

There are some aspects in the research of Fe/MnSODs that are widely believed to be true and these are:

1. There is inherent functional variation between members of the Fe/MnSODs family, which is derived from differences in amino-acid sequences.

2. Fe-specific SODs are different from Mn-specific SODs. Cambialistic SODs also exist but are distinct from metal-specific Fe/MnSODs.

3. The metal ion at the active site shuttles between reduced and oxidised states during catalytic turnover, with the metallo-enzyme, alternating between being a proton acceptor and a proton donor.

4. The minimum coordination of the metal centre is five, which may increase to six during normal catalysis and artificially through binding of small-molecule inhibitors

5. There is proton uptake coupled to active-site reduction.

There are some unresolved issues within the field of Fe/MnSODs for which there are multiple/contrasting hypotheses and explanations, some of which are touched on by this thesis:

1. Why does catalysis occur so rapidly in SODs?

2. How do the Fe and Mn cations perform similar chemistry even though they are chemically distinct?

3. What level of cooperative behaviour, if any, exists between the subunits of obligate dimer pair.

4. What is the role of residues around the active site that are structurally conserved but appear not to participate directly in any proposed enzyme catalysis?

5. What causes the differences in how different small-molecule inhibitors interact with FeSODs compared to MnSODs, for example, the two observed binding patterns for azide?

6. Which amino-acid residues are responsible for metal selectivity/specificity in FeSODs and MnSODs?

7. Why is product inhibition seen in MnSODs but not seen in FeSODs?

8. Where is(are) the site(s) of redox-coupled proton uptake located and whether there are multiple sites of proton uptake?

9. Which residues, if any, are associated with pH-dependent spectroscopic changes?

10. What causes the temperature-dependent change in MnSODs, a change that is more pronounced in the presence of azide?

11. What is the sequence of events that is required for efficient catalysis at the active site? As many as four substrates enter the active-site and two leave, presumably through the same narrow solvent-access channel.

2.22 Scope of this thesis

This majority of this thesis presents structural studies on three Fe/MnSOD crystal structures: an azide-inhibited Fe-substituted MnSOD from *E. coli*, the wild-type MnSOD from *Deinococcus radiodurans* and its azide-inhibited derivative structure. These results provide insight into:

1. How the active sites of MnSODs may be distinct from those of FeSODs.

2. Why catalysis is faster in some MnSODs than in others due to differences in product inhibition.

3. The way small molecules interact with a metal centre and by inference how superoxide interacts with the metal centre.

4. How the temperature transition alters the structure of azide-bound MnSODs.

5. The variation in product inhibition among MnSODs.

6. Potential proton-transfer pathways into the active site.

7. Potential communication pathways between subunits of the obligate dimer.

8. A proposed reaction mechanism.

Also presented are the preliminary results from four point mutants of the MnSOD from *E. coli* that have had their structures solved and partially refined.

2.23 Why research was undertaken

In SODs catalysis occurs extremely rapidly at the metal ion. This can be problematic in elucidating the mechanisms of enzyme activity, as the detection and quantification of transitory enzyme-substrate complexes are very difficult. The use of small molecule inhibitors, which mimic the metal-binding properties of superoxide, allow for the investigation of superoxide dismutases with spectroscopic and X-ray crystallographic techniques. Azide (N_3^-) and fluoride (F^-) are negatively charged molecules similar in size to superoxide that are commonly used in the investigation of manganese superoxide dismutases (Whittaker & Whittaker, 1991, Lah *et al.*, 1995) and iron superoxide dismutases (Miller *et al.*, 2005, Tabares *et al.*, 2006). They bind competitively to the active-site metal ions in a fashion assumed to be similar to superoxide, thereby inhibiting normal catalytic activity. The inhibited metallo-proteins are able to be characterised structurally as the inhibitors persist in the active site.

In general, under pseudo-physiological conditions of temperature and pH, the substrate-mimicking azide ion (N_3^-) binds to, and then inhibits, the FeSODs far more readily than MnSODs. This particularly includes the two Fe/MnSODs from the facultative-anaerobic gut bacterium *Escherichia coli.* This model organism has an Fe-specific SOD (*Ec*-FeSOD) that is azide vulnerable and an Mn-specific SOD (*Ec*-MnSOD) that is somewhat azide resistant. In the past the differences in inhibition profile were proposed

to distinguish the identity of FeSODs from MnSODs. However, there are notable exceptions to this pattern, for example the azide-resistant SOD from *Methanobacterium thermoautotrophicum* (Takao *et al.*, 1991), which mean that inhibition profiles are not absolutely indicative of metal specificity.

2.23.1 An iron-substituted form of a manganese-specific SOD inhibited by azide a substrate mimic

When Fe is substituted into *Ec*-MnSOD (*Ec*-Fe-MnSOD), not only does the catalytic turnover decrease at physiological pH ranges but also the affinity of this "wrong" metal SOD for azide is greatly increased. The K_D of azide dissociation from *Ec*-MnSOD is 7.2 mM, upon metal substitution with Fe the K_D decreases to 0.3 mM (Whittaker & Whittaker, 1997a). This implies that the environment of the active site of *Ec*-Fe-MnSOD is unique from both the *Ec*-MnSOD and *Ec*-FeSOD active-sites, but sharing some characteristics of both. In previous work the structure of *Ec*-Fe-MnSOD was solved (Edwards, Whittaker *et al.*, 1998) and a distorted active-site geometry was observed compared to known structures of *Ec*-FeSOD and *Ec*-MnSOD. Here is presented the structure *Ec*-Fe-MnSOD with an azide ion in the active-site (*Ec*-Fe-MnSOD-N_3^-) solved to 2.2 Å resolution. It was unknown whether azide would associate in a manner that was seen in an FeSOD-N_3^- from *Pseudomonas ovalis* (Stoddard, Ringe *et al.*, 1990), two previously solved FeSOD-N_3^- structures from *E. coli* (Lah *et al.*, 1995) and a camb-FeSOD-N_3- from *Propionibacterium shermanii* (Schmidt *et al.*, 1998), or in a manner that was seen in a previously solved MnSOD-N_3^- structure (Lah *et al.*, 1995), or whether azide would bind in a unique manner.

2.23.2 An MnSOD from an extremophile

The photosynthetic soil bacterium *Deinococcus radiodurans* is an extremophile that is able to survive levels of radiation that would kill most life on earth. It is also resistant to extremes of temperature, desiccation and pH. The bacterium has multiple systems implicated in its robustness. Its complicated and unique genome structure includes multiple chromosome copies and systems for DNA repair. However, once the MnSOD is knocked out the bacterium becomes mesophilic in its nature (Markillie *et al.*, 1999). The MnSOD from *Deinococcus radiodurans* (*Deino*-MnSOD) is able to catalyse the dismutation of superoxide at concentrations of superoxide which would saturate the MnSODs from mesophiles such as *E. coli* (Abreu *et al.*, 2008).

2.23.3 An azide-inhibited MnSOD solved at cryogenic conditions

This thesis presents the crystal structure of the manganese-specific superoxide dismutase from the radiation-resistant extremophile *Deinococcus radiodurans* with a bound azide molecule at its active site. This is the first structure of a native MnSOD with azide bound solved at cryogenic temperatures. The binding of azide to *Deino*-MnSOD (*Deino*-MnSOD-N_3^-) is reminiscent of that previously seen in an azide-inhibited FeSOD and an azide-inhibited camb-FeSOD (Schmidt *et al.*, 1998, Lah *et al.*, 1995). Importantly, the manner of azide binding in *Deino*-MnSOD-N_3^- is different to that seen in a room temperature azide-inhibited MnSOD from *Thermus thermophilus* (Lah *et al.*, 1995) or *Ec*-Fe-MnSOD-N_3^-.

Differences in thermodynamic fine tuning within the Fe/MnSOD family is proposed as the reason for the two azide-binding motifs seen within Fe/MnSODs.

3 Methods

3.1 Methods used to solve and refine the azide-inhibited iron-substituted MnSOD from *E. coli*

Crystallization and X-ray data collection of azide-inhibited iron-substituted MnSOD from *E. coli* (*Ec*-Fe-MnSOD-N_3^-) were performed by Ross Edwards. Subsequently, I solved and refined the structure and interpreted results.

3.1.1 Crystallisation

Iron-substituted MnSOD from *E. coli* (*Ec*-Fe-MnSOD) was prepared and purified as previously described (Whittaker & Whittaker, 1991), except media were supplemented with iron salts (Edwards, Whittaker *et al.*, 1998). The uptake of iron into the protein was confirmed by atomic absorption spectrophotometry. Diffracting crystals of *Ec*-Fe-MnSOD were grown in 0.1 M Tris HCl pH 8.5, 0.2 M $MgCl_2$, 19 % w/v PEG 4000. Prior to X-ray diffraction data collection, the crystal was dipped into a cryoprotectant containing 25% PEG 4000, 15% MPD, 0.1 M Tris/HCl pH 8.7 with 0.02% w/v sodium azide for ~60 seconds before being flash frozen. It is at this point that azide serendipitously entered the very fine needle-like crystal and associated with the active site of the enzyme. Sodium azide was present in the cryo-protectant to act as an anti-bacterial agent.

3.1.2 Data collection, merging and molecular replacement

The unit cell dimensions of *Ec*-Fe-MnSOD-N_3^- are a = 46.28 Å, b = 89.14 Å, c = 206.59 Å, which are very similar to those of *Ec*-Fe-MnSOD (a= 46.19 Å, b = 89.04 Å, c = 206.67 Å). There was also no change in space group ($C222_1$). Cu-Kα X-ray radiation was generated by a Rigaku RU-200B rotating anode generator, with a graphite monochromator. Diffraction data used to solve the structure were taken from a single crystal flash-frozen at 110K and collected using a Rigaku R-Axis IIc image-plate detector. Data collection and refinement statistics for both *Ec*-Fe-MnSOD-N_3^- and *Ec*-Fe-MnSOD (Edwards, Whittaker *et al.*, 1998) are given in Table 1.

Crystal	*Ec*-Fe-MnSOD	*Ec*-Fe-MnSOD-N_3^-
Space group	$C222_1$	$C222_1$
Unit cell	*a*= 46.190 Å	*a* = 46.277 Å
	b = 89.040 Å	*b* = 89.138 Å
	c = 206.671 Å	*c* = 206.592 Å
Resolution range	50-2.2 Å	50-2.2 Å
(high resolution shell)	(2.28 - 2.20 Å)	(2.28 - 2.20 Å)
Total # reflections	225,177	265,952
# unique reflections	22,227	22,346
Completeness	93.2% (82.6)	89.9% (68.6)
Redundancy	4.2	3.7
$< I/\sigma(I) >$	14.0 (4.6)	13.8 (3.0)
R_{merge}	0.090 (0.266)	0.080 (0.319)
R_{cryst}	0.205	0.166
R_{free}	0.234	0.199
# protein sites	3,256	3,267
# water sites	228	478
# metal sites	2	2
# azide sites	0	1
# hydroxide sites	3	3
RMS (bond distances)	0.006 Å	0.003 Å
RMS (bond angles)	1.3°	0.626°

Table 1. Data merging and refinement statistics for *Ec*-Fe-MnSOD and *Ec*-Fe-MnSOD-N_3^-.

The structure was solved by molecular replacement (MR) (Rossmann, 2001) using AMoRe (Navaza, 1994, 2001). The canonical Mn/FeSOD dimer of the wild-type *Ec*-MnSOD structure (Edwards, Baker *et al.*, 1998) PDB code 1VEW, was used as the search model with water molecules, metal ions and hydroxide ions omitted. The initial maps were of high quality; novel density peaks could be seen in the appropriate positions for conserved water molecules and large peaks could be seen at the active-sites for the Fe atoms. The MR solution was later verified using MOLREP (Vagin & Teplyakov, 1997), with a poly-alanine search model generated from the A chain of *Ec*-MnSOD. This solution was nearly identical in rotation, translation, and orientation and with novel density for side chains, metal centre and conserved waters.

3.1.3 Refinement

The set of reflections used to generate R_{free} (Brünger, 1992b) constituted 20 randomly generated shells that were created by DATAMAN (Kleywegt & Jones, 1996), rather than a truly random distribution of R_{free}. This was done to limit the expected effects of

non-crystallographic symmetry (NCS) on the refinement, as one half of the obligate dimer is related to the other half by a two-fold axis of rotation. The same set of R_{free} was used in all refinements in various different programming suites.

The initial $2|F_O|-|F_C|$ and $|F_O|-|F_C|$ electron-density maps were calculated by CNS (Brünger *et al.*, 1998), which incorporates some solvent flattening and density modification. Later in the refinement process, equivalent maps were generated using FFT (Read & Schierbeek, 1988), PHENIX (Adams *et al.*, 2002) or directly within COOT (Emsley & Cowtan, 2004) from weighted calculated structure factors. Automated rigid-body, energy-minimisation and temperature-factor refinements were performed with CNS (Brünger *et al.*, 1998) against a maximum likelihood target based on structure factors (Murshudov *et al.*, 1997). Geometric idealisation was performed with REFMAC (Murshudov *et al.*, 1999). Interactive refinement of the structure was performed using $2|F_O|-|F_C|$ and $|F_O|-|F_C|$ maps generated by CNS and visualised using TURBO-FRODO (http://afmb.cnrs-mrs.fr/) and later COOT (Emsley & Cowtan, 2004).

For quality control, the agreement between X-ray data and model was checked using omit maps generated by the SFCHECK program (Vaguine *et al.*, 1999). The macromolecular refinement of *Ec*-Fe-MnSOD-N_3^- was an iterative process alternating between automated refinement and manual refinement into $2|F_O|-|F_C|$ and $|F_O|-|F_C|$ electron-density maps with interactive programs. Geometric parameters such as amino acid bond angles and lengths were checked against validation tools of PROCHECK (Laskowski *et al.*, 1993) or within COOT itself.

As a monitor of phasing quality, in early rounds of refinement, one of the carboxyl-terminal oxygen atoms was purposely omitted from each protein subunit as a monitor of the reliability of phase information. When the structure was refined to a point where no further chemically sensible electron density could be found in electron-density maps, refinement was stopped. Any further information gained about phases from electron-density maps would be below a threshold where individual atoms could be seen per protein subunit, in the case of this protein, one atom per 205 amino acids.

Fe^{3+} atoms were built into extremely large densities, which dominated the active site at the 1.8 σ level in the $2|F_O|-|F_C|$ map. An azide ion and hydroxide ions were positioned into protrusions of electron density around the active-site metal. Positive peaks in the $|F_O|-|F_C|$ map supported the location of these coordinated ligands. Alternate orientations of azide ion were tested then rejected. New atoms, such as water molecules, were placed

at positions derived from the $2|F_O|-|F_C|$ map provided that there were also large positive peaks in the $|F_O|-|F_C|$ map. In later rounds, small positive and negative peaks near protein atoms in the $|F_O|-|F_C|$ map were interpreted as shifts in atomic coordinates.

During automated and manual refinement it became apparent that the large electron density at the active site associated with the iron dominated electron-density maps; at this resolution (2.2 Å) the electron density associated with the metal ion, in particular in the $2|F_O|-|F_C|$ map, overlapped with that of surrounding residues, which are all about 2.2 Å away. This proved problematic as automated refinement procedures tend to move atoms towards nearby density peaks. This necessitated the introduction of distance restraints between the Fe and ligands to prevent small molecule ligands, such as coordinated hydroxide ions, being moved into the density associated with the metal ion.

Towards the end of the refinement process the structure was subjected to restrained refinement of atomic positions and temperature factors with automated water refinement in the PHENIX programming suite (Adams *et al.*, 2002). This lead to a drastic improvement in the RMS values and in the R_{cryst} and R_{free} values for the structure. There was a concurrent improvement in map quality, as well as the identification of additional solvent molecules. Final parameters are presented in the Table 1, which show that the structure agrees with the experimental data and does not suffer from model bias.

3.2 Methods used to solve MnSOD from the extremophile *Deinococcus radiodurans*

3.2.1 Crystallisation and crystal mounting

The MnSOD from *Deinococcus radiodurans* (*Deino*-MnSOD) used in crystallisation trials was a generous gift from Diane Cabelli of the Brookhaven National Laboratory (Abreu et al., 2008). The protein solution was violet in colour and was diluted to a concentration of 20 mg/mL for storage as aliquots at -80°C. Crystalline material was seen in several conditions of the Crystal Screen™ and Crystal Screen2™ from Hampton Research after several days.

The crystal used in structural solution was grown using the hanging-drop vapor diffusion method: 1 μL of 20 mg/mL MnSOD from *Deinococcus radiodurans* was mixed with 1 μL of 1.6 M Na-Citrate pH 6.5. The crystal was clear and nearly colourless, and grew as a thick plate. The crystal was transferred with a nylon loop from the mother liquor to a cryo-protectant solution of 50% saturated with sucrose in 1.6 M

Na-Citrate pH 6.5. The crystal in cryo-protectant was flash-frozen in liquid nitrogen and maintained at 116 K throughout data collection.

3.2.2 Data collection

X-ray radiation was generated using a Rigaku-MM007 rotating-anode generator equipped with Osmic multilayer mono-chromating optics and the diffraction pattern was collected on a RAxisIV^{++} image-plate detector. From the initial images space group $P2_1$ was identified. The unit cell lengths were 75.00 Å, 106.77 Å and 80.81 Å for *a, b,* and *c* respectively and unit cell angles were $\alpha = \gamma = 90°$ and $\beta = 103.79°$. A total of 550 images each lasting 600 seconds was taken with a 0.3° width and a 0.3° step between images.

Data were scaled and averaged using CrystalClear™ software version 1.3.5 from Rigaku/MSC. Data processing and refinement statistics are given for *Deino*-MnSOD and the azide-inhibited structure in Table 2 (methods for generation of the azide derivative follow, in section 3.3). Structure factors were generated from measured intensities (French & Wilson, 1978), using the TRUNCATE program. A R_{free} set of reflections for structure validation (Brünger, 1992b) was generated from twenty randomly distributed shells of reflections, rather than a true random distribution, in an effort to ameliorate the effects of expected non-crystallographic symmetry using the DATAMAN program (Kleywegt & Jones, 1996).

Crystal	*Deino*-MnSOD	*Deino*-MnSOD-N_3^-
Space group	$P2_1$	$P2_1$
Unit cell	*a*=75.00	*a*=75.40
	b=106.77	*b*=106.82
	c=80.81	*c*=80.94
	α = γ = 90°	α = γ = 90°
	β = 103.79°	β = 104.44°
Resolution range	34.47 - 2.00 Å	19.87-2.00 Å
(high resolution shell)	(2.07 - 2.00 Å)	(2.07-2.00 Å)
Total # reflections	279,401	246,957
# unique reflections	83,267	83,117
Completeness	99.8 (99.9)	99.3 (99.9)
Redundancy	3.36 (3.29)	2.97 (2.89)
Reflections used	80,775	82,580
Test set	2,436 (2.9%)	4,370 (5.29%)
$< I / \sigma(I) >$	8.1 (3.1)	9.8 (3.2)
R_{merge}	0.096 (0.348)	0.073 (0.312)
R_{cryst}	0.1826	0.1781
R_{free}	0.2260	0.2102
# protein sites	6,480	6,485
# water sites	1,293	1,206
# metal sites	4	4
# azide sites	0	4
# hydroxide sites	4	4
RMS bond lengths	0.007Å	0.005 Å
RMS bond angles	1.041°	0.928°

Table 2. Data merging and refinement statistics for *Deino*-MnSOD and *Deino*-MnSOD-N_3^-.

3.2.3 Molecular replacement and initial maps

The structure was solved using the molecular replacement program AMoRe (Navaza, 2001) with the *E. coli* MnSOD monomer (Edwards, Baker *et al.*, 1998) as the search model. Four unique rotation solutions were identified and then each rotation solution was subjected to a translation search. Four monomers were identified with the final solution being comprised of two obligate dimers in the asymmetric unit. A nearly identical solution was identified using MOLREP (Vagin & Teplyakov, 1997). The solution underwent rigid-body refinement and energy minimisation using the CNS program suite (Brünger *et al.*, 1998), which brought the R_{cryst} to 33.24% and R_{free} to 36.37%, at which point initial maps of electron density were generated.

The structure was manually rebuilt using sequence information (Lin *et al.*, 1999) and information from $2|F_O|-|F_C|$ and $|F_O|-|F_C|$ maps visualised in TURBO-FRODO

(http://afmb.cnrs-mrs.fr) on a Silicon Graphics O2 work station or later using COOT (Emsley & Cowtan, 2004). After each round of manual rebuilding, the structure was subjected to simulated annealing, energy minimisation, geometric idealisation, and temperature-factor refinement against a maximum likelihood target based on amplitudes using both CNS (Brünger *et al.*, 1998) and REFMAC (Murshudov *et al.*, 1999) programs. Final rounds of refinement were performed in PHENIX (Adams *et al.*, 2002).

A total of eight rounds of manual and automated refinement of the structure were performed. Over the eight rounds of refinement NCS restraints were weakened and then eliminated. At the end of each round the geometry of the structure was checked using PROCHECK (Laskowski *et al.*, 1993) and in later rounds the agreement of the structure with the calculated structure factors was checked using SFCHECK (Vaguine *et al.*, 1999). After the third round of refinement, well defined water molecules were added into density peaks 2.6- 3.2 Å from hydrogen-bonding partners. During the fourth round of refinement the four metal ions were added to extremely large peaks at the active site, this reduced R_{cryst} to 22.7% and the $R_{free}$to 25.4%. In a subsequent round hydroxide ions were added into density peaks, roughly 2.2 Å from manganese, in all four sub-units. This brought the coordination of the active-site metal to five. There was no evidence of a sixth ligand in any of the subunits. In the final rounds of refinement the maps at the active site were of such high quality that restraints on metal-to-ligand distances or active-site angles were reduced and then eliminated.

3.3 Methods used to solve the azide-inhibited MnSOD from *Deinococcus radiodurans*

The methods used to solve *Deino*-MnSOD-N_3^- were similar to those used to solve the native structure.

3.3.1 Crystallisation and mounting

Wild-type *Deinococcus radiodurans* MnSOD used in crystallisation trials was violet in colour when diluted to a concentration of 20 mg/mL. The protein solution was mixed with 100 mM sodium azide in a 4:1 molar ratio; upon mixing, the colour of the protein solution changed from violet to clear. This decreased the protein concentration to 16 mg/ml with an azide concentration of 20 mM.

Crystallisation conditions were based on conditions identified in the Crystal Screen™ and Crystal Screen2™ from Hampton Research that had been used to crystallise the native protein. The crystal used to solve the structure was grown using the hanging-drop

vapor-diffusion method: 1 μL of 16 mg/mL *Deino*-MnSOD was mixed with 1 μL of 1.6 M Na-citrate pH 6.5. The original concentration of azide in the hanging drop is estimated to be 10 mM. The crystal was clear and colourless, and grew as a thick plate, reminiscent of native crystals grown in the absence of azide. The crystal was transferred with a nylon loop from the mother liquor to a cryoprotectant solution of 1.6 M Na-citrate pH 6.5 that was 50% saturated with sucrose. After brief immersion in cryoprotectant the crystal was flash frozen in liquid nitrogen and maintained at 116 K throughout data collection.

3.3.2 Data collection, reduction and merging

X-ray radiation was generated using a Rigaku-MM007 rotating-anode generator equipped with Osmic multilayer mono-chromating optics, and the diffraction pattern was collected on a RAxisIV^{++} image-plate detector. Initial images indicated that the space group of this crystal was the same as that for native crystals and the unit cell was of similar dimensions. From the initial images, space group $P2_1$ was identified with a unit cell with cell lengths 75.40 Å, 106.82 Å and 80.94 Å for *a*, *b*, and *c* respectively, and with unit cell angles $\alpha = \gamma = 90°$ and $\beta = 104.44°$. Merging and refinement statistics are given in Table 2.

Data were scaled and averaged using CrystalClear™ software version 1.3.5 from Rigaku/MSC. Structure factors were generated from measured intensities (French & Wilson, 1978) using the TRUNCATE program. The R_{free} set of reflections for structure validation (Brünger, 1992b) were the same reflections as those used to solve the native structure. This set of R_{free} reflections had been generated previously using the DATAMAN program (Kleywegt & Jones, 1996). Twenty randomly distributed thin shells of reflections were used as the R_{free} set, rather than a true random distribution. This was done in an effort to ameliorate the effects of the expected four-fold non-crystallographic symmetry, which can act as a restraint in both the crystal and the data-set. This is done because the non-crystallographic symmetry that is present in the crystal will also manifest in reciprocal space as relationships between NCS-related reflections.

3.3.3 Molecular replacement and initial maps

The structure was solved using the molecular replacement program MOLREP (Vagin & Teplyakov, 1997) using the A subunit of the *Ec*-MnSOD monomer (PDB id 1VEW) (Edwards, Baker *et al.*, 1998) as the search model. Water, manganese atoms and divergent loops (based on primary amino-acid sequence differences between *Ec*-MnSOD and *Deino*-MnSOD) were removed from the search model. Four unique

rotation solutions were initially identified. The final molecular replacement solution was comprised of two of the obligate dimers in the asymmetric unit. The solution was nearly identical to the native structure.

Initial $2|F_O|-|F_C|$ map was of high quality at 1 σ level. Density peaks were apparent for a fifth metal-binding ligand, the size and shape of an hydroxide, and for a sixth ligand, with the shape and size of an azide ion. The structure was manually rebuilt using sequence information (Lin *et al.*, 1999) and information from $2|F_O|-|F_C|$ and $|F_O|-|F_C|$ maps visualised in the real-space visualisation software TURBO (currently maintained at http://www.afmb.univ-mrs.fr/-TURBO-) and later in COOT (Emsley & Cowtan, 2004). After each round of manual rebuilding, the structure was subjected to energy minimisation, geometric idealisation, translation-libration-screw (TLS) and temperature-factor refinement against a maximum likelihood target based on amplitudes using CNS (Brünger *et al.*, 1998) and REFMAC (Murshudov *et al.*, 1999) and PHENIX (Adams *et al.*, 2002).

In early rounds of solvent building, water molecules had to satisfy strict criteria to be included: well defined spherical density peaks in both the $2|F_O|-|F_C|$ and $|F_O|-|F_C|$ maps, three peptide-derived hydrogen-bonding partners including two hydrogen-bond acceptors and one donor. After automated refinement the water molecule positions, temperature factors and agreement with electron density were checked and problematic waters were removed. In later rounds of refinement the inclusion criteria for waters were weakened; this meant that more waters on the surface of the protein could be built.

The geometry of the protein conformed well against geometric libraries within the PROCHECK structure validation tool (Laskowski *et al.*, 1993) and COOT (Emsley & Cowtan, 2004). The agreement of the X-ray data with the structure was checked using SFCHECK (Vaguine *et al.*, 1999).

3.4 Attempted high-temperature data collection

Numerous attempts were made to collect data and determine a structure of *Deino*-MnSOD-N_3^- close to ambient temperatures.

3.4.1 220 K data collection

Crystals of *Deino*-MnSOD were grown in the presence of azide and flash frozen in liquid nitrogen in a manner similar to that outlined above. Crystals were then transferred to diffractometer and maintained at ~116 K while initial diffraction images were taken.

Once a suitable diffracting crystal was detected, temperature was then increased to 220 K for data collection.

At this temperature crystals initially diffracted well, but over the time span of about an hour diffraction ceased and ice-rings became apparent, indicating that the disordered "glassy" water within the protein crystal had taken on the order characteristics of an ice crystal. Ice formation was enough to disrupt the ordered lattice of the protein crystal. The reported temperature for glass transition is 136 K (Johari *et al.*, 1987); at any temperature above this ice formation is likely, depending on the cryoprotectant.

3.4.2 Room temperature data collection

Azide-soaked crystals of *Deino*-MnSOD were prepared as above and mounted in glass capillaries for room temperature data collection. Once mounted in capillaries, crystals were stable and there was no discernable change in crystal shape and morphology, and the surrounding mother liquor remained clear. However, once placed in the X-ray beam, crystals initially diffracted, but then diffraction decreased over time; after three hours the diffraction was negligible. This was taken to indicate that *Deino*-MnSOD crystals were prone to radiation damage at ambient temperatures. Crystals removed from the diffractometer had maintained their shape and size, but the mother liquor in which they were suspended in had gained a violet tinge.

3.5 Structures of four *Ec*-MnSOD mutants

Most of the transformations, sterile procedures and culturing of *E. coli*, running of DNA agarose gels, sodium dodecyl sulfate polyacrylamide gel electrophoresis (SDS-PAGE) , *et cetera*, were performed using standard techniques (Sambrook *et al.*, 2006). Where appropriate, materials were sterilised by autoclave prior to use.

3.5.1 Materials

3.5.1.1 General

General lab reagents, supplies and consumables came from various sources including Sigma-Aldrich, Merck, Biolab, Bio-Rad, Invitrogen, and Amersham-Biosciences.

3.5.1.2 Enzymes

All enzymes used in genetic manipulations were purchased from Invitrogen™ and used as directed by manufacturer including Platinum® Pfx DNA Polymerase, *Eco*RI, *Bam*HI and T4 DNA Ligase using supplied buffers.

3.5.1.3 Crystallisation supplies and mounting equipment

Reagents used in crystallisation trials, in section 3.5.6, were purchased from Hampton Research. This included nylon loops and pins for mounting crystals for data collection under cryogenic conditions.

3.5.2 Mutation

Point mutants of *Ec*-MnSOD were generated from a plasmid that contained a fragment of the *E. coli* chromosome that contains the *Ec*-MnSOD gene (Touati, 1983). Degenerate primers were used to introduce mutations into the MnSOD gene using degenerate PCR based methods of strand overlap extension; refer to Figure 3-1. All primers were purchased from Sigma-Aldrich® and are listed in Table 3.

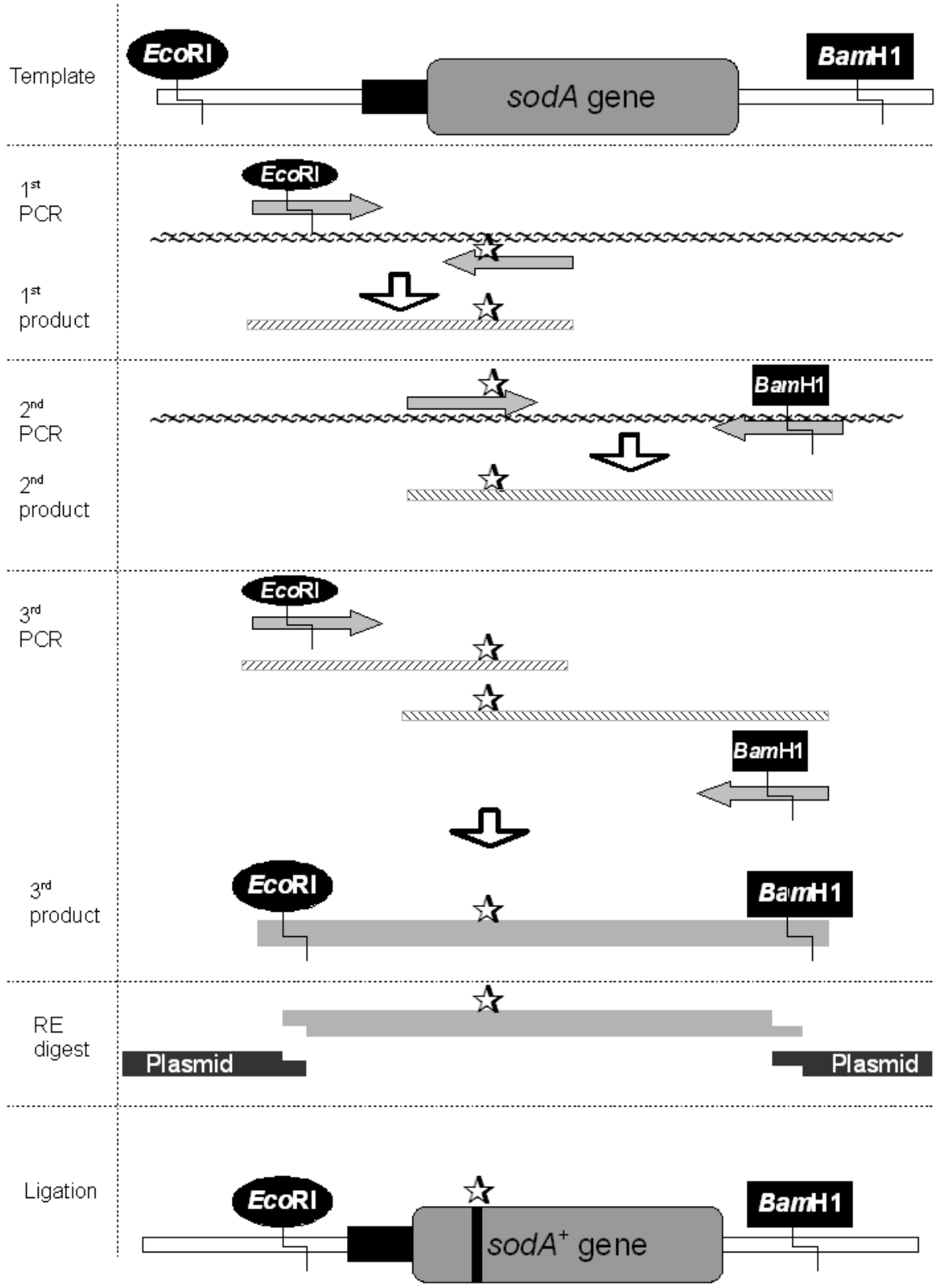

Figure 3-1. Strand overlap extension method used to generate point mutants.

Figure 3-1. The top panel shows the template DNA, which is a plasmid called pDT1-5 (Touati, 1983), that contains the gene of *Ec*-MnSOD that is under the control of the native promoter shown as a black rectangle. There are *Eco*RI and *Bam*HI restriction sites in the plasmid that are a legacy from the original cloning. In the first PCR the forward primer has an *Eco*RI recognition site that will be

propagated into the PCR product while the reverse primer introduces a point mutation, shown as a star, into the product. In the second PCR reaction the forward primer introduces the same, but complementary, mutation while the reverse primer contains a *Bam*HI recognition sequence. In the third PCR the products from the first and second PCR are mixed with the forward primer containing the *Eco*RI recognition site and the reverse primer containing the *Bam*HI recognition sequence. Between the two products there is enough overlap at the mutation site such that in the initial annealing rounds of the third PCR the polymerase will amplify the full-length product containing mutation. The distance (in nucleotides) between the *Eco*RI and *Bam*HI recognition sites in the third PCR product is substantially shorter, by 2 kb,than the distance between the *Eco*RI and *Bam*HI recognition sites in pDT1-5. The reaction product from the third PCR is digested with *Eco*RI and *Bam*HI and inserted into the digested pDT1-5 plasmid. This creates a plasmid that contains a gene that codes for a point mutant that is under the control of the native promoter region and 2 kb shorter than the pDT1-5 plasmid. Also on the plasmid is the gene for ampicillin resistance to act as a selective marker.

Primer #	Primer name	Primer sequence 5' →3'
1	***Eco*RI-forward**	CCGACTGACCACATGAATTCCCATGACCAT
2	***Bam*HI-reverse**	TCAGTGTTGATGGATCCGAAGATAGACATT
3	**S82T-forward**	GCTGGCGGTCACGCTAACCACACCCTGT
4	**S82T-reverse**	TTTCAGACCTTTCCAGAACAGGGTGTGGTTAGC
5	**L83M-forward**	GTCACGCTAACCACAGCATGTTCTGGAAAG
6	**L83M-reverse**	AGACCTTTCCAGAACATGCTGTGGTTAGCGTGA
7	**L133V-forward**	TCCGGCTGGGCATGGCTGGTGGTGAAAGGCGA
8	**L133V-reverse**	AGTTTATCGCCTTTCACCACCAGCCATGCCCAGC
9	**M164L/L166V-forward**	TCCGGCTTCCCGATTCTGGGCGTGGATGTGT
10	**M164L/L166V-reverse**	GCTCCCACACATCCACGCCCAGAATCGGGA

Table 3. PCR primers used for mutation

Table 3 shows a list of DNA primers used in the generation of S82T, L83M, L133V and M164L/L166V mutants. Primers number 1 and 2 contain recognition sites for the enzymes *Eco*RI and *Bam*HI respectively, which are underlined. The other eight primers are arranged in pairs where the overlap between pairs is underlined and the sites of mutation are shown in a larger font size.

Ligation products were transformed into BL-21-(DE3) *E. coli* cells by heat-shock and cultured overnight on plates of LB agar containing 100 μg/ mL ampicillin at 37°C. The next day colonies were selected and grown overnight at 37°C in 5 mL of LB containing 100 μg/ mL ampicillin. The following day plasmids were isolated using the High Pure™ Plasmid Isolation Kit from Roche. Isolated plasmids were initially screened using *Eco*RI and *Bam*HI restriction endonucleases for inserts of the correct size. Plasmids with inserts of the correct size were sent for in-house sequencing using a 3730 DNA analyser from Applied Biosytems.

Recombinant protein for crystallographic investigations (Edwards *et al.*, 2001a, b) was based on purification protocol from spectroscopic studies (Whittaker & Whittaker, 1991). A detailed explanation of protein purification follows.

3.5.3 Expression

Correctly sequenced plasmids that contained a mutant gene that codes for mutant *Ec*-MnSOD were transformed into the QC781 strain of *E. coli* that lacks endogenous SOD activity (Carlioz & Touati, 1986) by heat shock and plated onto LB agar containing 100 μg/ mL ampicillin and grown overnight at 37°C. The next day an individual colony was picked and grown overnight at 37°C in 100 mL of LB agar containing 100 μg/mL ampicillin as a seed culture. This culture was used to inoculate 2 L of LB agar containing 100 μg/mL ampicillin, supplemented with 100 mg of $MnCl_2$, and this was grown overnight at 37°C.

3.5.4 Isolation by ammonium sulfate cut

The cells were harvested by centrifugation at 6,500 rpm for 20 minutes at 4 °C in a GS3 rotor from Sorvall®. At this point cells were flash-frozen with liquid nitrogen for storage at -80 °C. The cells were re-suspended in 100 mL of 0.05 M potassium phosphate buffer at pH 7.8 and lysed using a French Press. Soluble protein was separated from insoluble by centrifuging at 9,500 rpm in GSA rotor for 45 minutes at 4 °C. The pellet was discarded. Solid KCl was added to bring the concentration of the lysate to 0.1 M. Ammonium sulfate was added to 50% of saturation and stirred for one hour. The solution was centrifuged at 9,500 rpm in GSA rotor for 45 minutes at 4 °C and the precipitate was discarded. More ammonium sulfate was added to 75% of saturation and stirred for one hour. The solution was centrifuged at 9,500 rpm in GSA rotor for 45 minutes at 4 °C and the supernatant was discarded. The pellet was re-suspended in 10 mL of 0.01 M potassium acetate pH 5.5 and transferred into a dialysis

bag. Sample was dialysed against 100 volumes of 0.01 M potassium acetate pH 5.5 for 96 hours with a buffer change every 12 hours.

3.5.5 Low pressure chromatography

3.5.5.1 Cation exchange chromatography

Soluble protein was transferred from the dialysis bag and loaded at 5 mL/min onto a column that contained Sephadex® CM-50 cation exchange resin from Sigma-Aldrich® equilibrated with 0.01 M potassium acetate pH 5.5. The outflow was monitored at 280 nm. When the first protein peak was eluted, a salt gradient was introduced using a 0.5 litre gradient mixer until the final concentration entering the column was 0.2 M potassium acetate pH 5.5. The second major peak was collected, pooled and concentrated using Vivaspin 20 spin columns with a 10,000 molecular weight cut-off membrane (Vivasciences). A SDS-PAGE of protein samples separated by cation-exchange chromatography is shown in Figure 3-2.

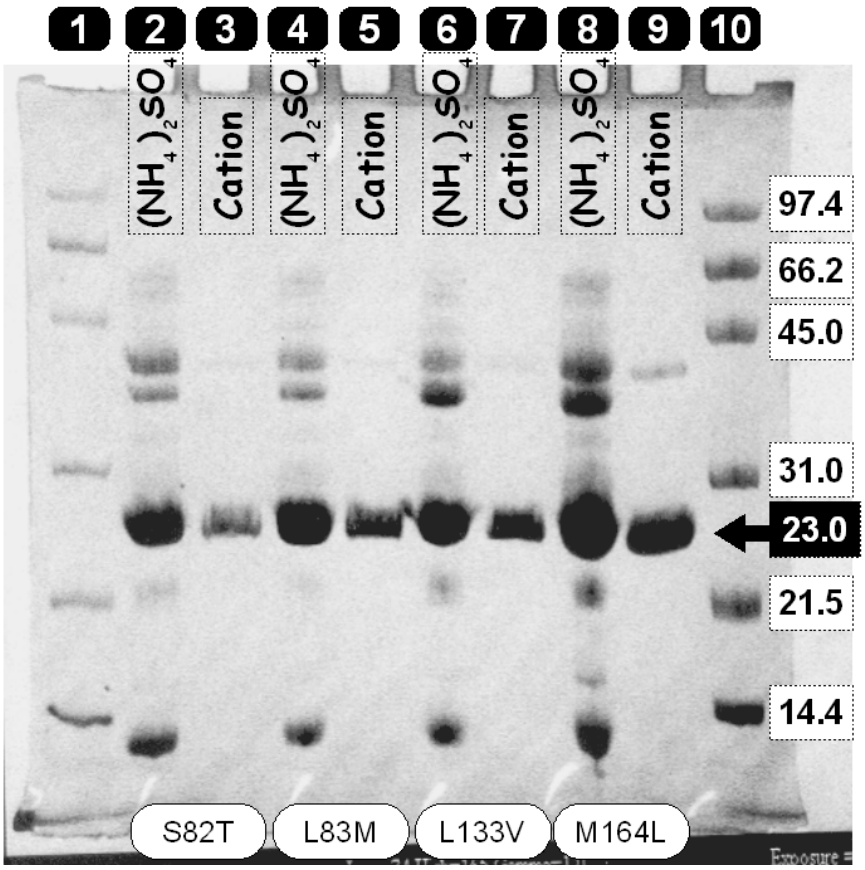

Figure 3-2 Photograph of a SDS-PAGE showing protein samples before and after cation-exchange chromatography for four mutants of *Ec*-MnSOD

Figure 3-2. The gel was stained using Coomassie Blue and photographed using a black and white camera. The first and tenth lanes contain molecular-weight standards. The major bands in the tenth lane have been annotated with molecular weights in kDa. The predicted weight of *Ec*-MnSOD is 23 kDa and is indicated

by a black arrow. Lanes 2-3, 4-5, 6-7, and 8-9 contain the mutants S82T, L83M, L133V and M164L/L166V respectively. Samples before cation exchange were loaded in lanes 2, 4, 6 and 8 (even numbers). Samples after cation exchange were loaded in lanes 3, 5, 7 and 9 (odd numbers). Cation-exchange chromatography selectively isolated *Ec*-MnSOD mutants.

3.5.5.2 Anion exchange chromatography

The protein sample was dialysed against 100 volumes of 0.005 M potassium phosphate pH 7.8 for 60 hours with a buffer change every 12 hours. Sample was then loaded onto a column of DEAE resin equilibrated with 0.005 M potassium phosphate at pH 7.8 at a flow rate of 5 mL/min. Fractions containing protein were collected and concentrated using Vivaspin 20 spin columns with a 10,000 molecular weight cut-off membrane (Vivasciences). A SDS-PAGE of protein samples separated by anion-exchange chromatography is shown in Figure 3-3. Protein solution at this point had a violet tinge. The yield from 2 L of culture was about 100 μL of protein solution at a concentration of about 15 mg/mL. There was minor variation in yield between mutants.

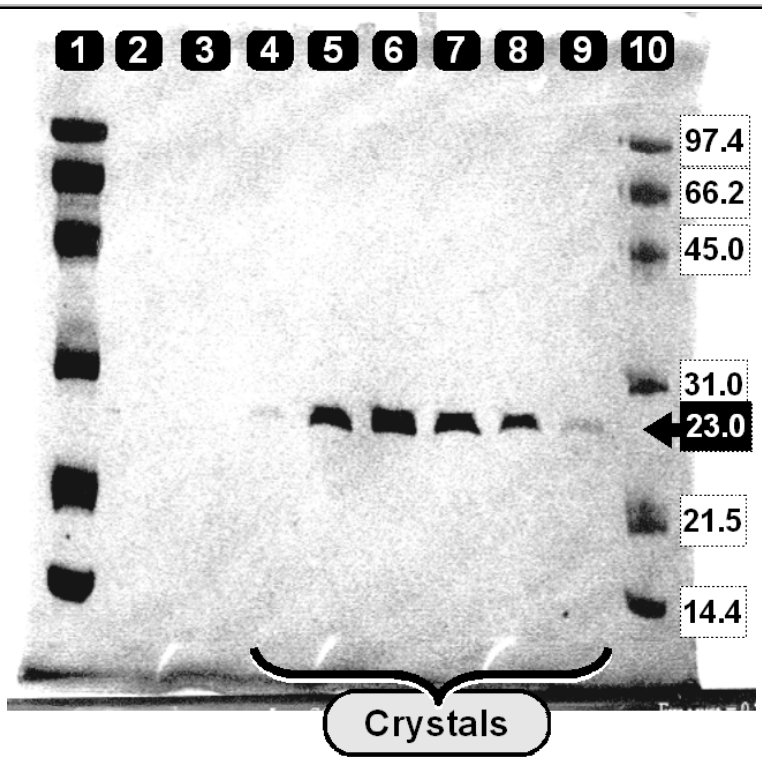

Figure 3-3 Photograph of a SDS-PAGE showing fractions after anion-exchange chromatography for S82T-MnSOD

Figure 3-3. The gel was stained using Coomassie Blue and photographed using a black and white camera. The first and tenth lanes contain molecular weight standards. The major bands in the tenth lane have been annotated with molecular weights in kDa and the predicted molecular weight of *Ec*-MnSOD, 23 kDa, has been indicated by a black arrow. Lanes 2-9 were loaded with fractions taken across the major eluted peak for a representative anion-exchange chromatography. Fractions containing protein were pooled for crystal trials.

3.5.6 rystallisation trials

Starting conditions for crystal trials had been previously established (Edwards, Baker *et al.*, 1998, Edwards *et al.*, 2001a, b). All crystal trials were set up in 24-well VDX plates from Hampton Research with siliconised cover-slides using the hanging-drop vapour diffusion method (Hampel *et al.*, 1968). The volume of the well solution was 1 mL made up to create a gradient of PEG 6000 (polyethylene glycol with molecular weights between 5,000 and 7,000) concentrations along the six wells of the long axis of the crystallisation plate, as shown in Table 4. In each well 2-methyl-2,4-pentanediol (MPD) was added as a cryoprotectant.

Variable →	15% PEG	17% PEG	19% PEG	21% PEG	23% PEG	25% PEG
Component↓						
MPD	100 μL	100 μL	100 μL	100 μL	100 μL	100 μL
0.5 Tris-HCl pH 8.5	200 μL	200 μL	200 μL	200 μL	200 μL	200 μL
PEG 6000	300 μL	340 μL	380 μL	420 μL	460 μL	500 μL
H_2O	400 μL	360 μL	320 μL	280 μL	240 μL	200 μL

Table 4. Components of crystal trial used to generate a gradient in the precipitant PEG 6000.

Generally three drops were set up on each cover-slide with different ratios of well solution to protein solution, typically 0.5 μL: 1 μL, 1 μL: 1 μL and 2 μL: 1 μL. Initial trials did not yield crystalline material. Crystallisation success was greatly improved by making PEG 6000 solution the day it was required. This improved the rate of crystallisation greatly so that roughly one quarter of all wells yielded crystalline material. Crystals used in diffraction studies were generally long thin rods.

3.5.7 Data collection

Data sets were collected on a RAxisIV^{++} image-plate detector. X-ray radiation was generated using a Rigaku-MM007 rotating-anode generator equipped with Osmic multilayer mono-chromating optics. Raw mages were integrated using MOSFLM (Steller *et al.*, 1997) and scaled together using SCALA (Evans, 2006). Pertinent data statistics are given in Table 5.

Crystal	S82T	L83M	L133V	M164L/L166V
Space group	$C222_1$	$C222_1$	$C222_1$	$C222_1$
Unit cell axes (/Å)	98.710 107.198 180.084	95.550 107.000 178.610	99.199 106.813 179.645	96.000 107.620 179.320
Resolution range (high resolution range) Total # reflections # unique reflections	20.48-2.10 (2.21-2.10) 229,784 (34,177) 55,828 (8,099)	24.40-2.10 (2.21-2.10) 157,425 (22,406) 52,458 (7,599)	36.35-2.20 (2.32-2.20) 199,602 (24,787) 48,615 (6,966)	24.49-2.10 (2.21-2.10) 206,527 (30,941) 50,693 (7,497)
Completeness Redundancy $< I/\sigma(I) >$ R_{merge}	99.8 (100.0) 4.1 (4.2) 13.3 (2.4) 0.122 (0.699)	98.1 (98.5) 3.0 (2.9) 11.1 (1.6) 0.108 (0.723)	99.8 (99.2) 4.1 (3.6) 12.8 (2.1) 0.121 (0.535)	93.7 (96.10 4.1 (4.1) 11.5 (1.5) 0.118 (0.696)
R_{cryst} R_{free}	0.3324 0.3305	0.3591 0.3701	0.3205 0.3328	0.3442 0.3653

Table 5. Data collection and initial refinement statistics for four point mutants of *Ec*-MnSOD.

3.6 Initial maps of four point mutants of *Ec*-MnSOD

All four structures were solved by molecular replacement using MOLREP (Vagin & Teplyakov, 1997) and then partially refined by rigid-body refinement using REFMAC (Murshudov *et al.*, 1997). A search model was generated from the monomer *Ec*-MnSOD lacking the mutated residues, water molecules and active-site cation.

3.6.1 General

The initial electron density maps of all mutant structures are well defined. In the active sites of all four mutants there were large electron density peaks associated with the metal cofactor and a smaller density peak for the coordinated solvent-derived fifth ligand. There were also well defined density peaks in the expected positions of water molecules. In the electron density maps of all four point mutants there was interpretable electron density around the sites of mutation allowing correct identification of rotamers of mutants.

4 Results

4.1 Structure of the azide-inhibited iron-substituted MnSOD from *E. coli* at 2.2 Å resolution

The uptake of Fe into *Ec*-MnSOD was measured using atomic absorption spectroscopy (Edwards, Whittaker *et al.*, 1998). There are other methods for quantifying the metal ion present at the active site such as colorimetric assays (Beyer & Fridovich, 1988) and spectroscopic studies (Whittaker & Whittaker, 1991).

4.1.1 Merging and MR

The quality of the 2.2 Å resolution X-ray data of *Ec*-Fe-MnSOD-N_3^- is slightly sub-optimal, but reliable enough for atomic resolution structure determination; refer to Table 1. This data set suffers from lower redundancy and completeness than the *Ec*-Fe-MnSOD, particularly in the highest resolution shell. However, at this resolution electron density maps were good enough to determine the position of ordered solvent molecules and the position of peptide side chains. For some side chains this resolution was not sufficient to identify specific rotamers. Where this occurred, rotamers were assigned based on a consideration of electron density, knowledge of hydrogen-bonding patterns and knowledge of which rotamers are most favoured. Residues with long side chains close to the solvent and not constrained by hydrogen bonds were the most problematic, as they probably exist as multiple rotamers within the crystal, as reflected by higher temperature factors.

4.1.2 Presence of azide ion at the active site

A feature of the electron density maps of the two active sites of *Ec*-Fe-MnSOD-N_3^- was the large density peak associated with the bound Fe; refer to Figure 4-1. However, closer examination of the active site showed that the A subunit contained a sixth ligand at the active site, which was different from *Ec*-Fe-MnSOD which contained only five metal-binding ligands at this active site. The fifth axial ligand was classified as an hydroxide in accordance with other Fe/MnSOD structures. The sixth ligand was ascribed as an azide ion based on size and shape of the electron density peak, and the fact that it was not seen in the Fe-MnSOD structure. It was elected not to build azide into the active-site until later in the refinement process, as the orientation of azide was thought to be different between FeSODs and MnSODs (Lah *et al.*, 1995).

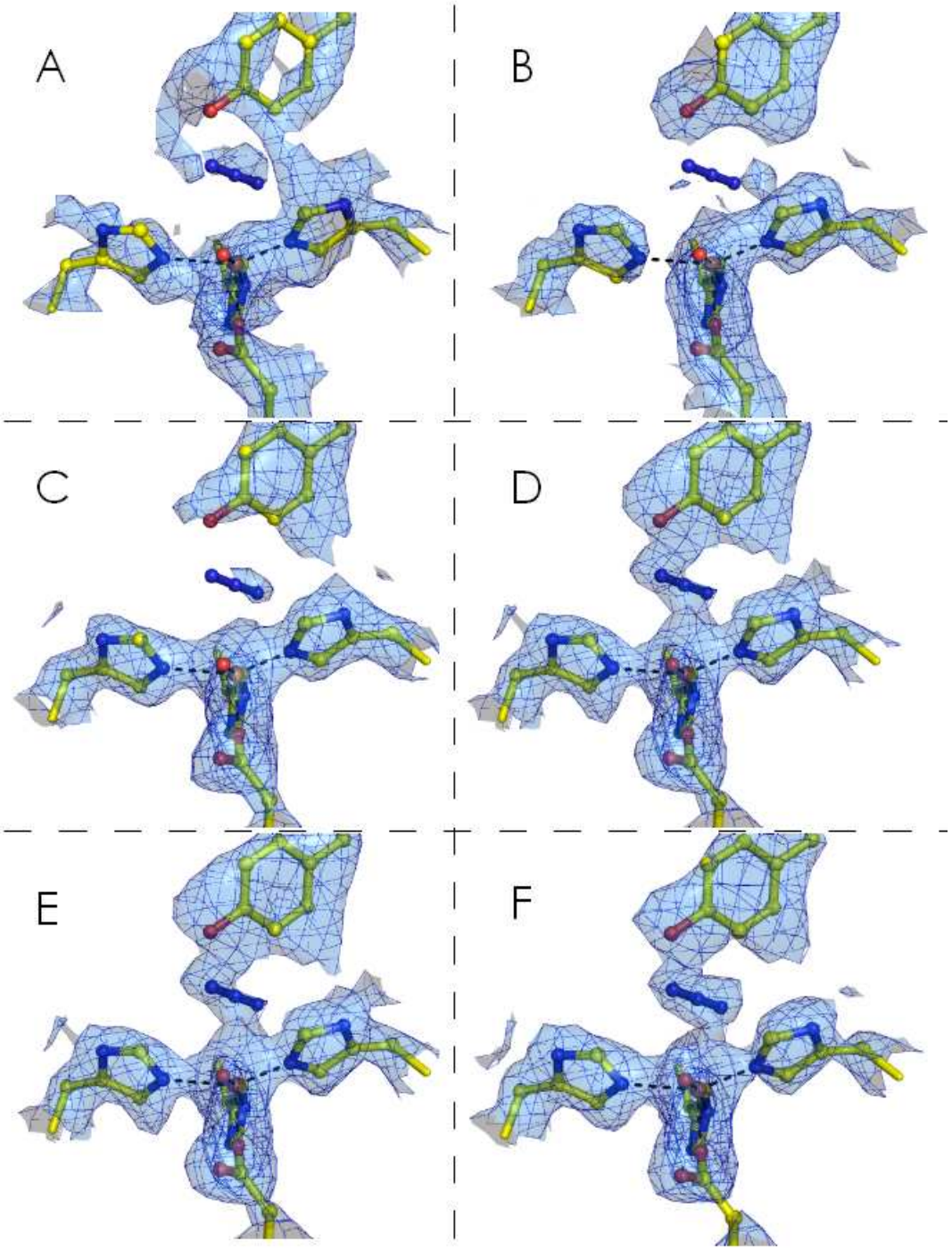

Figure 4-1. The improvement of omit maps during refinement from initial solution to final structure for the A subunit of *Ec*-Fe-MnSOD-N_3^-.

Figure 4-1. Images A to F show composite omit maps, generated by the SFCHECK program (Vaguine *et al.*, 1999), from various stages of the refinement process overlaid onto to coordinates of the final structure. All maps are contoured at the 0.8 σ level. The omit map in image A is derived from the initial molecular replacement solution where residues are replaced with alanine. At this early stage there are observable density peaks near the expected coordination site of a sixth ligand. The omit map in image B is derived from the MR solution. The omit map in image C is derived after the active-site metal has been added. Image D features an omit map derived after restrained refinement of the trial structure including the positions and

temperature factors of the metal ions. Image E shows the omit map from the structure after coordinated hydroxide, azide and many solvent molecules have been added to the structure. Image F shows the omit map derived from the final structure. Over the refinement process the maps became better defined. Tyr34 is not as well defined as other active-site residues indicating that it exists in multiple conformations, consistent with the partial occupancy of azide.

4.1.3 Refinement progress

Early in the refinement process it became apparent that the electron density associated with the tyrosine of the solvent-access funnel of the A subunit (*Ec*-Fe-MnSOD-N_3^-_*A*_Y34) was disordered (refer to Figure 4-1). That is, the tyrosine existed in multiple conformations. At that time, the occupancy of azide and hence the occupancy of conformers of *A*_Y34 were unknown. So, in early stages of refinement *A*_Y34 was replaced with a smaller amino-acid side chain, an alanine residue, which would maintain helix structure, until the electron-density maps became unambiguous and the rotamer position(s) of *A*_Y34 became distinct.

After the first round of manual rebuilding and then automated simulated annealing, energy minimisation and temperature-factor refinement, R_{cryst} was 0.2914 and the R_{free} 0.3026. Electron density in the vicinity of the metal ion is shown in Figure 4-2. At this point Fe^{3+} atoms were added to the structure along with some extremely well defined waters. As refinement progressed, waters were placed at positions of positive electron density at suitable hydrogen-bonding distances. NCS restraints between the subunits of the dimer were decreased and then eliminated over the course of refinement. The 2.2 Å resolution allowed the identification of hydroxide ions at the active sites of both subunits, and an azide ion at the active site of the A chain and a second hydroxide ion at the active site of the B chain. The azide ions were added during the fifth round of refinement when R_{cryst} was 0.262 and the R_{free} was 0.2702. The occupancy of the azide ion at the active site was initially set at unity but after temperature-factor refinement indicated that the molecule was not fully present, occupancy was set to 0.6. To test alternate azide-binding motifs, trial models with the azide anion in “sensible” orientations were also tested, but ultimately rejected based on map interpretation. After ten rounds of refinement, the final refinement, using CNS, was a restrained temperature-factor refinement with a maximum likelihood target based upon amplitudes.

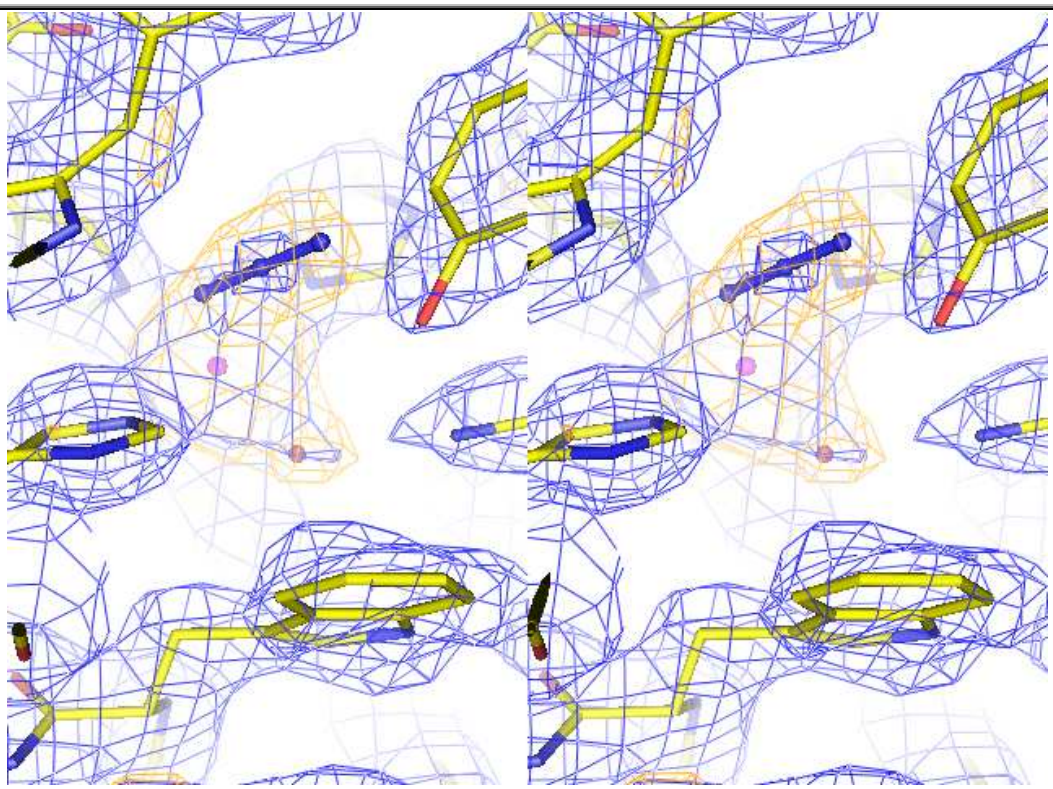

Figure 4-2. Stereo-image of the active site of subunit A of azide-bound *Ec*-Fe-MnSOD.

Figure 4-2. The atomic coordinates are from a trial-model, electron-density maps were generated from early refinement stages before the inclusion of metal cofactor and bound ligands. The $2|F_O|-|F_C|$ map is coloured blue, and is contoured at 1.2 σ, while the $|F_O|-|F_C|$ map is coloured orange and is contoured at 2.5 σ. The magenta sphere in a large density peak represents the bound Fe. Blue spheres and blue rods represent bound azide and a red sphere represents the bound hydroxide ion. The protein is shown as sticks in which the carbon atoms are shown as yellow, nitrogen as blue and oxygen as red. Tyrosine 34 is shown in the top right side within hydrogen-bonding distance of the terminal nitrogen of azide.

4.1.4 Building solvent structure

At this resolution range it is not sensible to refine the occupancy of atoms or side chains. The quality and appearance of the electron-density maps were good throughout the refinement process. In the $2|F_O|-|F_C|$ map, electron density was generally well defined at the 1 σ level for buried residues. Early in the refinement process, density peaks were seen in the positions of structurally conserved water molecules, this indicated that the diffraction data were good enough to resolve individual atoms in particular those close to the buried active site. For example, in both *Ec*-Fe-MnSOD and *Ec*-MnSOD there are two buried water molecules that are hydrogen-bonded to an active-site residue, His26; corresponding electron density peaks were seen in both subunits of *Ec*-Fe-MnSOD-N_3^-.

There were some regions that were not well defined, but these were mostly side chains at the surface of the molecule that protruded into solvent space and included residues such as

lysine, which has many possible rotamers. As refinement progressed many of the ambiguous regions became well defined. This was particularly true of solvent molecules. Once the initial shell of solvent molecules was built, other solvent molecules became more apparent and nearby peptide regions became better defined.

4.1.5 Dimer structure

The structure of *Ec*-Fe-MnSOD-N_3^- was overall very similar to the structures of native *Ec*-MnSOD and *Ec*-Fe-MnSOD. There are two protein molecules in the asymmetric unit that form the obligate dimer characteristic of all Fe/MnSODs. The four residues that bind the Fe were well defined during the refinement process with unambiguous density. The highly conserved loop structure that protrudes from the active site of one subunit into the active site of the other subunit is unchanged. The second coordination shell of the active site was also well defined during refinement with most residues in similar positions to those in *Ec*-Fe-MnSOD. However, the conserved solvent-access funnel tyrosine was found in partial occupancy in the A subunit due to azide ion associating with the iron ion. The B subunit was only slightly affected by azide, already having hydroxide bound as a sixth ligand.

4.1.6 Geometric parameters

The geometric characteristics of the structure, such as bond lengths and angles, were compared against a library of small-molecule data with the program PROCHECK (Laskowski *et al.*, 1993). All the mean bond lengths and mean bond angles were within one standard deviation of the equivalent values from small molecules. In the Ramachandran plot, 92.0% (333) of residues were in the most favoured regions corresponding mostly to α-helical and β-sheet domains, 6.9% (25) of residues were in additional favoured regions, and 0.8% (3) were in generously allowed regions. One residue was in a disallowed region: Asn145 in subunit A. This residue is part of sharp turn sequence, and a similar geometry is seen in other structures of Fe/MnSODs.

During the refinement process a carboxyl terminus oxygen atom was omitted from each subunit during refinement and map calculation. The electron density was monitored as an indication of the inherent background noise during refinement and a measure of the accuracy of phase information. During the refinement the density for both atoms was seen as positive density in the $2|F_O|-|F_C|$ map at a sigma level of 1.0. The density peak in the A subunit was greater than in the B subunit; this is to be expected as the B subunit generally had higher temperatures factors and is inherently less well defined. Throughout refinement, density of the omitted atoms was comparable to the surrounding density. Refinement was stopped when no new information on structure could be gained from the

$2|F_O|-|F_C|$ map at the 0.8 σ level or from the $|F_O|-|F_C|$ at the 3 σ level. The carboxyl oxygen atoms were then added to complete the structure.

4.1.7 Building of active site, hydroxides and azide

The tail of the azide ion is orientated towards the substrate-access funnel, and the tail of the ion lies between residues Tyr34 and His30 in subunit A forming a hydrogen bond to Tyr34_OH. Previous structures of FeSODs complexed with azide, as well *Deino*-MnSOD-N_3^- (presented in this thesis), showed a distinct azide-binding pattern where the "tail" of the azide molecule is buried in a small cavity close to the active site. It seemed prudent to test if this binding pattern was actually supported by the *Ec*-Fe-MnSOD-N_3^- data. Accordingly, a trial model was built with the azide in the alternate binding motif and tested against the experimental data. This refinement proved unstable with the temperature factors of the tail of the azide refining to nonsensical values. Calculated phases and subsequent electron density maps that were generated after the refinement, as shown in Figure 4-3, also show that this incorrect orientation of the azide was not supported by X-ray data. This approach was further supported by examination of omit maps; refer to Figure 4-1.

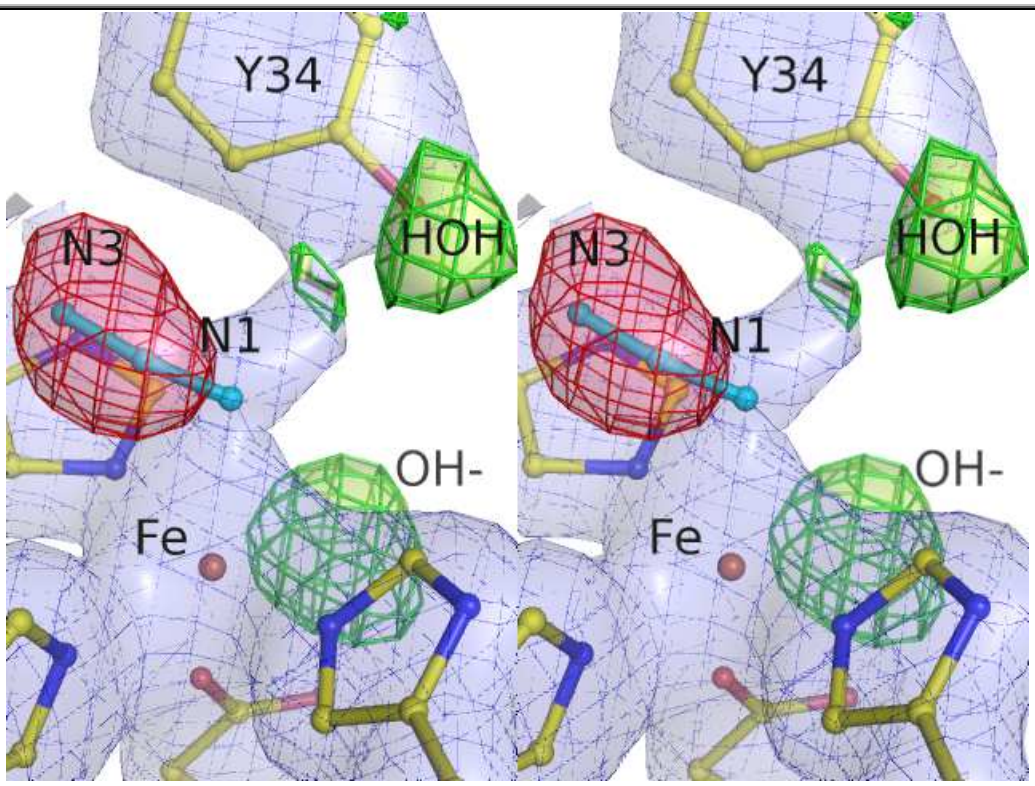

Figure 4-3. Testing the alternate azide-binding motif.

Figure 4-3 shows a wall-eyed stereo-pair that disproves potential interpretative bias in *Ec*-Fe-MnSOD-N_3^- by using a trial model with "incorrect" azide orientation. Before azide was added to the trial model of *Ec*-Fe-MnSOD-N_3^- in the correct orientation, an alternate, but feasible, azide-binding pattern was investigated. The trial model is shown as a ball-and-stick where the protein side chains are coloured yellow, blue and red to show carbon, nitrogen and oxygen respectively. The active-site metal, Fe, is shown as a red sphere labelled "Fe". The azide anion is also shown as cyan ball-and-stick where atom labelled N1 interacts with the metal centre and the atom labelled N3 sits in a nearby cavity.

The blue map, consisting of a thin blue mesh and transparent blue surface, shows a $2|F_O|-|F_C|$ map contoured at the 0.9 σ level. The green map, with thick green mesh and transparent green surface, shows positive peaks in a $|F_O|-|F_C|$ map contoured at the 3 σ level; negative peaks at the -3 σ level in a $|F_O|-|F_C|$ map are shown as a transparent red surface with a red mesh.

Phase information, particularly in the difference maps, is good enough to identify the position of individual atoms. This is evident by the large positive peak for a coordinated hydroxide, labelled "OH-", that is not included the trial model. A similar peak is seen for a nearby un-modelled water molecule, which is labelled "HOH". The position of the N1 atom is largely correct, as it falls well within the $2|F_O|-|F_C|$ map; however, the positions of the N2 and N3 atoms are incorrect as they do not lie comfortably within the $2|F_O|-|F_C|$ map but do lie in a negative peak in the $|F_O|-|F_C|$ map. This orientation of azide was therefore rejected.

4.1.8 Restraints

Azide binds preferentially at the five-coordinate Fe^{3+} active site in the A-chain of the dimer, while a six-coordinate Fe of the B-chain active site is only slightly affected; refer to Figure 4-4 and Figure 4-5. The occupancy of the azide molecule has been set to 0.6 in the active site of subunit A, and 0 in subunit B (absent).

The residue *A*_Y34 is disordered and likely sits in two conformations, azide-bound and azide-free, that can not be individually resolved. The position of the built *A*_Y34 is thus the average position of *A*_Y34, not as two conformations, and hence lies close to the density of the azide ion. No distance restraints between the *A*_Y34 and the azide ion were made.

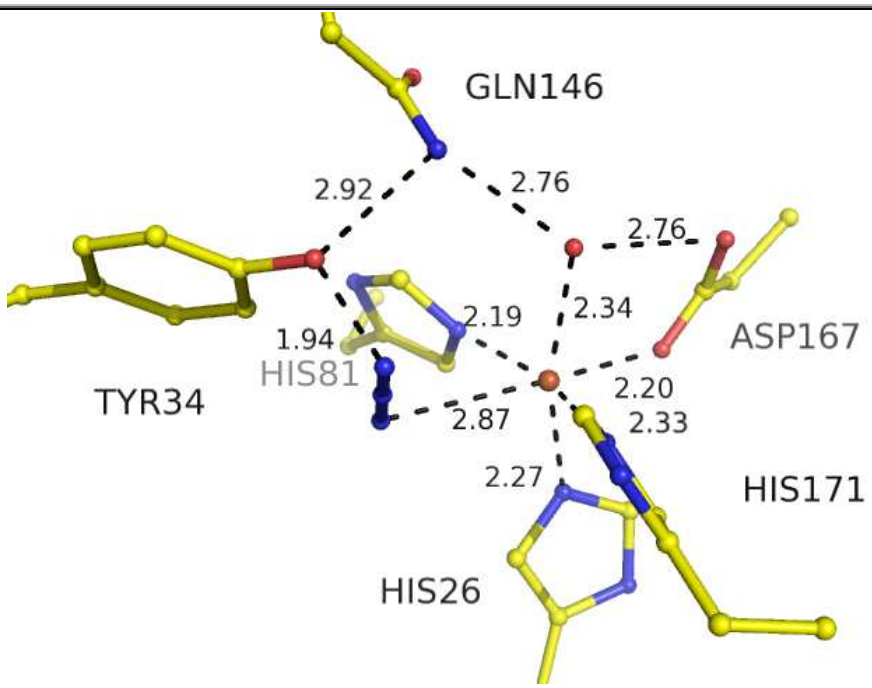

Figure 4-4. Active site of *Ec*-Fe-MnSOD-N_3^- for chain A.

Figure 4-4. Metal-ligating and selected residues of chain A of *Ec*-Fe-MnSOD-N_3^- shown as a ball-and-stick representation. The Fe^{3+} and the coordinated hydroxide ion are shown as orange and red spheres respectively. Interesting distances between atoms are shown as dashed black lines labelled with inter-atomic distances in Å.

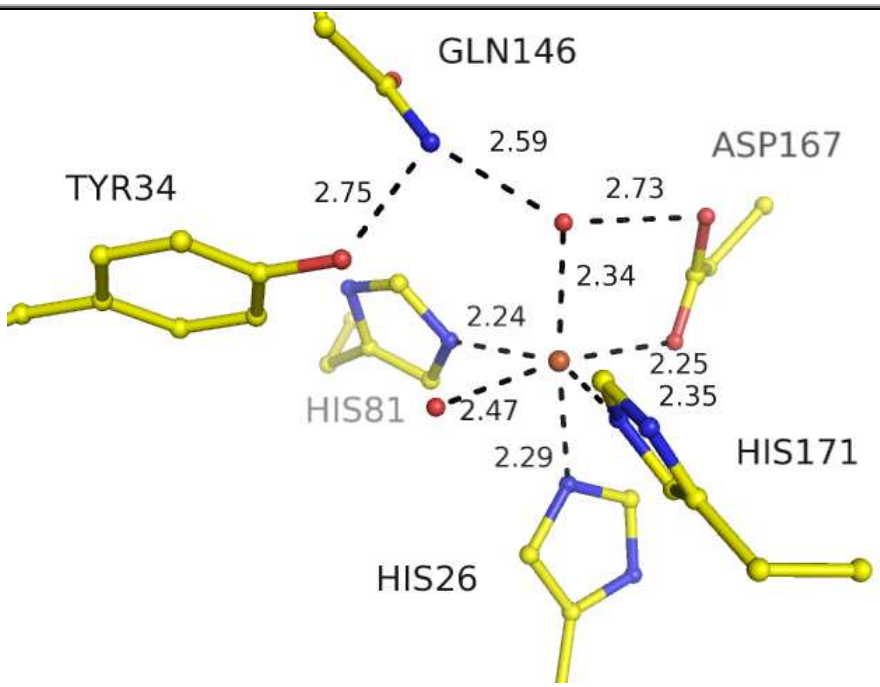

Figure 4-5. Active site of *Ec*-Fe-MnSOD-N_3^- for chain B.

Figure 4-5. The metal-ligating and selected active-site residues of the B chain of *Ec*-Fe-MnSOD-N_3^- shown as a ball-and-stick representation. The Fe^{3+} and the coordinated hydroxide ions are shown as orange and red spheres respectively. In this subunit *B*_Y34 is well ordered.

4.1.9 Structure of the active site of subunit A, with azide at 60% occupancy

The azide ion has associated with the Fe atom at the active site of subunit A only. It was originally thought that the azide ion would form a covalent bond, indicating an inner-sphere interaction, with the Fe at the active site as seen in other FeSOD work. This turned out not to be the case. As refinement progressed it became apparent that the distance between the azide ion and the metal centre precluded a covalent linkage. The structure of *Ec*-Fe-MnSOD-N_3^- indicates outer sphere interactions between the Fe and azide ion. The distance between the N1 of the azide ion and the Fe is 2.87 Å, the distance between N2 of the azide ion and Fe is 3.16 Å and the distance between the N3 atom and the Fe is 3.79 Å. The site of interaction between the inhibitor and the active-site metal is the N1 atom.

4.2 MnSOD from *Deinococcus radiodurans* at 2.0 Å resolution

4.2.1 Quality of data

The X-ray data derived from the crystal had a strong signal-to-noise ratio in outer shells as well as high redundancy and high completeness. Symmetry-related reflections also merged well, when the data were scaled and averaged together. There were higher resolution reflections detected but they had lower signal-to-noise ratio and suffered from lower average redundancy and were less complete, so were omitted.

4.2.2 Molecular replacement and initial map interpretation

The initial MR solution is shown in Figure 4-6. The initial maps were generally of high quality at 1 σ level, and where there were point differences in the amino-acid sequence between the *D. radiodurans* and the *E. coli* search model, differences were seen in electron maps, especially corresponding to side-chain differences; refer to Figure 4-7, which shows a regional side-chain difference and unambiguous electron density maps. Density corresponding to the backbone was generally well defined. The active-site region was well defined in all four subunits in the asymmetric unit. Positive peaks for water molecules could also be seen in initial maps.

4.2.3 Geometric parameters of *Deino*-MnSOD

The final structure of *Deino*-MnSOD was analysed by PROCHECK (Laskowski *et al.*, 1993). The geometry of the protein conformed well to the Ramachandran plot with 660 residues (93.1%) lying within allowed regions, 41 residues (5.8%) were in additionally allowed regions, 6 residues (0.8%) were in generously allowed regions and 2 residues (0.3%) in disallowed regions. This is consistent with other solved structures of this group, where an Asn in a loop just prior to the active site does not conform to Ramachandran predictions.

The bond lengths, planar groups and bond angles of *Deino*-MnSOD also agree well with small molecule data as reflected by the RMS values given in Table 2.

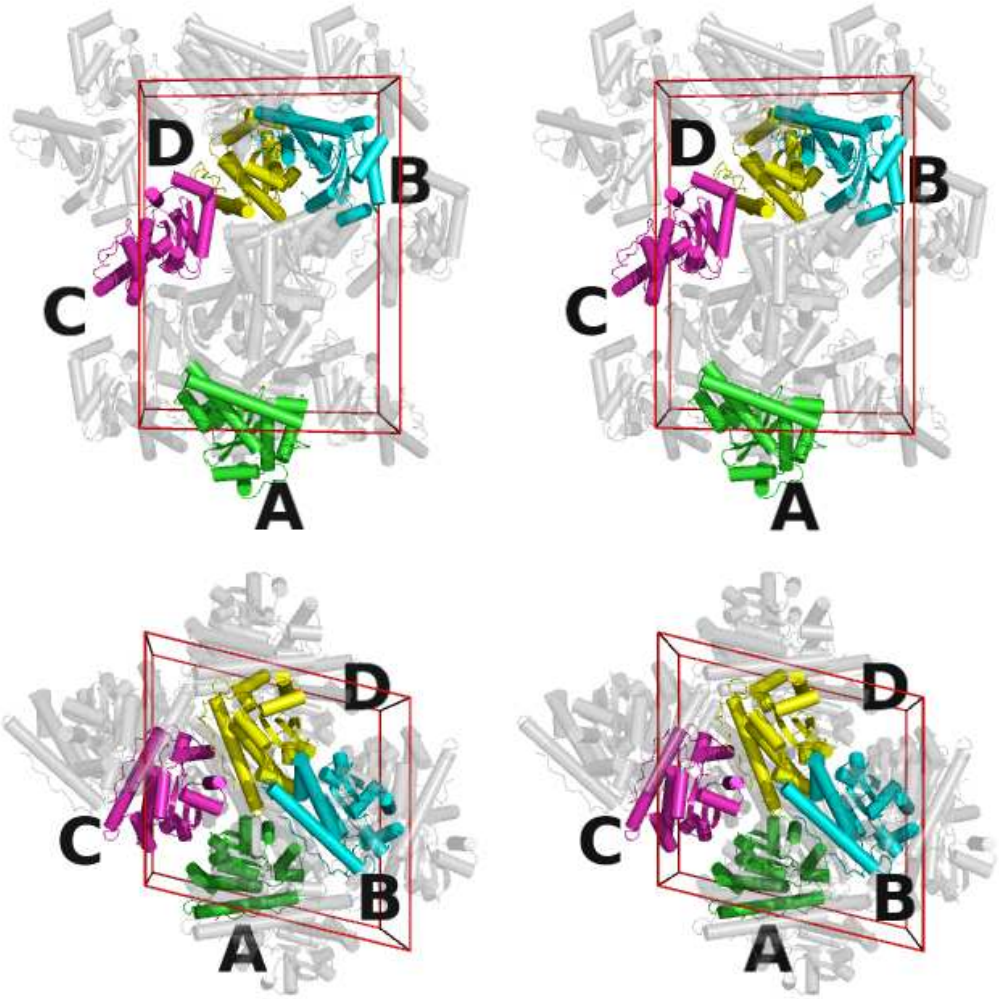

Figure 4-6. The MR solution of the *Deino*-MnSOD structure.

Figure 4-6**.** Two views are shown of the unit-cell packing of *Deino*-MnSOD. If the view shown in the top stereo-pair is rotated, 90°, around the x-axis, the bottom stereo-pair is created. In both views the unit cell is shown as a red box, the four monomers of the MR solution are shown as coloured cartoons, and symmetry-generated molecules are shown as transparent grey cartoons. The four subunits are coloured green, cyan, magenta and yellow for chains A, B, C and D respectively. The structure solution had no steric clashes.

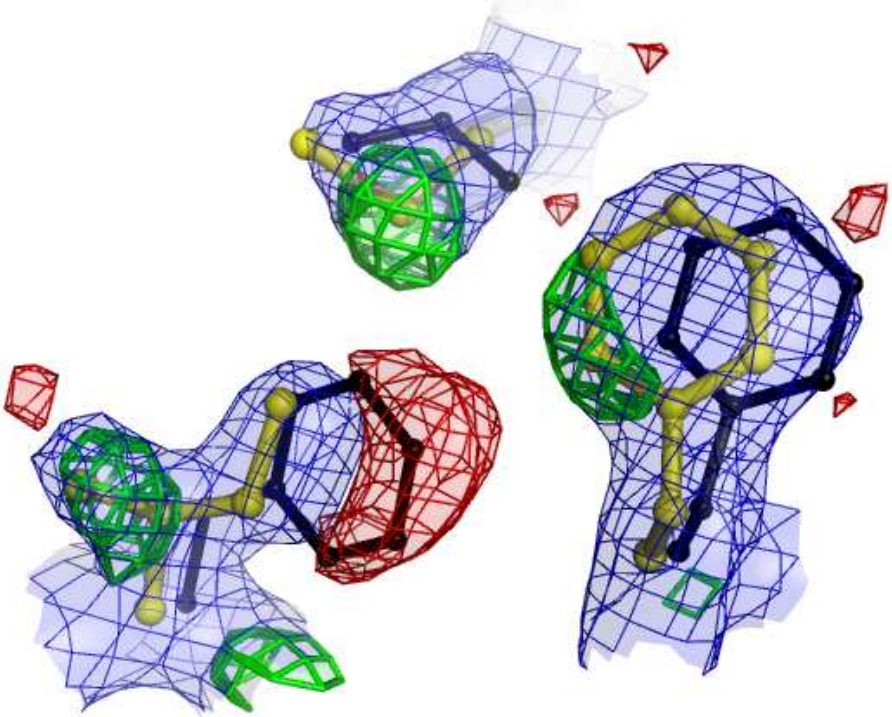

Figure 4-7. Electron-density maps from the molecular-replacement structural solution showing the quality of phases for *Deino*-MnSOD.

Figure 4-7. The image shows the quality of phasing in the electron-density maps claculated from the molecular-replacement solution and the final structure. The region shown is different between the molecular-replacement search model (1VEW) and the final *Deino*-MnSOD. Shown as black ball and sticks are three residues from the search model: Phe18, Leu88, and Phe188. Shown as yellow ball and sticks are the equivalent residues in *Deino*-MnSOD: Ile19, Met88, and Phe194 from the final refined structure. Point differences between the two structures are reflected in the electron density maps. The $2|F_O|-|F_C|$ map is contoured at the 1 σ level and is shown as both a blue mesh and a semi-transparent blue surface. Positive density peaks in the $|F_O|-|F_C|$ map at the 3 σ level are shown as a thick green mesh. Negative density peaks in $|F_O|-|F_C|$ map below -3 σ are shown as a red mesh and a semi-transparent red surface. Both maps were generated after rigid-body refinement of the MR solution by the PHENIX program suite.

4.2.4 Active-site structures of *Deino*-MnSOD

The structure of *Deino*-MnSOD is very similar to that of other MnSODs (and Fe-SODs). The protein fold and the obligate dimerisation were maintained in *Deino*-MnSOD. The active-site region was well defined throughout the refinement process. In early stages, the fifth ligand, the hydroxide, appeared as a protrusion of density from the large density peak associated with the metal ion. Also well defined were nearby solvent molecules in the solvent-access funnel; refer to Figure 4-8 to Figure 4-11, which show the four active sites and electron-density maps from the final refined structure..

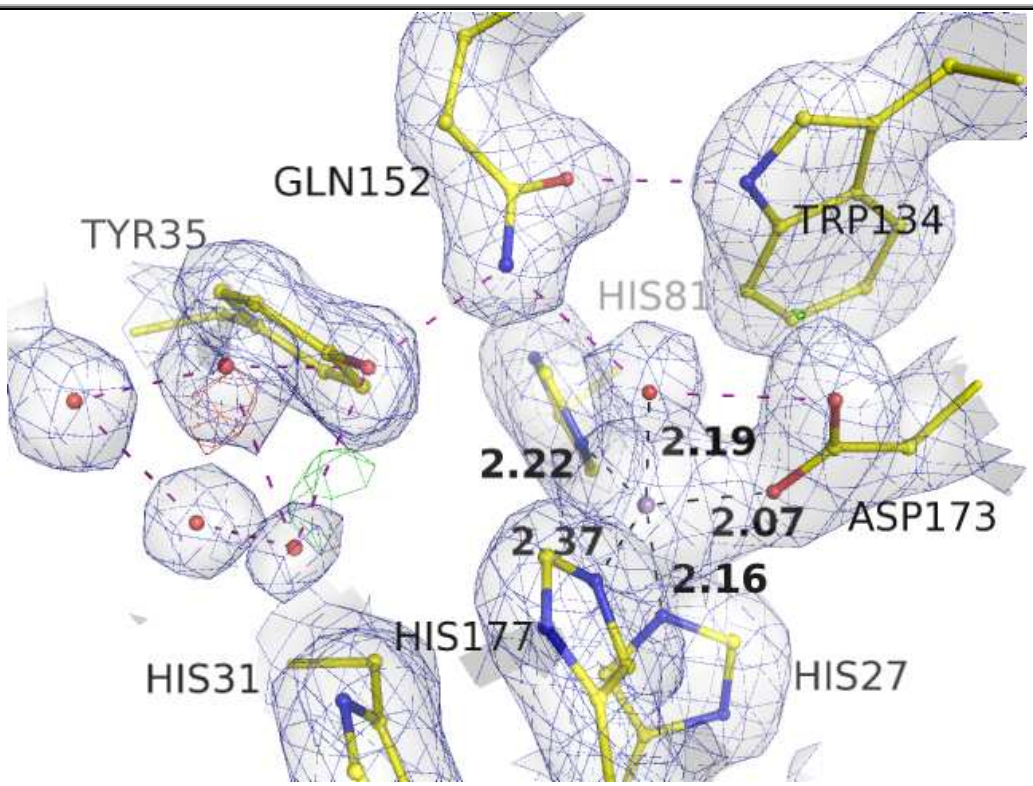

Figure 4-8. Active site of subunit A and nearby solvent-access funnel of *Deino*-MnSOD.

Figure 4-8, Figure 4-9, Figure 4-10 and Figure 4-11 show the four active sites of *Deino*-MnSOD for subunits A, B, C and D. Atoms are shown as a ball-and-stick representation coloured yellow, blue, red and magenta for carbon, nitrogen, oxygen and manganese respectively. Distances between the manganese cation and the five ligands are shown as dashed black lines with distances in Å. Hydrogen bonds are shown as purple dashed lines. The blue mesh shows a $2|F_O|-|F_C|$ map contoured at the 1 σ level. The green mesh shows positive density in a $|F_O|-|F_C|$ at the 3 σ level and the red mesh shows negative density contoured at the -3 σ level.

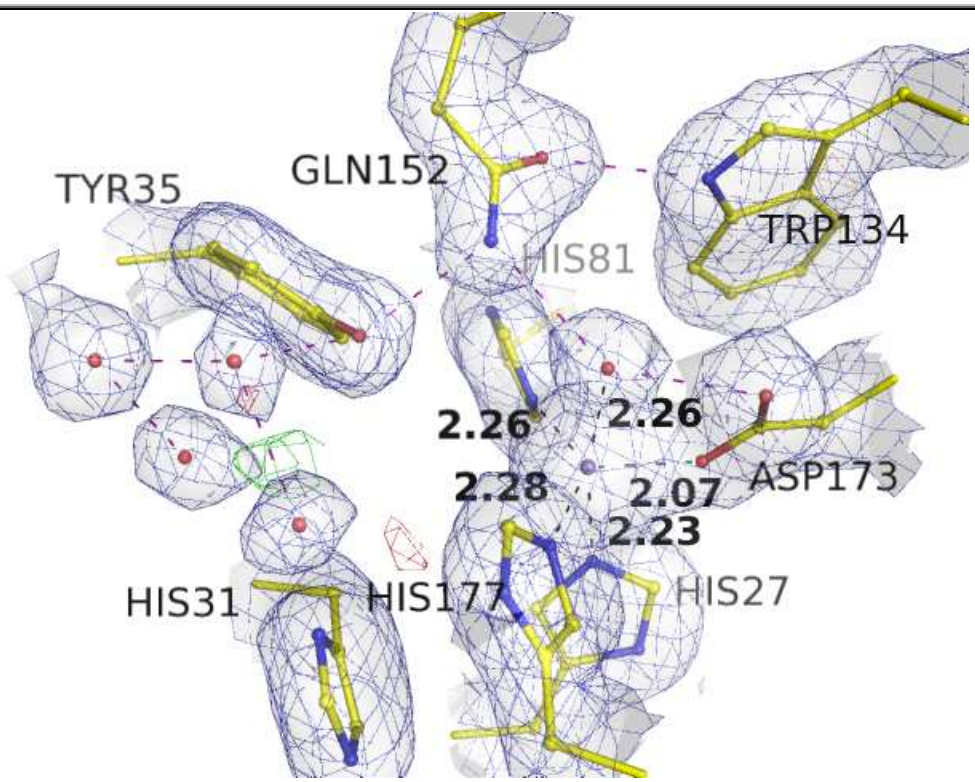

Figure 4-9. Active site of subunit B and nearby solvent-access funnel of *Deino*-MnSOD.

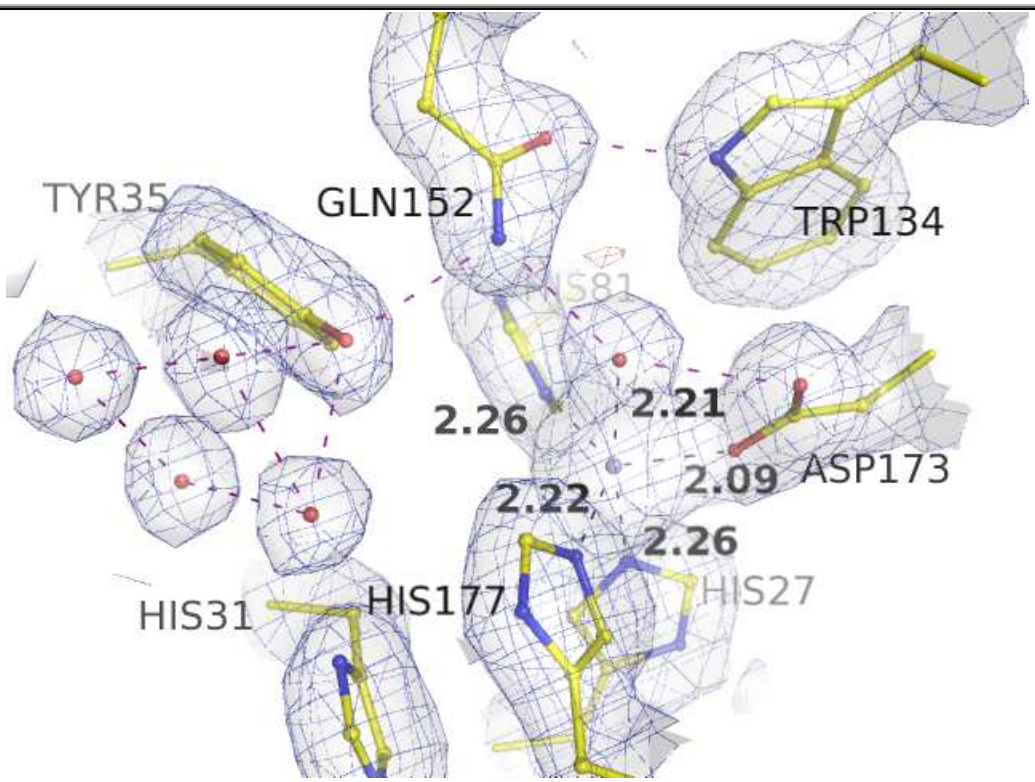

Figure 4-10. Active site of subunit C and nearby solvent-access funnel of *Deino*-MnSOD.

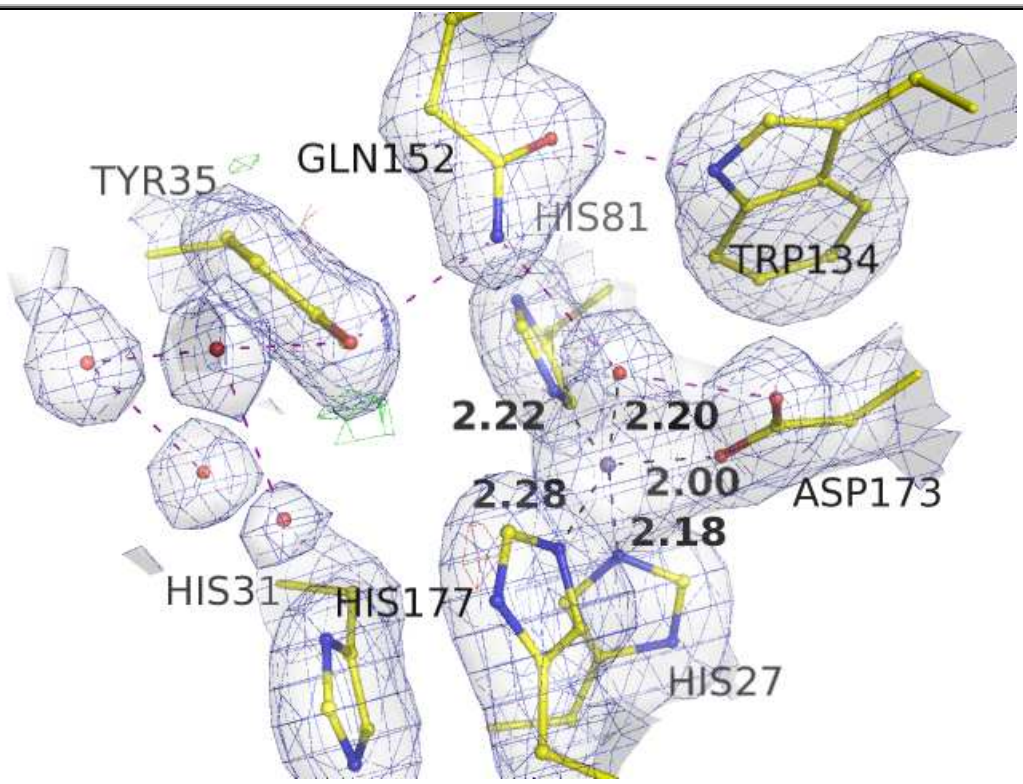

Figure 4-11. Active site of subunit D and nearby solvent-access funnel of *Deino*-MnSOD.

4.2.5 Comparisons among the active sites of the four subunits

In initial rounds of refinement there were weak NCS restraints among the four subunits. These restraints were weakened and eventually eliminated as refinement progressed. There were differences in rotamer conformations between the four subunits mostly at surface residues close to solvent molecules and at crystallisation contacts. At no point were there any NCS restraints on the position or temperature factors of water molecules.

When the active sites of all four subunits are overlaid there is high structural homology among the subunits; refer to Figure 4-12, which shows the four active sites and nearby solvent structure overlaid. Structural conservation extends to water molecules that line the solvent-access funnel.

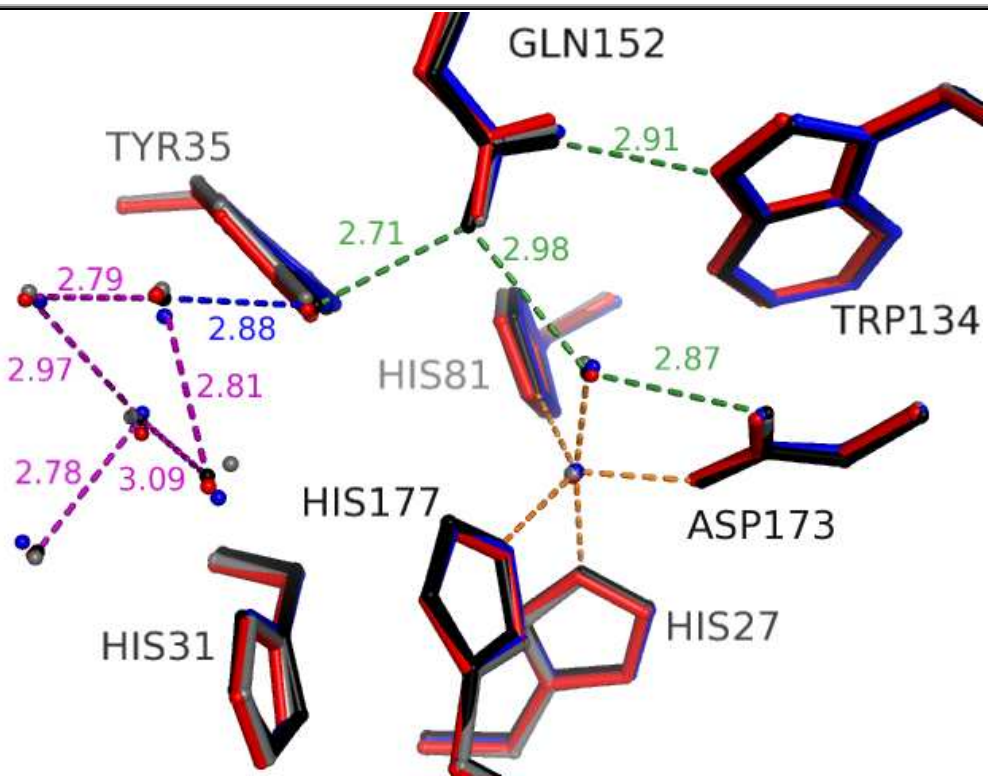

Figure 4-12. Overlay of the active sites of all four subunits of *Deino*-MnSOD.

Figure 4-12 shows an overlay of the active sites of all four subunits of *Deino*-MnSOD. Each of the four subunits is coloured a different colour: black, red, blue or grey. There is remarkable conservation of position across the four subunits, including the solvents of the substrate-access funnel. Protein side chains are shown as a stick representation. Water molecules, metal ions and the coordinated solvent molecule are shown as spheres. The active site is penta-coordinate, depicted as orange dashed lines without labels. Internal hydrogen bonds are shown as green dashed lines with distances, in Å, shown as green labels. Hydrogen bonds in the ordered solvent of the substrate-access funnel are shown as purple dashed lines. The hydrogen bond between the OH of Tyr35 and a solvent molecule is shown as a blue dashed line with blue label. All the hydrogen-bond distances are derived from the A subunit alone.

4.2.6 Description of the active site, angles and lengths of metal-binding ligands

The active site of *Deino*-MnSOD (refer to Figure 4-12) contains a manganese cation that is coordinated to three histidines (27, 81 and 177) and an aspartate (173). The fifth ligand is a solvent-derived molecule (assumed to be an hydroxide) that is stabilised by two hydrogen bonds, one to the aspartate ligand and the other to a nearby glutamine. This glutamine is involved in a hydrogen-bonding network that includes the solvent-access tyrosine (35) which is located within hydrogen-bonding distance of solvent molecules. The bond angles of the metal-ligating ligands are given in Table 6 and bond distances in Table 7.

	A	B	C	D	Ave	Std dev
∠His177_NE2•Mn•His81_NE2	131.35	136.06	131.60	132.20	**132.80**	2.20
∠His177_NE2•Mn•Asp173_OD2	113.30	114.51	115.55	114.78	**114.54**	0.93
∠His81_NE2•Mn•Asp173_OD2	115.05	109.40	112.75	112.93	**112.53**	2.33
∠His81_NE2•Mn•OH	94.94	95.54	88.31	94.07	**93.22**	3.33
∠His177_NE2•Mn•OH	84.46	90.30	95.97	89.44	**90.04**	4.72
∠Asp173_OD2•Mn•OH	84.57	84.16	85.43	82.19	**84.09**	1.37
∠His81_NE2•Mn•His27_NE2	94.34	90.91	93.58	94.77	**93.40**	1.73
∠His177_NE2•Mn•His27_NE2	92.88	91.19	89.29	89.77	**90.78**	1.61
∠Asp173_OD2•Mn•His27_NE2	87.31	85.33	85.78	87.96	**86.60**	1.24
∠His27_NE2•Mn•OH	169.63	169.03	171.06	168.74	**169.62**	1.03

Table 6. Bond angles of the active-site Mn and metal-ligating atoms of *Deino*-MnSOD.

Table 6 shows the bond angles of the coordinating ligands to the Mn cation at the active site of *Deino*-MnSOD. There are ten angles for each penta-coordinate metal ion. These angles, in degrees, are shown for all four subunits A-D along with the average angle, in bold, and the standard deviation for each of the recorded angles.

	A	B	C	D	Ave	Std-dev
Mn→His27_NE2	2.16	2.23	2.26	2.18	**2.21**	0.05
Mn→His81_NE2	2.22	2.26	2.26	2.22	**2.24**	0.02
Mn→His177_NE2	2.37	2.28	2.22	2.28	**2.29**	0.06
Mn→Asp173_OD2	2.07	2.07	2.09	2.00	**2.06**	0.04
Mn→OH	2.19	2.26	2.21	2.20	**2.22**	0.03

Table 7. Bond lengths between the active-site Mn and metal-ligating atoms of *Deino*-MnSOD.

Table 7 shows the bond distances between each of the five metal-binding ligands and the metal at each active site. The average distance is shown, in bold, together with the standard deviation of each bond. All distances are measured in Å.

4.3 MnSOD from *Deinococcus radiodurans* with azide at the active site solved to 2.0 Å resolution at 116 K

4.3.1 Crystal

The crystal used to solve *Deino*-MnSOD-N_3^- had similar size, shape and morphology to that used to solve *Deino*-MnSOD.

4.3.2 Merging, MR and initial maps

The X-ray data used to solve *Deino*-MnSOD-N_3^- were of high quality with good completeness, high redundancy and good merging statistics; refer to Table 2. The space group was the same and the unit cell angles and dimensions were similar to the crystal structure of *Deino*-MnSOD. Subsequent MR yielded a solution nearly identical to *Deino*-MnSOD.

4.3.3 Refinement

Density corresponding to the protein backbone was generally well defined for buried residues. The active-site metal ion was also well defined in all four subunits in the asymmetric unit in early maps as extremely large density peaks in both $2|F_O|-|F_C|$ and $|F_O|-|F_C|$ maps. There were also well defined, but much smaller, density peaks that corresponded to the oxygen atoms of the manganese-coordinated hydroxide. Unlike the native structure there were also density peaks at the active site that corresponded to a sixth ligand, with the expected size and shape of an azide ion. This is depicted in Figure 4-13, which shows positive density peaks of the active site associated with the fifth and sixth ligands, hydroxide and azide respectively. Where there were point differences between the search model (1VEW (Edwards, Baker *et al.*, 1998)) and *Deino*-MnSOD, this was apparent in density maps showing accurate determination of phases; refer to Figure 4-14. Many density peaks that were associated with water molecules were also seen in the initial maps.

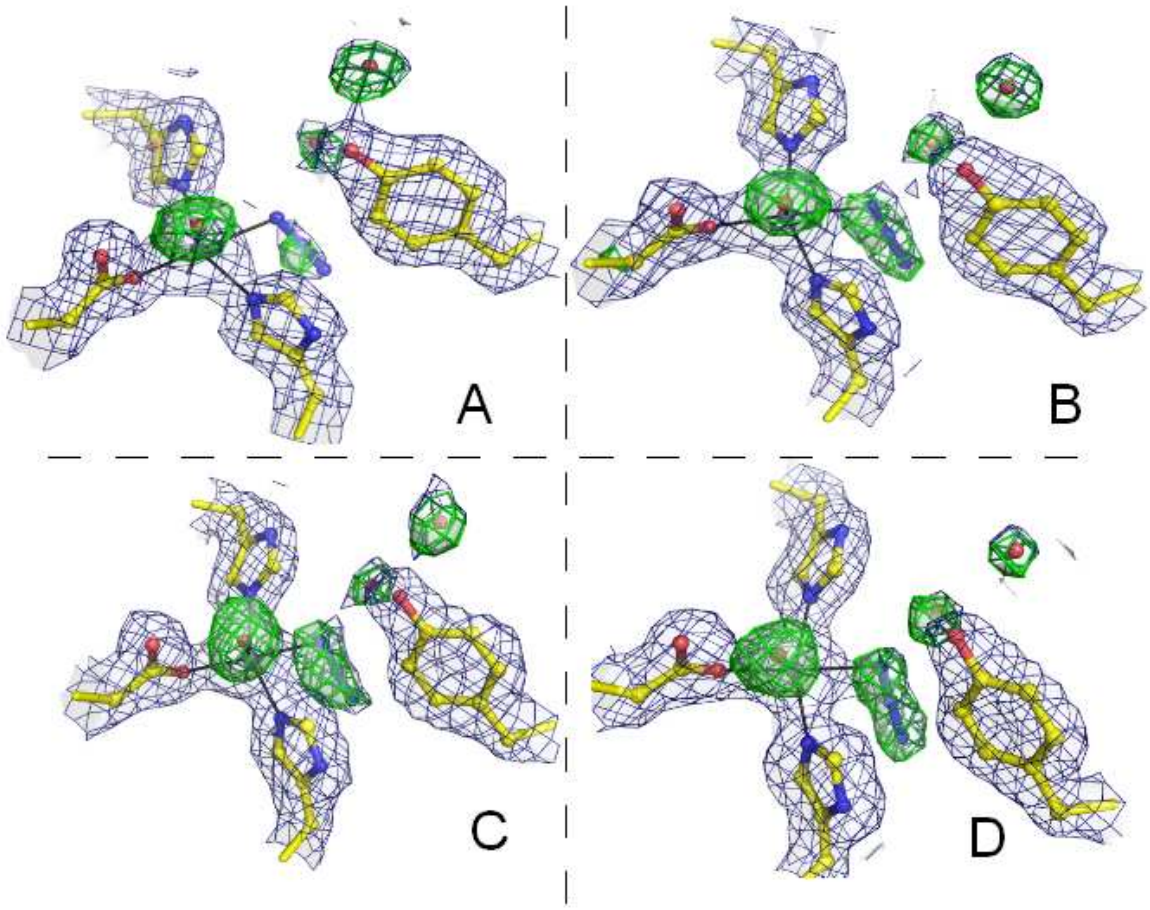

Figure 4-13. Difference density peaks of the fifth and sixth ligands of the active-site Mn for *Deino*-MnSOD-N_3^-.

Figure 4-13. shows the electron-density maps from early in the refinement of *Deino*-MnSOD-N_3^- overlaid onto coordinates from the final structure. At this stage in the refinement process the trial model does not contain a fifth or sixth ligand or any water molecules. The blue map shows a $2|F_O|-|F_C|$ map contoured at the 1 σ level, the green map shows positive peaks in the $|F_O|-|F_C|$ map contoured at the 3 σ level. A red map was rendered showing negative density peaks in the $|F_O|-|F_C|$ map at -3 σ, but in this region negative density is barely perceptible. All four active sites are shown in A-D with a similar orientation for each active site. A ball-and-stick representation is used for atomic positions coloured yellow, red, blue and magenta for carbon, oxygen, nitrogen and manganese respectively. In all four active sites there are positive density peaks in the $|F_O|-|F_C|$ map associated with the hydroxide, azide and water molecules.

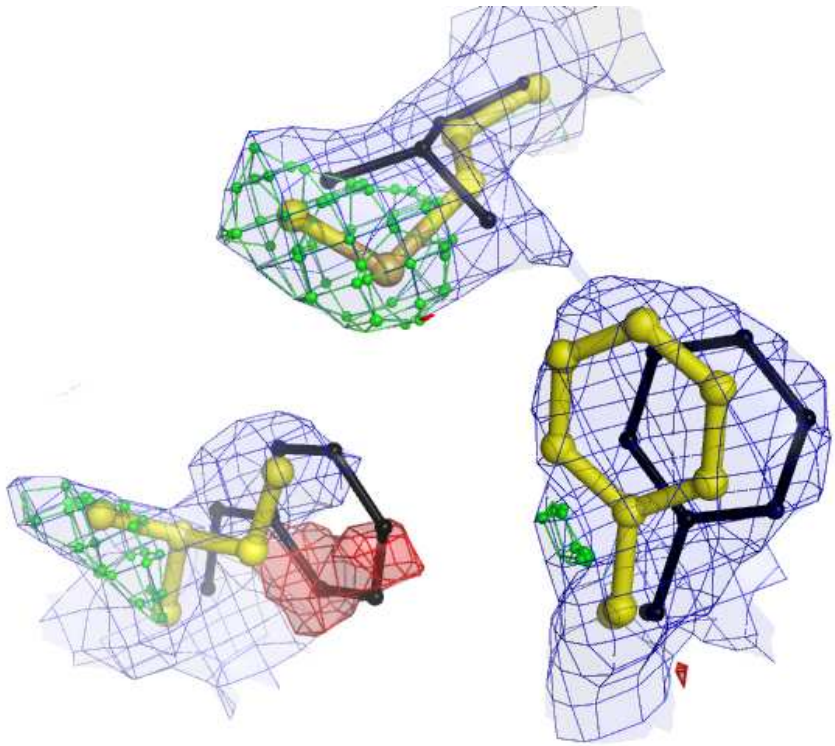

Figure 4-14. Quality of phase information from the solution of *Deino*-MnSOD-N_3^- as shown in electron-density maps from early rounds of refinement.

Figure 4-14 shows sequence and structural divergence between the A-chain of *Deino*-MnSOD-N_3^- and the *Ec*-MnSOD search model (chain A of 1VEW) used to solve the structure. This figure is intended to show the quality of phase information derived from the molecular-replacement solution. The phases for map generation were calculated after 10 cycles of rigid-body refinement of the initial MR solution by the REFMAC program. The blue mesh with a light blue semi-transparent surface represents a $2|F_O|-|F_C|$ electron-density map contoured at a 1.2 σ level. The green mesh with small spheres at the vertices depicts positive density in a $|F_O|-|F_C|$ map contoured at a 3.0 σ level. The red mesh with a transparent pink surface shows negative density in a $|F_O|-|F_C|$ map contoured at a -3.0 σ level. The yellow ball-and-stick representation shows three side chains from the final structure of *Deino*-MnSOD-N_3^- (Ile 19, Met 88 and Phe 194). The black ball-and-stick representation shows the equivalent three side chains from the initial *Ec*-MnSOD-based MR solution (Phe 18, Leu 88 and Phe 188). The quality of phases was such that correct rotamers of Ile 19 and Met 88 could be easily identified in the $2|F_O|-|F_C|$ electron density map. Also interpretation of the positive and negative density peaks in the $|F_O|-|F_C|$ map also showed where starting model did not agree with the search model.

In subsequent rounds, analysis of difference Fourier maps indicated that the occupancy of each of the four azide ions was less than 100%. In the final structure they are present in 60%, 80%, 80% and 90% for subunits A, B, C and D respectively and this is reflected in the comparative size of density peaks as shown in Figure 4-13. This led to stable refinement of active-site temperature factors with *B* values similar to those of neighbouring residues and manganese ions. In final rounds there were no distance or angle restraints between the metal and ligands. In final rounds of refinement solvent was built using the automated procedure within PHENIX. In each of the four subunits there was a loop region for which the electron density was ambiguous and models attempting to fit this data did not refine well.

In all, eight rounds of manual and automated refinement of the structure were performed. Over the eight rounds of refinement, NCS restraints were weakened and then eliminated. At the end of each round, the geometry of the structure was checked using PROCHECK (Laskowski *et al.*, 1993) and in later rounds the agreement of the structure with the calculated structure factors was checked using SFCHECK (Vaguine *et al.*, 1999). After the third round of refinement well defined water molecules were added into density peaks 2.6-3.2 Å from hydrogen bonding partners. During the fourth round of refinement the four metal ions were added to extremely large peaks at the active site, which reduced R_{cryst} to 22.7% and the R_{free} to 25.4%. Hydroxide ions were built into large density peaks at the fifth ligand-binding site. Azide ions were built into large well defined density peaks in the vacant sixth ligand-binding site. Final refinement statistics are given in Table 2. The final electron density maps are shown at the active sites of all four subunits in Figure 4-15, Figure 4-16, Figure 4-17 and Figure 4-18.

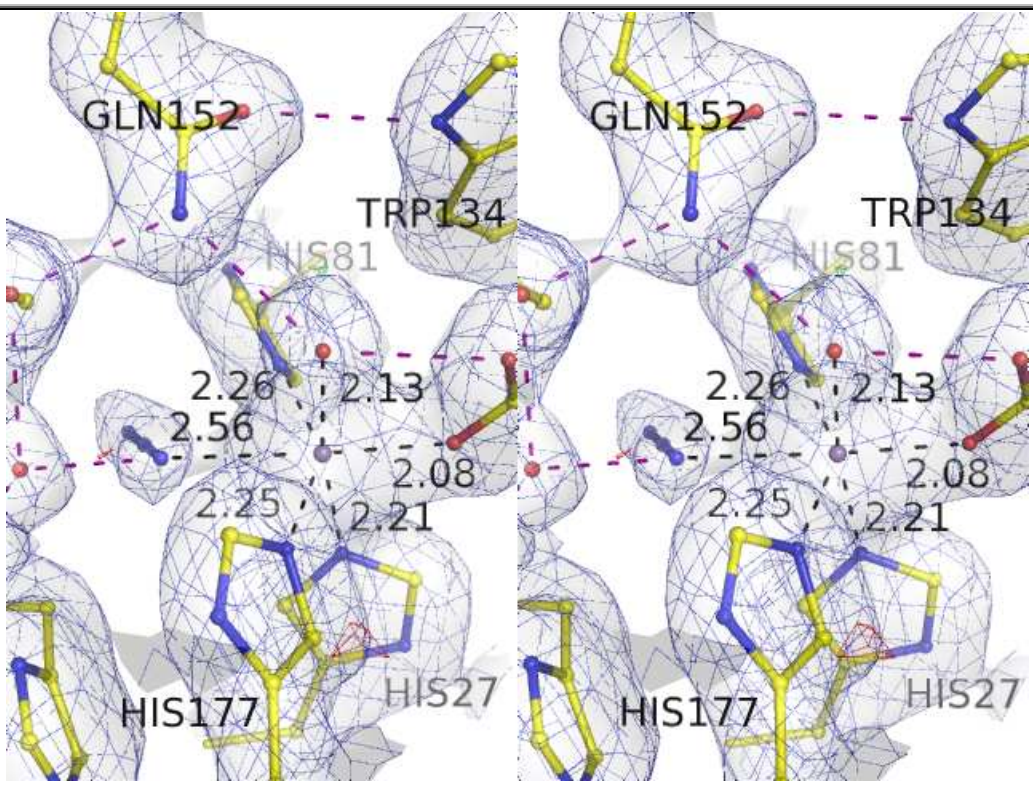

Figure 4-15. Wall-eyed stereo-diagram showing electron-density maps at the active-site of the A subunit of *Deino*-MnSOD-N_3^-.

Figure 4-15, Figure 4-16, Figure 4-17 and Figure 4-18 show atoms and bonds as a ball-and-stick representation coloured yellow, blue, red and magenta for carbon, nitrogen, oxygen and manganese. The blue electron density map shows a $2|F_O|-|F_C|$ map contoured at the 1 σ level. Positive density peaks, above 3 σ, in the $|F_O|-|F_C|$ map are shown by green density. Negative density peaks, below -3 σ, in the $|F_O|-|F_C|$ map are shown as red density. Probable hydrogen bonds are shown as dashed purple lines. Bonds between the metal-ligating residues and the active-site manganese are shown as black dashed lines labelled with distances in Å. The active-site metal is hexa-coordinate. Three of the metal-ligating residues are histidines, the fourth is an aspartate, the fifth is a solvent derived molecule and the sixth ligand is an azide ion.

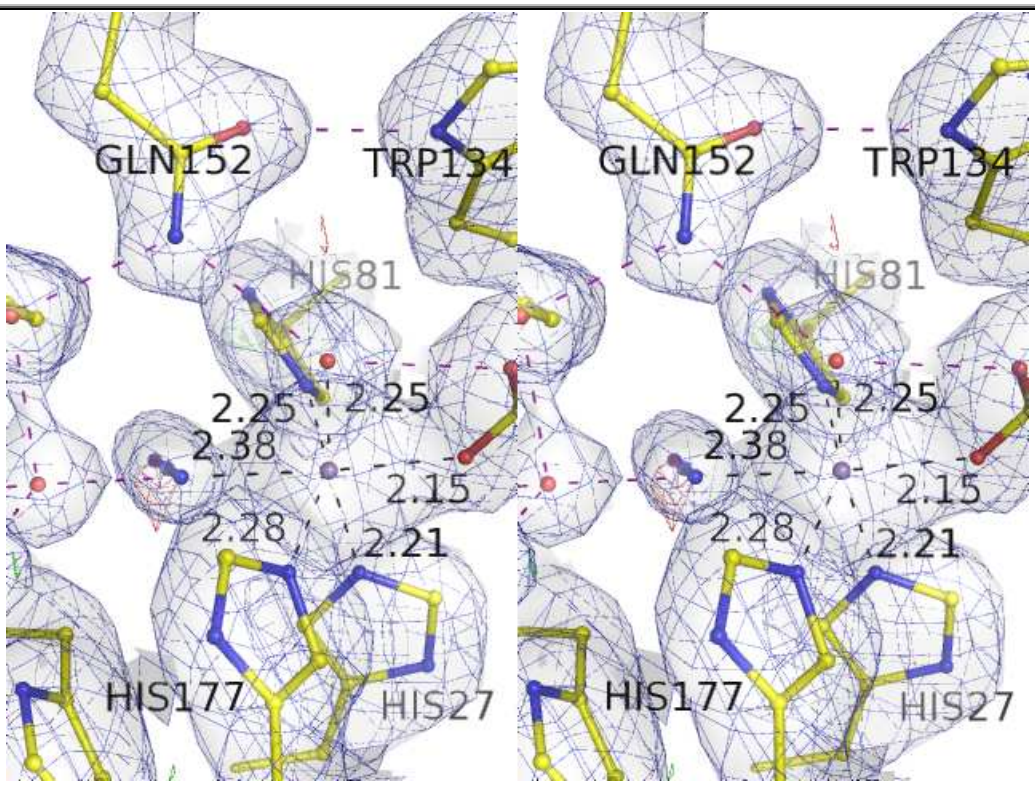

Figure 4-16. Wall-eyed stereo-diagram showing electron-density maps at the active site of the B subunit of *Deino*-MnSOD-N_3^-.

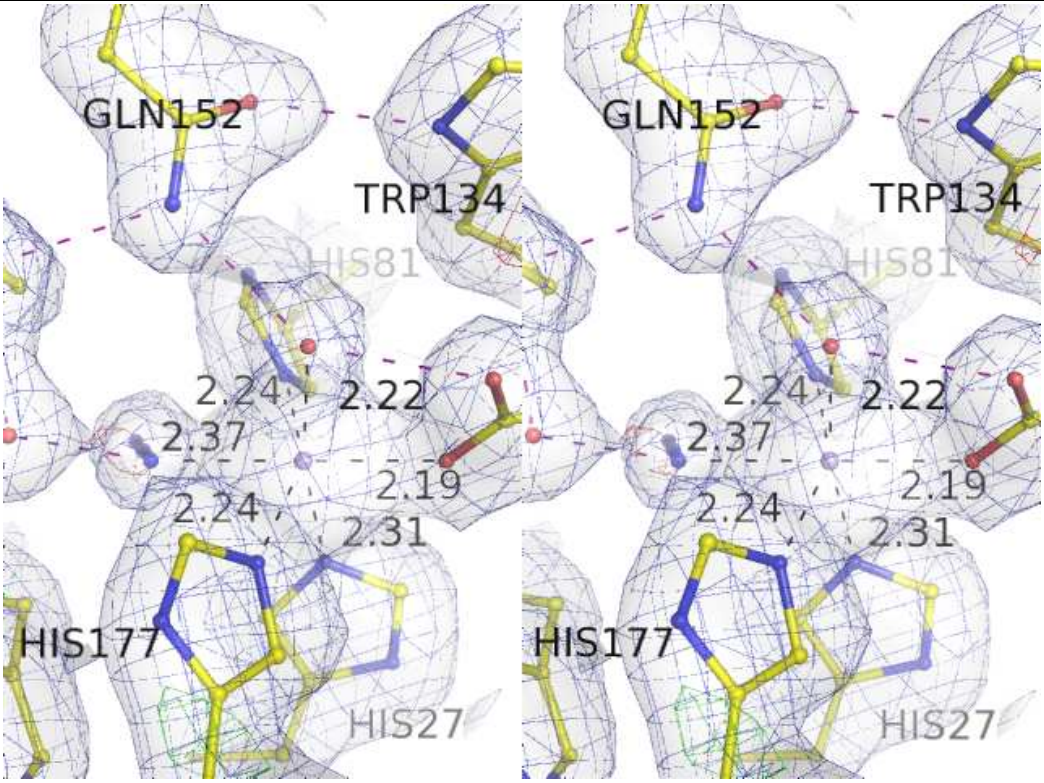

Figure 4-17. Wall-eyed stereo-diagram showing electron-density maps at the active site of the C subunit of *Deino*-MnSOD-N_3^-.

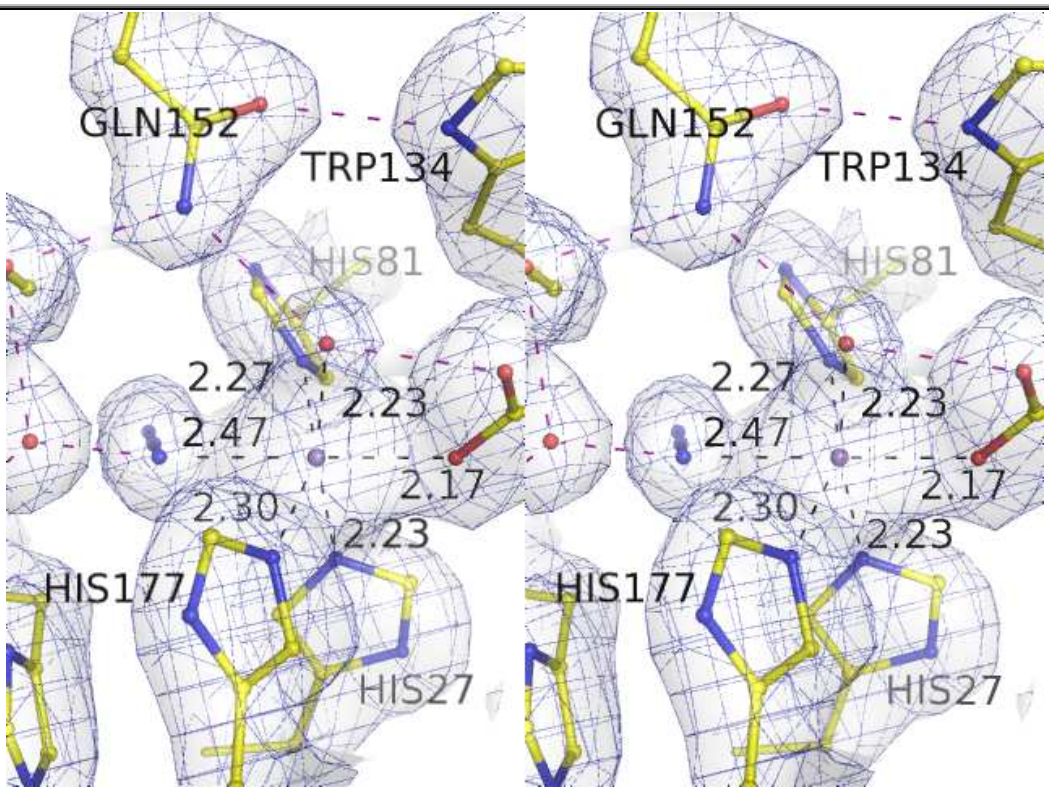

Figure 4-18. Wall-eyed stereo-diagram showing electron-density maps at the active site of the D subunit of *Deino*-MnSOD-N_3^-.

4.3.4 Geometric parameters

The quality of the geometric criteria such as bond lengths and angles of *Deino*-MnSOD-N_3^- structure were checked using the internal validation tools of TURBO and COOT as well as dedicated programs such as PROCHECK (Laskowski *et al.*, 1993). The agreement of the structure with the phase information was checked using omit maps generated by CNS (Bhat, 1989) and SFCHECK (Vaguine *et al.*, 1999).

Analysis of Ramachandran plot (Ramachandran *et al.*, 1963) showed 666 (93.9%) of the residues lying within allowed regions, 35 (4.9%) in additionally allowed regions, 6 (0.8%) residues were in generously allowed regions and 2 (0.3%) residues were in disallowed regions. The two residues in disallowed regions in the Ramachandran plot are Asn151 from chain A and chain C. The corresponding residues in chain B and D are in permitted regions, just. This is consistent with other solved Fe/MnSOD structures, where the equivalent Asn has atypical torsion angles in a loop just prior to the active site. Other geometric parameters such as bond lengths, angles, planar and chiral groups were all within acceptable tolerances.

4.3.5 Azide ion

The orientation of azide was similar in each of the four subunits. The pattern of azide binding is more reminiscent of that seen in FeSODs and a camb-FeSOD (Lah *et al.*, 1995, Schmidt *et al.*, 1998) than that seen in the previously solved MnSOD-N_3^- from *Thermus*

thermophilus (Lah *et al.*, 1995). There is also a rearrangement of the solvent molecules of the solvent-access funnel; most noticeable is the movement of a water molecule into the active site to make hydrogen bonds with the azide ion, the solvent-access funnel tyrosine and two other solvent molecules. This provides a potential proton-transfer pathway from the solvent to the N1 atom of the azide, and by inference to the bound superoxide during normal catalysis. This will be discussed later in section 6.7.8 and in proposed mechanisms in chapters 7 and 8.

4.3.6 Comparison of active sites between subunits

There is a high conservation of atomic positions between the active sites of the four subunits, including the water molecules; refer to Figure 4-19, which shows an overlay of the metal-ligating residues and nearby solvent molecules for all four subunits. The first atom that the azide-associated water can interact with is the N1 atom of the bound azide. The second hydrogen-bonding contact is the OH atom of the structurally conserved tyrosine that gates the active site from solvent molecules. The other two hydrogen-bonding contacts of the azide-bound water are solvent molecules of the solvent-access funnel. The azide-associated water molecule provides a possible proton pathway between the bulk solvent and the active site.

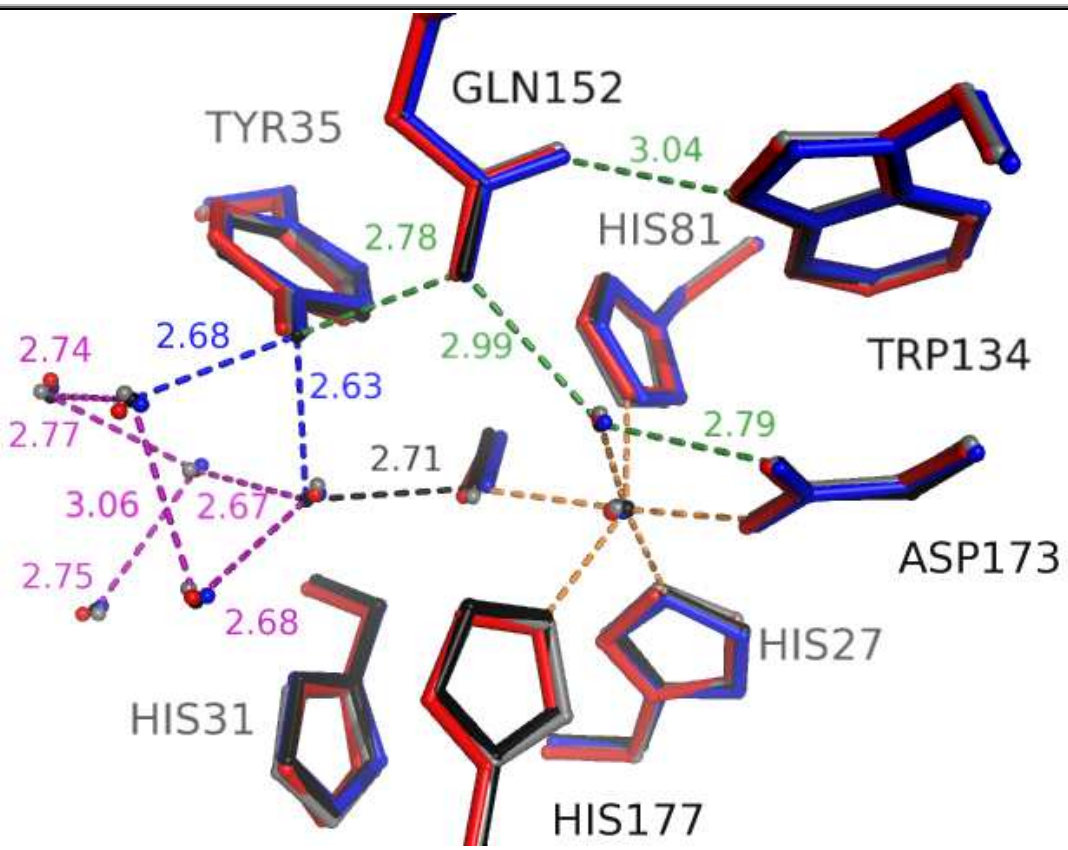

Figure 4-19. Hydrogen-bonding network that links the active site of *Deino*-MnSOD-N_3^- to the ordered solvent of the substrate-access funnel.

Figure 4-19 is an overlay of the active sites of all four subunits of *Deino*-MnSOD-N_3^-. Each of the four subunits is coloured a different colour: black, red, blue or grey for chains A-D. There is remarkable conservation of position across the four subunits, including the water molecules of the substrate-access funnel. Protein side chains and the azide ion are shown as a stick representation. Water molecules, metal ions and the coordinated solvent molecule are shown as spheres. The active site is hexa-coordinate, depicted as orange dashed lines without labels. Internal hydrogen bonds are shown as green dashed lines with distances, in Å, with green labels. Hydrogen bonds in the ordered solvent of the substrate-access funnel are shown as purple dashed lines. Hydrogen bonds between the OH of Tyr35 and solvent molecules are shown as blue dashed lines with blue labels. The hydrogen bond between the N1 of the azide molecule is shown as a black dashed line with a black label. All distances depicted are derived from the A subunit alone.

4.3.7 Description of the active site of the azide-bound form

The active-site metal is hexa-coordinate with four ligands being supplied by the protein. Three of the metal-binding protein ligands are histidines (27, 81 and 177) and the fourth ligand is an aspartate (173). The fifth ligand is a solvent-derived molecule, a hydroxide, which is stabilised by two hydrogen bonds, one to the active-site aspartate and the other to a glutamine (152). The sixth ligand is an azide ion that has bound end-on via the N1 atom; the other atoms of the azide ion site sit in a nearby cavity. The bond angles of the active site metal are given in Table 8 and metal-to-ligand distances are given in Table 9. The N1 atom of azide forms a hydrogen bond to a nearby water molecule. The azide-stabilised water maintains a tetrahedral hydrogen-bonding structure interacting with the azide, two waters, and the solvent-access funnel tyrosine (35). The hydroxyl group of this tyrosine also hydrogen bonds to the glutamine that stabilises the bound solvent-derived ligand.

	A	B	C	D	Ave	Std dev
∠His177_NE2•Mn•His81_NE2	148.05	154.73	154.05	157.86	**153.67**	4.10
∠His177_NE2•Mn•Asp173_OD2	106.46	104.45	102.93	101.29	**103.78**	2.20
∠His81_NE2•Mn•Asp173_OD2	105.32	100.79	102.74	100.51	**102.34**	2.22
∠His81_NE2•Mn•OH	91.42	93.57	91.49	85.83	**90.58**	3.32
∠His177_NE2•Mn•OH	87.44	91.17	94.96	93.52	**91.77**	3.28
∠Asp173_OD2•Mn•OH	86.07	81.79	83.78	81.74	**83.35**	2.05
∠His81_NE2•Mn•His27_NE2	93.32	91.58	85.59	93.88	**91.09**	3.80
∠His177_NE2•Mn•His27_NE2	92.40	89.24	92.28	91.29	**91.30**	1.46
∠Asp173_OD2•Mn•His27_NE2	85.59	85.54	86.44	86.35	**85.98**	0.48
∠His27_NE2•Mn•OH	171.25	167.01	168.92	167.82	**168.75**	1.84
Azide specific angles						
∠AZI_N1•Mn•His27_NE2	96.53	95.43	94.15	95.23	**95.34**	0.98
∠AZI_N1•Mn•His81_NE2	72.75	79.33	77.70	81.20	**77.75**	3.62
∠AZI_N1•Mn•His177_NE2	75.37	75.44	76.67	76.89	**76.09**	0.80
∠AZI_N1•Mn•Asp173_OD2	177.18	176.13	179.29	177.60	**177.55**	1.31
∠AZI_N1•Mn•His27_OH	91.90	97.41	94.15	95.23	**94.67**	2.29

Table 8. Bond angles between the active-site Mn and the metal-ligating atoms of *Deino*-MnSOD-N_3^-.

Table 8 shows the bond angles of the coordinating ligands to the hexa-coordinate Mn cation at the active site of *Deino*-MnSOD-N_3^-. These angles, in degrees, are shown for all four subunits A-D, along with average angle, in bold, and the standard deviation for each of the recorded angles. The first ten angles in the table also exist in the penta-coordinate *Deino*-MnSOD; the last five angles in the list involve the azide ion.

	A	B	C	D	Ave	Std dev
Mn→His27_NE2	2.21	2.21	2.31	2.23	**2.24**	0.05
Mn→His81_NE2	2.26	2.25	2.24	2.27	**2.26**	0.01
Mn→His177_NE2	2.25	2.28	2.24	2.30	**2.27**	0.03
Mn→Asp173_OD2	2.08	2.15	2.19	2.17	**2.15**	0.05
Mn→OH	2.13	2.25	2.22	2.23	**2.21**	0.05
Sixth ligand						
Mn→AZI	2.56	2.38	2.37	2.47	**2.45**	0.09

Table 9. Bond lengths between the active-site Mn and metal-ligating atoms of *Deino*-MnSOD-N_3^-.

Table 9 shows the bond distances between each of the six metal-binding ligands and the cation at each active site of *Deino*-MnSOD-N_3^-. The first five distances in the list exist in the wild type structure, the sixth distance is formed by the binding of azide. The average distance is shown, in bold, as is the standard deviation of each bond. All distances are measured in Å.

4.4 Attempted high-temperature structure determination of *Deino*-MnSOD-N_3^-

As one of the key differences between the structural determination of *Deino*-MnSOD-N_3^- at 116 K and *Thermus*-MnSOD-N_3^- at ambient temperatures is the temperature of data collection. This lead to the hypothesis that the observed differences in azide orientation between the two structures may be the result of the difference in the temperature of data collection. There is a documented temperature-dependent transition in the spectra of *Ec*-MnSOD-N_3^- (Whittaker & Whittaker, 1996) and *Thermus*-MnSOD-N_3^- (Whittaker & Whittaker, 1997b) at 220 K and 300 K respectively. This transition is far more pronounced in the azide-inhibited forms than wild-types.

4.4.1 Results of attempted high-temperature data collection

Unfortunately the determination of a high-temperature structure of *Deino*-MnSOD-N_3^- did not occur. During experiments the crystals initially diffracted, but then as time progressed diffraction decreased and then ceased all together. This time-dependent loss of diffraction was most visible in the high resolution shells (the shells of most interest). In initial images individual high resolution reflections had significant signal-to-noise ratios compared to the background and a well defined shape. As the experiment progressed reflections lost intensity and their morphology became blurry before disappearing all together over a period of one to three hours. This was taken to indicate that the crystals were prone to radiation damage.

4.4.2 Intermediate temperatures, below 0 °C

When crystals of *Deino*-MnSOD-N_3^- were mounted at temperatures below freezing point rings formed in the diffraction pattern, which is characteristic of ice forming in the crystal.

There was also a concurrent loss of diffraction with time. It is likely that the ice was disrupting the three-dimensional lattice of the ordered crystal.

4.5 Point mutants of *Ec*-MnSOD

4.5.1 Crystals

Crystalline material was readily produced; however, some of the mutants crystallised more readily as large crystals, such as S82T-*Ec*-MnSOD. The size of the crystals was not large enough to determine visually any colouration in an accurate manner. Long, thin, needle-like crystals also grew, but were not used in diffraction studies as they could not be easily manipulated.

4.5.2 Quality of X-ray data, MR and initial maps

All four data sets have high redundancy, completeness and significant intensity at high resolutions, enough to allow accurate atomic resolution determination of structures. All four mutants were readily solved using MOLREP (Vagin & Teplyakov, 1997) and refined using rigid-body refinement. In initial maps the electron density was interpretable and there were detectable peaks associated with metal ions and solvent molecules. Importantly in the regions surrounding the sites of mutations there were detectable differences to WT-*Ec*-MnSOD indicating that residues surrounding the sites of mutation have shifted. These mutants were not further refined, due to time constraints.

5 Critical evaluation of the structures of azide-inhibited MnSOD and FeSODs

The structure of *Deino*-MnSOD-N_3^- shows an azide-binding pattern similar to that seen in two FeSOD-N_3^- structures, *Ec*-FeSOD-N_3^- (Lah *et al.*, 1995) and *Psherm*-FeSOD-N_3^- (Schmidt *et al.*, 1998) and the mutant structure Y174F-*Ec*-MnSOD-N_3^- (PDB code 1ZLZ, work by co-workers) from *E. coli, Propionibacterium shermanii* and *E. coli* respectively. On the other hand, azide binding in *Ec*-Fe-MnSOD-N_3^- follows a pattern seen in MnSOD-N_3^- from *Thermus thermophilus.* This raises questions as to which binding pattern is correct. Alternately both patterns may be possible; if so then any comprehensive explanation of SOD function must also explain how and why both binding motifs are stabilised. The reliability of azide-inhibited SODs must then be critically evaluated; this is particularly true of the azide-inhibited MnSOD from *Thermus thermophilus* which is, to our knowledge, the only wild-type MnSOD that has been solved in the presence of azide prior to this thesis. This chapter provides a critical analysis of azide-inhibited SOD structures.

5.1 The structure of *Thermus*-MnSOD-N_3^-

In the structure of azide-inhibited MnSOD from *Thermus thermophilus* (*Thermus*-MnSOD-N_3^-) the binding of azide causes a change in the penta-coordinate Mn at the active site in azide-free wild-type enzyme (*Thermus*-MnSOD) to a hexa-coordinate Mn. The conserved access-funnel tyrosine moves to accommodate the azide molecule; refer to Figure 5-1. The actual structure is a mixture of azide-bound (designated L in the PDB file 1MNG) and azide-free forms (designated U in the PDB file 1MNG), each refined at approximately half occupancy.

5.1.1 Structure solution and refinement protocols of *Thermus*-MnSOD-N_3^-

It must be stressed that Lah and co-workers followed procedures and protocols that were appropriate for the time in which they worked. But since then data treatment and refinement practices have improved due in part to better instrumentation, computing hardware, and X-ray crystallography software for data collection, structure solution and refinement. There has also been an increase in structure validation and analysis tools. This is due, in part, to improved awareness of model bias and phase dominance. Model bias occurs when incorrect building of a structure dominates the calculation of phases so that subsequent electron density maps support these poorly built regions. Modern structures are expected to agree both with geometric constraints derived from knowledge of peptide structures and with phase information derived from experimental data.

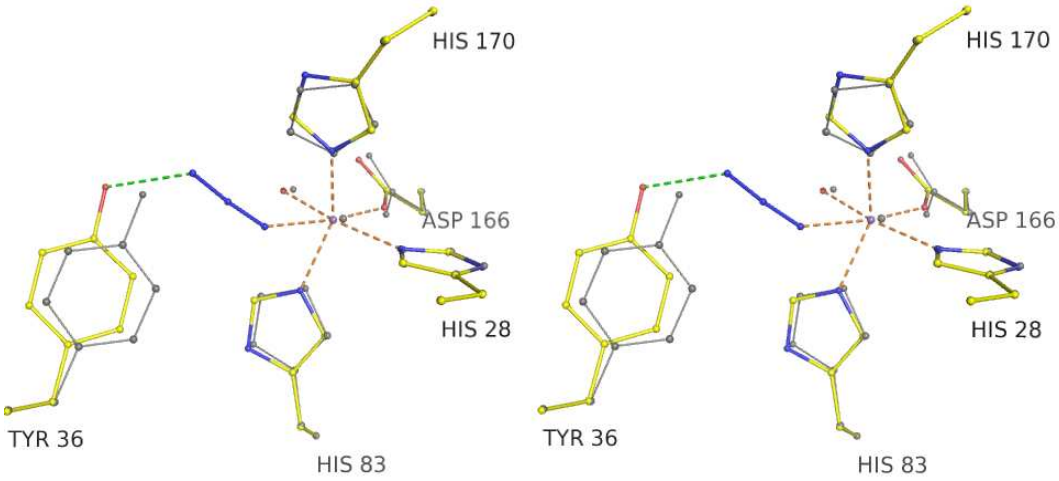

Figure 5-1. The split-occupancy active site of azide-inhibited *Thermus*-MnSOD superposed onto the native structure.

Figure 5-1. Wall-eyed stereo-diagram of the active site of the A subunit of *Thermus*-MnSOD-N_3^- derived from 1MNG. Both the azide-bound conformation (described here with "L" in subscript as the letter "L" descrbes the azide-bound conformation in 1MNG file), which has 51% occupancy, and the azide-free conformation (indicated by the letter "U" in 1MNG file), which has 52% occupancy, are shown. The azide-bound conformation is shown with thicker bonds that are coloured with carbon atoms shown in yellow, nitrogen in blue, oxygen in red and manganese in purple. The azide-free conformation, which is highly similar to the native structure 3MDS, is shown in grey with thinner bonds. In the azide-bound state, the hydrogen bond between the OH_L: atom of $Tyr36_L$ and the $N3_L$ atom of azide is shown as a green dashed line. The six bonds that are made by the azide bound manganese ion are shown as orange dashed lines. The manganese ion is bound to three histidine residues, one aspartate residue and the fifth ligand is a solvent derived species. The small-molecule inhibitor, azide, is the sixth ligand which binds to the metal centre opposite the aspartate oxygen. This changes the coordination of the metal from a penta- to a hexa-coordinate state. The most substantial change is the rotation of $Tyr36_L$ out of the active site, relative to $Tyr36_U$, and the formation of a hydrogen bond between the tyrosine and the tail of the azide molecule. There are also minor changes in the positions of the coordinated ligands, the lengths of ligand-to-metal bonds and a slight movement of the active-site metal. There are differences between the A subunit and the B subunit, most importantly in the ordered solvent structure.

The starting model for the refinement of *Thermus*-MnSOD-N_3^- was the native *Thermus*-MnSOD including all water molecules with refined temperature and occupancy factors. This means that model bias from earlier structures and refinements may have diminished any new phase information from measured X-ray data. At the time the concept of model bias was poorly understood by X-ray crystallographers (Hodel *et al.*, 1992, Bhat, 1989). Potential sources of error are first discussed for *Thermus*-MnSOD-N_3^- which is presented in one paper (Lah *et al.*, 1995), then for the *Thermus*-MnSOD structure, which was initially solved at low resolution (Stallings *et al.*, 1981, Stallings *et al.*, 1984), then medium resolution (Stallings *et al.*, 1985) and finally extended to include high resolution data (Ludwig *et al.*, 1991). Figure 5-2 shows the flow of information used to solve *Thermus*-MnSOD-N_3^- from the initial low resolution studies.

The structure of *Thermus*-MnSOD-N_3^- collected at ambient temperatures is an important structure (Lah *et al.*, 1995). The binding of azide perturbs the native structure (*Thermus*-MnSOD), which had been earlier determined by the same research group (Ludwig *et al.*, 1991). Many research groups, from many disciplines and backgrounds, are interested in the MnSOD and FeSOD field and have based research outcomes, theories and conjecture on the structures of azide-bound derivative as models of superoxide binding. The paper that presents the structure of *Thermus*-MnSOD-N_3^- (Lah *et al.*, 1995) is cited in nearly 200 research articles. A subset of these papers are primarily interested in the *Thermus*-MnSOD-N_3^- structure rather than the three *Ec*-FeSOD structures that were co-presented with it. This large body of work includes explanations of MnSOD enzymatic activity (Carrasco *et al.*, 2007, Tabares *et al.*, 2006), spectroscopic investigations (Jackson *et al.*, 2004, Tabares *et al.*, 2006), theoretical models (Rulíšek *et al.*, 2006, Rulíšek & Ryde, 2006) and various review articles (Christianson, 1997). Much of this work may need to be re-evaluated or extended to include knowledge derived from the novel *Deino*-MnSOD-N_3^- structure.

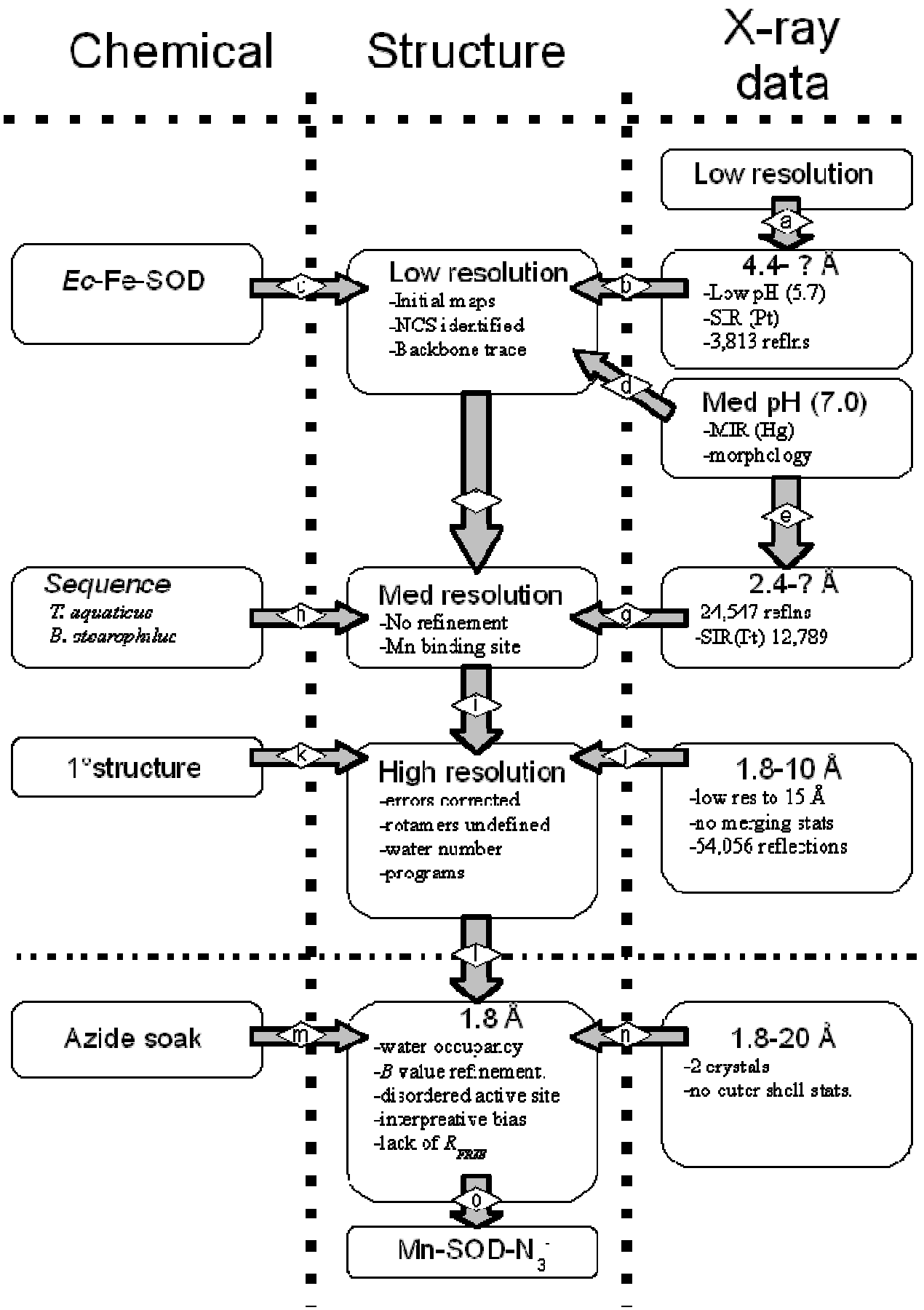

Figure 5-2. Flow diagram of the information used to solve the structure of *Thermus*-MnSOD-N_3^-.

Figure 5-2 shows the information utilised to solve *Thermus*-MnSOD-N_3^- divided into three categories, chemical, structure, and X-ray data. Information flow has been shown by arrows and labelled with letters. There are multiple potential sources of model and phase bias. Structural studies started in earnest once diffracting crystals were grown. Once unit cell and space group were determined *a)* this allowed low resolution native and platinum derivative data-sets to 4.4 Å to be collected and these were used to generate SIR phases and maps *b).* The backbone of *Ec*-FeSOD *c)* was fitted into initial maps. Map quality was improved by changing the pH at which crystals were grown and a di-mercurial derivative data set was collected *d).* When the resolution was improved to 2.4 Å, the starting point was phasing *e)* from the previous study and the previous structure *f).* The maps were improved *g)* and the model was rebuilt using sequence information from two related proteins *h).* This structure was used as the starting point *i)* for the high-resolution refinement against data to 1.8 Å *j)* with the correct amino-acid sequence *k).* This refined structure *l)* was used as the starting point for the structure of the azide-soaked crystals *m)* with the data from two crystals *n)* to give the final structure *o)* which is much referenced.

5.1.2 Summary of potential sources of error in *Thermus*-MnSOD-N_3^-

The paper by Lah and co-workers (Lah *et al.*, 1995) presents a total of four crystal structures, three of the structures are *Ec*-FeSOD structures, which are isomorphous and have nearly identical data statistics. The fourth structure is of *Thermus*-MnSOD-N_3^-, which has a different space group and data statistics, and is more closely related to the structure of *Thermus*-MnSOD (Ludwig *et al.*, 1991). Several potential sources of bias and errors in the structure of *Thermus*-MnSOD-N_3^- are listed below and discussed in detail in the following sections, 5.1.3 to 5.1.10.

1. Resolution and coordinate errors.
2. Possible interpretative bias.
3. Use of multiple crystals.
4. Methodology used for data reduction/ processing.
5. Possible refinement bias/ misinterpretation.
6. Lack of R_{free} statistic.
7. Treatment of waters.
8. Biased starting structure.

5.1.3 Resolution and coordinate errors

As the X-ray data were recorded to 1.8 Å resolution, this is the ultimate limiting factor in determining the fine detail of electron density maps, and hence atomic positions. At this resolution range the ability to clearly differentiate an active site with two conformations

must be inherently limited. This structure was solved before it was commonplace to submit structure factors with atomic coordinates.

The distance between the alternate positions of the two Mn atoms with approximately half occupancy in the A subunit is 0.38 Å and in the B subunit the distance is 0.41 Å. At this resolution range this would likely manifest as a large aspherical peak in electron-density maps at the active site rather than a defined sphere. The other major effect of azide binding is that $Tyr36_L$ (the equivalent of Tyr35 in *Deino*-MnSOD) tilts away from the active-site metal. The OH_L of $Tyr36_L$ has moved 1.0 Å in the A subunit (refer to Figure 1-1), and 1.1 Å in the B subunit. This movement is less than the reported resolution. No images of electron density of the active-site metal or mobile tyrosine are given.

5.1.4 Interpretative bias

The most likely bias in the structural solution of *Thermus*-MnSOD-N_3^- is a possible misinterpretation of electron density maps. When the structure of *Thermus*-MnSOD-N_3^- is overlaid with the structure of *Deino*-MnSOD-N_3^-, the binding mode of azide is clearly different between the two.

Figure 5-3 shows an overlay of the electron density maps from the refinement of *Deino*-MnSOD-N_3^- with the coordinates of the active-site from *Thermus*-MnSOD-N_3^-. In this overlay, the position of the N3 atom of the azide ion falls into a density peak that has been ascribed to a water molecule in *Deino*-MnSOD-N_3^-. The length of an azide molecule is 2.2 Å, which is approaching the approximate length of a short hydrogen bond, 2.55 Å. It is possible that the "tail" of the azide molecule of *Thermus*-MnSOD-N_3^- was added to density that corresponded to a water molecule that had entered into the active site and hydrogen bonded to the N1 atom of the azide; refer to Figure 6-6 for naming convention of the azide ion, although at this resolution the orientation of an azide molecule should be clear. The temperature factors of the N2 and N3 atoms are higher than the N1 atom. The N3 atom of azide is also higher than its hydrogen-bonding partner $Tyr36\_OH_L$ which is 2.60 Å away. Lah and co-workers attribute this to the azide having some degree of freedom, but it may also be an indication that the azide molecule has been built incorrectly. The temperature factors in the active site of the A subunit of *Thermus*-MnSOD-N_3^- are shown in Figure 5-4.

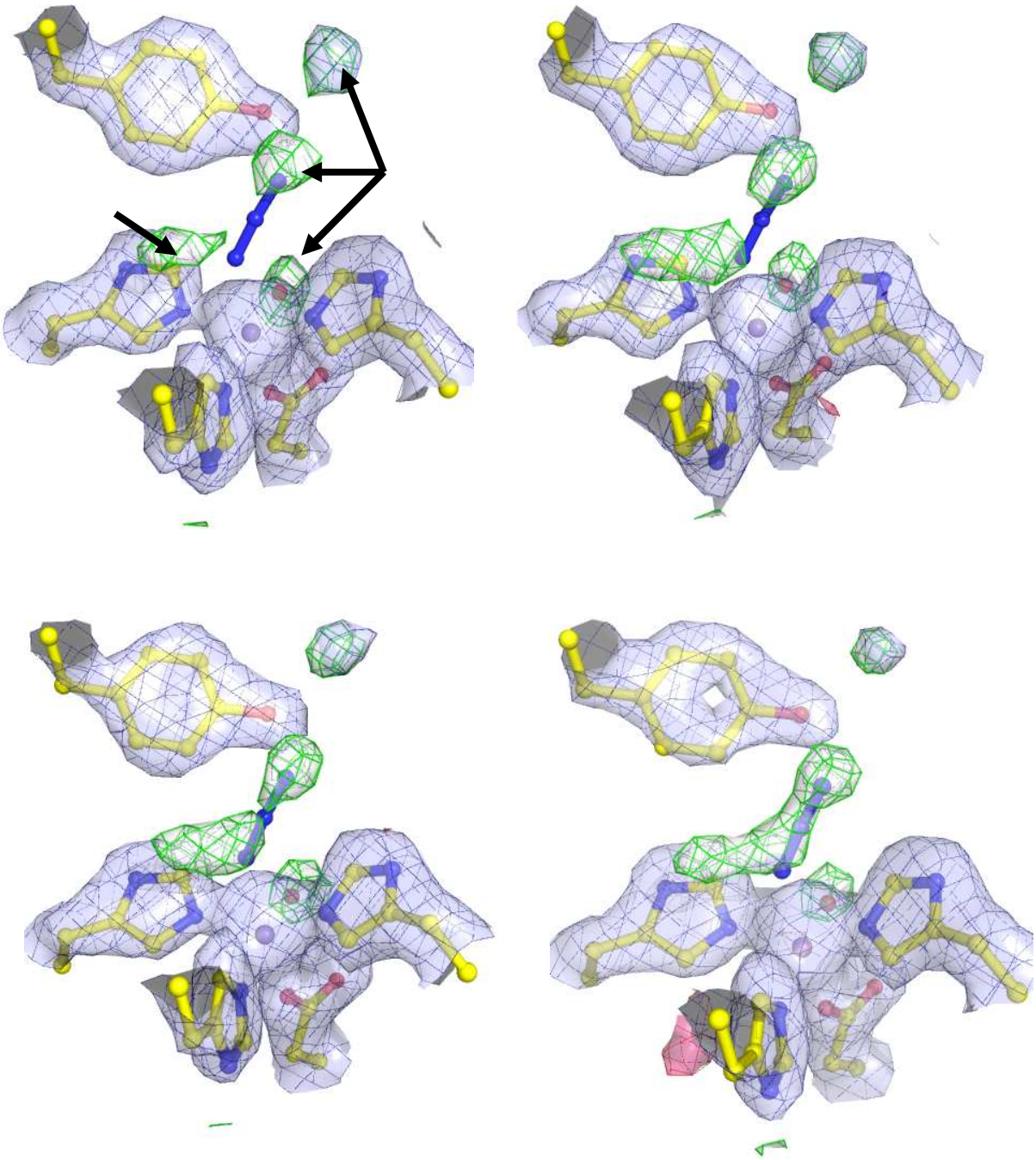

Figure 5-3 The active site of *Thermus*-MnSOD-N_3^- overlaid onto the electron-density maps for the four active sites of *Deino*-MnSOD-N_3^- showing a possible interpretative bias.

Figure 5-3 For each of the images A-D a similar orientation with respect to the active site is shown. The thin blue mesh with a light blue transparent surface represents a $2|F_O|-|F_C|$ electron density map is contoured at a 1.3 σ level. The thick green mesh with a transparent grey surface depicts positive density in a $|F_O|-|F_C|$ map contoured at a 4.0 σ level. The thin red mesh with a transparent pink surface shows negative density in a $|F_O|-|F_C|$ map contoured at a -3.0 σ level. The electron density maps that are shown were derived during the refinement of *Deino*-MnSOD-N_3^-. At the time of map generation, the active-site manganese had been built into the

structure but the coordinating ligands, a solvent molecule and azide had not been added. The images A-D show the electron density that corresponds to the active sites A-D of *Deino*-MnSOD-N_3^-respectively.

In all four images, the azide-bound conformation of the active site of the A subunit of *Thermus*-MnSOD-N_3^- (derived from 1MNG) is shown as a ball and stick representation. The yellow atoms represent carbon atoms, blue nitrogen, red oxygen and purple represents the manganese ion. The coordinates of *Thermus*-MnSOD-N_3^- were superposed onto the coordinates of *Deino*-MnSOD-N_3^- using only CA atoms. Tyr36 (*Thermus*-MnSOD numbering) is the topmost residue that hydrogen bonds to N3 atom of the azide molecule that in turn is bound from N1 atom to the active-site manganese ion. Surrounding the active-site manganese are four amino acids, His28 (proximal to the viewer), His83 (left-most), His170 (right-most), Asp166 (distal), and the coordinated solvent molecule (distal and located in a positive density peak in the difference map). The positions of the shown side chains overlay well with density of the $2|F_O|-|F_C|$ electron density map.

In all four subunits, the position of the N1 atom of azide in *Thermus*-MnSOD-N_3^- overlays or is very close to a positive density peak in the difference map. That corresponds to the N1 atom of the azide ion in *Deino*-MnSOD-N_3^-. However, the N3 atom overlays with a density peak that is clearly a water molecule in *Deino*-MnSOD-N_3^-. At this σ level, the most ambiguous density presented here is that seen in subunit D. This ambiguity is resolved when the σ level is increased and the density corresponding to the water molecule and azide molecule become distinct. It is possible and probable that Lah and co-workers built an azide molecule into ambiguous density that corresponds to a water molecule while the positioning of the protein side chains is largely correct.

Figure 5-4. Both conformations are shown as a ball-and-stick representation, and the same residues are shown as in Figure 5-1. The base colour of the azide-free conformation is dark grey. The azide-bound conformation is shown coloured green, red, blue and magenta for carbon, oxygen, nitrogen and manganese respectively. Temperature factors are shown in the same base colour as the atom they are associated with. All nitrogen, oxygen, manganese and α carbon atoms have temperature factors shown. The “tail” of the bound azide has higher temperature factors than the “head” and the OH of Tyr36 is slightly higher in the azide bound conformation than in the azide free conformation.

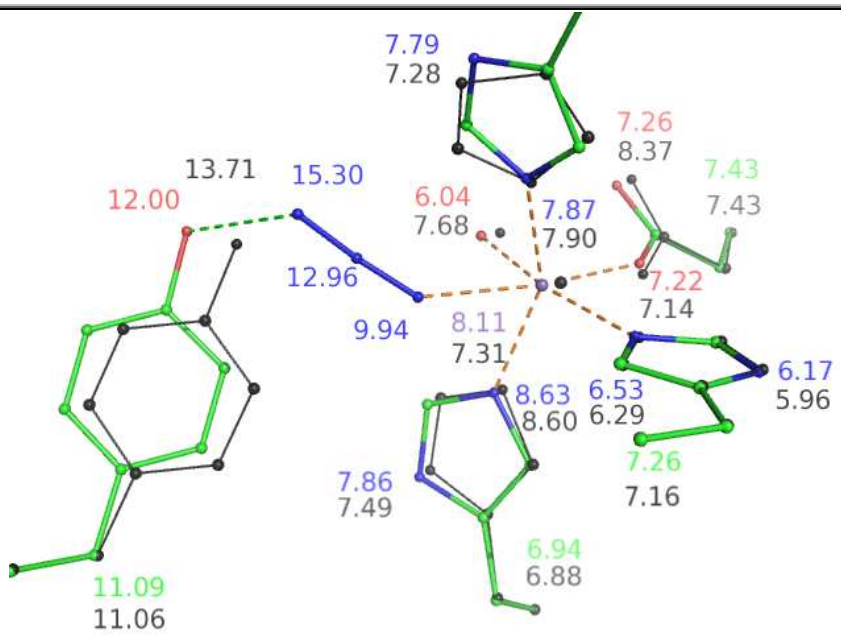

Figure 5-4. Selected temperature factors within the active site of the A subunit of *Thermus*-MnSOD-N_3^-.

At the active sites of Fe/MnSODs, the maps of electron density are dominated by the positive peaks of metal ions. Also present are electron density peaks for the four protein ligands. In high-resolution structures, the electron density peaks for the coordinated non-protein ligands becomes apparent as well. The structure of the solvent molecules within the substrate-access funnel that links the active site to the bulk solvent will also become resolved in high-resolution studies. The fifth ligand is a solvent-derived molecule, which has been attributed to either an hydroxide or a water molecule. The sixth ligand, if present, can either be a small-molecule inhibitor such as azide or alternately a second solvent-derived molecule.

In the refinement of *Thermus*-MnSOD-N_3^-, the fifth and sixth ligands were reported to be added to a difference map that was generated when the metal-associated ligands were omitted from refinement. The N1 atom of the azide is located 2.2 Å from the Mn atom. This binding mode supports spectroscopic data that indicate that the binding of azide to MnSODs forms a hexa-coordinate Mn. The binding distance and position of the N1 atom of the azide ion is reminiscent of that seen in the FeSOD azide complexes and *Deino*-MnSOD-N_3^-. Spectroscopic techniques, which are usually specific to the local environs of the active-site metal atom, are not able however, to clearly elucidate the position of the N2 and N3 atoms of the coordinated azide ion.

In the paper that presents *Thermus*-MnSOD-N_3^-, there is a stereo figure of a difference density map contoured at 2.5 sigma level where the solvent and azide molecules had been omitted from refinement; refer to Figure 5-5. Interestingly, other figures of difference

maps of the FeSOD structures presented in this paper are contoured at the 3.0 sigma level. The difference density peak that is associated with the coordinated solvent molecule is much larger than that associated with the azide ion, possibly because of the partial azide occupancy (~50%). The solvent peak is also aspherical, Lah and co-workers interpreted this as being a water in a split conformation. The density that is associated with the azide ion is hard to interpret as the chosen orientation (the same for all the figures of the active site within this paper) looks down the azide ion at an oblique angle. In contrast, when examining *Ec*-FeSOD-N_3^-, the chosen view is easily interpreted and unambiguous.

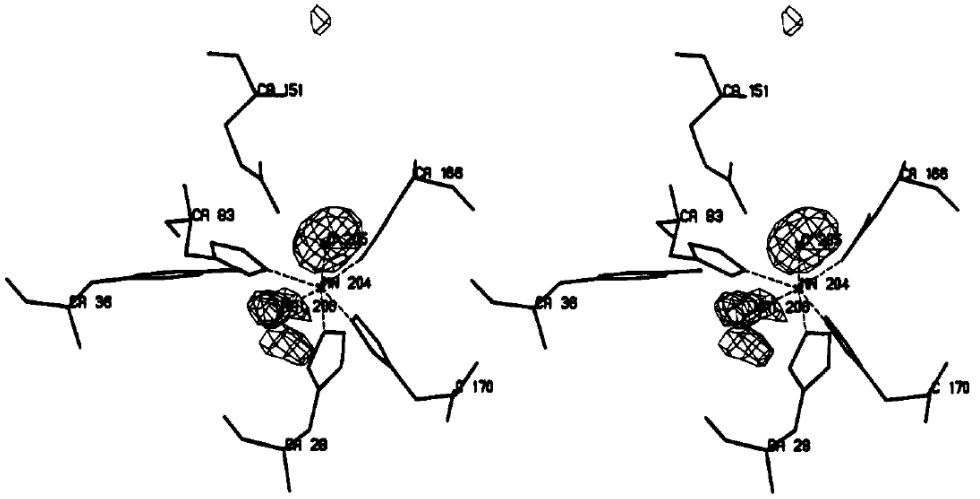

Figure 5-5. Reproduction of the stereo-diagram showing peaks used to fit azide into *Thermus*-MnSOD-N_3^- (Lah *et al.*, 1995).

Figure 5-5. The omit density is contoured at 2.5 σ level. In this view the shape and appearance of the azide ion is difficult to interpret. It is difficult to say whether the density is "dumbbell"-shaped or "sausage"-shaped. Other features to notice are the large size of the peak associated with the coordinated solvent-derived molecule and the aspherical density of the third peak, a water that may be present in split occupancy (in the refined structure it is present in full occupancy at one active site.). It may have been more appropriate to use an orientation similar to Figure 5-1 or Figure 5-3 to present this data where azide molecule is side-on.

Azide decomposes over time by oxidation,

$$2N_3^- \rightarrow 3N_2 + 2\,e^-$$

Equation 3

to diatomic nitrogen. The azide ion can also be eliminated by reduction,

$$8\ e^- + N_3^- + 9\ H^+ \rightarrow 3\ NH_3$$

Equation 4

to ammonia which may readily leave the active-site and this will occur more rapidly at ambient temperatures than at cryogenic conditions. Both of these have been demonstrated to occur in the presence of light (Nosaka *et al.*, 1984) to give overall

$$3N_3^- + 3H_2O \rightarrow NH_3 + 4N_2 + 3OH^-$$

Equation 5

which is assumed to occur in a crystal in an X-ray beam. X-ray radiation may stimulate the production electrons for Equation 4.

5.1.5 The use of two crystals

The data set used to solve *Thermus*-MnSOD-N_3^- is derived from two crystals, whereas the other three *Ec*-FeSOD structures presented in this paper are derived from the X-ray data from individual crystals. The reason for using two crystals is not expressly stated. The physical size of only one crystal is given in the tables of X-ray data statistics. So it must be assumed, perhaps incorrectly, that the two crystals used in data collection are of similar dimensions. The authors may simply be mimicking the methodology used to solve native *Thermus*-MnSOD structure, in which two crystals were also used, one for low resolution data to 2.4 Å and, in a later publication, a second crystal was used to extend the resolution of the data to 1.8 Å. It is also unclear if the data from the two crystals were collected on the same apparatus. No information is given on the R_{merge} between the two data sets, and R_{merge} and intensity data are also lacking in the high-resolution shells. Possible reasons for using two crystals in data collection are given below.

5.1.5.1 Saturated detector

Low-resolution reflections are generally more intense, and may saturate a multi-wire detector making it difficult to measure individual reflections. Data collection may then require a separate short-exposure data set for low-resolution data and a second long-exposure data set for higher-resolution data.

5.1.5.2 Radiation damage

There are other reasons for using multiple crystals to collect a complete data set. One reason is that the crystals suffer radiation damage as the experiment proceeds. This manifests itself as a loss in reflection intensity and a decrease in resolution of data with time. This is an important factor to consider in dealing with metallo-proteins, as free radicals caused by X-ray damage can alter the oxidation state of bound metal ions. The

amount of radiation damage suffered by a protein crystal during a typical X-ray diffraction experiment is also going to be influenced by the strength of the incident beam of X-rays, the total time the crystal spends in the X-ray beam, and the temperature of data collection. Radiation damage has been quantified as low in native *Thermus*-MnSOD, 0.25% per hour at 3.6 Å over an 80-hour period, but this is for medium resolution reflections using an undefined X-ray source (Stallings *et al.*, 1981) with crystals grown at a different pH range to *Thermus*-MnSOD-N_3^- crystals. The advent of cryo-crystallography techniques has limited many of the problems associated with X-ray damage. Free radicals created by X-ray beam diffuse less quickly through solvent channels when the solvent is frozen and more ordered.

Collecting X-ray diffraction data at room temperature requires the use of sealed capillaries containing the protein crystal. If improperly sealed, capillaries can slowly lose moisture and dehydrate the protein crystal over time often causing a loss in diffraction.

5.1.5.3 Missing data

Another problem associated with X-ray data collection using the standard oscillation/rotation method is the measurement of reflections close to the rotation axis of the crystal which will be poorly measured as they are spread out over many successive frames. This problem can be further exacerbated if the angle of rotation of the crystal lines up with a screw axis or rotation axis of a crystal causing a "missing cone" of reflections in reciprocal space. If this occurs, the extent of the missing data may not become apparent until the raw X-ray data are scaled and merged into a set of unique reflections. The crystals used to solve *Thermus*-MnSOD-N_3^- belong to space group $P4_12_12$, which has a four-fold screw axis, two-fold screw axes and two-fold rotation axes. Alignment of any of these with the axis of crystal rotation would lead to poor sampling of reciprocal space. The unit cell and space group of a crystal have strong influences on crystal growth and the faces of a crystal often relate directly to the internal structure. The capillary mounting of crystals, with an octahedral morphology (Stallings *et al.*, 1981), could predispose the flat faces of the crystal to align with the inside of the capillary. This could in turn predispose rotation axes to align with the axis of crystal rotation.

There is also the possibility that there is also some defect in the crystal that may not be apparent at the start of the diffraction experiment. The mosaicity of the crystal may have increased over time as crystal undergoes radiation damage. If a crystal is severely anisotropic, especially for high-resolution data, it may not be apparent until late in the X-ray diffraction experiment or even until the data are scaled and merged. A crystal can also

be damaged during transfer into a capillary. If cracks and fissures develop in a crystal then splitting of individual diffraction spots may not be detected until crystal data are processed.

5.1.5.4 Inherent difference in azide concentration between the crystals

The largest potential problem in using two crystals soaked in inhibitor overnight is that it is difficult to quantify how much inhibitor diffused into each crystal. Protein crystallographers often encounter crystals that appear similar but are in reality subtly different. It is possible that one of the crystals used had a higher saturation of azide than the other, due to minor differences in crystal packing and the age of the crystal or other minor differences. The only method used to quantify the amount of azide entering crystals was a visual inspection. The authors noted a loss of purple hue associated with a change in coordination was expected, but was not seen in a convincing manner.

If one of the crystals used had full azide occupancy and the other crystal with low azide occupancy then it would be inappropriate to merge the two data sets. The X-ray data would then represent two separate structures and averaging would not represent either of the two unique structures. This would be very difficult to detect based on reflection data alone, as the differences in measured intensities between two data sets will be minor. The two conformations detected in the active site, both at 50% occupancy, native and azide-bound, might actually reflect that the phase information is actually an average of two crystals. A more valid approach may have been to solve the structure with the data from each crystal in turn and then evaluate the electron-density maps before merging the two data sets.

5.1.5.5 Oxidation state

To further complicate matters, there is also the possibility that the active sites within the crystals are a mixed population of oxidised and reduced active sites. In particular, the active sites that are azide-free may contain Mn^{2+}, which binds azide very poorly. Over the time course of data collection, the metal centres may also be reduced as a result of X-ray damage. Changes in redox state of *Thermus*-MnSOD-N_3^- may cause changes in active-site stereochemistry.

Little information is given on the actual X-ray diffraction experiment. There is no information given on the amount of time that crystals spent in the X-ray beam, the wavelength of X-rays used, the flux of the X-ray beam, the exposure time per image and the number of images taken for each crystal. Two different X-ray detectors were used to collect X-ray data for the FeSOD experiments. It is not clear that the two sets of data

collected to solve *Thermus*-MnSOD-N_3^- were collected on the same apparatus. The authors had access to the University of California, San Diego (UCSD) Multi-wire Detector Facility with a rotating-anode X-ray source (Xuong *et al.*, 1985), as well an in-house dual multi-wire detector with an unknown radiation source.

There is also the possibility that the merging of two data sets may not have been required at all. There is no indication as to whether Lah and co-workers tried to solve the structure of *Thermus*-MnSOD-N_3^- using data derived from either of the single crystals. Interpretable structural information can still be derived from partial and low-resolution data sets. Even low quality electron density maps of the active site may have been enough to determine the mode of azide binding.

5.1.6 Data reduction

Detail on the software and methods that were used for scaling and merging are lacking. Also lacking is information on what criteria were used in the acceptance and rejection of reflections. The other three *Ec*-FeSOD structures presented in this paper have a low resolution data cut off at 40 Å whereas the *Thermus*-MnSOD with bound azide has a low-resolution cut-off at 20 Å. Inclusion of data in the 20-40 Å range can be important in the modelling of bulk solvent. The authors had access to equipment that was capable of measuring low-resolution data in the range.

The incorporation of high-resolution data is an extremely desirable trait for an X-ray data set, as this greatly improves the quality of electron-density maps used in the refinement of biological macromolecules. As the resolution of diffraction increases there is a decrease in the average intensity of the reflections measured. High-resolution data must have significant average signal above the average background noise to be recorded precisely.

The authors do give an indicator of the inherent signal strength of their data, an $I/\sigma(I)$ of 10.6, which is less than that for the FeSOD datasets. This is the average signal: noise ratio for the whole data set and provides no indication of signal strength at high resolution. The modern practice is to give measurement of average signal strength, such as $I/\sigma(I)$, for the whole data set and a similar statistic for just the high-resolution data. There is also no indication if the $I/\sigma(I)$ between the two crystals used was comparable. The underlying completeness of the data set at 1.8 Å is reasonably high at 93% for 52,673 reflections with $|F|>0.1$, but without knowledge of the intensity, redundancy and completeness in the outer resolution shells the quality of the high-resolution data can not be ascertained.

Reflections with low redundancy and therefore less precision at high resolution may contribute towards the reported completeness. The reported redundancy is 6.5. As two sets of data have been merged together there will be a set of common reflections. The reflections in the overlap will have a higher average redundancy than the other reflections. There may well be regions of the data with low average redundancy than the rest of the data. The expression for R_{merge} is

$$R_{merge} = \sum_{hkl}\sum_{i}\left|I_i(hkl) - \overline{I(hkl)}\right| \Big/ \sum_{hkl}\sum_{i} I_i(hkl)$$

Equation 6

where individual reflections are measured across multiple crystals. The expression for R_{sym} is similar but for symmetry-related reflections from the same crystal. The R_{sym} and R_{merge} (Equation 6) data quality statistics are highly dependent on redundancy of data (Diederichs & Karplus, 1997). The R_{sym} of the X-ray data set is given as 7.7%, which is a measure of the agreement between symmetry-related reflections over the whole data set. It may have been appropriate to use the R_{merge} data statistic as well, which measures the agreement of individual reflections from multiple crystals. In modern crystallography there is often no distinction made between R_{sym} and R_{merge} and they are used interchangeably (Diederichs & Karplus, 1997).

The $I/\sigma(I)$, R_{sym} and R_{merge} statistics should be calculated independently for the high-resolution shell, and should be co-evaluated with data completeness and redundancy in the outer shell. High-resolution shells are where X-ray radiation damage and discrepancies between two data sets will most likely be detected. The R_{sym} and R_{merge} are mostly determined by low-resolution data which will have more redundant, complete, intense reflection data that is less affected by radiation damage.

Raw X-ray reflections are often corrected for absorption effects, time-dependent loss of diffraction and anisotropy when they are scaled together. The scaling procedure used at the UCSD Multi-wire Detector Facility has been briefly described (Xuong *et al.*, 1985). Information on which reflections are scaled and the amount of scaling during the scaling and merging of data is not given any weight in R_{sym} and R_{merge} statistics. Consequently a weak high-resolution reflection that is recorded twice imprecisely and corrected for adsorption/anisotropy will be given equal weighting to an intense low-resolution reflection that has been recorded precisely with high redundancy. There is a tendency for R_{sym} and

R_{merge} values to increase with an increase in the redundancy and decrease with lower redundancy.

The R_{sym}, which is averaged for the entire data set, may appear to be reasonable, but in fact may be masking inconsistencies in data. Other reasons for using two crystals in data collection should also affect interpretation of R_{sym} as there may be underlying differences in intensities and redundancy between the two crystals used.

5.1.7 Possible sources of error within refinement

No information on refinement target is given but it is likely to have been based on a conjugate-gradient least-squares method as maximum likelihood methods had not been commonly introduced (Pannu & Read, 1996). The X-PLOR group of programs was used to refine the structure in real and reciprocal space. Several rounds of refinement were included in the refinement process including rigid body, positional, temperature, occupancy and simulated annealing. It is unclear if non-crystallographic symmetry (NCS) was used as a constraint or restraint on position or temperature refinement of atoms. It was implemented in X-PLOR (Brünger, 1992a) and had been applied during refinement of the native structure. Within the asymmetric unit of *Thermus*-MnSOD there are two potential binding sites for azide, one per monomer. In the final structure both active sites have azide present with approximately 50% occupancy. On the other hand, azide may have been preferentially bound to one of the active sites, but when NCS constraints/restraints were applied the structure then represented an average of two slightly different active sites. There are several examples of SOD structures that are made up of slightly different asymmetric dimers such as *Ec*-Fe-MnSOD, *Ec*-Fe-MnSOD-N_3^-, and Y174F-*Ec*-MnSOD-N_3^-.

5.1.8 The refinement of water molecules, temperature factors and occupancy factors in *Thermus*-MnSOD-N_3^-

The bulk of the solvent molecules within a crystal will be disordered and lie in solvent channels between the protein molecules. The contribution of this bulk solvent towards X-ray scattering can be determined. A smaller proportion of the water molecules will be ordered and should be included in the refined structure. The starting model for the refinement of *Thermus*-MnSOD-N_3^- was the native *Thermus*-MnSOD, including water molecules with refined positions, temperature factors, and occupancy. The inclusion of too many waters from the native structure in early rounds of refinement is likely to bias the starting model toward the native structure and decrease the amount of novel information that can be derived from the azide-derivative X-ray data sets. During the refinement of

Thermus-MnSOD-N_3^-, the positions, temperature factors and the occupancy of water molecules were further refined. The results of this refinement are that within the submitted structure of *Thermus*-MnSOD-N_3^- there are water molecules that have: full occupancy and low temperature factors; full occupancy and high temperature factors; low occupancy and low temperature factors; and low occupancy and high temperature factors; refer to Table 10. The treatment of waters in the structure is sub-optimal and there is likely fitting of data to structure rather than fitting structure to data.

			B-factor <25	B-factor >25
Total # of H_2O	202	→	139 + \	63 - \
	↓			
Occupancy > 80%	135 \+		76 + +	59 - +
Occupancy < 80%	67 \ -		64 + -	3 - -

Table 10. The distribution of occupancy and temperature factors of ordered solvent within *Thermus*-MnSOD-N_3^-.

Table 10 shows the 202 solvent molecules of *Thermus*-MnSOD-N_3^- categorised by temperature factor and occupancy. The threshold for B-factors was chosen to put roughly one third of water molecules into the high temperature factor category. Waters with low temperature factors and high occupancy are indicated by (++). Waters with either low occupancy or high temperature factors are indicated by (- +) or (+ -). Low quality water molecules with low occupancy and high temperature factors are shown by (- -). Less than half the water molecules fall into the (++) category.

Typically, ordered water molecules are built into spherical peaks of electron density at suitable hydrogen bonding distances from the protein and other water molecules. In early rounds of refinement only the first shell of hydration, within about 3.5 Å of the peptide, can be built reliably. During further refinement, if experimental data warrant it, more water molecules can be added.

Initially as iterative refinement between map interpretation and refinement proceeds, the signal-to-noise ratio in maps improves. Eventually, however, the amount of novel structural information that can be derived from electron density maps decreases due to increased model bias. In later cycles of refinement the size of density peaks associated with novel solvent molecules will decrease. In final rounds of refinement when there is very little influence of X-ray derived information on electron density maps, water peaks will become indistinguishable from noise. If care is not taken during the refinement process, water molecules can be added incorrectly to ambiguous density peaks that are the result of Fourier ripples or side chains in multiple conformations. During automated

refinement by computer programs the position of a water molecule within a protein structure is less restrained by bond distances and angles than the atoms of the peptide and during refinement have greater degrees of freedom.

The temperature factors and occupancies are specific to individual atoms and are targets for refinement within the structure. These variables are correlated (Bhat, 1989) and they can both can act as “fudge factors” to make an individual atom agree with the X-ray data without altering the Cartesian position of the atom. Both occupancy and temperature factors are measures of the proportion of time that an “average” atom is at a point within the unit cell. In the interpretation of electron density maps a water molecule with low occupancy is almost indistinguishable from of a water molecule with a high temperature factor (Kundrot & Richards, 1987).

In high- and medium-resolution structures it is more sensible to refine temperature factors than occupancy. The majority of protein atoms have limited movement and most atoms will have 100% occupancy and low temperature factors. Subsequently regions with some conformational freedom, such as the long flexible side chains of surface lysines and arginines, can be built with full occupancy and high temperatures factors. Well defined water molecules will have low temperature factors and poorly defined waters will have high temperature factors.

Well-defined water molecules should have temperature factors that are comparable to surrounding atoms after temperature-factor refinement. If the temperature factor of an individual water atom is distinctly higher than surrounding atoms it may indicate that the solvent molecule should be removed as it is may be derived from a false peak. The temperature factors of a structure should vary smoothly over the whole structure. The analysis of temperature factors can give an indication of how much individual atoms of a structure contribute to the calculated X-ray data. Atoms with very high temperature factors essentially contribute very little to the calculated structure factors, especially for high-resolution data. This is particularly relevant to older structures where the structure factors have not been submitted.

Alternatively, water molecules can have their occupancy refined. It has been suggested to manually set occupancy based on the interpretation of the electron density for possible water molecules (Jensen, 1990). This approach can also be used for waters that are clearly split between two conformations. Split occupancy waters will manifest away from peptide as two peaks closer than hydrogen-bonding distances or as dumb-bell shaped projections

in electron-density maps. The refinement of water occupancy becomes viable only with ultra high resolution data. After occupancy refinement, waters that have low occupancy should be removed as they are not relevant to the bio-molecule or are the result of Fourier ripples. Protein crystals contain large amounts of solvent, sometimes more than 60% of the volume of the crystal (Matthews, 1968). The water molecules close to the protein will have some ordered qualities created by hydrogen bonding partners and electrostatic forces. Ordered waters will have interpretable electron density.

The optimal methods for building of solvent in protein structures are much debated at present (Brown & Ramaswamy, 2007, Kleywegt, 2000) as it was at the time the structure of *Thermus*-MnSOD-N_3^- was solved (Kleywegt & Jones, 1995, Kundrot & Richards, 1987).

5.1.9 The lack of R_{free} statistic

After an initial solution of a structure, the agreement between the model and data should improve. The least-squares refinement of X-ray structures is an effort to minimise the differences between $|F_{Obs}|$ (the observed structure factor amplitude from X-ray data) and $|F_{Calc}|$ (the calculated structure factor amplitude that is derived from the model). This hopefully leads to refinement of calculated phases towards the "true" phases and therefore better electron-density maps. This is done by iteratively modifying the Cartesian position, temperature factors and occupancy of atoms of the starting model as well as introducing new atoms to the structure. As the structure improves, the *R*-factor, refer to Equation 7, should drop until no more useful information can be derived from electron density maps. Refinement is usually constrained or restrained by chemical knowledge such as bond lengths and angles, as the number of X-ray data divided by the number of adjustable parameters is generally between 1 and 2 in all but ultrahigh resolution structures.

$$R = \frac{\Sigma \left| \, |F_{obs}| - |F_{calc}| \, \right|}{\Sigma |F_{obs}|}$$

Equation 7

With a data-to-parameter ratio not much greater than one there is a problem of model bias entering into the refinement process. An error with relatively few atoms in the wrong positions will be transferred to the calculation of $|F_{Calc}|$ for all reflections, which is further perpetuated into the refinement of occupancy, temperature factors and atomic shifts of all parameters. This will, in turn, affect the $|F_{Calc}|$ in further rounds of refinement. Model bias can be the result of misinterpretation of ambiguous electron density, poor treatment of

waters, wrong rotamers, incorrect weighting of X-ray data and incorrect constraints or restraints on protein geometry. Model bias is almost impossible to eliminate entirely, but efforts should be made to minimise model bias and errors.

The structures of *Thermus*-MnSOD-N_3^- and the native *Thermus*-MnSOD were solved and refined before the widespread use of the R_{free} statistic (Brünger, 1992b). The R_{free} dataset is a subset of all reflections that are excluded from all structural refinements and electron density calculations, and this set is typically 5 to 10% of the total number of reflections. This subset of refelections is used to calculate the R_{free} in the same manner as a traditional *R*-factor, refer to Equation 7, while the rest of the data is used to calculate R_{cryst}. Comparison between R_{cryst} and the R_{free} gives an indication on how much bias the structure has. Typically a separation of more than 5% is taken as being indicative of over-refinement or model bias in the structure. Prior to the use of R_{free} it was possible to refine a structure against X-ray data to a false minimum with acceptable geometry and no indication from difference maps of any errors or model bias.

All protein structures that were submitted to the protein data bank (Berman *et al.*, 2000), commonly known as the PDB, in the 1990s have been analysed for their overall quality and their agreement with the X-ray data (Kleywegt & Jones, 2002). However, in 1995, the year *Thermus*-MnSOD-N_3^- was published, only a third of submitted structures reported R_{free} values.

It is possible and likely that the *Thermus*-MnSOD-N_3^- and *Thermus*-MnSOD have been over-refined and too much weight given to the X-ray data, such that the *R*-factor was minimised at the expense of structural accuracy. When the Ramachandran plots (Ramachandran *et al.*, 1963) of *Thermus*-MnSOD-N_3^- and *Thermus*-MnSOD are analysed using criteria defined in PROCHECK (Laskowski *et al.*, 1993), there are no residues in disallowed regions.

5.1.10 Problems with the starting model

The *Thermus*-MnSOD-N_3^- crystal structure was solved by using the native structure as the starting model. The native structure of *Thermus*-MnSOD contained refined positions of all of the protein atoms, both active-site manganese atoms per subunit and 187 associated solvent molecules with refined positions, temperature factors and occupancy. Any errors in the starting model will be likely to persist into the derivative and may be compounded by further refinement. It is possible that structures built before the requirement of R_{free} contain bias/errors due to over refining and do not accurately reflect the data.

5.2 *Thermus*-MnSOD

The native 1.8 Å resolution *Thermus*-MnSOD structure is based largely on a previously published 2.4 Å medium-resolution *Thermus*-MnSOD structure. Any errors in the 2.4 Å structure may have introduced model bias into the high-resolution structure. Similarly the 2.4 Å medium-resolution structure may also be inherently biased because it is itself an extension of a 4.4 Å resolution structure. Possible sources of error in the solution and subsequent refinement of *Thermus*-MnSOD will be discussed chronologically.

5.2.1 The 4.4 Å resolution structure of *Thermus*-MnSOD

5.2.1.1 Original *Thermus*-MnSOD structural solution

The initial crystallisation of octahedral crystals of *Thermus*-MnSOD and X-ray analysis revealed the space group and diffraction to 1.4 Å (Stallings *et al.*, 1981) although measures of signal strength at this resolution are not given. In later studies, which utilised multi-wire detectors (Xuong *et al.*, 1985), resolution did not reach this range probably due to time constraints. This study was done using precession techniques (Buerger, 1964, 1942) in conjunction with density studies; the composition of the asymmetric unit was initially incorrectly determined to be a tetramer.

The original structural solution of *Thermus*-MnSOD was solved to 4.4 Å at pH 5.7 and was solved by single isomorphous replacement (SIR). The platinum derivative was created by soaking crystals overnight with one platinum atom binding per protein subunit. This was enough to generate a set of trial phases for 3,813 unique reflections and phase refinement yielded a map where helices were seen and the Fe/MnSOD fold could be identified. NCS operators were also determined and used to generate averaged maps. Crystal morphology and size were improved by changing the pH of crystallisation to 7.0; it is unclear if this improved the quality of diffraction. A dimercurial derivative crystal was prepared and this was reported to generate less ambiguous multiple isomorphous replacement (MIR) difference maps into which the backbone structure of *Ec*-FeSOD could be overlaid.

Any interpretation of these maps will thus be biased towards agreeing with *Ec*-FeSOD. A modern comparison between the *Ec*-FeSOD and *Thermus*-MnSOD amino-acid sequences reveals many point differences as well as loop insertions and deletions; at the time the primary amino-acid sequence of *Thermus*-MnSOD was unknown. No statistics on data completeness and reflection intensities are given for either the native or derivative structures in this paper. Any inherent bias or error in the phases of the 4.4 Å study could be transmitted to work that built upon it.

5.2.2 The 2.4 Å resolution structure of *Thermus*-MnSOD

5.2.2.1 Phasing of medium-resolution *Thermus*-MnSOD structure

When the resolution limits were extended to 2.4 Å, the number of unique reflections observed increased to 24,547, a more than six-fold increase for both the native and platinum derivatives. There was again no mention of a low-resolution cut-off. Also lacking are statistics on data-set completion, redundancy and average signal strength. Some X-ray data statistics from *Thermus*-MnSOD at 2.4 Å and data from other structural projects are given in a table for X-ray data collected at the University of California, San Diego Multi-wire Detector Facility (Xuong *et al.*, 1985). The data given in this table are generally in agreement with those presented in the *Thermus*-MnSOD structure. However, the presentation of the data is incomplete and ambiguous. Lower resolution limits are not given, no indication of data completeness is given, high-resolution shells are not treated separately, and data are given for entire multi-crystal projects (including metal derivatives) rather than separate data for individual crystals.

The method used to derive structure factors from measured intensities is not expressly given. Most likely, structure factors were estimated using Gaussian distribution approaches (Wilson, 1949) or Bayesian distributions (French & Wilson, 1978). The strongest 12,789 reflections, about half the total number of reflections, were used to refine the positions of the Pt binding using low-resolution results as a starting point. It is unclear whether the low resolution data set used was derived from crystals grown at pH 5.7, pH 7.0 or averaged information from both pH ranges. This allowed for the refinement of F_H (structure factors of metal component) for the 2.4 Å platinum structure factors. There is no mention as to whether F_P (structure factors of the protein component) were calculated *de novo*, or whether the F_P were derived from low resolution SIR and MIR experiments as a starting point. The phases were then refined and extended to 22,922 reflections, although the approach used for extension and refinement of phases is not given or whether the initial structure solution contributed phase information. Weighted Fourier maps were generated then averaged using the NCS operators derived from the low-resolution data.

This may have been a suboptimal approach to use, as it entails transferring information about phases from the low-resolution data set derived from a poorly diffracting crystal measured on older equipment to a dataset with inherently better characteristics collected on more modern equipment. It may have been more appropriate to repeat the SIR and MIR experiments to 2.4 Å. In the low-resolution study the use of a dimercurial soak allowed the generation of phase information by MIR and these maps were of better quality than the SIR maps.

5.2.2.2 Refinement of medium resolution *Thermus-MnSOD* structure

The starting point for structural refinement was the backbone of *Ec*-FeSOD which had been overlaid onto the low-resolution density. Building was done using primary amino-acid sequences of MnSODs from *Thermus aquaticus* and *Bacillus stearothermophilus*. There are point differences between these sequences and that for *Thermus*-MnSOD. These differences are likely to introduce bias into the structure. In particular side chains may have been fitted into ambiguous electron density incorrectly.

The protein structure was built into the NCS-averaged map density, but unaveraged map density was also available for interpretation. The use of NCS-averaged maps for building may introduce bias (Fabiola *et al.*, 2006). Where the differences in atomic positions between the NCS partners are negligible, this bias in the NCS maps will also be negligible, as the "true" density will be averaged with other "true" density. When there are real differences in atomic positions between NCS partners within a crystal the use of NCS maps can introduce errors as "true" density is averaged with "noise", regions of low density and "wrong" density such as solvent. The regions of a protein that are the most convergent in NCS maps are buried residues, and the most divergent will be residues that have multiple rotamers and are exposed to the solvent. This may have been compounded by inaccurate primary amino-acid sequence. Modern practice is in early cycles of building to use NCS-averaged maps to build the buried core of the protein and then, after the structure has improved, to do the final stages of building in un-averaged maps.

The building of this structure does not appear to have been an iterative process between real-space refinement and refinement of phases, which may mitigate the effect of using incorrect amino-acid sequences. As more of a structure is built this should lead to improved phasing and hence better maps. There is no refinement of the structure against the X-ray data or against any geometric parameter, even though at the time there were computer programs available at the time. There is also no validation of the structure against the X-ray data (such as an *R*-factor) or against geometric parameters (such as a Ramachandran plot). There is only mention of three non-protein atoms: the active-site manganese, its bound water-derived molecule and a water peak associated with one histidine. At 2.4 Å resolution, it is not unreasonable to expect to see well ordered waters such as those associated with the dimer-dimer interface and the solvent-access funnel. At this resolution the metal bound at the penta-coordinate active site was designated to be Mn^{3+} with four ligands derived from the protein and the fifth ligand being a solvent. No evidence of a sixth ligand was detected. Some of the rebuilt regions are described in the body text, but there is no indication as to how many of the residues have definite

assignment and how many are modelled as alanine or glycine. There is also no indication as to how well the NCS-related atoms agree.

The authors state that the coordinates would be submitted to the PDB, but it appears that this structure was superseded by the 1.8 Å structure.

5.2.3 The 1.8 Å resolution structure of *Thermus*-MnSOD

5.2.3.1 High-resolution structure of Thermus-MnSOD

The structure solved to 2.4 Å was used as the starting model when the X-ray data were again extended to 1.8 Å by inclusion of a second data set (Ludwig *et al.*, 1991). Possible errors in the scaling and averaging of X-ray data from multiple crystals were discussed earlier. None of the phase information from previous studies was used as a target in refinement or in the generation of maps. Depending on the quality of phasing gained from previous SIR it may have been desirable to use that phase information rather than generating phases based entirely on the starting structure, and as refinement proceeded, to decrease the weighting of the phasing from the SIR experiment. The authors state that there were no NCS restraints used during PROLSQ refinement but since the 2.4 Å resolution structure was built using NCS-averaged maps, early refinements of the starting structure were affected by NCS operations.

The automated refinement program PROLSQ was used to refine the atomic coordinates and therefore improve the agreement of $|F_{Calc}|$ with $|F_{Obs}|$. In each cycle of conjugate-gradient least-squares refinement, the initial calculation of $|F_{Calc}|$ is determined by the positions, temperature factors and occupancies of individual atoms of the trial structure. Any errors in the trial structure will sully initial calculation of $|F_{Calc}|$. At the end of an automated refinement any improvements in $|F_{Calc}|$ will be transferred to real space as shifts in atomic positions, changes in temperature factors and changes in occupancies. Monitoring of the agreement between $|F_{Calc}|$ and $|F_{Obs}|$ is achieved using *R*-factor values. Over the refinement process, the estimation of the phases should improve and the *R*-factor will decrease. This did occur, as the *R*-factor drops from 0.361 in the initial rounds of refinement to 0.176 after the final round.

5.2.3.2 Treatment of data

The number of reflections used throughout the refinement of *Thermus*-MnSOD increased from 7,556 to 54,056 in the last rounds of refinement, which on the surface appears a good way to treat data. However, the treatment of low-resolution data is of concern. Low-resolution data from 10 to 5 Å were used in early and late rounds of refinement but excluded in middle rounds of refinement; this seems unusual as the low resolution data

had contributed valuable information in the low-resolution study. Low-resolution data were excluded when most of the structure was rebuilt and solvent molecules added. The selective exclusion of X-ray data gives more weighting towards the trial structure. The only X-ray data used in all refinement steps in the high-resolution study is a narrow range from 5 to 3 Å. The only reflections used in all the refinement steps from the low resolution study to the final structure are intense reflections in the range from 5 to 4.4 Å. What this also means is that comparisons of *R*-factors made between refinement cycles are difficult because the data ranges and therefore the number of reflections are different. In a typical refinement, the *R*-factor should steadily decrease as the structure improves. Increases in *R*-factor imply that there is less of an agreement between the structure and the data. In the refinement of *Thermus*-MnSOD the *R*-factor generally decreases but with some oscillation.

The complete elucidation of the amino-acid sequence allowed the errors in the 2.4 Å structure to be corrected and the sequence extended until density corresponding to the entire primary amino-acid sequence could be seen. During the refinement process, waters were added to the structure with the inclusion of a range of low-resolution X-ray data from 5 to 15 Å. A large number of these waters were subsequently removed after individual isotropic temperature factor refinement and occupancy refinement until the number of waters was 178. As refinement proceeded, data from 10 to 15 Å were excluded, as this led to erratic refinement; this may imply discrepancies between the structure and low resolution data.

The treatment of ordered waters in structure refinement is extremely important as they are less constrained than atoms in a macromolecule. The correct building of ordered water allows a sensible hydrogen-bonding network to be built up and may also aid in the assignment of the protein side-chain rotamers. The positions of water molecules within a protein structure are typically dependent on hydrogen bonds, which are weaker than the covalent bonds within peptides. Typically water molecules are built into positive density peaks at suitable hydrogen-bonding distances, generously from 2.5 to 3.3 Å, to hydrogen bonding partners. Water molecules can be refined in terms of occupancy, temperature and position in *x*, *y* and *z* directions while atoms within a macromolecule are subject to additional restraints such bond angles, lengths, chirality, *et cetera.* If water molecules are given too many degrees of freedom in refinement their shifts can mask any intrinsic differences between $|F_{Calc}|$ and $|F_{Obs}|$ due to the protein itself leading to false minima and an artificial drop in R-factor. Waters can also be falsely added, as peaks in electron density can arise from Fourier ripples or density derived from protein in multiple conformations

with low occupancy. If over-refinement occurs then false assignments may be supported. The incorporation of "bad" waters into a structure will have the effect of cementing badly built regions into place. This is due to the fact that refinement programs treat ordered areas with predictable scattering differently to regions of disordered solvent to which models of bulk scattering are applied.

During refinement of *Thermus*-MnSOD the number of waters first built into the structure was 129. In a subsequent round the number of solvent molecules reached 355 and then in later refinements the number was dropped to 178 with the removal of 177 waters based on criteria such as hydrogen-bonding distances and low occupancy. However, the 177 "bad" waters were present in several rounds of refinement and phase information from the "bad" waters would have been transferred to the rest of the poly-peptide chain in the form of atomic shifts and changes in occupancy and temperature factors. All the refinements after the addition of bad solvent molecules in large numbers should be viewed with some caution.

There was a significant increase in *R*-factor when the correct sequence information was used to correct the structure. The number of non-solvent atoms had increased by 234 atoms but there was no indication as to which residues were added and which residues were completely rebuilt from the 2.4 Å structure without the *R*-factor dropping. This is complicated by the fact that 129 water atoms are added in the same round of the refinement and may mask the effect of any protein sequence corrections. The rise in *R*-factor may also be interpreted that the 2.4 Å solution was over-refined to fit the X-ray data at the point when sequence data were used. Thus, reverting to an earlier model, such as the *Ec*-FeSOD backbone used at the start of refinement for the 2.4 Å structure, may have been a better approach.

5.2.3.3 Discrepancies between published and deposited structures of *Thermus*-MnSOD

The submitted structure has the PDB identifier code 3MDS. There are some discrepancies between the submitted structure and what is described in the publication. The number of water molecules reported in the native structure is 180 in the abstract of the cited article but there are 187 solvents in the starting structure for the solution of the azide derivative. There are 187 water molecules in the submitted coordinates at the PDB. No information on how the 7 additional waters were added is given, but it is likely that the native structure was further refined and the structure improved by authors but the details were not published. In the publication there is a table of residues that are poorly defined in omit electron-density maps or have multiple conformations. In the submitted PDB file of

atomic coordinates the troublesome residues are all present in only one rotamer conformation at full occupancy with refined temperature factors higher than the surrounding residues. It is unclear why these residues, which do not agree with the omit maps, were kept in the structure or what criteria was used to decide the conformation of the residues in the submitted structure. The *R*-factor of the native structure listed in the PDB header for 3MDS is 0.19 for data from 20 to 1.8 Å. In the research article the *R*-factor is given as 0.176 for all data from 10.0 to 1.8 Å. Data from 15 to 10 Å is briefly used in 5 cycles (out of 88 cycles) of refinement but was then eliminated as it made refinement unstable, possibly indicating a problem with the bulk solvent model. Inclusion of data from 20 to 10 Å may have been required to identify and refine the 7 unaccounted for waters.

There is another minor discrepancy between the information submitted in 3MDS and what was reported in the publication. The paper makes reference to only one automated refinement program, PROLSQ (Hendrickson, 1985). The information contained in the header of the submitted atomic co-ordinates states that a second program, X-PLOR (Brünger, 1992a), was used. There are differences between how these two programs refine structures. The PROLSQ program uses a restrained diagonalised least-squares method which has a low radius of convergence, whereas X-PLOR uses a conjugate-gradient method to minimise a combined energy and X-ray function.

At present the PDB maintains current structures as well as the coordinate files of withdrawn structures and structures that have been superseded by improved structures. An example from within the field of SOD literature is the structure of human mitochondrial MnSOD which was originally solved (Borgstahl *et al.*, 1992) and coordinates submitted as 1ABM, then later revisions were made and new coordinates submitted as 1N0J. There is only one version of 3MDS at the PDB. There have been no revisions of *Thermus*-MnSOD since it was deposited. The other possibility, though highly unlikely, is that information in the header pertaining to data range, refinement programs and *R*-factor of the PDB entry 3MDS is wrong.

The native *Thermus*-MnSOD structure lacks many statistics that would be expected in a modern paper. The reported *R*-factor for the final model is 0.176. The paper was written before the use of the free-*R* statistic had become commonplace. Prior to the use of this data validation tool, it was possible to over-refine a structure to the point where information from the atomic structure overwhelmed any information derived from the diffraction

experiment. After this there are several possible sources of bias in the *Thermus*-MnSOD structure and its derivative azide structure.

5.3 Azide-inhibited FeSOD from *E. coli*

The structure of *Ec*-FeSOD-N_3^-, solved to 1.8 Å resolution, was co-reported with the structure of *Thermus*-MnSOD-N_3^- (Lah *et al.*, 1995) and may suffer from many of the same biases. However, as this structure is derived from only one crystal and therefore only one data set, it is inherently more reliable than the *Thermus*-MnSOD-N_3^- structure as there was no need to merge data from multiple crystals. The refinement of *Ec*-FeSOD-N_3^- also included a larger range of low-resolution data, from 20-40 Å, which may have improved refinement. This structure also lacks R_{free} so agreement between X-ray data and the refined structure may be subject to model bias.

5.3.1 Refining temperature factors and occupancy of water molecules

The starting model for refinement had no waters, a less biased starting point than that for *Thermus*-MnSOD-N_3^-. During refinement the number of waters increased to 334, then bad waters were removed to leave the final number, 272. The water molecules were refined in both temperature and occupancy parameters; refer to Table 11. But the water molecules appear more sensibly refined than those in *Thermus*-MnSOD-N_3^- as shown in Table 10.

			B-factor <35		B-factor >35	
Total # of H_2O	272	→	181	+ \	91	- \
Occupancy > 80%	243 \ +		152	+ +	91	- +
Occupancy < 80%	29 \ -		29	+ -	0	- -

Table 11. The distribution of occupancy and temperature factors of ordered solvent within *Ec*-FeSOD-N_3^-.

Table 11 shows the 272 solvent molecules of *Ec*-FeSOD-N_3^- categorised by temperature factor and occupancy. The threshold for temperature factor is 35 $Å^2$, chosen to put roughly one third of waters in the high B-factor range. This threshold is higher than that used in Table 10. Waters with low temperature factors and high occupancy are indicated by (++). Waters with either low occupancy or high temperature factors are indicated by (+ -) or (- +). There are no low quality water molecules with low occupancy and high temperature factors are shown by (- -). More than half the water molecules fall into the (++) category.

5.3.2 Refining alternate conformations of the active site

The structure of *Ec*-FeSOD-N_3^- was refined with two conformations at the active site of each dimer. The occupancy of each conformation is approaching ~50%. In the A subunit the occupancies are 48 and 51% and in the B subunit 50 and 53%. If these conformations

are true then the temperature factors of the refined alternate conformations should be similar. This is true of the A subunit. However, this is not reflected by the temperature factors of the B subunit where the azide-free conformation has temperature factors ~40% higher than those for the azide-bound conformation. For instance, the *B*-factors of the active-site Fe are 6.23 $Å^2$ in the azide-bound and 10.94 $Å^2$ in the azide-free conformation. This may indicate that the occupancy of the azide is greater than the ~50% reported for subunit B.

5.4 Azide-inhibited FeSOD from *Pseudomonas ovalis*

The first reported crystal structure of an azide-inhibited Fe/MnSOD was a 2.9 Å structure of an FeSOD from *Pseudomonas ovalis* (*Pseudo*-FeSOD-N_3^-). It was reported that azide had associated as the fifth ligand, displacing the bound solvent-derived ligand (Stoddard, Ringe *et al.*, 1990). There were other major changes in the active site as well. All other Fe/MnSOD-N_3^- structures, including those presented in this thesis, have azide binding in the vacant sixth ligand-binding site.

Azide could not be soaked into native crystals as they broke down in the presence of azide. Azide was instead soaked into chemically cross-linked crystals. At this resolution the ability to discern between an azide and hydroxide ion was severely limited.

Neither the atomic coordinates nor the structure factors for this structure were submitted to the PDB. So it is impossible to analyse the structure in great detail. This work is not often cited in the literature, and if it is cited it is very rarely in relation to the azide binding. The Fe/MnSOD-N_3^- structures from other sources (Lah *et al.*, 1995, Schmidt *et al.*, 1998) are more widely referenced.

5.5 Azide-inhibited cambialistic FeSOD from *Propionibacterium shermanii*

The structure of *Psherm*-camb-FeSOD-N_3^- (Schmidt *et al.*, 1998) is a modern high-resolution structure derived from data to 1.55 Å that has an R_{cryst} of 17.1% and an R_{free} of 19.8%. Azide occupancy was built at 55 and 56% in the A and B subunits and the temperature factors of the refined active site support this. There are only minor concerns with this structure. There is a probable misinterpretation of electron density where the wrong rotamer of His146, which links the solvent-access funnel tyrosine to the coordinated solvent by hydrogen bonds, may have been built with an incorrect rotamer. This only becomes apparent if the hydrogen bonding network is considered; refer to Figure 5-6 and Figure 5-7, and would not have been apparent from electron density alone.

Analysis of the temperature factors of the side-chain of His146 also indicate that an alternate rotamer should be considered.

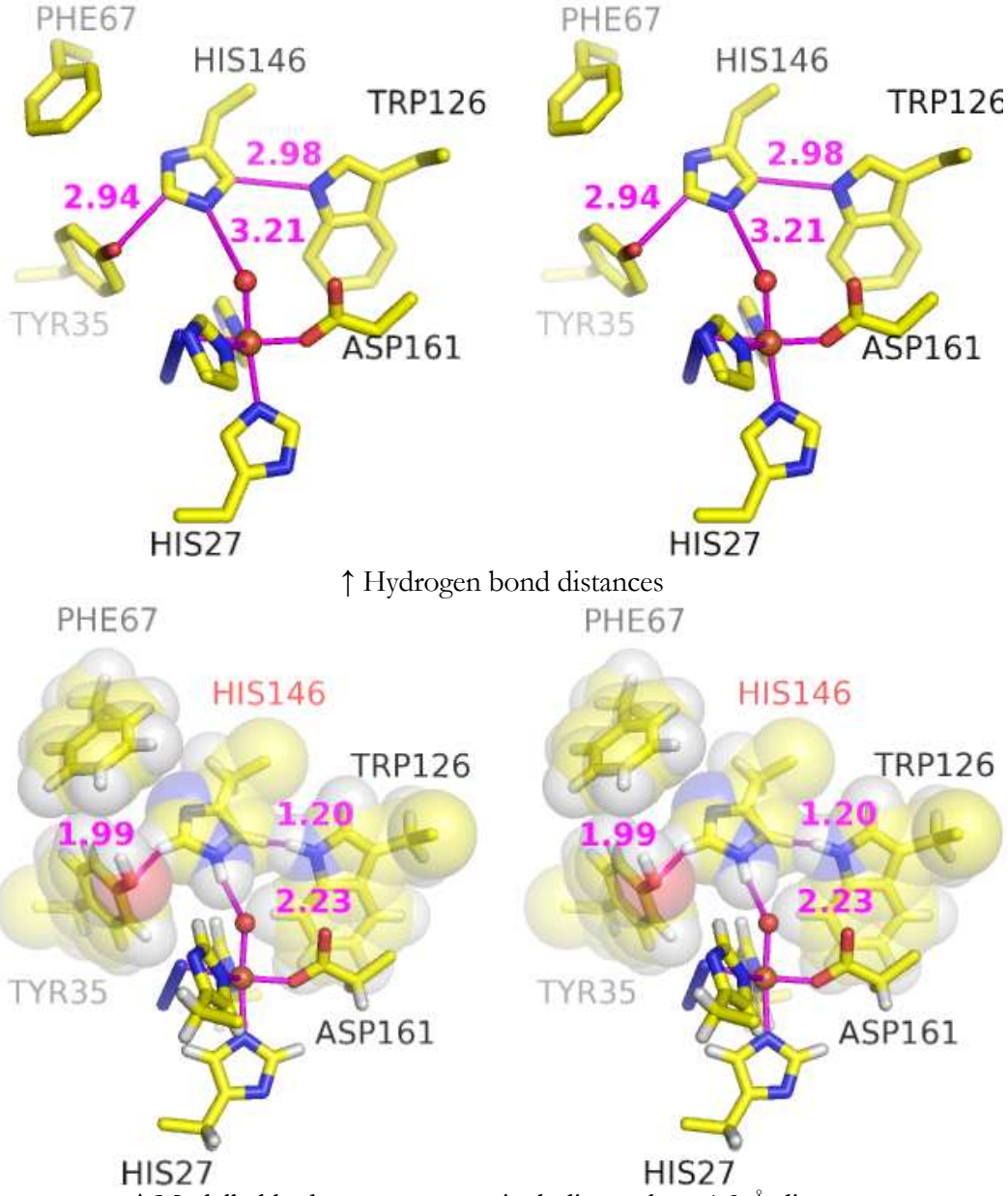

Figure 5-6. Wall-eyed stereo-view of a potential steric clash of His146 with Trp126 in the submitted structure of *Psherm*-camb-FeSOD-N_3^-.

Figure 5-6. Top-most stereo pair shows the hydrogen-bonding network in the vicinity of His146, inter-atomic distances are shown as labelled magenta lines. The lower stereo-pair shows the structure in the vicinity of His146 in *Psherm*-camb-FeSOD-N_3^- after hydrogen atoms have been generated in their riding positions by the CCP4 program HGEN (Bailey, 1994). In both stereo-pairs the active-site Fe and solvent-derived ligand are shown as small spheres. The rest of the displayed residues are shown in a stick form. Atoms are coloured white, yellow, blue, red and orange to show hydrogen, carbon, nitrogen, oxygen and iron respectively. In the lower stereo pair, the van der Waals radii are shown for the side-chains of Tyr35, Phe67, Trp126 and His146 as transparent spheres, the same colour as the base atoms. The active-

site metal is hexa-coordinate, as shown by magenta lines without labels, but is partially obscured by a histidine residue. The labelled magenta lines show the distance between the atoms of His146 and neighbouring residues. Note the short distance in the lower stereo-pair between His146 and Trp126 of 1.2 Å that indicates a potential steric clash, a modelled correction is shown in Figure 5-7.

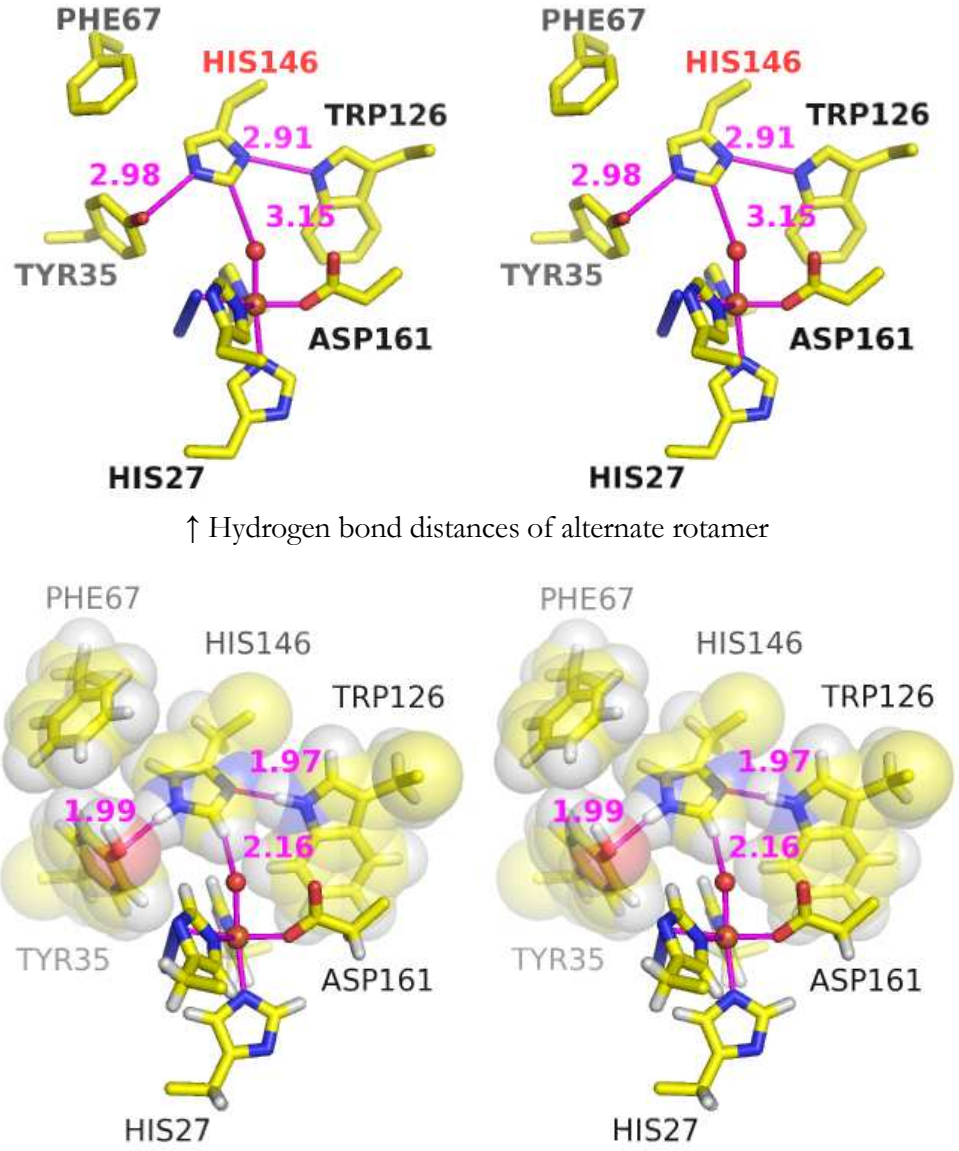

Figure 5-7. Wall-eyed stereo-diagram of the modelled alternate rotamer of His146 that does not clash with Trp126, derived from the coordinates of *Psherm*-camb-FeSOD-N_3^-.

Figure 5-7. The upper and lower stereo-pairs show a model, derived from *Psherm*-camb-FeSOD-N_3^-, where an alternate rotamer of His146, generated within COOT (Emsley & Cowtan, 2004), was utilised to generate hydrogen atoms in riding positions with HGEN. The atom representations and colouring scheme are the same as in Figure 5-6. The distances between the modelled His146 and neighbouring residues are shown as labelled magenta lines. The distance between His146 and Trp126 is 1.97 Å, a distance far more reasonable than the equivalent distance in the

lower stereo-pair of Figure 5-6. Other hydrogen bonding contacts are similarly more reasonable with this altered rotamer.

The only other concern with *Psherm*-camb-FeSOD-N_3^- is that temperature factors do not vary smoothly over the whole structure. There is a distinct jump in temperature factors when comparing solvent molecules to nearby protein residues; this includes highly ordered waters. However, this is a better approach to use than refining both water occupancies and temperature factors.

5.6 The inherent reliability of structures of azide-inhibited Fe/MnSODs

The active-sites of Fe/MnSODs are generally well defined within X-ray structures as they are buried within the protein core and as such electron density maps are well defined. This means that the X-ray data has the potential to overwhelm any refinement bias.

5.6.1 *Ec*-FeSOD-N_3^-, *Psherm*-camb-FeSOD-N_3^- and Y174F-*Ec*-MnSOD-N_3^-

Based on a preponderance of structural evidence the azide-binding pattern seen in *Ec*-FeSOD-N_3^- (Lah *et al.*, 1995), *Psherm*-camb-FeSOD-N_3^- (Schmidt *et al.*, 1998) and Y174F-*Ec*-MnSOD-N_3^- have been reliably interpreted. This is evident in that they all have good Ramachandran plots, which reflect geometric parameters that are independent of refinement bias.

5.6.2 *Thermus*-MnSOD-N_3^-

During the initial rounds of refinement of *Thermus*-MnSOD-N_3^-, electron-density peaks for the azide ion would become apparent. This structure suffers from some poor treatment of X-ray data from two crystals and potentially biased refinement of the structure of *Thermus*-MnSOD-N_3^- with too much structural information transferred from the native structure, particularly the ordered water molecules. However, this structure most likely reflects the true binding of azide to *Thermus*-MnSOD at ambient temperatures. This is further supported by the structure of *Ec*-Fe-MnSOD-N_3^- at cryogenic temperatures, presented in this thesis, which has better treatment of data and less biased refinement. *Ec*-Fe-MnSOD-N_3^- shows azide binding in a similar, but not identical manner. This is in stark contrast to the structures of *Deino*-MnSOD-N_3^-, *Ec*-FeSOD-N_3^- (Lah *et al.*, 1995), *Psherm*-camb-FeSOD-N_3^- (Schmidt *et al.*, 1998), and Y174F *Ec*-MnSOD-N_3^- (1ZLZ in the protein data bank), where azide binds in a different manner. A more detailed comparison is given in section 6.4.

5.6.3 *Pseudo*-FeSOD-N_3^-

The azide-binding motif seen in *Pseudo*-FeSOD-N_3^- (Stoddard, Ringe *et al.*, 1990) is unique and not regarded as being analogous to superoxide binding.

5.7 Convergent errors in azide-inhibited Cu/ZnSODs

At present there are two Cu/ZnSOD structures with bound azide. There are, however, some potential sources of errors in these structures, which are similar to the potential sources of error in *Thermus*-MnSOD-N_3^- discussed above.

The azide-bound Cu/ZnSOD from the yeast (1YAZ) was solved at pH 7.5 to 1.7 Å resolution (Hart *et al.*, 1999). If this structure is overlaid with the oxidised and reduced *yeast*-Cu/ZnSOD (refer to image A in Figure 5-8) then the N1 and N3 of the azide molecule are very close to ordered solvent molecules. The structure of reduced *bovine*-Cu/ZnSOD complexed with azide at pH 5.0 (Ferraroni *et al.*, 1998) was solved to 2 Å using synchrotron radiation (1SXZ). Also co-reported in the paper were the structures of the reduced form of *bovine*-Cu/ZnSOD (1SXN) and a thiocynate-inhibited reduced *bovine*-Cu/ZnSOD (1SXS). If the A-subunits of all three of these structures are overlaid then the position of the azide and thiocyanate fall on the coordinated solvent molecule and a solvent molecule in the second coordination sphere of the reduced native structure; refer to image B in Figure 5-8. If the B-subunits are overlaid, the N1 of the azide, which coordinates with the active site Cu, are positioned on top of the coordinated solvent with the N3 of the inhibitor falling close to a solvent in the second coordination sphere; refer to image C in Figure 5-8. It is possible that the Cu/ZnSOD-N_3^- structures have suffered from an interpretative bias where density peaks that correspond to solvent molecules have been ascribed as azide due to misinterpretation of ambiguous density maps.

The recently solved structure of NiSOD (Barondeau *et al.*, 2004) has been combined with electron paramagnetic resonance (EPR) spectroscopy as a basis for models of azide, and therefore superoxide, binding. However, there is no actual azide-bound structure of NiSOD.

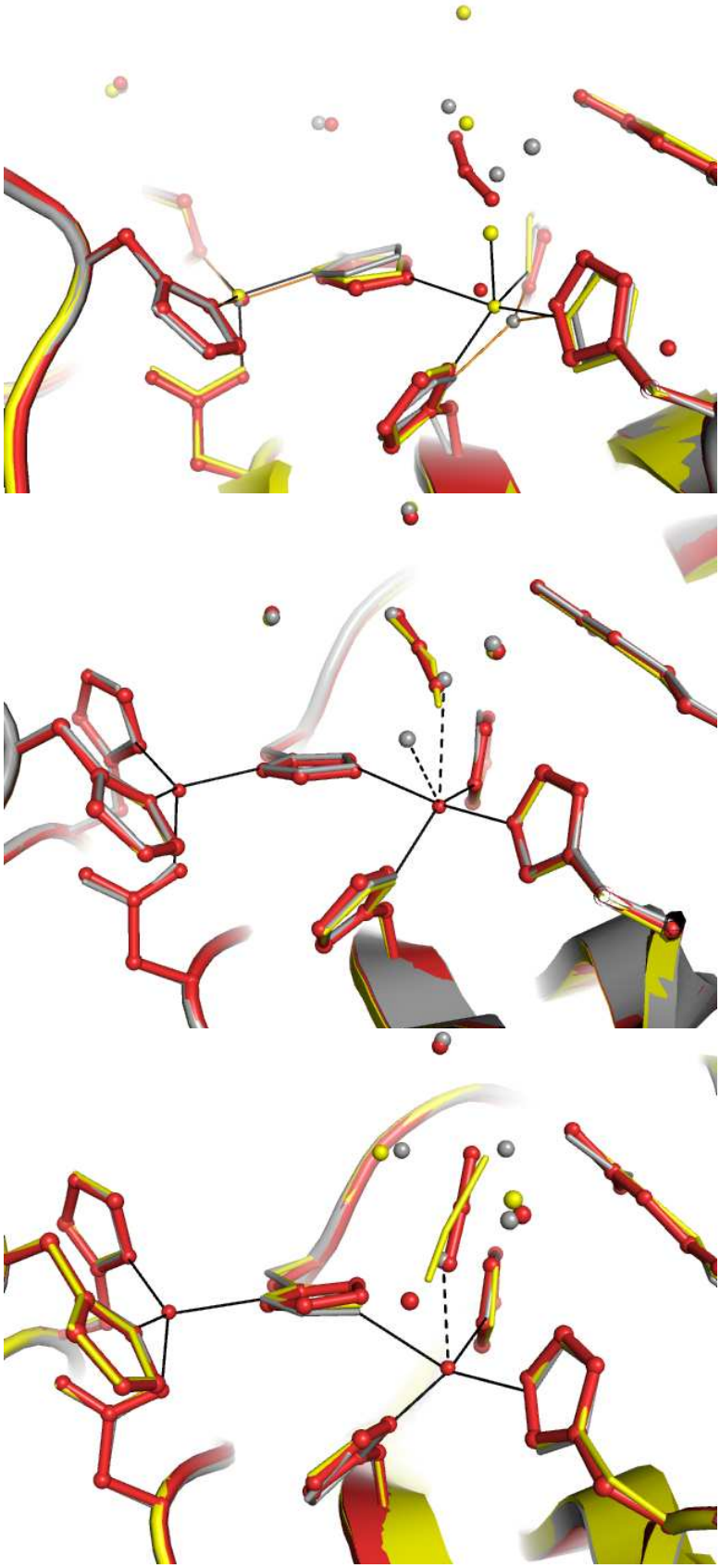

Figure 5-8. Structure of azide-bound Cu/ZnSODs, overlaid onto native structures, where the inhibitor displaces solvent molecules.

Figure 5-8. All three images show ball-and-stick representations of important active site residues and cartoon representations of the peptide backbone. Image A shows the active-site of yeast Cu/ZnSOD in oxidised (yellow), reduced (grey) and azide-bound (red) derived from the coordinates of 1SDY, 1JCW and 1YAZ respectively. The oxidised Cu^{2+} is bound with four histidines and a solvent molecule. Reduction to Cu^{+} causes changes in solvent, disassociation of the bridging histidine and the copper atom moves as the geometry changes from a square-planar to trigonal-planar. Azide binds in a similar position to the solvent molecule with the tail of the azide molecule also occupying a solvent position. In the coordinates of 1YAZ there is a water molecule, number 215, that is only 1.4 Å from His120 that is likely an error in the structure.

Images B and C are generated from a series of crystallisation experiments on the reduced bovine Cu/ZnSOD dimer and show the active sites of the A and B subunits respectively. For both B and C, the grey representation shows the reduced native bovine Cu/ZnSOD (1SXN), the green representation shows a thiocyanate bound structure (1SXS) of the reduced enzyme and the azide-inhibited Cu/ZnSOD (1SXZ) is shown in red. There are minor differences between the two subunits probably due to differences in crystal packing. For instance, in the reduced structure the Cu^{+} in the A-subunit is coordinated by two solvent molecules and the Cu^{+} of the B-subunit binds one solvent molecule. The binding of azide or thiocyanate overlay well in both subunits and overlay well with solvent molecules of the reduced native structure. This is particularly true of the A-subunit, which has less conformational freedom than the B-subunit.

5.7.1 Quality of SOD structures

There is abundant structural information on the three SOD families; this is particularly true of the Fe/MnSODs and the Cu/ZnSODs which have been investigated for several decades using structural techniques, mainly by x-ray crystallography. Most of these crystal structures accurately represent the biological molecule. However, it is possible and probable that there are errors in some of these structures, especially in older structures solved before the requirement of the R_{free} statistic. These minor errors were the result of then-valid over-interpretation of data, refinement practices, uncertain inhibitor occupancy and poor handling of x-ray data. The modern interpretation and referencing of scientific literature from the past is valid, as long as there is an awareness of the merits and deficiencies of techniques and practices used to generate findings.

6 Comparisons with other structures and discussion of results

Superoxide dismutases are commonplace in nature and provide protection from the oxygen-derived free radical superoxide (O_2^-), which can be a major cause of oxidative damage to cells. These obligate metallo-enzymes are amongst the most catalytically efficient enzymes known, with reaction rates approaching diffusion limits. The negatively charged superoxide molecule is attracted to a positively charged metal ion at the active site, where it is alternately converted to oxygen and hydrogen peroxide coupled respectively to the alternate reduction and oxidation of the active-site metal ion. Catalysis occurs so rapidly in Fe/MnSODs that gaining information on transition states is difficult. The use of substrate analogues of superoxide, such as the azide anion, allows for long duration experiments, such as structure determination by X-ray crystallography. The structures of *Ec*-Fe-MnSOD-N_3^- and *Deino*-MnSOD-N_3^-, together with comparisons with other azide-bound SODs, give insights into the binding of superoxide and its subsequent dismutation at the active site.

6.1 Analysis and implications of the structure of *Ec*-Fe-MnSOD-N_3^- at 2.2 Å resolution

The binding of azide to *Ec*-Fe-MnSOD occurs at 60% occupancy and leads to observable structural changes, most noticeable being the movement of the solvent-access funnel tyrosine away from the active site. The binding of azide is reminiscent, but not identical, to that seen previously in *Thermus*-MnSOD-N_3^- (Lah *et al.*, 1995) and different to that seen in previously solved azide-inhibited Fe/MnSODs with Fe at the active site (Lah *et al.*, 1995, Schmidt *et al.*, 1998). This shows that the binding of azide (and by inference superoxide) is not absolutely determined by the active-site metal ion, but may be multi-factorial and influenced by pH, temperature and, importantly, the polypeptide component.

6.1.1 pH-dependent processes in *Ec*-Fe^{3+}-MnSOD and *Ec*-Fe^{3+}SOD

At near-physiological pH, the iron-substituted MnSOD from *E. coli* (*Ec*-Fe-MnSOD) stabilises a six-coordinate state much more readily than the wild-type *Ec*-MnSOD or *Ec*-FeSOD, which are five-coordinate systems. The sixth ligand is a solvent-derived hydroxide. This sixth ligand blocks access of superoxide to the metal, decreasing catalysis at the active site preventing electron transfer from superoxide to iron cation. *Ec*-Fe-MnSOD is more prone to stabilise a sixth ligand than native MnSODs (Vance & Miller,

1998b, Edwards *et al.*, 2001a, Tabares *et al.*, 2003), as also observed for the Fe forms of Mn-preferring cambialistic SODs (Yamakura *et al.*, 2003).

At lower pH ranges, the hydroxide probably becomes protonated to a water molecule that readily dissociates from the iron. As a consequence, the activity of Fe-MnSOD increases (Yamakura *et al.*, 1995), as the sixth ligand, a hydroxide, becomes less tightly bound, if it is bound at all (Jackson *et al.*, 2002).

In *Ec*-Fe^{3+}SOD the coordination number changes from five to six when moving from pH 7 to pH 10, with the midpoint of this transition being pH 9.4 (Tierney *et al.*, 1995). When comparing FeSOD and Fe-MnSOD it is easy to draw parallels between their apparent pH dependencies. However, the p*K* associated with hydroxide anion binding is different being 6.7 in *Ec*-Fe-MnSOD; refer to Figure 6-1. This value is 2 orders of magnitude lower than in FeSOD (or MnSOD); refer to Figure 2-6 and Figure 2-7, and occurs without a large change in EPR spectra. A second p*K* seen in Fe-MnSOD at pH 8.5 is associated with a large change in EPR signal (assumed to be associated with the deprotonation of Tyr34) (Vance & Miller, 1998a). The separation of pK associated with anion binding and that with changes in EPR signals seen in the wrong-metal form may be the key to why the Fe-MnSOD is inactive at physiological pH (Vance & Miller, 1998a), as the sixth coordinated ligand, an hydroxide ion, is not eliminated from the active site preventing activity. In native FeSOD the coordination of the hydroxide occurs at a higher pH close to the point where the conserved tyrosine loses H^+ and the enzyme loses activity.

Figure 6-1 shows the change in the structure of the active site of *Ec*-Fe^{3+}-MnSOD over physiological pH ranges. At low pH ranges the structure of *Ec*-Fe^{3+}-MnSOD is reminiscent of *Ec*-FeSOD and *Ec*-MnSOD. As pH increases an hydroxide enters the active site and associates with the bound metal, changing the coordination of Fe^{3+} from five to six with the midpoint of this transition occurring at pH 6.7. As pH further increases there is a second pH-dependent transition, a loss of the proton from solvent-access funnel tyrosine, the mid point of this transition occurring at pH 8.5.

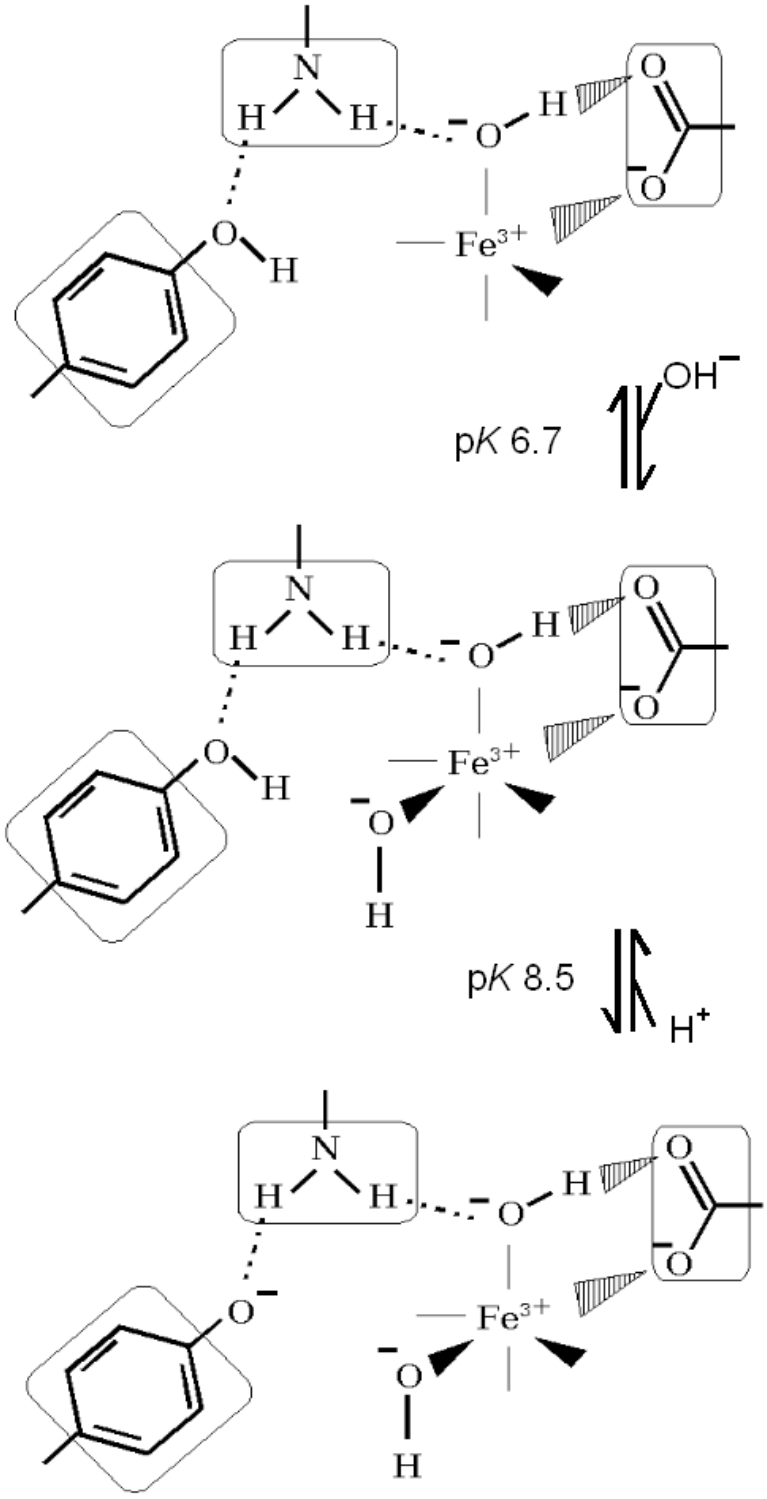

Figure 6-1. Proposed pH-dependent transitions with p*K* values in *Ec*-Fe^{3+}-MnSOD.

6.1.2 Structural features of *Ec*-Fe-MnSOD

The original structure of *Ec*-Fe-MnSOD (Edwards, Whittaker *et al.*, 1998) was solved at pH 8.5 and featured a dimer in the asymmetric unit. The amino-acid residues involved in metal ligation in both subunits are His26, His81, His171 and Asp167 (the same as in the native *Ec*-MnSOD). There is, however, a pronounced difference between the active sites of the A and B subunits. The Fe of the A subunit (*A*_Fe) is penta-coordinate, whereas the Fe of the B subunit (*B*_Fe) is hexa-coordinate; refer to Figure 6-2 and Figure 6-3 respectively.

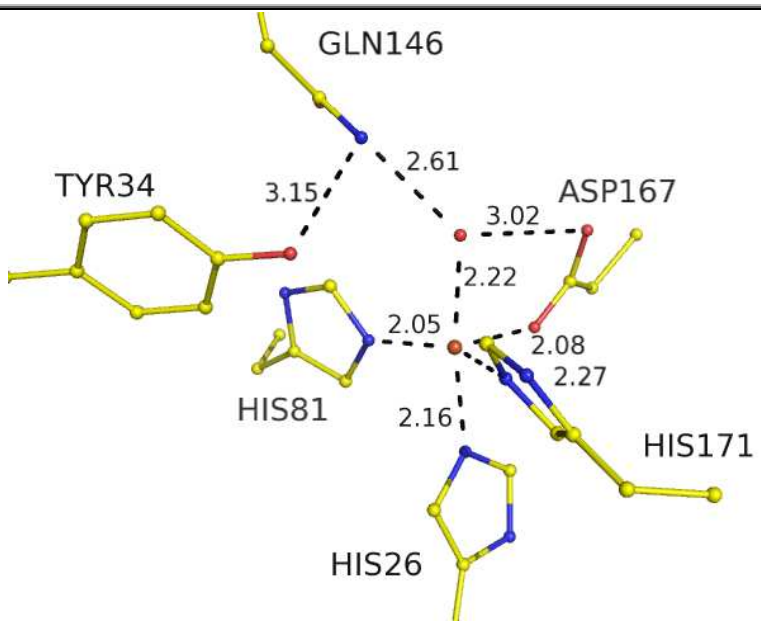

Figure 6-2. The active site of subunit A of *Ec*-Fe-MnSOD.

Figure 6-2 shows an image that was generated from the A chain of the PDB file 1MMM. It shows the amino-acid side chains of metal-ligating and selected residues as a ball-and-stick representation. The penta-coordinate Fe^{3+} and the coordinated hydroxide ion are shown as orange and red spheres respectively. Key hydrogen bonds and bonding contacts are shown as dashed black lines labelled with inter-atomic distances in Å. The distances are different to those seen in the A subunit of *Ec*-Fe-MnSOD-N_3^- as shown in Figure 4-4. The structure of the active site of the B chain is different and shown in Figure 6-3.

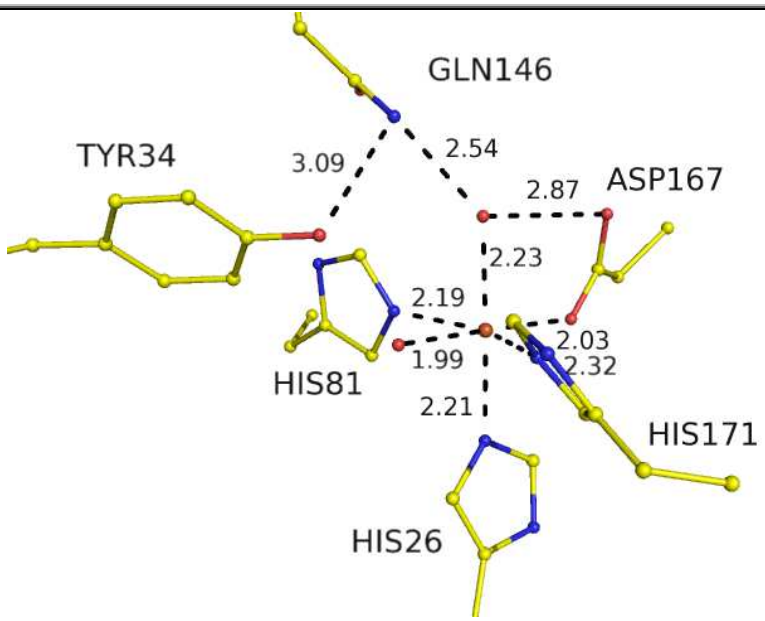

Figure 6-3. The active site of subunit B of *Ec*-Fe-MnSOD.

Figure 6-3 shows an image that was generated from the B chain of the PDB file 1MMM. It shows the amino-acid side chains of metal-ligating and selected residues as a ball-and-stick representation. The hexa-coordinate Fe^{3+} and the coordinated hydroxide ions are shown as orange and red spheres respectively. Key hydrogen bonds and bonding contacts are shown as dashed black lines labelled with inter-atomic distances in Å. There are minor differences compared to subunit B of *Ec*-Fe-MnSOD-N_3^- as shown in Figure 4-5.

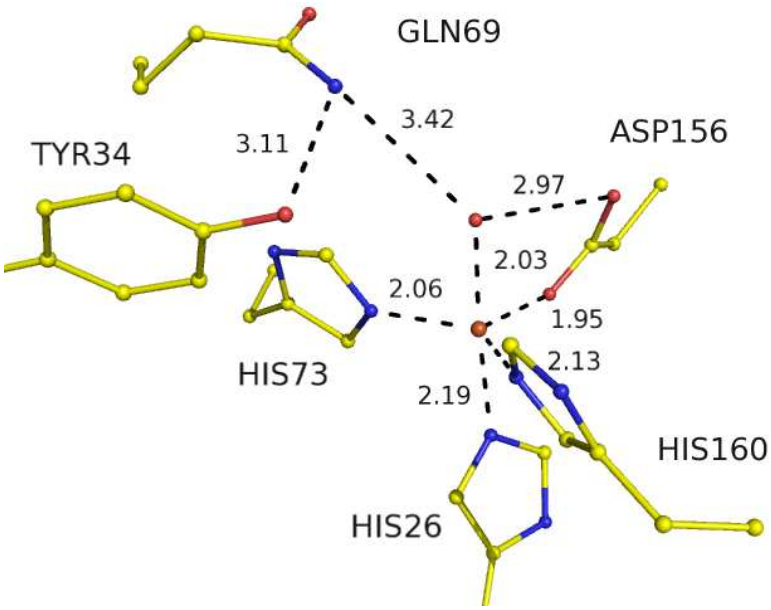

Figure 6-4. The active site of subunit A of *Ec*-FeSOD.

Figure 6-4 shows an image that was generated from the PDB file 1ISA. It shows the amino-acid side chains of metal-ligating and selected residues as a ball-and-stick representation. The penta-coordinate Fe^{3+} and the coordinated hydroxide ion are shown as orange and red spheres respectively. Key hydrogen bonds and bonding contacts are shown as dashed black lines labelled with inter-atomic distances in Å. The active site of the B subunit is almost identical.

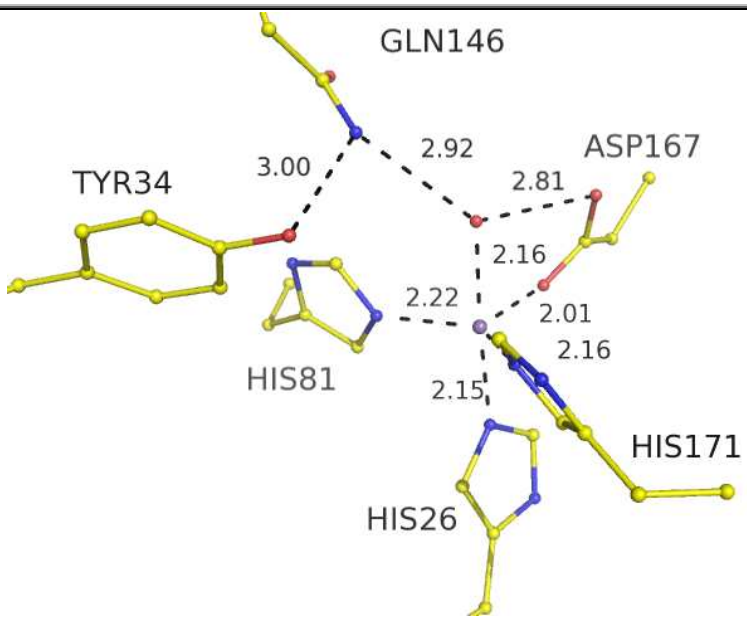

Figure 6-5. The active site of subunit A of *Ec*-MnSOD.

Figure 6-5 shows as image derived from the PDB file 1VEW. It shows the amino-acid side chains of metal-ligating and selected residues as a ball-and-stick representation. The penta-coordinate Mn^{3+} and the coordinated hydroxide ion are shown as magenta and red spheres respectively. Key hydrogen bonds and bonding contacts are shown as dashed black lines labelled with inter-atomic distances in Å. The active sites of the B, C and D subunits are almost identical.

It is likely that in solution, close to physiological pH ranges, *Ec*-Fe-MnSOD exists as a mixture of both penta- and hexa-coordinate states. Assuming that the obligate dimer persists, then there are three possible dimer combinations: penta/penta, penta/hexa, or hexa/hexa. It remains unclear what the stoichiometry and relative stability of the three possible combinations are relative to one another, and the degree to which they change with pH. The original structure of *Ec*-Fe-MnSOD at pH 8.5 was solved in the penta/hexa-form only. It remains unclear if the penta/hexa state of the crystal structure of *Ec*-Fe-MnSOD is due to the relative stability of penta/hexa allowing crystallisation to occur, if the crystallisation conditions enforced the penta/hexa state, or if there is intrinsic asymmetry in the obligate Fe/MnSOD dimer (as will be discussed in section 6.2.6).

In the structure of *Ec*-Fe-MnSOD, both active sites of the dimer have slightly distorted geometries compared to native Mn and FeSODs; compare Figure 6-2 and Figure 6-3 to Figure 6-4 and Figure 6-5. A six-coordinate state was seen in subunit B, where the sixth ligand was inferred to be an hydroxide. Interestingly, the other active site, in subunit A, had a five-coordinate Fe system with a vacant site, predisposed for the binding of a sixth ligand. Moreover, *A*_Y34, which stands at the gateway to the active site, is disordered in subunit A, but the equivalent subunit B residue *B*_Y34 is ordered.

6.1.3 Two active-site conformations imply communication across the dimer interface

These differences were taken as an indication that there may be some degree of communication between the two active sites (Edwards, Whittaker *et al.*, 1998), such that the coordination of Fe at one active site influences the Fe coordination at the other site. As a consequence one form of the metal-substituted enzyme crystallises. The active sites within each dimer are linked through a hydrogen-bonding network. This pathway consists of three residues that link the metal ion at one active site to the metal ion in the second subunit over a distance of 18 Å. The metal ion at the active site of subunit A of *Ec*-MnSOD is bonded directly to *A*_H171 which is located on a highly conserved loop bearing the active-site residues (*A*_H171 and *A*_Asp167) and the dimer interface residues (*A*_Gln170 and *A*_Tyr174). The residue *A*_Glu170 in turn hydrogen-bonds to *B*_His171 across the dimer interface, which is bonded to the metal ion at the active site of subunit B. The reciprocal arrangement is also true, where *B*_Glu170 hydrogen bonds to the *A*_His171. The point mutation E170A abolishes dimerisation and eliminates catalytic activity (Whittaker & Whittaker, 1998). The linking of active sites is preserved in Fe-MnSOD as is the rest of the hydrogen bonding network (Edwards, Whittaker *et al.*, 1998).

6.1.4 Other differences between substituted and native forms

The reduction potential for $Fe^{3+} + e^- \rightarrow Fe^{2+}$ is 0.3 V in wild-type FeSOD and decreases to -0.24 V in Fe-MnSOD. This means that the Fe^{3+} state in Fe-MnSOD is more stabilised with respect to the Fe^{2+} state than in wild-type FeSOD. The replacement of Mn with Fe in *Ec*-MnSOD causes other changes: noticeably the affinity of Fe-MnSOD, in its Fe^{3+} state, for azide, a potent inhibitor of SODs and other metallo-enzymes, is much higher than either the native MnSOD or FeSOD, and the binding of azide perturbs the optical and EPR spectra of Fe-MnSOD more than FeSOD (Vance & Miller, 1998a). The affinity for azide is greater at low pH ranges, the five-coordinate state, than at higher pH ranges that favour the hexa-coordinate hydroxide bound state. The mid-point of this change in azide affinity is associated with the p*K* of 6.7 shown in Figure 6-1. The structural basis for this change in azide affinity is likely to be the distorted geometry, indicated in the A subunit, which favours the stabilisation of a sixth ligand much more than the native Mn form of the enzyme.

Like the sixth ligand, the hydroxide, the affinity of the small-molecule inhibitor azide for *Ec*-Fe-MnSOD is much greater than for wild type MnSOD. The 2.2 Å resolution structure of *Ec*-Fe-MnSOD with coordinated azide (*Ec*-Fe-MnSOD-N_3^-) reveals a distorted active site compared to wild-type *Ec*-MnSOD, *Ec*-FeSOD and *Ec*-Fe-MnSOD.

6.1.5 The mobile solvent-access funnel tyrosine

The most drastic change, and easily observed, between *Ec*-Fe-MnSOD and *Ec*-Fe-MnSOD-N_3^- is the movement of *A*_Y34 away from the active-site metal (*A*_Fe). Upon azide association the distance between *Ec*-Fe-MnSOD_*A*_Y34_OH and *Ec*-Fe-MnSOD_*A*_Fe increases from 4.44 Å to 5.30 Å in *Ec*-Fe-MnSOD-N_3^-. The Tyr34 of the A subunit, which lines the solvent channel to the active site of subunit A, was slightly disordered due to close association with the azide ion present in only 60% occupancy. As a result the temperature factors of this residue are slightly higher than those of the surrounding residues. A nearby buttressing residue, *B*_Phe124, tilts to allow the movement of *A*_Y34. There is a slight increase in the *B*_Y34 to *B*_Fe distance compared the same distance in *Ec*-Fe-MnSOD.

In the final structure of *Ec*-Fe-MnSOD-N_3^-_*A*, Tyr34 has been built in one conformation that represents the average position of the tyrosine in the crystal. An alternative approach would have been to build in two, or even multiple conformations, with partial occupancy. At no point during the refinement did the density of the electron density maps around the side-chain of *A*_Y34 become distinct enough to merit splitting the residue. The OH of *A*_Y34 is in close proximity to the N3 atom of the azide ion (naming convention used for atoms within the azide ion are given in Figure 6-6).

The active site of subunit B was extremely well ordered without any areas of ambiguity in the electron-density maps. The refined orientation of Tyr34 of subunit B is slightly towards the solvent-access funnel of subunit B compared to that seen in Fe-MnSOD. The distance between *Ec*-Fe-MnSOD_*B*_Y34_OH and *Ec*-Fe-MnSOD_*B*_Fe increases from 4.38 Å to 4.71 Å in equivalent residues in *Ec*-Fe-MnSOD-N_3^-; this may be due to the binding of azide at very low occupancy, displacing the tyrosine in a manner similar to that of the active site of subunit A. In a low-resolution room-temperature study with data to 2.7 Å by co-workers, whose results are not presented, azide saturation was more complete and displaced the sixth ligand, a coordinated hydroxide, in subunit B.

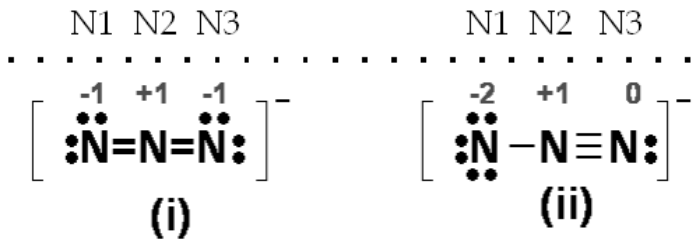

Figure 6-6. Resonance Lewis structures of the azide ion.

Figure 6-6 shows the two possible Lewis structures of the azide ions: symmetrical i) and asymmetric ii). In both structures, atoms are labelled N1, N2 and N3. In i) the atoms designated N1 and N3 are identical and this arrangement probably reflects the nature of azide in solution. However, in ii) N1 and N3 are not identical with N1 being more negatively charged and this probably reflects the structure of azide in the asymmetric environment of a SOD. The azide nitrogen that is metal bound is always designated N1.

The binding of azide has effects on the other ligands, shown pictorially in Figure 6-7, that are bound to the metal ions. Most noticeable are the effects on the fifth ligand, an hydroxide ion, whose bond has lengthened from 2.2 Å to 2.41 Å on azide association. This in turn disrupts the local hydrogen-bonding network. The distance between the hydroxide and *A*_D167_OD1 decreases from 3.02 Å to 2.86 Å. The decrease in distance between hydroxide ion and *A*_Q146_OD1, from 2.61 Å to 2.55 Å, is not significant.

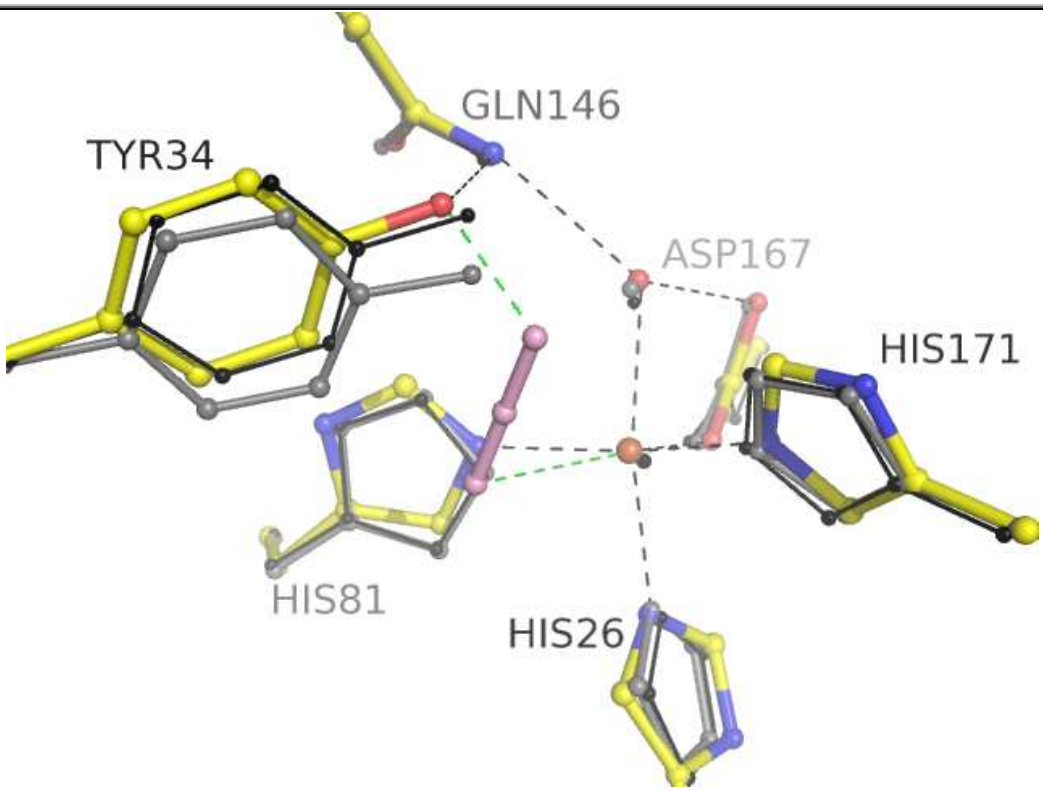

Figure 6-7. Overlay of the active site of the A subunits of *Ec*-MnSOD, *Ec*-Fe-MnSOD and *Ec*-Fe-MnSOD-N_3^-.

Figure 6-7 shows the active site of three structures all shown as ball-and-stick representations. The native *Ec*-MnSOD, derived from 1VEW, is shown as a black ball-and-stick with the radii of the spheres and sticks in this representation the least of all representations. The active site of subunit A of *Ec*-Fe-MnSOD is shown as a grey ball-and-stick, derived from 1MMM, with intermediate stick and sphere radii. The active site of subunit A of *Ec*-Fe-MnSOD-N_3^- is shown as a multi-coloured ball-and-stick representation where the stick radii are the largest shown. In *Ec*-Fe-MnSOD-N_3^- carbon, nitrogen, oxygen and iron are coloured yellow, blue, red and orange respectively. The azide molecule has been coloured pink. Important bonds, in *Ec*-Fe-MnSOD-N_3^-, have been shown as black dashed lines and the bonds the azide ion makes are shown as green dashed lines.

The two manipulations, metal substitution and subsequent azide soak, have the effect of perturbing active-site residues. The most movement is seen in the coordinated hydroxide and nearby Tyr34. However, the active site maintains the same overall geometry.

Binding of azide alters the positions of the waters within the substrate channel. In the azide-inhibited structure there are fewer waters in the substrate-access funnel relative to the A subunit of *Ec*-Fe-MnSOD, indicating substantial disruption of the hydrogen-bonding network around the active site. Since the binding of azide to the active site is not complete, as reflected in the occupancy of 0.6, this region of the crystal structure must be subject to some degree of disorder making the refinement of individual atoms such as the oxygens of water difficult. In order to remain objective, only waters that refined with full occupancy and sensible temperature factors are present in the final structure; any other waters may be the result of artefacts of refinement or waters that have very low occupancy.

The interaction between the N1 of the azide ion and the Fe^{3+} is described here as an outer-sphere interaction and not as a covalent bond. This is based primarily on the distances of the azide ion from the iron ion. The closest distance is 2.87 Å between the N1 and the Fe, much larger than the Fe^{3+}-OH^- separation of 1.99 Å in subunit B in *Ec*-Fe-MnSOD.

The distance between N3 of the azide ion and the average position of *A*_Tyr34_OH in the structure is 2.63 Å, which is a reflection of the mixture between azide-free and azide-bound active sites that co-exist within the crystal. In the azide-bound state this interaction is probably a hydrogen bond, typically on the order of 2.8 Å.

6.1.6 Structure of the active site of subunit B, without azide

Based on interpretation of electron density maps there was negligible evidence of azide ion binding at the active site of subunit B. The density peak of the sixth ligand had the shape and size of an hydroxide ion. However, there are several indirect indicators that

azide is binding in low occupancy. The most significant is that *B*_Y34 has tilted slightly away from *B*_Fe, relative to *Ec*-Fe-MnSOD, as shown in Figure 6-8. There is some evidence that azide has partly displaced an hydroxide from the active site of subunit B: a rise in the temperature factor of the hydroxide and a slight displacement of Tyr34 are observed compared to Fe-MnSOD and a change in the length of the bond between the Fe and the hydroxide. Eventually, given enough time soaking the crystal in the azide solution, the hydroxide would in all probability have been replaced by azide at the active site of subunit B. The kinetics of this process would be much slower than binding at the vacant site, as hydroxide would have to be displaced before azide could be bound to the active site.

The other difference between the two subunits is that subunit B forms fewer crystal contacts than subunit A and is surrounded by more solvent. This may have effects on the rate at which azide associates with metal centre as subunit B has more conformational freedom.

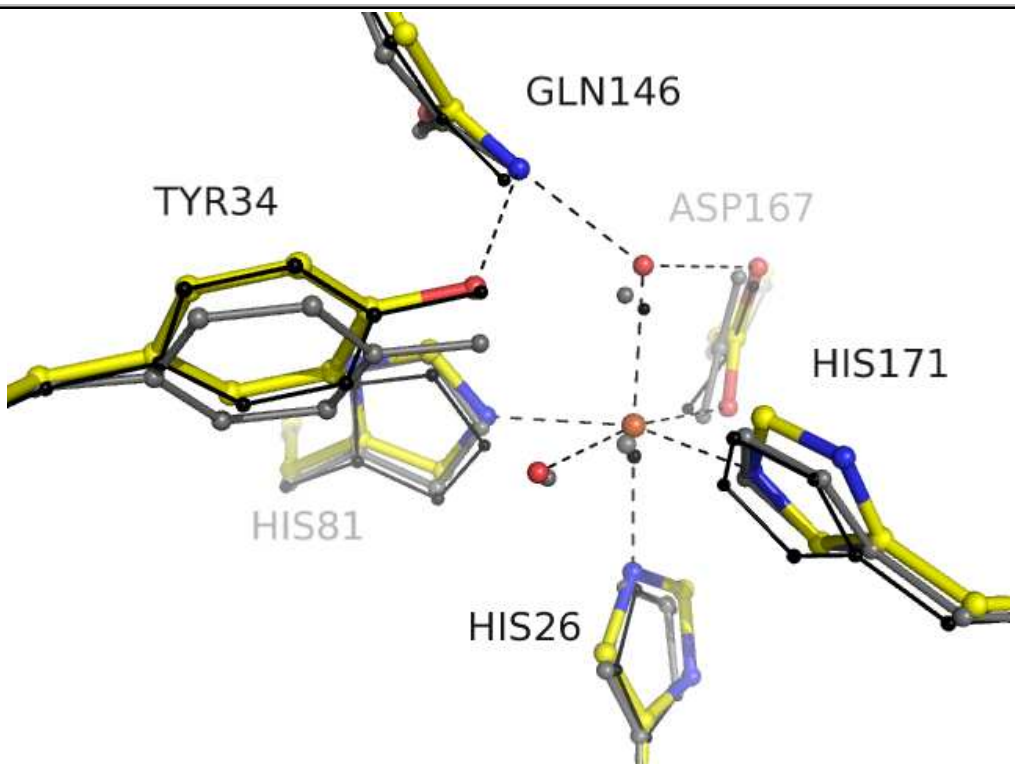

Figure 6-8. Overlay of the active site of the B subunits of *Ec*-MnSOD, *Ec*-Fe-MnSOD and *Ec*-Fe-MnSOD-N_3^-.

Figure 6-8 shows the active site of three structures all shown as ball-and-stick representations. The native *Ec*-MnSOD, derived from 1VEW, is shown as a black ball-and-stick with the smallest radii for the spheres and sticks in this representation. The active site of subunit B in *Ec*-Fe-MnSOD is shown as a grey ball-and-stick, derived from 1MMM, with intermediate stick and sphere radii. The active site of subunit B in *Ec*-Fe-MnSOD-N_3^- is shown as a multi-coloured ball-and-stick

representation where the stick and sphere radii are the largest shown. In *Ec*-Fe-MnSOD-N_3^- carbon, nitrogen, oxygen and iron are coloured yellow, blue, red and orange respectively. Important bonds in *Ec*-Fe-MnSOD-N_3^- are shown as black dashed lines.

Changing the metal from the native Mn to Fe, black to grey, has the effect of changing the coordination of the active site from five to six. This causes perturbation of the active-site residues and movement of Tyr34 between *Ec*-MnSOD and *Ec*-Fe-MnSOD. The subsequent soaking of azide leads to extremely low occupancy at the active site, which manifests primarily as a small shift of the Tyr34 in *Ec*-Fe-MnSOD-N_3^-.

6.1.7 Implications of the *Ec*-Fe-MnSOD-N_3^- structure

The affinity of azide for MnSODs is generally much lower than for FeSODs (Whittaker & Whittaker, 1991). The original structure of Fe-MnSOD represents the transition from a five-coordinate to a six-coordinate system, as both states are seen in the same structure. *In vitro* the transition between a five-coordinate system to the six-coordinate system is largely pH dependent. Complementary research has been performed on the pH dependence of the binding of a sixth ligand to the Fe form of the cambialistic SOD from *Propionibacterium shermanii* (Meier *et al.*, 1998). The structure has been solved at four different pH including some above and below the pH where coordination changes from five to six (Schmidt, 1999). The occupancy of the sixth ligand, a hydroxide, increases as pH increases and is mimicked by the binding of the small-molecule inhibitor fluoride, which binds with partial occupancy in neutral pH ranges.

To our knowledge there exists no structure of WT-*Ec*-MnSOD complexed with azide. There exists an azide-inhibited mutant structure, Y174F-*Ec*-MnSOD-N_3^- (PDB code 1ZLZ, Dr Jim Salvador of Massey University) that follows the pattern seen in Fe-SODs as does *Deino*-MnSOD-N_3^- co-presented in this thesis.

6.1.8 Orientation of azide in *Ec*-Fe-MnSOD-N_3^- and comparisons with other azide-inhibited Fe/MnSODs

In the structure of *Ec*-Fe-MnSOD-N_3^- the azide is oriented reminiscent to, but not identical to, that seen in an MnSOD from *Thermus thermophilus* (Lah *et al.*, 1995), where the tail of the azide is orientated towards the substrate-access funnel making a hydrogen bond to the Tyr34_OH; refer to Figure 6-9. However, possible errors in the *Thermus*-MnSOD-N_3^- have been discussed earlier in section 5.1. This orientation is different from that observed in three FeSOD structures, *E. coli* (*Ec*-FeSOD-N_3^- (Lah *et al.*, 1995)), *P. shermanii* (*Psherm*-camb FeSOD-N_3^- (Schmidt *et al.*, 1998)) and Y174F *Ec*-MnSOD-N_3^- (1ZLZ in the protein data bank), where the azide points its terminal nitrogen atom into a cavity

between the second-shell residues equivalent to His30 and His81 in the *Ec*-MnSOD numbering.

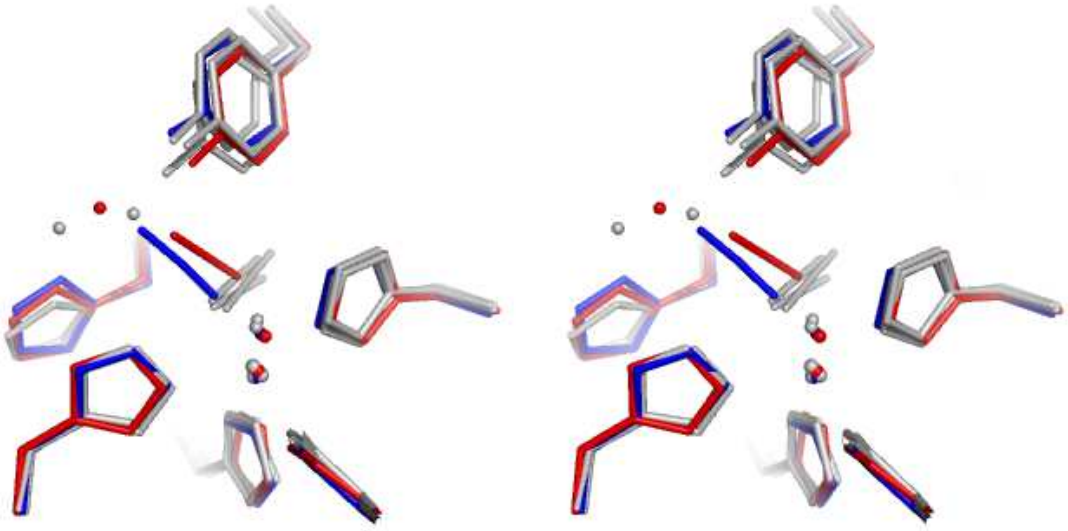

Figure 6-9. Wall-eyed stereo-image of an overlay of the active site of previously solved azido-Fe/MnSODs.

In Figure 6-9, the grey-coloured structures represent the azide binding that is seen in *Ec*-FeSOD-N_3^- (Lah *et al.*, 1995), *Psherm*-FeSOD-N_3^- (Schmidt *et al.*, 1998) and Y174F-*Ec*-MnSOD-N_3^- (PDB code 1ZLZ). The blue representation shows the *Thermus*-MnSOD-N_3^- structure (Lah *et al.*, 1995) and the red representation shows the structure of *Ec*-Fe-MnSOD-N_3^-. The orientation of azide in *Ec*-Fe-MnSOD-N_3^- shows a unique binding pattern that is more reminiscent of *Thermus*-MnSOD-N_3^- than other Fe/MnSOD structures with bound azide.

The unique structure of the active site of *Ec*-Fe-MnSOD-N_3^- with long Fe to azide separation indicates that there is no covalent or inner-shell linkage between the metal centre and azide, rather a weak complex has formed. The interaction appears to be between the N1 of the sixth ligand binding site and the Fe centre.

6.1.9 How the structure of *Ec*-Fe-MnSOD-N_3^- relates to what is known

Most wild type Fe/MnSODs have an E^O between 0.2 and 0.4 V (Barrette *et al.*, 1983). The metal substitution of Fe into *Ec*-MnSOD changes E^O to -0.24 V in *Ec*-Fe-MnSOD, a value that precludes the oxidation of superoxide at physiological pH ranges, and may also prevent the formation of a covalent bond between the Fe^{3+} and N1 of azide ion.

Spectroscopic examinations of Fe-MnSOD (Vance & Miller, 1998a) have shown that the enzyme has EPR signals quantitatively similar to FeSOD. However, binding of azide to Fe-MnSOD gives rise to EPR signals that indicate a mode of binding different to that seen in *Ec*-FeSOD-N_3^- and possibly similar to that seen in the 50% occupancy *Thermus*

thermophilus MnSOD azide complex (Lah *et al.*, 1995). The structure of *Ec*-Fe-MnSOD-N_3^- presented here may confirm this spectroscopic observation.

6.1.10 The solvent-access funnel tyrosine and hydrogen-bonding network

In the structures of MnSOD from *E. coli* (Edwards, Baker *et al.*, 1998) and *Thermus thermophilus* (Ludwig *et al.*, 1991) the tyrosine (Tyr34 in *E. coli* numbering) that lines the substrate-access funnel has fewer interactions with surrounding residues than the equivalent conserved tyrosine in FeSODs from *E. coli* and *P. shermanii*. Thus, Tyr34 is likely to show increased conformational motion. This would allow the tail end of the azide to be stabilised by a hydrogen bond to this tyrosine. In FeSOD structures for which there are azide derivatives, *E. coli* (Lah *et al.*, 1995) and *Propionibacterium shermanii* (Schmidt *et al.*, 1996), the motion of this tyrosine is more restrained by interactions with other residues and as a result the azide is located in a cavity between two helices.

There are minor differences in the surrounding residues and the hydrogen-bonding network that links the active-site ligands to the tyrosine. As focus of attention moves away from the active sites of these SODs, there are also differences in the orientation of aromatic residues that buttress against the substrate-funnel tyrosine. An example of such a residue is Phe124 in *E. coli* MnSOD, which is conserved in bacterial SODs. The part of the protein that surrounds the conserved tyrosine is important in the formation of the substrate-access funnel and in stabilizing the dimer interface, and is more variable than the region surrounding the active site.

6.1.11 Thermochromic shifts

In wild-type *Ec*-MnSOD-N_3^-, there is a pronounced temperature-dependent change in active-site structure moving from ambient to cryogenic temperatures (Whittaker & Whittaker, 1996). Taken on its own it is unclear if the binding pattern seen in *Ec*-Fe-MnSOD-N_3^- is more relevant to the ambient (high entropy) or cryogenic (low entropy) structure of *Ec*-MnSOD-N_3^- or whether it is a unique binding pattern due to the effects of metal substitution.

There has been no detection of thermochromic shifts in FeSODs, so the azide binding pattern seen in *Ec*-FeSOD-N_3^- (Lah *et al.*, 1995) and *Psherm*-FeSOD-N_3^- (Schmidt *et al.*, 1998) represent a true energy minima (low entropy state). As the structure of *Deino*-MnSOD-N_3^- and the structure of Y174F-*Ec*-MnSOD-N_3^- were determined at cryogenic temperatures, these structures most likely represent a low-entropy binding of azide, with

the *Thermus*-MnSOD-N_3^- representing high-entropy binding mode as the X-ray data were collected at room temperature.

I propose there is an energy barrier between a high-entropy MnSOD-N_3^- structure and low-entropy MnSOD-N_3^-, which is associated with a rearrangement of the solvent-access funnel tyrosine coupled to the breaking of the hydrogen bond between atom N3 of the azide ion and the OH of the tyrosine. This allows the two atoms of the tail of the azide molecule to move into a buried cavity. This energy barrier is likely to be a lot less for the substrate, superoxide, as the tyrosine will have to move less distance to allow entry of only the one atom tail into the nearby cavity.

The pattern of azide binding seen in *Ec*-Fe-MnSOD-N_3^- is puzzling as it is most reminiscent of the high-entropy state but was collected at low-entropy conditions. This indicates that metal substitution perturbs the thermodynamic fine tuning of *Ec*-MnSOD preventing azide from reaching the true energy minimum seen in *Deino*-MnSOD-N_3^-. Disrupted thermodynamic fine tuning may be why *Ec*-Fe-MnSOD stabilises a sixth ligand at physiological pH and temperature ranges relative to the correct metal form. The mechanism by which active-site metals alter the thermodynamic fine tuning of the Fe/MnSODs is unknown. A more detailed discussion of the thermodynamic implications of the two states of azide-binding will occur later in this chapter.

6.2 Analysis and implications of the structure of *Deino*-MnSOD

6.2.1 Background

Deinococcus radiodurans is a small red pigmented soil bacterium that can withstand 3000 times more ionising radiation than humans, and is therefore a model organism for radiation tolerance. The major mechanism of radiation resistance is likely to be the enhanced ability of *D. radiodurans* to repair DNA damage, including hundreds of double strand breaks.

However, the enzyme that detoxifies the O_2^- free radical has also been implicated in radiation resistance and recovery (Markillie *et al.*, 1999). MnSOD is up-regulated after a radiation insult (Lipton *et al.*, 2002, Liu *et al.*, 2003) and engineered strains of *D. radiodurans* that lack the MnSOD gene have a 3-90 fold reduced ability to recover from a radiation insult (Markillie *et al.*, 1999).

6.2.2 Other *Deino*-MnSOD structures

The structure of *Deino*-MnSOD presented here is the wild type protein with correct metal (called WT-*Deino*-MnSOD in this section for increased clarity). Within the PDB there are a total of four *Deino*-MnSOD structures all derived from recombinant protein with expression tags, described here as Rec1-*Deino*-MnSOD, Rec2-*Deino*-MnSOD Rec3-*Deino*-MnSOD and Rec-*Deino*-Fe-MnSOD. What is known about these structures is summarised in Table 12. The specific activity has been determined at 3,300 U/mg and 3,560 U/mg for native (with trace iron) and a Mn-reconstituted *Deino*-MnSOD respectively (Juan *et al.*, 1991).

Name	Code	Metal	ResÅ	U/ mg	# of dimers	Reference
WT-*Deino*-MnSOD		Mn	2	3560§	2	(Juan *et al.*, 1991), this study
Rec1-*Deino*-MnSOD	**2CDY**	Mn	2	1250	2	(Dennis *et al.*, 2006)
Rec2-*Deino*-MnSOD	**2CE4**	Mn	2.2	1250	1	(Dennis *et al.*, 2006)
Rec-*Deino*-Fe-MnSOD	**1Y67**	Fe	1.85	?	2	PDB code 1Y67
Rec3-*Deino*-MnSOD	**2AW9**	Mn	2.7	?	1	PDB code 2AW9

Table 12. Summary of known *Deino*-MnSOD structures within the PDB.

§ inferred, as the amino-acid sequence is the same as native sequence, and correctly folded.

The reported specific activity of two of the four recombinant proteins, Rec1-*Deino*-MnSOD and Rec2-*Deino*-MnSOD (Dennis *et al.*, 2006) is well below that from native source (Juan *et al.*, 1991). The addition of an expression tag apparently perturbs the active enzyme. The other two recombinant *Deino*-MnSOD structures do not have an associated publication and their specific activity is unknown. Curiously one of these structures, 1Y67, appears have been solved with Fe at the active site, so is more accurately termed Rec-

Deino-Fe-MnSOD. The regions surrounding the active site of the three recombinant *Deino*-MnSODs are isostructural to WT-*Deino*-MnSOD and the reason for their lower specific activity remains unknown. The structure of WT-*Deino*-MnSOD presented in this study supersedes other structures as it most accurately reflects the native fully active enzyme since it lacks an expression tag, and because there is a derivative structure with a substrate analogue (*Deino*-MnSOD-N_3^-) that gives insight into catalytic mechanism.

6.2.2.1 Structural comparison with Rec-*Deino*-Fe-MnSOD

There are minor differences in the solvent structure between WT-*Deino*-MnSOD and Rec-*Deino*-Fe-MnSOD, shown in Figure 6-10, where a water molecule that is present in all four subunits of the wild-type is only present in one of the four of the metal-substituted forms.

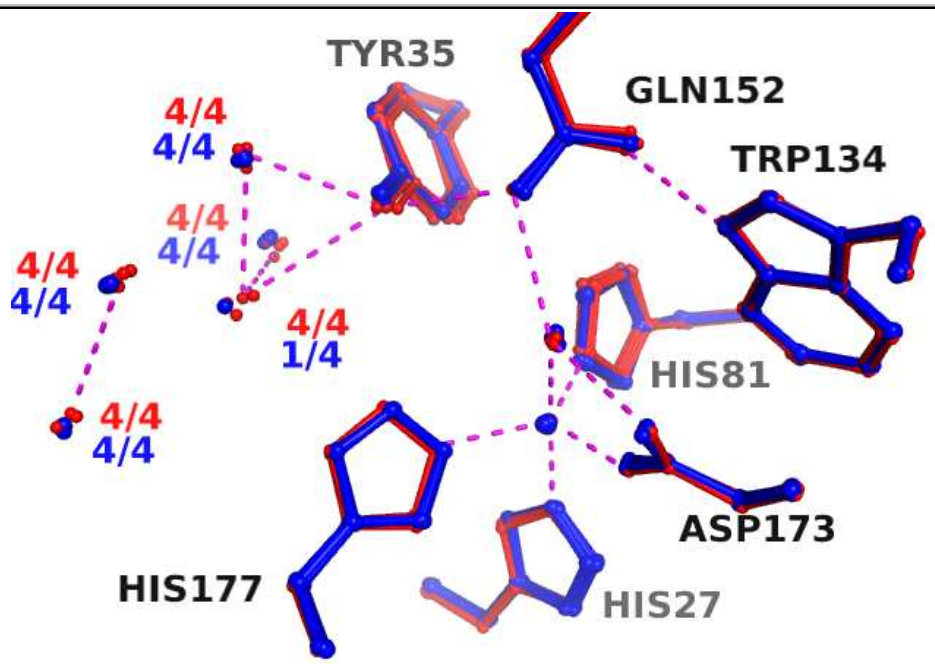

Figure 6-10. Overlay of the active sites and nearby water molecules of WT-*Deino*-MnSOD and recombinant-*Deino*-Fe-MnSOD.

Figure 6-10 shows a ball-and-stick representation of important residues while non-bonded atoms are shown as spheres. All four active sites from the wild type are shown in red and the four active sites from the metal-substituted form are coloured blue. Hydrogen bonds and metal-ligand interactions are shown as dashed magenta lines. There is high structural conservation between WT-*Deino*-MnSOD and recombinant-*Deino*-Fe-MnSOD in the area around the active site. Water molecules are labelled by their presence across all four subunits. Most water molecules are present in four out of four subunits; however, one of the waters from *Deino*-Fe-MnSOD is present in only one out of four subunits.

Differences in water structure due to metal substitution with the "wrong" cation may indicate that the "correct" metal ion and peptide interact to "fine-tune" the local

environment. How differences at the active-site metal are transmitted to the distant solvent molecules remains unknown as there is little side-chain movement; refer to Figure 6-10.

However, until the specific activity of Rec-*Deino*-Fe-MnSOD is determined relative to *Deino*-MnSOD (wild-type and Rec3-*Deino*-MnSOD), detailed comparisons are not merited as any decrease in activity may be attributed to expression tags rather than metal substitution. When MnSOD is purified from *Deinococcus radiodurans* (native-*Deino*-MnSOD) its activity is slightly lower than manganese-reconstituted form (WT-*Deino*-MnSOD) indicating the presence of iron at the active site (of native-*Deino*-MnSOD). Similarly iron reconstitution (to form *Deino*-Fe-MnSOD) had 1.5% the activity of WT-*Deino*-MnSOD (Juan *et al.,* 1991) indicating that metal substitution is deactivating.

6.2.3 Lack of product inhibition

Product inhibition occurs to a degree in all MnSODs, but is more pronounced in some members. In particular, the human *mito*-MnSOD is strongly inhibition prone (Abreu *et al.*, 2008). The other unique characteristic of *Deino*-MnSOD is its near complete lack of product inhibition. The two half-reactions of normal catalysis of an MnSOD are,

$$(\text{SOD-M}^{+}) + O_2^{-} + H^{+} \xrightarrow{k_1} (\text{SOD-M})\text{-}H^{+} + O_2$$

Equation 8

$$(\text{SOD-M})\text{-}H^{+} + O_2^{-} + H^{+} \xrightarrow{k_2} (\text{SOD-M}^{+}) + H_2O_2$$

Equation 9

where k_1 and k_2 are rate constants for Equation 8 and Equation 9 respectively. However, during abnormal catalysis a long-lived by-product may form,

$$(\text{SOD-M})\text{-}H^{+} + O_2^{-} \xrightarrow{k_3} (\text{SOD-M}^{+})\text{-}H^{+}\text{-X}$$

Equation 10

that slowly breaks down by a first-order process,

$$(\text{SOD-M}^{+})\text{-}H^{+}\text{-X} \xrightarrow{k_4} (\text{SOD-M}^{+}) + HO_2^{-}$$

Equation 11

to leave active enzyme, quickly followed by

$$H^+ + HO_2^- \xrightarrow{k_5} H_2O_2$$

Equation 12

where k_3 and k_4 are rate constants for the formation and removal of X (the unknown by-product) in Equation 10 and Equation 11 respectively. The measure of product inhibition is determined by the ratio k_2/k_3. The reported k_2/k_3.values for the *mito*-MnSOD, *Ec*-MnSOD and *Deino*-MnSOD are 1, 5 and 16 respectively from most prone to least prone and this is attributed to differences in kinetic behaviour (Abreu *et al.*, 2008). Similar analysis was performed on Y35F-*Deino*-MnSOD which behaved like *mito*-MnSOD indicating a role of the conserved solvent-access funnel tyrosine in determining susceptibility to product inhibition. Two structure-based hypotheses as to the cause of product inhibition are given below.

6.2.4 Role of the catalytic cavity in by-product inhibition

As catalysis and product inhibition are likely to occur in a buried cavity near the active-site metal, presumably where azide binds in *Deino*-MnSOD-N_3^-. This cavity is bounded from the solvent-access funnel by the conserved solvent-access funnel tyrosine and differences in this cavity may have functional consequences. Comparison of the size and shape of this cavity has been performed between *mito*-MnSOD, *Ec*-MnSOD and *Deino*-MnSOD; refer to Figure 6-11. The size of a protrusion of this cavity appears to be correlated with product inhibition. This cavity is largest in *mito*-MnSOD, the most inhibition prone, and smallest in *Deino*-MnSOD, the least inhibition prone, with *Ec*-MnSOD being intermediate.

This cavity probably has roles in controlling conformational flexibility of the solvent-access funnel tyrosine. In *mito*-MnSOD the solvent-access funnel tyrosine will have the most freedom of movement of the three studied MnSODs and therefore will most readily stabilise incorrect by-products. In a similar fashion in *Deino*-MnSOD this tyrosine is constrained and therefore less likely to be able to form incorrect intermediates. In *Ec*-MnSOD this tyrosine will have intermediate freedom.

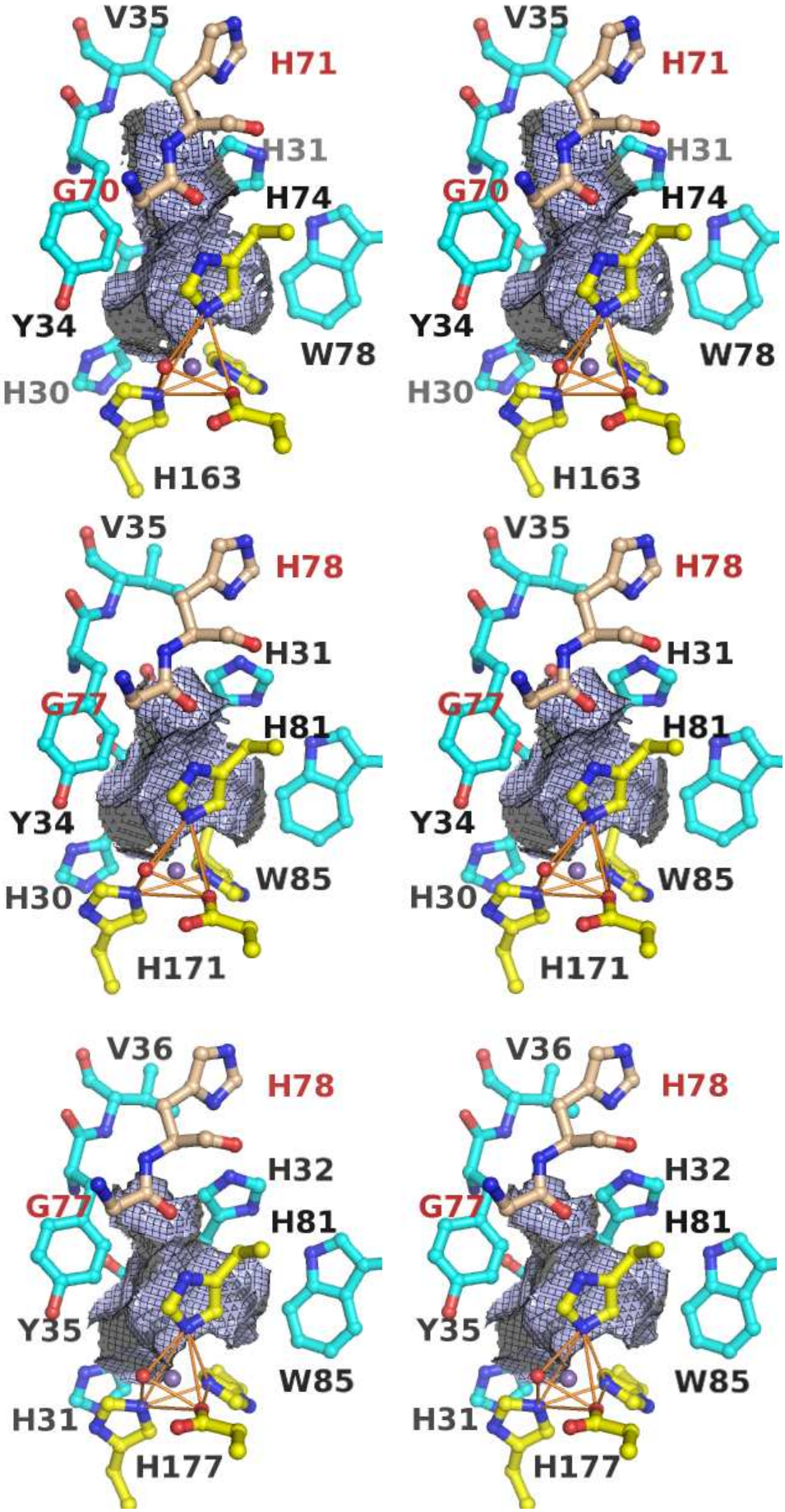

Figure 6-11. Walled-eyed stereo-images showing comparisons of the cavity behind the sixth ligand-binding site between *mito*-MnSOD (top), *Ec*-MnSOD (middle) and *Deino*-MnSOD (bottom).

Figure 6-11. All three stereo-images show the cavity that exists behind the solvent-access funnel tyrosine. The structures shown are derived from *mito*-MnSOD (1LUV), *Ec*-MnSOD (1VEW) and WT-*Deino*-MnSOD for the top, middle and bottom stereo-pairs respectively. Atomic coordinates are shown as ball-and-sticks; the carbon atoms of the four metal-binding protein ligands are yellow. The carbon atoms of the residues that surround the cavity are cyan, while for the residue(s) at the top of the cavity the carbons are coloured beige. The surface of the cavity is coloured light purple in all three stereo-pairs. The cavity in each image was created using VOIDOO (Kleywegt & Jones, 1994).

The cavity is branched with a protrusion into the space behind the conserved tyrosine, Tyr34 in *mito*-MnSOD. This protrusion is variable in size among the three structures. In *mito*-MnSOD, which is most prone to product inhibition, this protrusion is largest. In *Ec*-MnSOD, which suffers minor product inhibition, the cavity protrusion is moderate. And following this trend in WT-*Deino*-MnSOD, which is by-product resistant, this protrusion is smallest.

Comparisons have been made between the environment surrounding the conserved solvent-access tyrosine of *mito*-MnSOD, *Ec*-MnSOD and *Deino*-MnSOD. There are significant differences in the residues that buttress the tyrosine, as shown in Figure 6-12. These differences also likely influence the dynamic freedom of the tyrosine.

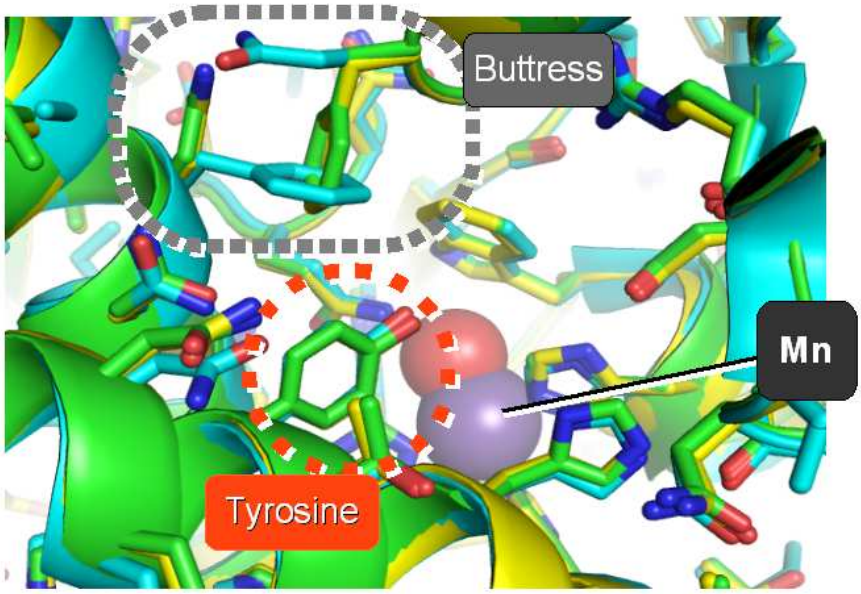

Figure 6-12. Overlay of the region surrounding the solvent-access funnel tyrosine in *mito*-MnSOD, *Ec*-MnSOD and *Deino*-MnSOD.

Figure 6-12 shows a view looking down the solvent-access funnel towards the active site of three overlain structures, *mito*-MnSOD, *Ec*-MnSOD and *Deino*-MnSOD, shown in cyan, green and yellow respectively. The phenylalanine that buttresses the tyrosine is supplied from a different region of the peptide in *mito*-MnSOD than in *Ec*-MnSOD and *Deino*-MnSOD.

6.2.5 Variation in a hydrophobic second-sphere residue across MnSODs that vary in product inhibition susceptibility

As the first shell of metal-ligating ligands is conserved, both in terms of identity and position, among *mito*-MnSOD, *Ec*-MnSOD and *Deino*-MnSOD, variations in the first coordination sphere are unlikely to cause variation in product inhibition. Within the next shell (residues in close contact with the first shell) the majority of residues are also conserved among the three MnSODs, such as the tryptophan residues shown in Figure 6-11. There is one residue of pronounced variability within the second shell of residues: this residue precedes the active-site aspartate (residue *n*-1, where *n* is the position of the active-site aspartate); refer to Figure 6-13. This residue (*n*-1) is an Ile158, Leu166 and Val172 in *mito*-MnSOD, *Ec*-MnSOD and *Deino*-MnSOD respectively. This variable side chain is hydrophobic in all three structures but varies in protrusion length into the αβ-domain. The most protruding residue, isoleucine, occurs in *mito*-MnSOD, the most inhibition-prone, whereas the least protruding residue, valine, occurs in the inhibition-resistant *Deino*-MnSOD. In moderately susceptible *Ec*-MnSOD the equivalent residue is a leucine that is intermediate in protrusion depth between valine and isoleucine. Variations in this residue may translate, via the adjacent aspartate, to variations in active-site ability to stabilise by-products.

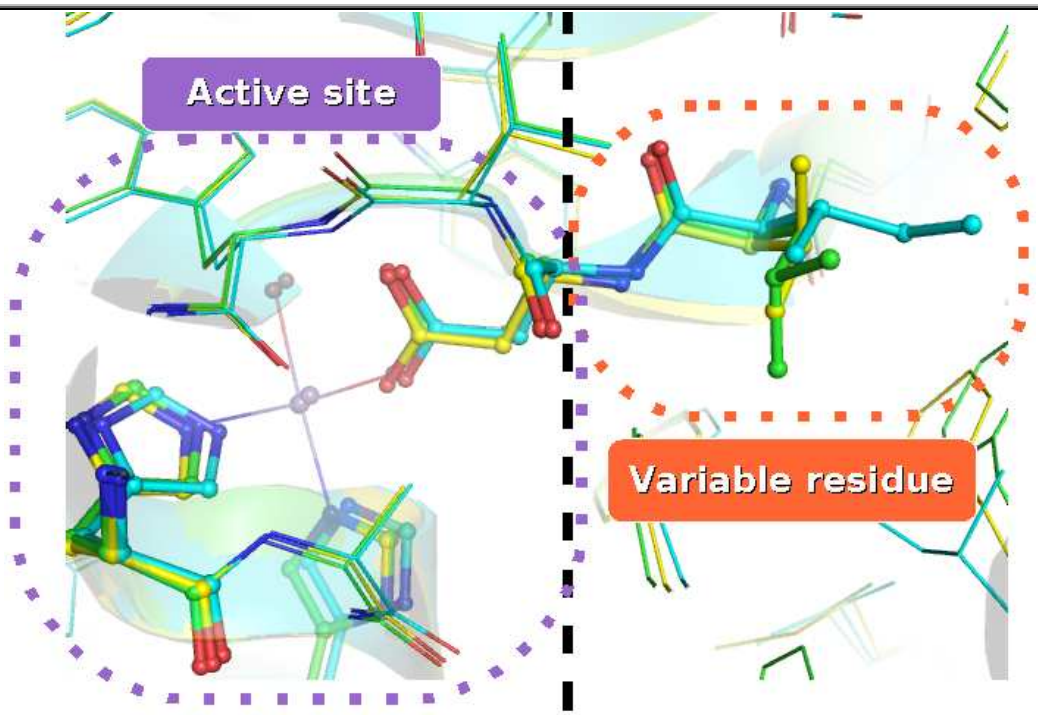

Figure 6-13. A variable hydrophobic residue in the second-sphere of *mito*-MnSOD, *Ec*-MnSOD and *Deino*-MnSOD.

Figure 6-13 shows an overlay of the active site and variable second-shell residue of *mito*-MnSOD, *Ec*-MnSOD and *Deino*-MnSOD. The active site and the variable residue are shown as a ball-and-stick representation; other residues are shown as

thin-sticks. A transparent ribbon cartoon representation of all three structures is shown for all three structures. The carbon atoms are coloured cyan, green and yellow for *mito*-MnSOD, *Ec*-MnSOD and *Deino*-MnSOD respectively. In all three structures oxygen, nitrogen and manganese atoms are coloured red, blue and magenta respectively. The variable residue (*n*-1) is Ile158 in *mito*-MnSOD, Leu166 in *Ec*-MnSOD and a Val172 in *Deino*-MnSOD. The variable residue falls at the end of a piece of β-strand just prior to the start of a loop that contributes several metal-ligating residues Asp (*n*) and His (*n*+4)

In reality variations in by-product stability between *mito*-MnSOD, *Ec*-MnSOD and *Deino*-MnSOD are most likely multifactorial, a combination of the ability to stabilise the by-product (structural) and differences in the rates of by-product formation/elimination (biochemical).

6.2.6 Asymmetrical proton environment at the dimer interface of *Deino*-MnSOD (and other Fe/MnSODs)

There is an interesting hydrogen-bonding network at the axis of pseudo-symmetry, in the dimer interface of *Deino*-MnSOD (and most Fe/MnSODs), shown in Figure 6-14. Where one serine (residue 132 in *Deino*-MnSOD) must be a hydrogen-bond donor, the other serine must be a hydrogen-bond acceptor (residue 132 on the other subunit, *Deino*-MnSOD numbering). As the hydrogen bonding distance (approaching 2.8 Å) is not consistent with a strong symmetrical hydrogen distance, this creates asymmetry at the dimer interface that is propagated to nearby waters to maintain tetrahedral hydrogen-bonding contacts. For each of the monomers, there is a water molecule near the axis of pseudo symmetry in hydrogen-bonding distance to four partner atoms. The first atom (*Deino*-MnSOD_*A*_E176_N) is an obligate hydrogen-bond donor. The other three atoms (*Deino*-MnSOD_*A*_S132_OG, *Deino*-MnSOD_*B*_E176_OE1 and the equivalent water in the other sub-unit) may be either hydrogen-bond donors or acceptors. There is also a potential hydrogen bond between the two serines, (*Deino*-MnSOD_*A*_S132_OG and *Deino*-MnSOD_*B*_S132_OG) across the dimer interface.

The hydrogen bond between the two pseudo-symmetrically related water molecules must then also be inherently asymmetric as each water molecule can be either a hydrogen bond donor or acceptor but not both at the same time. A proposed hydrogen-bonding scheme is shown in Figure 6-15, which satisfies the following criteria: the coordination of each water molecule is roughly tetrahedral, there are no steric clashes between hydrogen atoms, each water molecule donates two hydrogen bonds and each water molecule receives two hydrogen bonds. The hydrogen-bonding pattern of the dimer-interface serines is also asymmetrical. The serines and water molecules illustrated in Figure 6-14 are seen in all

high-resolution Fe/MnSOD structures to date. This serine is very strongly, but not absolutely, conserved across the Fe/MnSOD family as part of the AGSG(W/F)X(W/X) dimer-interface motif where X is a hydrophobic residue. The only notable exception are the Fe/MnSODs from the *Halobacteria* family (Joshi & Dennis, 1993). The strongly conserved WEH motif is also involved, where the histidine is an active-site ligand and the glutamate is involved in active site stablisation, refer to section 2.3.

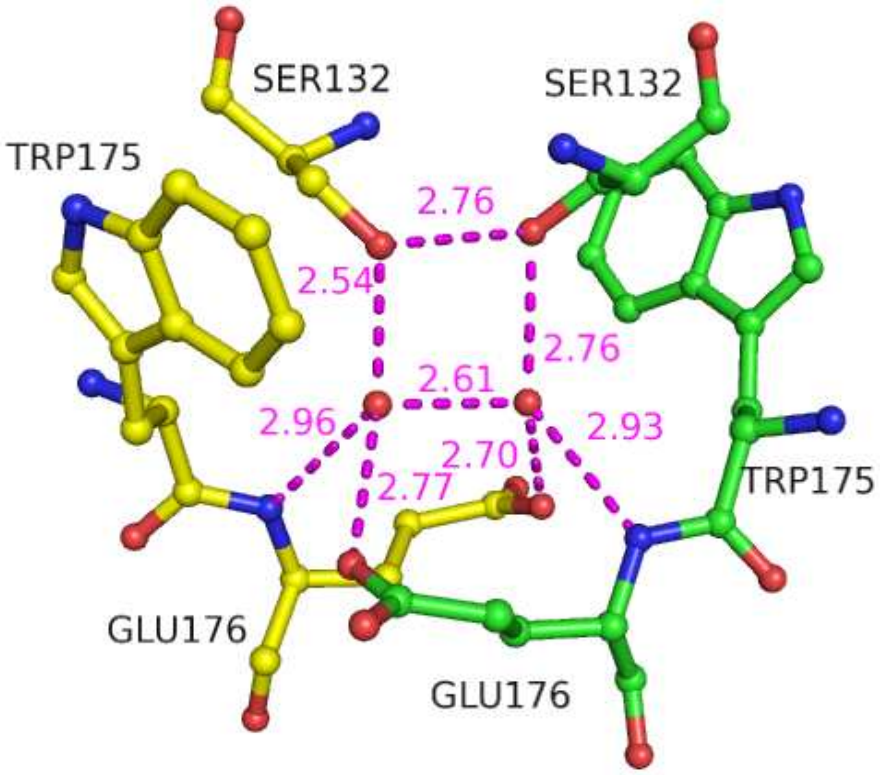

Figure 6-14. The hydrogen-bonding network at the dimer interface of *Deino*-MnSOD.

Figure 6-14. A ball-and-stick representation is shown where oxygen atoms are coloured red and nitrogen atoms are coloured blue. The carbon atoms from one subunit are coloured yellow and carbon atoms from the other subunit are coloured green. Two water molecules are shown as red spheres. Potential hydrogen bonds are shown as magenta dashed lines, labelled with hydrogen bond lengths in Å. There is an axis of pseudo-rotational symmetry that exists passing through the centre of this image such that the non-hydrogen atoms of one subunit can be transposed onto the other by a 180° rotation. The residue Glu176 is an ultra-conserved residue that protrudes across the dimer-interface and forms a hydrogen-bond with active-site residue His177 of the other subunit, as well as with two water molecules of the dimer interface.

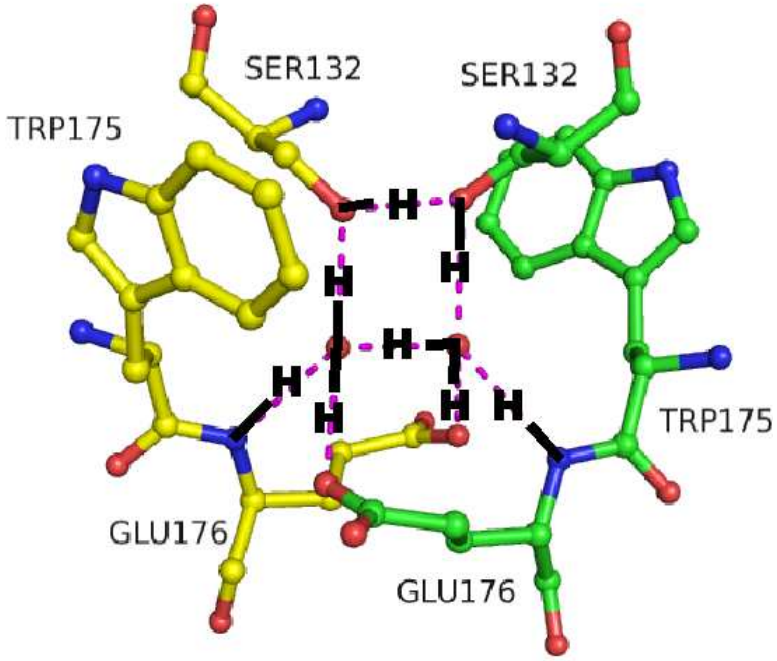

Figure 6-15. Asymmetric pattern of hydrogen atoms at the dimer interface of *Deino*-MnSOD.

Figure 6-15 is a ball-and-stick representation coloured in a similar manner to Figure 6-14. The proposed positions of hydrogen atoms and their bonds are shown in black. The two water molecules maintain a tetrahedral coordination to two hydrogen-bond acceptors and two hydrogen-bond donors. There is also a hydrogen bond between the two Ser132 residues, where the yellow partner is the hydrogen-bond donor and the green partner is the acceptor. The hydrogen-bond donor (yellow) of the Ser132-Ser132 hydrogen bond receives a hydrogen bond from a water molecule, whereas the hydrogen-bond acceptor (green) of the Ser132-Ser132 hydrogen bond donates a hydrogen bond to a water molecule. The hydrogen-bonding pattern is inferred from the position of non-hydrogen atoms. A second possible hydrogen-bonding pattern can be generated by rotating around the axis of pseudo-symmetry.

This asymmetry across the dimer interface of all Fe/MnSODs may explain why the basic crystallographic unit, the asymmetric unit, of all solved crystal structures is a dimer (at least) and not a monomer. If this asymmetry did not exist then it is conceivable that a monomer of an Fe/MnSOD could crystallise in the asymmetric unit of a space group with a two-fold crystallographic rotational axis where the other half of the obligate dimer is generated by crystallographic symmetry operations.

It is unclear if this asymmetry at the dimer interface of Fe/MnSODs is propagated to the rest of the obligate dimer but it might explain why there are a number of asymmetrical structures, usually in solvent structure but sometimes also in active-site structure, such as in *Ec*-Fe-MnSOD and *Ec*-Fe-MnSOD-N_3^- and noticeably in Y174F-*Ec*-MnSOD-N_3^- (1ZLZ) where azide is present in full occupancy, implying Mn^{3+}, in one subunit and not in the other, implying Mn^{2+}.

The asymmetric distribution of protons at the dimer interface shown in Figure 6-15 could easily switch to a second conformation (generated by rotating around the axis of pseudo-symmetry) by the concerted movement of four protons in a clockwise manner. Such a rearrangement of protons could potentially occur rapidly. This is a potential communication pathway between the dimer partners, perhaps acting in synergy with the nearby glutamate bridge, described in section 2.3. So that the redox state of the active site of one monomer may modulate the active site of the other monomer and vice versa. If dimer cross-talk is required for full activity this may explain why there are no Fe/MnSODs that are functional as monomers.

6.3 Analysis and implications of the azide-inhibited MnSOD from *Deinococcus radiodurans*

6.3.1 Background: the use of azide as a substrate mimic

Compared to the wild-type structure in *Deino*-MnSOD-N_3^- there are differences in the water structure of the solvent-access funnel. Most noticeably a solvent molecule has moved into the active site. This rearrangement of the hydrogen-bonding network provides a possible path for protons to move into the active site, although the site of protonation remains unidentified.

The pattern of binding of azide to *Deino*-MnSOD is markedly different to that previously seen in the MnSOD from *Thermus thermophilus* with bound azide (Lah *et al.*, 1995). The most plausible reason for the differences between the two azide-inhibited MnSOD structures is the temperature of X-ray data collection, which was at ambient temperatures for the *Thermus*-MnSOD and at cryo-crystallographic temperature for *Deino*-MnSOD. Low-temperature thermochromism has been previously spectroscopically observed in the MnSOD from *Escherichia coli* (*Ec*-MnSOD) at intermediate temperatures (Tabares *et al.*, 2005, Whittaker & Whittaker, 1996) and similar work has been done in *Thermus*-MnSOD (Whittaker & Whittaker, 1997b).

Combining the information from both azide-inhibited MnSOD proteins gives better insight into the dynamic process of superoxide binding. Azide (and by inference superoxide) in solution is steered to the solvent-access funnel by electrostatic forces. The initial binding of azide to the Mn^{3+} at the active site of the SOD likely follows the pattern seen in *Thermus*-MnSOD. The active-site metal becomes hexa-coordinate as azide binds as the sixth ligand. The “tail” of the azide molecule (atom N3) hydrogen bonds to OH of the conserved tyrosine. This structure is stable enough to be investigated by X-ray crystallography (Lah *et al.*, 1995); on the other hand the inferred superoxide structure is

extremely transitory. Subsequently there is a change in conformation in which the tyrosine tilts away from the active site allowing the "tail" of the azide to move into an orientation seen in our *Deino*-MnSOD structure (and also in the azide derivatives of Y174F-*Ec*-MnSOD, *Ec*-FeSOD and *Psherm*-camb-FeSOD). A solvent molecule also moves into the active site of all four subunits allowing a novel pathway for the entrance of protons for the second half-reaction reaction.

There is also the distinct possibility that there are errors in the structure of *Thermus*-MnSOD-N_3^-. The use of then-valid practices in the treatment of X-ray diffraction data and possible misinterpretation of electron-density maps may have given rise to a false structure. The azide-inhibited structure was solved using the native structure of *Thermus*-MnSOD as a starting model and may suffer from model bias and misinterpretation of electron density maps in partly disordered structure. This was discussed, in detail, in chapter 5.

6.3.2 Implications of the *Deino*-MnSOD-N_3^- structure

The novel pattern of azide binding to a wild-type MnSOD provides insight into the biochemical processes of *Deino*-MnSOD-N_3^-, as the inhibited structure is likely to be similar to transition states of the enzyme during catalytic turnover of superoxide. A model of bound superoxide is shown in Figure 6-16. This is of particular importance as *Deino*-MnSOD is one of the fastest and most efficient enzymes known, as it is not susceptible to product inhibition like other MnSODs.

Along with the difference in azide orientation, the other major change between the native *Deino*-MnSOD and *Deino*-MnSOD-N_3^- structures is the movement of a water molecule into the active site of the inhibited structure, altering the hydrogen-bonding pattern; refer to Figure 6-17. This water is in hydrogen-bonding distance to the N1 of the azide and to three important atoms that may have roles in normal catalytic turnover. The appearance of an equivalent water molecule at this position has been seen but not noted in previously solved azide-inhibited FeSODs (Lah *et al.*, 1995, Schmidt *et al.*, 1998) in about half the azide-affected active sites. The movement of azide into the active-site cavity also displaces Tyr35, which tilts away from the active-site metal. Despite the movement of an azide ion and a water molecule into the active site and the tilting of Tyr35, all other hydrogen bonds within *Deino*-MnSOD are maintained in *Deino*-MnSOD-N_3^- but their distances and angles have changed.

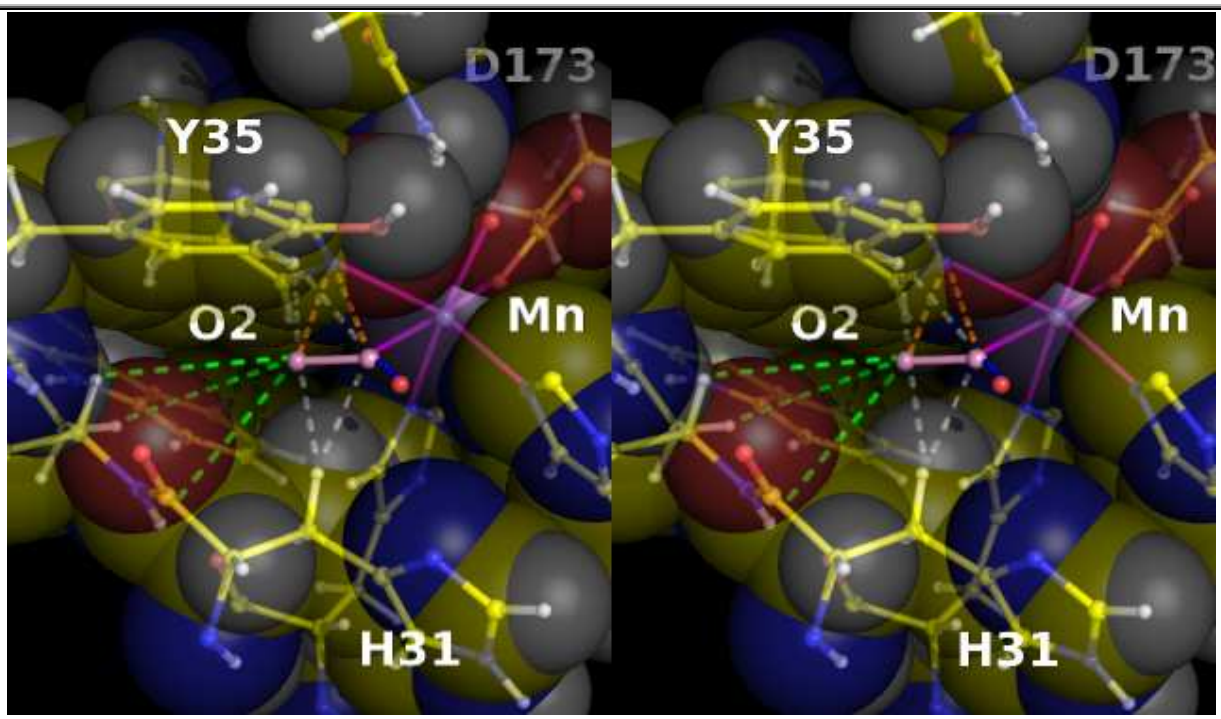

Figure 6-16. Wall-eyed stereo-image of the modelled binding of superoxide, based on the structure of *Deino*-MnSOD-N_3^-.

Figure 6-16 shows a model of the binding superoxide to the active-site manganese. Metal-bound superoxide is shown in pink, binding to the active-site manganese as a sixth ligand. A water molecule is shown hydrogen bonding to the O1 atom of superoxide ion. Other atoms are shown as a ball-and-stick representation with carbon, nitrogen, oxygen, hydrogen and manganese are coloured yellow, blue, red, white and magenta respectively. Van der Waals surfaces are shown as semi-transparent spheres. The starting point for this model was the atomic coordinates of *Deino*-MnSOD-N_3^-. Hydrogen atoms were generated by the program HGEN. The position of the modelled O1 atom of superoxide is the same as the N1 atom of the azide ion in *Deino*-MnSOD-N_3^-. The position of the O2 atom is modelled in the equivalent orientation of the tail of the azide ion in *Deino*-MnSOD-N_3^- but with the O1 to O2 bond distance from small molecule data. The bonds between the metal and metal-ligating atoms are shown as magenta lines. Interactions between superoxide and hydrogen atoms of nearby Tyr35 and His31 are shown as dashed grey lines. Interactions between the superoxide ion and nearby His81 are shown by orange dashed lines. The distances from back of the active-site cavity to the superoxide are shown as green dashed lines.

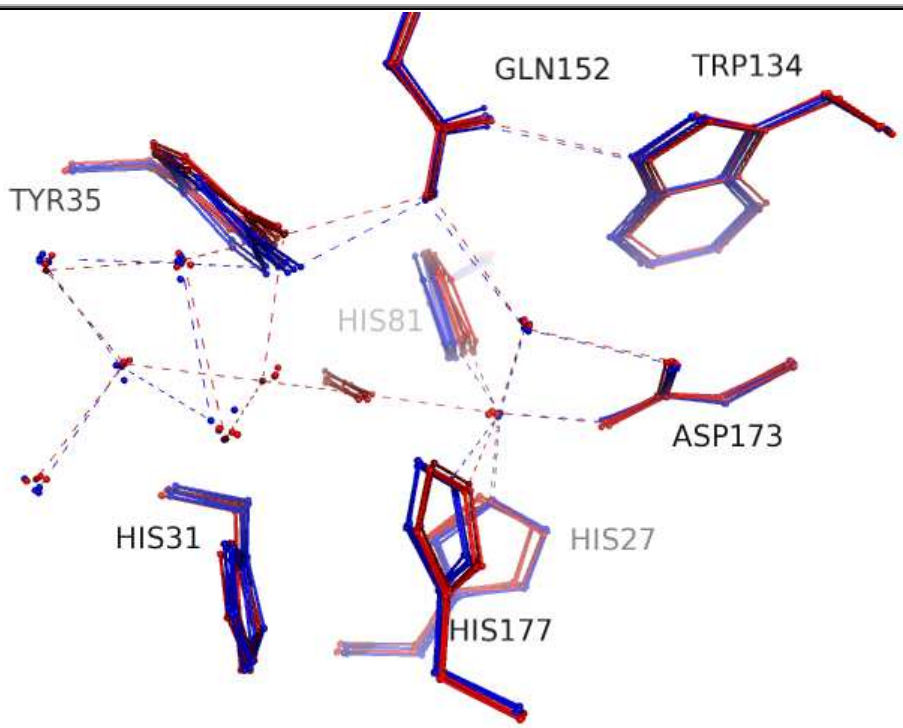

Figure 6-17. Overlay of the pertinent active-site structures of *Deino*-MnSOD and *Deino*-MnSOD-N_3^-, showing the movement of water into the active site upon azide binding.

Figure 6-17. The active sites of all four subunits from *Deino*-MnSOD are coloured blue. The active-site residues of the four subunits of the azide derivative are coloured red. Both structures are shown as ball-and-stick representations where hydrogen bonds and metal-to-ligand interactions are shown as dashed lines. For clarity the hydrogen bonds from only the A subunit of the native and inhibited structures are shown. Azide binding perturbs the native active-site structure in two ways: Firstly, it changes the coordination of the metal ion from five to six and this has effects on the position of metal-ligating residues. Secondly, a water molecule moves into the active site, hydrogen bonding to the azide, the conserved tyrosine and two solvent molecules. These linked events alter the hydrogen bonding network of the active site, as new hydrogen bonds are made and existing hydrogen bonds are modified. The most affected side chain is the solvent-access tyrosine, which tilts away from the active-site manganese. Related images are shown in Figure 4-12 and in Figure 4-19.

The binding of azide changes the coordination of the metal from penta-coordinate to hexa-coordinate. This changes bond angles at the active site most, noticeably the three angles in the equatorial plane; refer to Table 13. Binding of azide leads to an increase in the ∠His177_NE2•Mn•His81_NE2 of ~21° and a decrease in the ∠His177_NE2•Mn•Asp173_OD2 and ∠His81_NE2•Mn•Asp173_OD2 angles of ~11° and ~10° respectively. There are other minor changes in bond angles, along with new bond angles between the N1 of azide and other metal-ligating residues.

Angle	***Deino*-MnSOD**	**SD**	***Deino*-MnSOD-N_3^-**	**SD**	**Difference**
∠His177_NE2•Mn•His81_NE2	132.8	2.2	153.7	4.1	**20.87**
∠His177_NE2•Mn•Asp173_OD2	114.5	0.9	103.8	2.2	**-10.75**
∠His81_NE2•Mn•Asp173_OD2	112.5	2.3	102.3	2.2	**-10.19**
∠His81_NE2•Mn•OH	93.2	3.3	90.6	3.3	-2.64
∠His177_NE2•Mn•OH	90.0	4.7	91.8	3.3	1.73
∠Asp173_OD2•Mn•OH	84.1	1.4	83.3	2.1	-0.74
∠His81_NE2•Mn•His27_NE2	93.4	1.7	91.1	3.8	-2.31
∠His177_NE2•Mn•His27_NE2	90.8	1.6	91.3	1.5	0.52
∠Asp173_OD2•Mn•His27_NE2	86.6	1.2	86.0	0.5	-0.61
∠His27_NE2•Mn•OH	169.6	1.0	168.8	1.8	-0.87
Azide specific angle					
∠AZI_N1•Mn•His27_NE2			95.3	1.0	
∠AZI_N1•Mn•His81_NE2			77.7	3.6	
∠AZI_N1•Mn•His177_NE2			76.1	0.8	
∠AZI_N1•Mn•Asp173_OD2			177.6	1.3	
∠AZI_N1•Mn•OH			94.7	2.3	

Table 13. Effect of azide binding on bond angles at the active-site manganese ion.

Table 13 presents the effect of azide binding to *Deino*-MnSOD on average bond angles. The average bond angles of *Deino*-MnSOD, in second column, are taken from Table 6. The average bond angles from *Deino*-MnSOD-N_3^-**,** in the fourth column, are taken from Table 8. The difference in bond angles between the two structures is given in the sixth column, with major changes in bold.

Bond	***Deino*-MnSOD**	**SD**	***Deino*-MnSOD-N_3^-**	**SD**	**Difference**
Mn→His27_NE2	2.21	0.05	2.24	0.05	0.03
Mn→His81_NE2	2.24	0.02	2.26	0.01	0.01
Mn→His177_NE2	2.29	0.06	2.27	0.03	-0.02
Mn→Asp173_OD2	2.06	0.04	2.15	0.05	**0.09**
Mn→OH	2.22	0.03	2.21	0.05	-0.01
Azide specific bond					
Mn→AZI			2.45	0.09	

Table 14. Effect of azide binding on bond lengths at the active-site Mn.

Table 14 presents the effect of azide binding to *Deino*-MnSOD on bond lengths of metal-binding ligands. The average bond lengths of *Deino*-MnSOD, in second column, are taken from Table 7. The average bond lengths from *Deino*-MnSOD-N_3^-, in the fourth column, are taken from Table 9. The difference in bond lengths between the two structures is given in the sixth column, with the major change in bold.

There are also small changes in the lengths of bonds between metal-ligating residues and the active-site cation; refer to Table 14: The most noticeable change is an increase in the

bond length between the active-site manganese and Asp173_OD2 of 0.09 Å. The average distance between the atom N1 and the active-site Mn is 2.45 Å, this is longer than other azide-inhibited Fe/MnSODs which range from ~1.9 Å to 2.3 Å. This indicates that the active-site cation is Mn^{2+} rather than Mn^{3+} and the metal-azide bond is not a covalent linkage.

The protonation of the side chains and solvent molecules surrounding the active site can not be directly detected by X-ray crystallography at this resolution, but some of their positions can be inferred. The N1 atom of azide is likely to be negatively charged (δ-) and the nearby water molecule is likely a hydrogen bond donor (δ+) to the N1 of the azide. This water molecule is a potential source of protons to the active site.

6.3.3 Relevance of *Deino*-MnSOD-N_3^- to transition state

It is assumed that the *Deino*-MnSOD-N_3^- approximates the structure of a superoxide bound to Mn^{3+} before an electron is passed from the superoxide to the metal centre. The *Deino*-MnSOD-N_3^- derived orientation of superoxide probably represents the true energy minimum, or a low entropy state. The structure may also be analogous to the transition structure before the second half-reaction, prior to electron transfer from Mn^{2+} to the bound superoxide. This structure also is a potential starting point for modelling the species that is responsible for product inhibition.

6.4 Comparative effects of azide binding on hydrogen-bonding networks in Fe/MnSODs

In the much studied parent structure of *Ec*-MnSOD, in addition to the four amino acid side chains bonded to the Mn ion, there is a fifth ligand, a hydroxide. The hydroxide is hydrogen bonded to *Ec*-MnSOD_*A*_Gln146_NE2 at a distance of 2.9 Å. This residue is located on a conserved loop that surrounds the active site. The terminal nitrogen of this glutamine makes a hydrogen bond of 3.0 Å to *Ec*-MnSOD_*A*_Tyr34_OH. The tyrosine is slightly buttressed by *Ec*-MnSOD_*B*_Phe124 from the other subunit which is 3.8 Å away. In the wild-type structure, the binding of azide causes spectral changes to the Mn in the active site (Whittaker & Whittaker, 1991). Unfortunately there is no structure of native *E. coli* MnSOD complexed with azide, but this may be hard to achieve.

In *Thermus*-MnSOD (Stallings *et al.*, 1985, Ludwig *et al.*, 1991), the hydroxide at the active site makes a 3.01 Å hydrogen bond to the *Thermus*-MnSOD_*A*_Gln151_NE2 (equivalent to *Ec*-MnSOD_*A*_Gln146_NE2). This atom in turn makes a 3.11 Å hydrogen bond to *Thermus*-MnSOD_*A*_Tyr36_OH. This tyrosine interacts with *Thermus*-

MnSOD_*B*_Phe128 in a similar fashion to *Ec*-MnSOD. When azide binds to the metallo-protein there are changes in the active site (Lah *et al.*, 1995), modelled as two conformations each with approximately half occupancy. There are rotations in the active-site residues, as well as a substantial rotation around the CA-CB bond in the conserved tyrosine by 10.5° that shifts the *Thermus*-MnSOD_*A*_Tyr36_OH 1.04 Å from its original position. The distance to *Thermus*-MnSOD_*B*_Phe128 is reduced from 4.57 to 3.51 Å. The terminal nitrogen of the azide also makes a 2.60 Å hydrogen bond to the terminal oxygen of the tyrosine. The length of the hydrogen bond between *Thermus*-MnSOD_*A*_Tyr36_OH and *Thermus*-MnSOD_*A*_Gln151_NE2 increases slightly to 3.2 Å and the length of the hydrogen bond between the *Thermus*-MnSOD_*A*_Gln151_NE2 and hydroxide increases to 3.1 Å.

6.4.1 Effects of azide binding on hydrogen-bonding networks of FeSODs

In the *Ec*-FeSOD structure (Stallings *et al.*, 1983, Carlioz *et al.*, 1988), the hydroxide ion forms a longer hydrogen bond to atom *Ec*-FeSOD_*A*_Gln69_NE2 than in MnSOD structures. In this enzyme the glutamine side chain is contributed from a different part of the protein. *Ec*-FeSOD_*A*_Gln69 lays on the second helix of the N-terminal α domain, but its side chain is inserted into the active site such that its terminal NE2 is in a similar location to that of *Ec*-MnSOD_*A*_Gln146_NE2. *Ec*-FeSOD_*A*_Gln69 makes a 3.11 Å hydrogen bond to Tyr35_OH. There is also a difference in the stacking interactions with *Ec*-FeSOD_*B*_Phe118, which is 4.11 Å from *Ec*-FeSOD_*A*_Tyr35, a longer distance than the equivalent distance in *Ec*-MnSOD. This may constrain the ability of the tyrosine to move, as any further separation of the tyrosine and the phenylalanine would create a void that may be extremely unfavourable energetically.

In *Ec*-FeSOD-N_3^- (Lah *et al.*, 1995), there is a slight shift in the conserved His30 and His73 as the tail of the azide molecule sits in a cavity between the histidines. The active site His160 also shifts slightly and the conserved tyrosine rotates about the CA-CB bond by 5.5° so that the terminal oxygen is 0.57 Å from its original position. The distance from the tyrosine to the phenylalanine changes insignificantly from 4.6 Å to 4.5 Å. No change in the orientation of the phenylalanine is seen (Lah *et al.*, 1995).

The structure of the *Psherm*-camb-FeSOD is the most divergent SOD compared to *Ec*-MnSOD to be solved with an azide bound at the active site. It has significant activity with either Fe or Mn at the active site (Meier *et al.*, 1982). This SOD has been solved with both Mn and Fe at the active site, as well as a structure with azide complexed to the Fe. There is little change in the hydrogen-bonding networks when a different metal ion is bound. When

this structure was published it was believed that the fifth coordinated molecule was water; current opinion is that it is an hydroxide ion based on information gathered from spectral studies. In this enzyme the coordinated "water" forms a hydrogen bond to *Psherm*-camb-FeSOD_*A*_His146, which in turn hydrogen bonds to the conserved tyrosine at a distance of 3.1 Å. This tyrosine makes a hydrophobic contact with *Psherm*-camb-FeSOD_*A*_Phe67 from the same subunit. This phenylalanine has a different orientation to *Ec*-MnSOD_*B*_Phe124 and other SODs described here. It sits at roughly a right angle to that seen in other structures and is contributed from a completely different part of the protein. In the structure of *Psherm*-camb-FeSOD-N_3^-, there is little change to the active site, the conserved tyrosine has much the same position, there are slight shifts in His31 and His75 to accommodate the tail of azide (comparative distances are summarised in Figure 6-19 and Figure 6-20).

The most obvious sign of difference between the azide binding seen in *Thermus*-MnSOD-N_3^- and *Ec*-Fe-MnSOD-N_3^- compared to other Fe/MnSODs is a dihedral angle, illustrated in Figure 6-18 and given in Table 15 (along with other relevant bond angles and distances). Two atoms of the dihedral are given by the active-site aspartate and the other two are given by the azide ion.

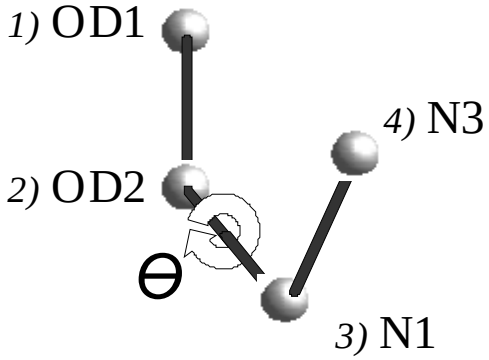

Figure 6-18. Torsion angle that is drastically varied amongst different Fe/MnSODs solved with bound azide.

Figure 6-18. The atoms labelled 1), 2), 3), and 4) form a dihedral angle, θ, around the vector between 2) and 3). Atoms 1) and 2) are OD1 and OD2 from the metal-ligating aspartate of the active site where the OD2 atom is metal bound, and atom 3) is the metal-ligating atom of the azide ion, N1, and N3 is the azide atom furthest from the metal ion. The active-site metal ion is approximately located on the vector between 2) and 3). The values of θ for all azide inhibited Fe/MnSODs are given in Table 15.

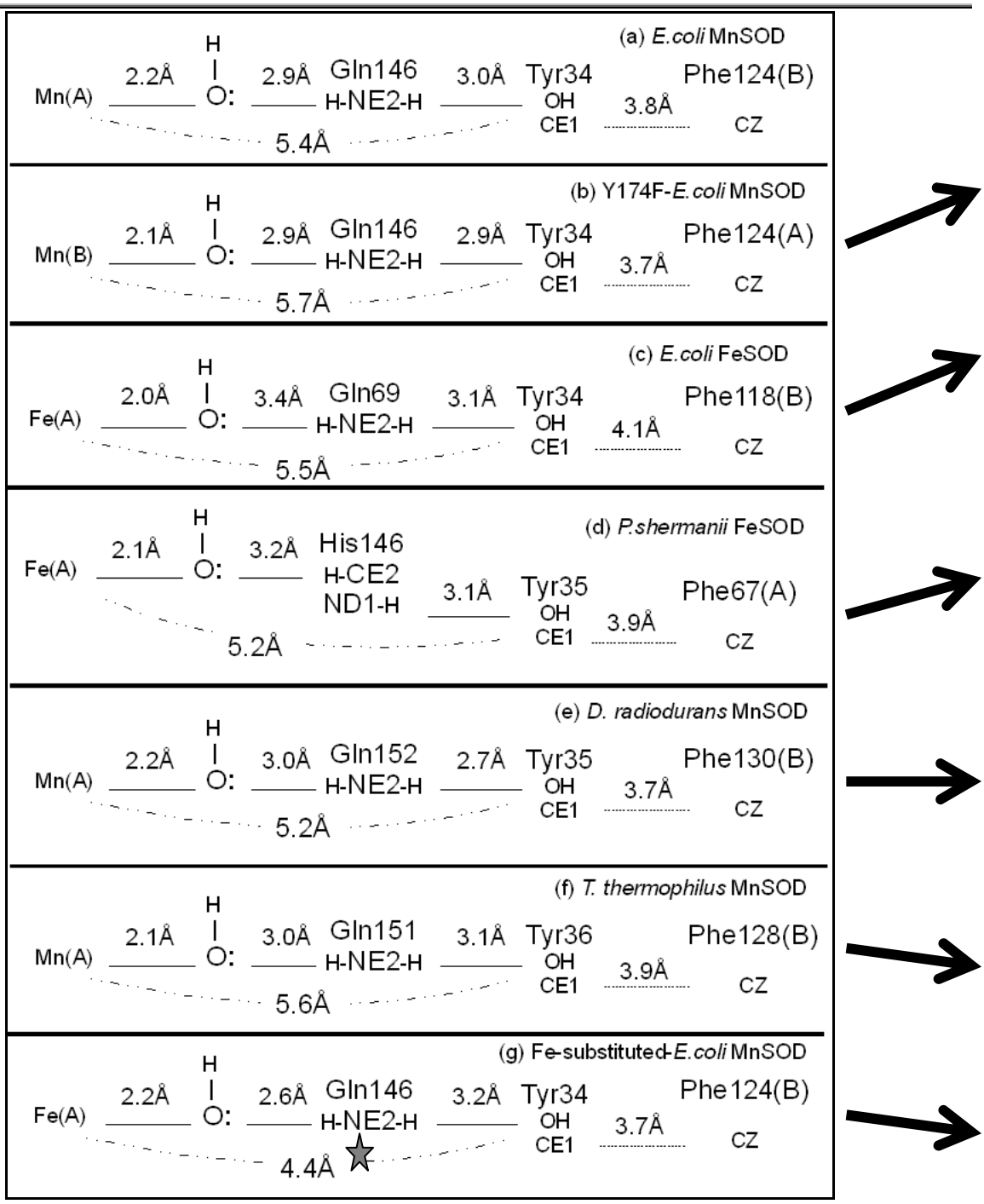

Figure 6-19. System diagram part 1, azide-free Fe/MnSODs.

Figure 6-19 shows residues and bond distances affected by the binding of azide to the active site of several SODs prior to azide binding, as well as similarities and differences among some representative Fe and MnSOD structures. Figure (a) represents the *Ec*-MnSOD and shows the path that links the Mn to Phe124 on the neighbouring subunit via a coordinated hydroxide, a glutamine (or histidine) and solvent-access funnel tyrosine. A similar pathway is shown in (b), (c), (d), (e), (f) and (g) for, Y174F-*Ec*-MnSOD, *Ec*-FeSOD, *Psherm*-FeSOD (refer to section 5.5 for discussion on orientation of His146), *Deino*-MnSOD, *Thermus*-MnSOD, and *Ec*-Fe-MnSOD respectively. There is variation amongst these Fe/MnSODs in terms of bond distances and places where residues are contributed from. The distance between Tyr34_OH and Fe is unusual and shown by a star.

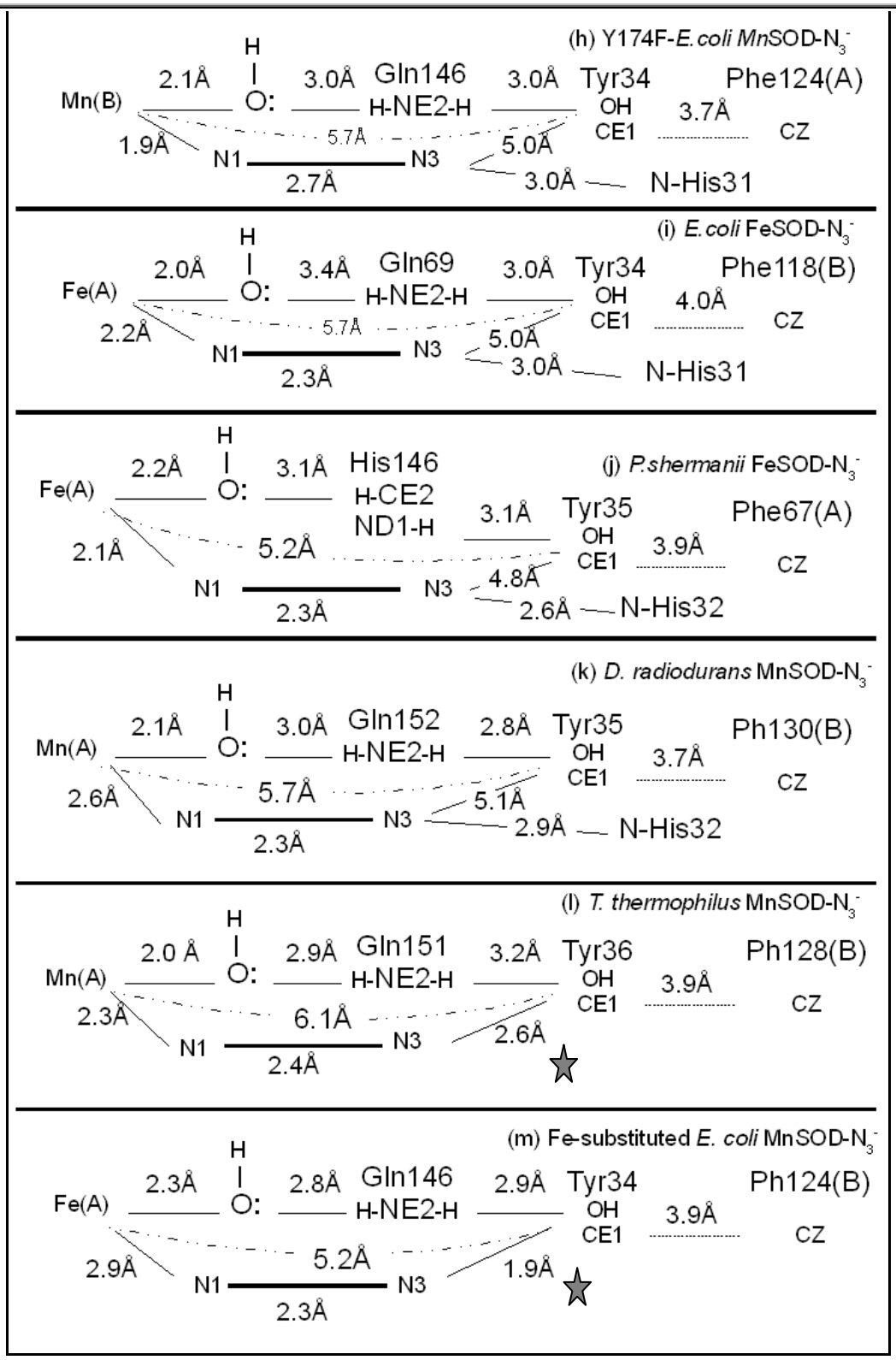

Figure 6-20. System diagram part 2, azide-bound Fe/MnSODs.

Figure 6-20 follows on from the Figure 6-19, which shows residues and bond distances affected by the binding of azide to the active site of several Fe/MnSODs. The three top schemes, (h), (i), (j) and (k), show azide binding in one orientation. The two lower schemes, (l) and (m), show the second azide-binding orientation with the N3 atom being located closer to OH of tyrosine (shown by a star). Note that in (m) Tyr34 represents the average position of a disordered residue so the Tyr34_OH to N3 distance appears to short to be chemically sensible.

	Deino-MnSOD-N_3^-	Y174F-*Ec*-MnSOD-N_3^-	*Ec*-FeSOD-N_3^-	*Psherm*-FeSOD-N_3^-	*Thermus*-MnSOD-N_3^-	*Ec*-Fe-MnSOD-N_3^-
(azide ions)/(monomers in ASU)	**4/4**	1/2	2/2*	2/2	2/2*	1/2
Bond distances Å(SD)						
Mn→His27_NE2	2.24 (0.05)	2.17	2.2 (0.02)	2.18 (0.01)	2.12 (0.08)	2.27
Mn→His81_NE2	2.26 (0.01)	2.10	2.1 (0.00)	2.14 (0.01	2.08 (0.04)	2.19
Mn→His177_NE2	2.27 (0.03)	2.16	2.2 (0.00)	2.16 (0.04)	2.12 (0.01)	2.33
Mn→Asp173_OD2	2.15 (0.05)	2.04	2.0 (0.02)	1.92 (0.02)	2.15 (0.03)	2.20
Mn→OH	2.21 (0.05)	2.14	2.0 (0.03)	2.09 (0.08)	1.97(0.03)	2.34
Mn→AZI	2.45 (0.09)	1.94	2.1 (0.05)	2.26 (0.03)	2.22(0.11)	2.87
Bond Angles						
∠His177_NE2•Mn•His81_NE2	154 (4)	148	161 (3)	151 (1)	148 (4)	156
∠His177_NE2•Mn•Asp173_OD2	104 (2)	106	104 (1)	111 (1)	106 (0)	98
∠His81_NE2•Mn•Asp173_OD2	102 (2)	106	95 (3)	98 (1)	106 (4)	106
∠His81_NE2•Mn•OH	91 (3)	91	85 (6)	90 (0)	91 (2)	90
∠His177_NE2•Mn•OH	92 (3)	90	91 (1)	90 (4)	91 (2)	89
∠Asp173_OD2•Mn•OH	83 (2)	85	91 (5)	90 (1)	87 (0.)	79
∠His81_NE2•Mn•His27_NE2	91 (4)	96	96 (5)	92 (1)	93 (4)	96
∠His177_NE2•Mn•His27_NE2	91 (1)	86	90 (2)	91 (2)	91 (1)	94
∠Asp173_OD2•Mn•His27_NE2	86 (0)	88	88 (7)	85 (1)	83 (0)	83
∠His27_NE2•Mn•OH	169 (2)	171	174 (5)	174 (1)	170 (0)	161
Azide specific angles						
∠AZI_N1•Mn•His27_NE2	95 (1)	96	96 (4)	98 (8)	108 (3)	93
∠AZI_N1•Mn•His81_NE2	78 (4)	75	86 (0)	78 (1)	73 (1)	105
∠AZI_N1•Mn•His177_NE2	76 (1)	74	76 (2)	73 (0)	75 (4)	93
∠AZI_N1•Mn•Asp173_OD2	178 (1)	176	176 (1)	174 (2)	**169** (3)	**169**
∠AZI_N1•Mn•OH	95 (2)	92	90 (1)	87 (7)	82 (3)	105
Torsion angle						
Θ (refer to Figure 6-18)	133.2 (2.8)	131	130 (5)	144 (3)	**-31** (2)	**-32**

Table 15. Bond distances, bond angles and selected torsion angles of metal-ligating atoms in azide-inhibited Fe/MnSODs.

Table 15. This table shows selected bond distances, bond angles and torsion angles for six known azide-inhibited Fe/MnSODs. The numbering scheme in the first column is derived from *Deino*-MnSOD-N_3^-. There are four sections of data given for each of the Fe/MnSODs. The first row of data gives the fraction of active-sites that have azide bound (* indicate two active-site conformations). The next six rows of data give bond distances from the active-site metal in Å with estimated standard deviation where there are multiple measurements. The next fifteen rows of data are bond angles around the metal centre. The final row gives a torsion angle, as shown in Figure 6-18. This torsion angle is different in *Thermus*-MnSOD-N_3^- and *Ec*-Fe-MnSOD-N_3^-, by approximately 160°, compared to other azide-inhibited Fe/MnSODs.

6.4.2 The problem of evolving two azide-binding patterns from a unique common ancestor

As discussed in the introduction, the active sites of the MnSODs and FeSODs have high structural homology that is most likely the result of divergent evolution from a common ancestor. The common ancestor to FeSODs, MnSODs and camb-Fe/MnSODs likely had one preferred superoxide binding mode during catalysis. Thus, the likelihood of there being two divergent azide-binding patterns, and by inference superoxide binding motifs, within a protein family seems less appealing than a common mode of inhibitor binding and by inference superoxide binding.

The differences seen between *Deino*-MnSOD-N_3^- and *Thermus*-MnSOD-N_3^- can be interpreted in several ways, and give rise to several hypotheses: the structure of *Deino*-MnSOD-N_3^- is wrong; the structure of *Thermus*-MnSOD-N_3^- is wrong; and finally that both the structures are correct and the difference between the structures is real. Potential sources of error in the structural solution of *Thermus*-MnSOD-N_3^- were discussed in detail in chapter 5.

6.4.3 Potential sources of error in *Deino*-MnSOD-N_3^-

It is possible that there are errors in the structure of *Deino*-MnSOD-N_3^-; errors in structures solved by X-ray crystallography are inevitable (Kleywegt *et al.*, 2003) due to misinterpretation of ambiguous electron-density maps. The most likely parts of the structure to be misinterpreted are the side chains close to solvent and water molecules inserted into false peaks. However, as the electron-density maps of the active site were unambiguous after molecular replacement and throughout refinement the likelihood of there being major differences at the site are minor.

Efforts have been made to minimise these errors but mistakes in building structures may never be completely eliminated. Also techniques and technologies will probably

improve still further the quality of protein structures. Error identification has been attempted by correct treatment of X-ray data and by use of validation tools such as PROCHECK (Laskowski *et al.*, 1993), SFCHECK (Vaguine *et al.*, 1999) and the internal validation tools of COOT (Emsley & Cowtan, 2004).

6.4.4 Possible implications if the structure of *Thermus*-MnSOD-N_3^- is incorrect

The structure of *Thermus*-MnSOD-N_3^- is an important structure that has been cited by numerous subsequent papers. At present nearly 200 research articles cite the work of Lah and co-workers, a smaller subset of these papers are primarily interested in the *Thermus*-MnSOD-N_3^- structure rather than the three *Ec*-FeSOD structures that were co-presented with it. Many research groups, from many disciplines and backgrounds, are interested in the MnSOD field and have based research outcomes, theories and conjecture on the structure of *Thermus*-MnSOD-N_3^-.

This body of work includes explanations of MnSOD enzymatic activity (Carrasco *et al.*, 2007, Tabares *et al.*, 2006), spectroscopic investigations (Jackson *et al.*, 2004, Tabares *et al.*, 2006), theoretical models (Rulíšek *et al.*, 2006, Rulíšek & Ryde, 2006) and various review articles. Much of this work may need to be re-evaluated or extended to include knowledge derived from the novel *Deino*-MnSOD-N_3^- structure.

6.4.5 Possible implications if the structure of *Deino*-MnSOD-N_3^- and *Thermus*-MnSOD-N_3^- are both correct

If both the structures of *Deino*-MnSOD-N_3^- and *Thermus*-MnSOD-N_3^- are true, then the difference in azide orientation between the two structures is a real phenomenon that must be explained and integrated into theories of MnSOD structure and function. There are a number of important differences in the experimental setup between the *Deino*-MnSOD-N_3^- and *Thermus*-MnSOD-N_3^-, which may be the reason for the difference in azide conformation. Between the two structures there are major differences in the amino acid sequences, pH of the crystals and, importantly, the temperature of data collection. Each of these differences will be discussed independently with reference to what has previously been seen in the literature. However, this thesis proposes that the temperature of data collection is the principal determinant of azide orientation.

6.4.6 Differences in amino-acid sequence

Within the Fe/MnSOD family there is much sequence divergence but the overall protein fold, which is functionally active as a dimer, is conserved. The residues of the active site, which bind metal ion, are also highly conserved. It is possible that minor

differences in amino-acid sequence may affect the active site, and in turn affect the way that azide interacts with the active-site manganese or iron.

As explained in the introduction, within the Fe/MnSOD protein family there are many slight variations in the function, structure and activity. Within bacterial Fe/MnSODs there are differences in catalytic rates, metal specificity, pH dependence, hydrogen peroxide resistance, and the requirement of some SODs to further associate into tetramers for activity. At present there is no cohesive theory, only speculation, to explain how and why differences in the primary amino-acid sequences manifest as differences in SOD function. Indeed, at present in structural biology, there is no way to reliably predict protein structure and function from primary amino acid sequence.

Both *Thermus thermophilus* and *Deinococcus radiodurans* are extremophiles, but they have evolved into divergent environments, and can survive in environmental extremes that would kill most other organisms. The bacterium *Thermus thermophilus,* which was originally isolated from a hot spring in Japan (Oshima & Imahori, 1971), is a well studied thermophile that grows optimally above 65 °C. *Deinococcus radiodurans* is a soil bacterium that is resistant to high doses of radiation, freezing and complete desiccation. It was originally isolated from a can of irradiated meat (Anderson *et al.*, 1956). Over time these bacteria have undergone different selective pressures based on their divergent environments. Random mutations in the MnSOD gene that "optimise" the enzyme for a specific environment will accumulate over time causing divergence from a common ancestor. For instance *Thermus*-MnSOD folds correctly, acquires the correct metal co-factor and exhibits enzymatic activity at temperature ranges more than 30 degrees higher than the temperatures at which *Deino*-MnSOD is usually grown. So *Deino*-MnSOD and *Thermus*-MnSOD may be fundamentally different and this is reflected in the different azide orientations.

When the peptide sequences of *Deino*-MnSOD and *Thermus*-MnSOD are aligned (refer to Figure 6-21), there is high sequence homology and identity. This is also evident when atomic coordinates of the structures are aligned. There is high structural homology between the two enzymes, particularly around the active site. Further away from the active site there is more sequence divergence, with the greatest divergence occurring in the external loop regions.

```
therm       PYPFKLPDLGYPYEALEPHIDAKTMEIHHQKHHGAYVTNLNAALEKYPYLHGVEVEVLLR   60
deino        MAYTLPQLPYAYDALEPHIDARTMEIHHTKHHQTYVDNANKALEGTEFAD-LPVEQLIQ   58
              .:.**:* *.*:********:****** ** :** * * ***   : . : ** *::

therm      HLAALPQDIQTAVRNNGGGHLNHSLFWRLLTPG----GAKEPVGELKKAIDEQFGGFQAL   116
deino      QLDRVPADKKGALRNNAGGHANHSMFWQIMGQGQGQNGANQPSGELLDAINSAFGSFDAF   118
           :*  :* * : *:***.*** ***:**:::  *    **::* *** .**:. **.*:*:

therm      KEKLTQAAMGRFGSGWAWLVKDPFGKLHVLSTPNQDNPVM----EGFT--PIVGIDVWEH   170
deino      KQKFEDAAKTRFGSGWAWLVVKD-GKLDVVSTANQDNPLMGEAIAGVSGTPILGVDVWEH   177
           *:*: :**  *********  .  ***.*:**.*****:*     *.:  **:*:***** *

therm      AYYLKYQNRRADYLQAIWNVLNWDVAEEFFKKA- 203
deino      AYYLNYQNRRPDYLAAFWNVVNWDEVSKRYAAAK 211
           ****:*****.*** *:***:*** ..: :  *
```

Figure 6-21. Alignment of the amino-acid sequences of *Thermus*-MnSOD and *Deino*-MnSOD, performed by ClustalW (version 2.0.5).

Figure 6-21. This alignment of the primary amino acid sequences was performed using ClustalW (Larkin *et al.*, 2007). There is a high degree of identity and similarity between the two sequences. There are some regions of divergence, most notably differences in loops distant from the active site. Important residues involved in metal ligation and dimer formation are shown bold in a larger font.

6.4.7 pH differences between *Deino*-MnSOD-N_3^- and *Thermus*-MnSOD-N_3^-

There is a pronounced relationship between MnSOD activity and pH. This pH-dependence is due to changes in side-chain protonation around the active site, availability of protons for catalysis and the co-ordination of an hydroxide as the sixth ligand to the active-site manganese. At higher pH ranges, the activity of MnSODs generally decreases. The pH dependence has been investigated spectroscopically, biochemically and structurally.

The structure of *Deino*-MnSOD-N_3^- was solved at pH 6.5 while *Thermus*-MnSOD-N_3^- was solved at pH 7.0, which are close to one another and close to physiological values. However, between the two structures there may be pH-dependent changes in active-site structure. This pH range is close to the p*K*a of histidine side-chains, although this p*K*a may shift due to local environment. Unfortunately X-ray crystallography, at these resolution ranges, is unable to accurately determine the position and occupancy of hydrogen atoms, so side-chain protonation and hydrogen-bonding networks are not directly measured, but must be inferred.

6.4.8 Temperature of data collection

The main experimental difference between *Deino*-MnSOD-N_3^- and *Thermus*-MnSOD-N_3^- is the temperature of data collection at cryo-crystallographic temperatures and ambient conditions respectively. Temperature-dependent changes in the spectra of MnSOD have been observed in the presence of azide. These changes are well characterised in *Ec*-MnSOD-N_3^- (Whittaker & Whittaker, 1996) and *Thermus*-MnSOD-N_3^- (Whittaker & Whittaker, 1997b). Importantly there is no documented temperature-dependent shift in the FeSODs. This leads to the hypothesis that there is a high temperature, or high entropy, structure for *Ec*-MnSOD-N_3^- and *Thermus*-MnSOD-N_3^- that is different from the structure at cryogenic temperatures, or a low entropy state.

6.5 Attempted ambient temperature X-ray diffraction data for *Deino*-MnSOD-N_3^-

In an effort to test the temperature-dependence hypothesis, numerous attempts were made to collect high temperature structures of *Deino*-MnSOD-N_3^-. This proved largely unsuccessful as crystals could not endure extended periods in the beam due to radiation damage that manifested as a large drop in the intensities of reflections.

Poor quality low-resolution data were collected and a structure solved; data are not shown. However, the quality of the electron-density maps was poor, the position of metal-binding ligands and conserved water molecules could not be determined, so the structure refinement was abandoned. There was no way to determine definitively the position and occupancy of azide within the protein. Perhaps the most telling sign that the crystals were failing was that the colour of the mother liquor that surrounded *Deino*-MnSOD-N_3^- crystals changed from clear to magenta-tinged during data collection. This indicates that there is a change in the coordination of the Mn at the active site over the period of data collection. This was seen as an indication that azide was leaving the system, possibly as hydrazoic acid which is volatile and may leak out of the capillaries.

6.6 Mutants of *Ec*-MnSOD: preliminary crystallographic results

Four point mutants of *Ec*-MnSOD have been generated to investigate several aspects of MnSOD function. The mutation approach used here was to make conservative mutations of residues that are not absolutely conserved across all Fe/MnSODs. These mutations are unlikely to disrupt protein folding, slightly perturb protein structure and hence maintain an active enzyme. A conservative mutation is more likely to produce variation in metal specificity, catalytic activity, and inhibitor specificity without

completely abolishing catalytic behaviour. All the structures are isomorphous to the native structure (Edwards, Baker *et al.*, 1998).

6.6.1 S82T-*Ec*-MnSOD: preliminary results

The residue Ser82 is the residue that follows the metal-ligating residue His81 on a long α helix. While His81 is buried in the active site, Ser82 is a solvent-exposed residue. In the structure of S82T-*Ec*-MnSOD there is slight movement of His81. However, the most noticeable change is visible movement of water molecules close to the site of mutation. There are also changes in the solvent structure around the active site, including water molecules close to the solvent-access funnel tyrosine.

6.6.2 L83M-*Ec*-MnSOD: preliminary results

This residue, Leu83, is a potential candidate for determining variation in product inhibition as the equivalent residue is a methionine in *Deino*-MnSOD and an isoleucine in *mito*-MnSOD. In the L83M-*Ec*-MnSOD structure there is minor variation in the positions of water molecules and residues surrounding the site of mutation. Minor variation is seen at the active site.

6.6.3 L133V-*Ec*-MnSOD: preliminary results

The majority of point mutation studies have focussed on residues close to the active site and dimer interface while other structurally conserved regions have been neglected. The residue, Leu133, is variable among *mito*-MnSOD, *Ec*-MnSOD and *Deino*-MnSOD, so it is a potential determinant of variation in product inhibition. Also this residue is in a distant region from the active site where there is conserved secondary structure but the primary amino-acid identity is not absolutely maintained.

In the mutant structure, L133V-*Ec*-MnSOD, there is little change at the active site but surrounding the site of mutation there are small movements in several loops, including loops that are equivalent to those involved in tetramer formation in *mito*-MnSOD.

6.6.4 M164L/L166V-*Ec*-MnSOD: preliminary results

As shown in Figure 6-13 this residue, Leu166, is extremely close to the active site and variable among *mito*-MnSOD, *Ec*-MnSOD and *Deino*-MnSOD, so it is a potential candidate for determining vulnerability to product inhibition. In the mutant M164L/L166V-*Ec*-MnSOD it appears that there have been minor effects at the active site. There are detectable changes in the position of metal-ligating residues. Most noticeable is movement of the fifth metal-binding ligand, a solvent-derived molecule.

6.7 Discussion

6.7.1 Entropic considerations of azide binding

The second law of thermodynamics, which states that the entropy of the universe is ever increasing, gives rise to a derivation of the Gibbs energy function (at a constant temperature and pressure),

$$\Delta G = \Delta H - T\Delta S$$

Equation 13

where G is the Gibbs free energy, H is enthalpy, T is temperature in K and S is entropy. For a reaction or transition to occur spontaneously ΔG must be negative. This gives rise to four conditions;

1. When both ΔH and ΔS are positive, spontaneous reactions/transitions will occur above a set temperature point, when $T > \frac{\Delta H}{\Delta S}$.

2. When both ΔH and ΔS are negative, spontaneous reactions/transitions will occur below a set temperature point, when $T < \frac{\Delta H}{\Delta S}$.

3. When ΔH is positive and ΔS is negative, spontaneous reactions/transitions will never occur.

4. When ΔH is negative and ΔS is positive, the reaction will occur spontaneously at any temperature.

The apparent temperature dependence of azide binding seen between *Deino*-MnSOD-N_3^- and *Thermus*-MnSOD-N_3^- (Lah *et al.*, 1995) is also evident in the temperature-linked changes in the spectrum of the active site of *Ec*-MnSOD-N_3^- and *Thermus*-MnSOD-N_3^- with midpoints at 220K and 305K respectively (Whittaker & Whittaker, 1997b). These experimental observations seem to satisfy the second condition listed above. In solution, the unbound azide ion has a high entropic value, as it has a high number of degrees of freedom. Initial binding of azide to the metallo-protein will reduce the entropy of the azide ion. The enthalpy of the system will largely be determined by the ordered properties of the protein, solvent and metal, and is mostly (but not completely) temperature independent. At lower temperatures the inherent chaos of the

system decreases and the entropic component decreases and azide is able to bind in final orientation with lowest entropy.

The fact that there has been no detected temperature transition in FeSODs in the presence of the competitive inhibitor azide can satisfy conditions 1 and 2 above. In FeSODs the temperature transition, where ΔG is 0, occurs outside the measured temperature range, so azide binds to FeSODs at effectively all temperature ranges. This implies that the FeSODs are thermodynamically different from MnSODs; this is shown in Figure 6-22.

If this line of reasoning is followed the question arises; what is the basis for the different thermodynamic properties in FeSODs and MnSODs: is it the protein or the metal component? The structure of *Ec*-Fe-MnSOD-N_3^-, which has the "wrong" metal bound, shows an azide binding pattern reminiscent of the high-entropy state ascribed to *Thermus*-MnSOD-N_3^- even though data were collected at cryogenic temperatures. This indicates azide binding is primarily determined by the protein component not the metal ion, and furthermore in *Ec*-Fe-MnSOD-N_3^- the point of temperature transition has been lowered to a point below 110 K or abolished, so in this structure azide is trapped in high entropy state. The mechanism by which the variation in the amino-acid sequence between FeSODs and MnSODs results in different thermodynamic fine tuning remains unknown, but proposed future investigations are outlined in section 9.2.

Figure 6-22 shows reaction coordinate proposed to occur in Fe/MnSODs, based on information from both structural and spectral studies. In each of the six images (a) represents high-entropy azide binding, (c) represents low entropy binding (analogous to the catalytic step) and (b) represents an energy barrier between high entropy and low entropy. For MnSODs at high temperatures (1) azide ion will exist in a high-entropy state; at low temperatures (2) the azide ion will populate the low-entropy state. In FeSODs, which lack this temperature-dependent transition, azide will exist in low-entropy state at both high temperatures (3) and low temperatures (4). In Fe-MnSOD azide binds in the high-entropy state in both high (5) and low (6) temperatures.

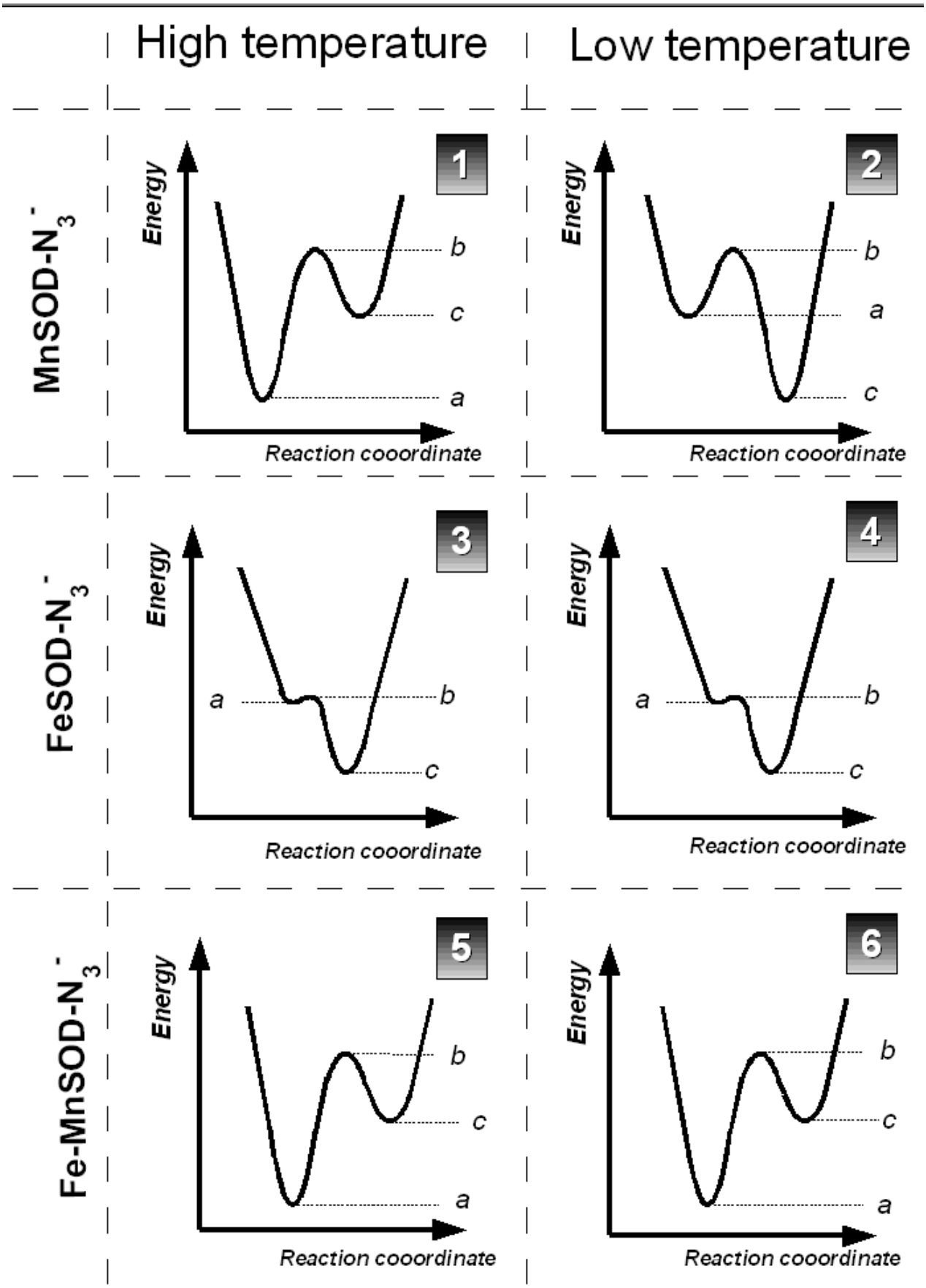

Figure 6-22. Reaction-coordinate diagrams of MnSOD, FeSOD, and Fe-MnSOD in the presence of azide at high and low temperatures.

6.7.2 Other variation between FeSODs and MnSODs interpreted as thermodynamic variation

6.7.2.1 Reduction potentials

A difference in thermodynamic fine-tuning may also explain how MnSODs and FeSODs are able to acquire the correct metals from an environment where both Mn and Fe are present, such as the cytoplasm. The other major observed difference between FeSODs and MnSODs is their differing effect on redox potentials of the Fe and Mn cations (Vance & Miller, 1998b). This phenomenon may also be a manifestation of differences in the thermodynamic fine-tuning as redox chemistry is also subject to the second law of thermodynamics,

$$\Delta G = -nF\Delta E$$

Equation 14

where n is the number of electrons transferred, F is the Faraday constant and E is the electrochemical potential. Combining Equation 13 and Equation 14 gives

$$\Delta H - T\Delta S = -nF\Delta E$$

Equation 15

which shows that redox chemistry is temperature dependent, and subject to entropic and enthalpic contributions.

6.7.2.2 Differences in solvent structure between azide-inhibited FeSODs and MnSODs

If the solvent structure of *Deino*-MnSOD-N_3^- is compared to the solvent structures of *Ec*-FeSOD-N_3^- (Lah *et al.*, 1995) and *Psherm*-FeSOD-N_3^- (Schmidt *et al.*, 1998), there are differences in the presence of the water molecule in hydrogen bonding distance to the N1 atom of the azide. In *Deino*-MnSOD-N_3^- this water is present in all subunits, in both the *Ec*-FeSOD-N_3^- and *Psherm*-FeSOD-N_3^- this water molecule is present in half the active sites. This implies that the active-site environment and vicinity are different between FeSODs and MnSODs.

6.7.2.3 The altered pK of *Ec*-Fe-MnSOD

The binding of hydroxide to the active site of Fe/MnSODs is a thermodynamic process, which usually only occurs at high concentrations of hydroxide (high pH) in FeSODs and MnSODs and not at low concentrations of hydroxide (moderate pH to low pH). Changing the concentration of reactants affects the entropy of a system. Upon metal substitution, the p*K* values of *Ec*-Fe-MnSOD (refer to Figure 6-1) are perturbed relative

to both FeSODs (refer to Figure 2-6) and MnSODs (refer to Figure 2-7). This manifests as a coordination of an hydroxide ion as a sixth ligand at the active site at physiological pH ranges (low concentration of hydroxide) as seen in *Ec*-Fe-MnSOD (Edwards, Whittaker *et al.*, 1998). This may be seen as evidence that metal substitution perturbs thermodynamic fine tuning as the concentration of hydroxide required for binding at the active site is reduced. However, as residue protonation is pH dependent, metal substitution may also affect patterns of protonation.

6.7.3 Second inhibition site

Early in the history of biochemical characterisation of Fe/MnSODs it was speculated that there was a primary inhibitor binding site, where the small molecule inhibitors with only 1- 3 atoms, such as azide and fluoride (as well as substrate superoxide), bound with high affinity. A second inhibitor binding site was proposed for larger inhibitors such as SCN^- and ClO_4^- that bind with low affinity and are affected by a protonated group (Bull & Fee, 1985). With the advent of detailed structures this cavity is likely to be the substrate-access funnel and the protonated residue, the conserved tyrosine. The two azide-binding patterns seen may be an indication that there is indeed a second inhibition site. In an *in vivo* situation the enzyme will be exposed to a barrage of negatively charged by-products of metabolism, the tyrosine with its terminal OH moiety will provide an energy barrier that separates the positively charged active site from the cytoplasm, favouring the selection of superoxide over other negatively charged molecules.

6.7.4 SODs with very low affinity for azide

There are some FeSODs that have very low affinity for azide. There are differences in the residues surrounding the conserved tyrosine that have been proposed to confer azide resistance. For example in the thermophile *Methanobacterium thermoautotrophicum*, the FeSOD has an extremely low affinity for azide (Takao *et al.*, 1991). The conserved tyrosine protrudes into the substrate-access funnel and is more tightly constrained against a tryptophan, see structure 1MA1 in the protein data bank (Berman *et al.*, 2000). This would make dynamic motion of this tyrosine difficult, and may prevent the entry of azide into the active site.

In the human mitochondrial form of MnSOD, mutating a histidine (equivalent to His30 in *Ec*-MnSOD), which is opposite the conserved tyrosine, to a valine decreases the enzyme's affinity for inhibitors. There is also a significant loss of activity. The mutant

residue sticks into the solvent-access channel, blocking off access to the active site and making close contacts to the tyrosine (Hearn *et al.*, 2004, Hearn *et al.*, 2003).

6.7.5 Thermodynamic implications for native FeSODs and native MnSODs

The thermodynamic fine-tuning hypothesis proposed in this thesis has implications on proposed catalytic mechanisms, which may be subtly different between FeSODs and MnSODs. In the following chapters two proposed mechanisms are given for catalysis in MnSODs that take into account initial, high-entropy binding of superoxide and subsequent rearrangement of the active site to allow superoxide to bind in a low-entropy state stabilised by a water molecule.

6.7.6 Remote effects

Matters for Fe and MnSODs are further complicated by the fact that changes in the protein structure distant from the active site can have drastic effects on protein function. In the MnSOD from *Porphyromonas gingivalis* mutation of a glycine, which is mostly conserved in MnSODs, to a threonine affects metal specifity even though it is 10 Å away from the active site (Yamakura *et al.*, 2003).

6.7.6.1 Electrostatic

In the SOD from *Propionibacterium shermanii* manipulating surface residues, with the aim of altering electrostatic interactions between the substrate and the substrate-access funnel (Gabbianelli *et al.*, 1997), had drastic affects on the enzyme activity. Site-directed mutagenesis of a surface Lys175 to an isoleucine decreased activity by 85%, whereas the more conservative mutation to an arginine had little effect on enzyme activity. Lys175 is involved in the secondary structure of this protein (Schmidt *et al.*, 1996), and extreme changes in the residue may have effects on the active site as well as affecting electrostatic interactions with substrate and solvent.

6.7.6.2 Tetramers

All SODs function as dimers and some go on to form tetramers, the significance of which is not clearly understood. In human mitochondrial MnSOD a seemingly conservative mutation of an isoleucine to a threonine that is distant from the active site (Borgstahl *et al.*, 1996) is enough to destabilise the tetrameric interface (Borgstahl *et al.*, 1992) seen in the native structure and to give rise to dimers that have lower activity, showing that for this SOD formation of a tetramer is important for activity.

6.7.7 The role of mobile tyrosine

As azide enters through the substrate-access funnel of the Fe/MnSODs described here, the conserved tyrosine re-orientates itself to accommodate the tail of the azide molecule. This is evident in changes in the distance between metal centre and Tyr34_OH (*Ec*-MnSOD numbering); refer to Figure 6-19 and Figure 6-20. This is seen as an extremely strong indicator that this residue has conformational freedom during normal catalytic turnover.

6.7.8 The role of conserved solvent-access funnel tyrosine in separating active site from solvent

The conserved Tyr34 and its partner His30 (*Ec*-MnSOD numbering) form part of a "gate" to the active site, through which azide, other inhibitors and superoxide must pass in order to gain access to the active site; refer to Figure 2-3. This tyrosine is also involved in stabilizing the active site through a hydrogen-bonding network of the enzyme and is very strongly conserved. Mutation of His30 or of Tyr174, which eliminates an inter-subunit hydrogen bond between them, leads to activity 30-40% of that of the wild type (Edwards *et al.*, 2001b).

The selection pressure to maintain the conserved Tyr34 in SODs is likely to be multifactorial. There is strong indication that this residue has structural roles in stabilising second-shell residues and that it is involved in "gating" of the active site to preferentially accept superoxide in favour of other negatively charged small molecules. Mutations of this residue do not affect enzyme activity in some MnSODs but do affect FeSOD activity. Mutants also have altered affinity for competitive inhibitors and altered susceptibility to by-products in MnSODs.

There is a strong indication from results presented here and from other solved structures that altering the amino acids that surround this tyrosine will lead to changes in the ability of the conserved tyrosine to stabilise the active site as well as the way inhibitors enter the active sites.

However, mutation of Tyr34 to a phenylalanine or an alanine has little effect on the catalytic activity of *Ec*-MnSOD (Whittaker & Whittaker, 1997a) or on the hydrogen-bonding network in the structure of Y34F mutant. The affinity of *Ec*-MnSOD mutants Y34A and Y34F for azide is greater than that of the native enzyme; this is likely due to the active site being more accessible to the solvent. Tyrosine 34 had been proposed as a candidate for the supply of protons to the active site for the second half reaction of

enzyme catalysis (Maliekal *et al.*, 2002, Parker & Blake, 1988, Stoddard, Howell *et al.*, 1990, Lah *et al.*, 1995), but it is likely that protons come from a different source for *Ec*-MnSOD (Whittaker & Whittaker, 1997a), possibly via the water molecule that moves into the active site along with the azide ions as seen in the active site of *Deino*-MnSOD-N_3^-.

When similar approaches are used on FeSODs (fusion proteins for which affinity tags have been removed) there are pronounced differences. In *E. coli* FeSOD the mutation of the conserved tyrosine to a phenylalanine decreases the activity of the mutant enzyme to 40% of the wild type, changes the pH sensitivity and decreases the thermal stability of the enzyme (Hunter *et al.*, 1997).

I propose that proton supply during catalysis is dependent on Tyr34_OH (*Ec*-MnSOD) atom in FeSODs, but is dependent on ordered water molecules in MnSODs. In MnSODs the role of Tyr34_OH is to stabilise water molecules in transition states, eliminate by-product and also to prevent incorrect small negatively charged molecules from entering the active site. This explains why conservative mutation of this residue to a phenylalanine is so drastic in FeSODs but has only minor effects in MnSODs as water molecules supply the protons.

6.7.9 Serious alterations to hydrogen-bonding network

As discussed in the introduction, mutations of other residues in the second coordination shell critically impair enzyme function as well as disrupting the hydrogen-bonding network. Mutating the conserved Gln146 in *E. coli* MnSOD has greater effects on the hydrogen-bonding network than mutations that affect the conserved tyrosine. In the mutant Q146E activity is abolished, whereas Q146L and Q146H mutants have 5-10% of wild type activity, which is still significant. Of this series of mutants, Q146H most closely resembles FeSODs, where there is some activity of Fe-substituted Gln146His at pH 7.8. When pH is lowered to 6.5, activity of the Fe form of Gln146His is greater than that of the Mn form (Edwards *et al.*, 2001a). All three of these structures have altered orientations of the Tyr34. Similar work has been done in introducing point mutations into first and second coordination shells in human mitochondrial MnSOD, generally with little effect on the protein structure, but with great effects on the enzyme activity. Structures exist for Y34F (Guan *et al.*, 1998),W161F (Cabelli *et al.*, 1999), Q143N (Hsieh *et al.*, 1998) and Q143A (Lévêque *et al.*, 2000).

6.7.10 Final thoughts and summing up

The Fe/Mn family of SODs is widely distributed across numerous species, with many examples being highly metal-specific, while there are other SODs that are far less metal-specific. The structural basis, determined by differences in primary amino-acid sequence between MnSODs and FeSODs, for metal specificity is largely unknown but appears to modulate the thermodynamic fine tuning of the MnSODs in a different way to the FeSODs. This manifests as differences in azide binding, midpoint reductive potentials and coordination of the active site cation at physiological pH ranges. These differences become apparent when the metal content is manipulated. These indicate there are subtle differences in metal-substituted forms between native MnSODs and native FeSODs.

In section 1.6 five proposed theories as to how enzymes speed up catalysis were described. The results presented in this thesis indicate that the enzymatic mechanism of Fe/MnSODs is most consistent with the fifth scheme which, in summary, proposes enzymes work by coordinating ordered protein movements to reaction progress. This is mostly due to the observations that FeSODs and MnSODs may have different thermodynamic fine tuning and that seemingly benign point mutations remote from the active site can perturb function. Alternative active-site based theories can not readily explain differences such as inhibitor specificity and metal specificity between FeSODs, MnSODs and wrong metal forms despite nearly identical active sites.

As Fe/MnSODs operate at close to optimum efficiency, protein movements during both catalysis steps will be slight and hence rapid. Most of the movement will be at the active-site metal as it changes from a penta-coordinate to a hexa-coordinate state, accompanied by small changes in solvent structure and changes in hydrogen-bond distances, as indicated by Figure 6-17. Catalysis does not require major domain, loop or cofactor movement such as that seen in slower enzymes that, in general, process much larger substrates.

7 Inner-sphere proton-transfer mechanism for MnSODs

7.1 Linking structure and function of MnSODs

The following discussion is an attempt to merge structural information, derived from novel X-ray crystal structures, with widely believed mechanisms and spectroscopic data. Two possible reaction schemes are described: the first scheme in which proton uptake occurs at a coordinated hydroxide is dubbed "inner-sphere"; the second scheme proton uptake occurs distant from the active-site metal and is dubbed here "outer-sphere". Both are an attempt to link information derived from the structures of *Deino*-MnSOD-N_3^- and *Ec*-Mn-FeSOD-N_3^- with what is already known about MnSODs. The major requirement for any reaction scheme that involves a SOD is that it is streamlined for both speed and specificity.

7.2 Known biochemistry

The generally accepted reaction for all SODs is

$$2O_2^{\cdot-} + 2H^+ \xrightarrow{\text{SOD}} O_2 + H_2O_2$$

Equation 16

where the four substrates give rise to two products. This occurs at the active site of a SOD in two half-reactions,

$$(\text{SOD-M}^+) + O_2^{\cdot-} + H^+ \rightarrow (\text{SOD-M})\text{-}H^+ + O_2$$

Equation 17

$$(\text{SOD-M})\text{-}H^+ + O_2^{\cdot-} + H^+ \rightarrow (\text{SOD-M}^+) + H_2O_2$$

Equation 18

where M^+ is the oxidised active-site cation, M is the reduced active-site cation and SOD refers to peptide and coordinated solvents.

In both the first half-reaction (Equation 17) and second half-reaction (Equation 18) binding of superoxide bind near the metal centre is required for the reactions to proceed. In Equation 17, catalysis occurs through an inner-sphere electron transfer mechanism where electron orbitals of Mn^{3+} and superoxide overlap. However, in Equation 18 catalysis may occur through an outer-sphere electron-transfer mechanism where the electron orbitals of Mn^{2+} and superoxide do not overlap to any great extent.

The binding of superoxide, and subsequent release of products, will have multiple, but linked effects, which include:

- distortion of the active site
- change in the coordination of the metal from five to six, then from six to five
- change in bond lengths and bond angles of the active-site, in particular of the solvent-derived ligand
- alteration of the electrical environment of the active-site.

These effects are likely to be subtly different in each of the two half-reactions, as there are differences in active-site structure between the reduced and oxidised forms of the protein. Also, for rapid reaction, it is essential that movements of metal and protein ligands are small.

In a symmetrical environment, such as in solution, the extra electron of superoxide will be delocalised and shared equally between both atoms of superoxide. In an unsymmetrical environment, such as in the vicinity of a metal ion, the electron distribution of superoxide will be distorted with the extra electron spending more time associated with the superoxide atom closest to the positive cation; refer to Figure 7-1.

The atom of the superoxide ion with the extra electron is referred to here as the “head”, whereas the other atom is referred to as the “tail”. Only the “head” can transfer an electron to the bound Mn^{3+}. The electronic attraction between the “head” and the cation will act as a distance restraint, while the “tail” lacks this restraint and has more conformational freedom.

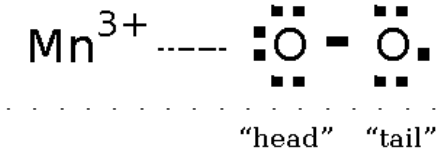

Figure 7-1. Unsymmetrical distribution of electrons within the superoxide molecule near the active-site Mn^{3+}.

Figure 7-1. When superoxide is in the vicinity of the active-site metal, the distribution of electrons becomes asymmetrical, with the superoxide atom closest to the cation having an extra electron. Here the atom with the extra electron is dubbed the “head” and the other atom the “tail”. The “tail” of the superoxide is expected to have more dynamic freedom.

7.3 "Inner-sphere" scheme

The mechanism discussed below is a modification and expansion of the 5-6-5 mechanism (Lah *et al.*, 1995) to incorporate the knowledge derived from the novel structures of *Deino*-MnSOD-N_3^- and *Ec*-Fe-MnSOD-N_3^- which are added to the existing knowledge from spectroscopic, point-mutation studies and the previous structure of *Thermus*-MnSOD-N_3^-. The original 5-6-5 mechanism was described for FeSODs and inferred for MnSODs.

In MnSODs the site of proton uptake during reduction (Equation 17) is widely believed to be the coordinated hydroxide (Lawrence & Sawyer, 1979), converting it to a water molecule, and the active-site cation accepts the electron from the superoxide directly. In the superoxide reduction step (Equation 18) the transfer of one of the protons is from the coordinated water and the second proton comes from the bulk solvent while the superoxide accepts an electron directly from the reduced metal cation. Thus, Equation 17 can be expanded to show individual substrate paths, specific for MnSODs. The site of proton uptake is presumed to be the fifth ligand, a metal coordinated-hydroxide

$$Mn^{3+} + O_2^{\cdot -} \rightarrow Mn^{2+} + O_2$$

Equation 19

$$OH^- + H^+ \rightarrow H_2O$$

Equation 20

So that for MnSODs Equation 17 can be rewritten,

$$SOD\text{-}Mn^{3+}\text{-}OH^- + H^+ + O_2^{\cdot -} \rightarrow SOD\text{-}Mn^{2+}\text{-}OH_2 + O_2$$

Equation 21

where OH^- is the hydroxide coordinated to the active-site manganese. The processes shown in Equation 19 are directly coupled to those of Equation 20. The change in the oxidation state of the active-site manganese is likely to alter the bond between the manganese and hydroxide, facilitating or promoting the uptake of a proton to the bound hydroxide. For the process in Equation 20 to occur a proton must travel from the bulk solvent to the buried hydroxide.

In a similar fashion, the events of Equation 18 can be expanded to show paths of the four individual substrates: two protons, superoxide and an electron.

$$H_2O \rightarrow OH^- + H^+$$

Equation 22

$$Mn^{2+} \rightarrow Mn^{3+} + e^{-}$$

Equation 23

$$O_2^{-} + H^{+} + e^{-} \rightarrow HOO^{-}$$

Equation 24

$$HOO^{-} + H^{+} \rightarrow H_2O_2$$

Equation 25

In a similar fashion Equation 18 can then be rewritten,

$$SOD\text{-}Mn^{2+}\text{-}OH_2 + H^{+} + O_2^{-} \rightarrow SOD\text{-}Mn^{3+}\text{-}OH^{-} + H_2O_2$$

Equation 26

The water in Equation 22 is the fifth ligand, a solvent molecule that is manganese associated. The reactions depicted by Equation 22, Equation 23, and Equation 24 occur almost simultaneously and are triggered by the association of superoxide with the metal centre. The reaction products, H^{+} and an e^{-}, from Equation 22 and Equation 23 respectively are generated and then combined to make a peroxo species in Equation 24. A second solvent-derived proton is then utilised in Equation 25 to generate hydrogen peroxide.

7.4 First half-reaction: oxidation of superoxide by Mn^{3+}SOD

7.4.1 Starting point: oxidised MnSOD

In vivo Fe/MnSODs will exist as a mixed population of reduced and oxidised enzyme, The proposed mechanism starts in an oxidised un-protonated state. The resting state of MnSOD in the oxidised form is presumed to have a coordinated hydroxide as the fifth ligand; refer to Figure 7-2. The hydroxide ion is stabilised by a hydrogen bond to the conserved glutamine. This glutamine in turn is hydrogen bonded to the solvent-access funnel tyrosine. This starting state is supported by a number of oxidised MnSOD structures. Importantly, the active site is penta-coordinate.

The two substrates of the initial half-reaction, superoxide and a proton, are found in the solvent surrounding the peptide. The positive charge of the Mn^{3+} at the active-site is a driving force for the initial association of superoxide.

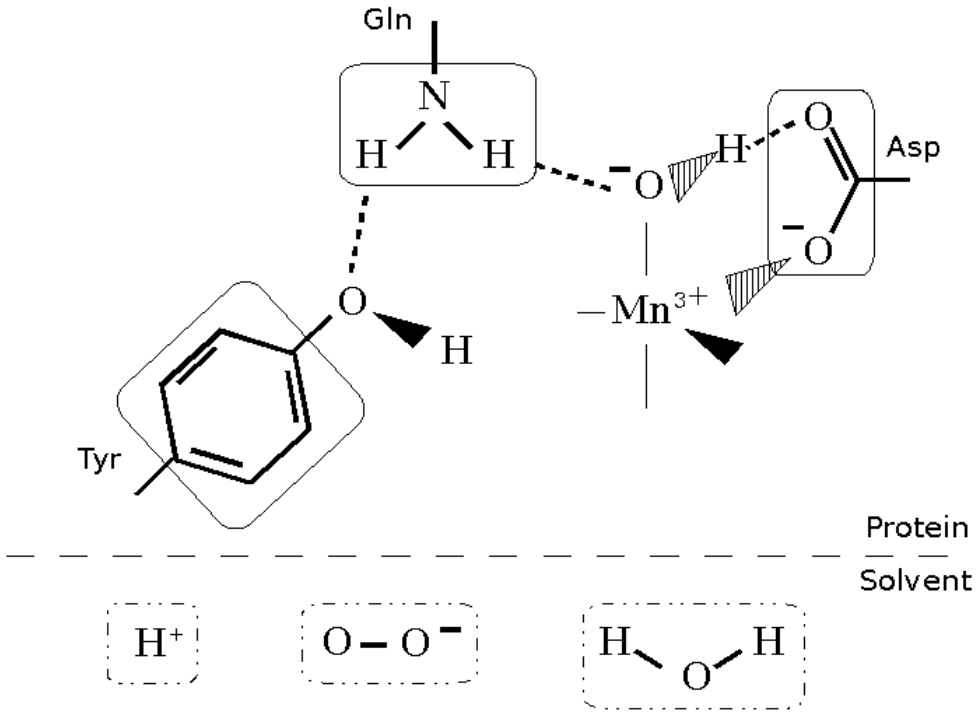

Figure 7-2. Starting state for the first half-reaction of the inner-sphere mechanism.

Figure 7-2 is a schematic representation of the active-site of an MnSOD, such as *Ec*-MnSOD, *Deino*-MnSOD or *mito*-MnSOD. In this stylised representation the perspective is looking down the solvent-access funnel. The most dominant feature of the active site is the Mn^{3+}, which is penta-coordinate at the start of the reaction cycle. Three out of the five manganese ligands are depicted as being in plane, two histidines (which are not shown) and the oxygen atom of the coordinated hydroxide. One manganese ligand is depicted behind the manganese plane, the aspartate, labelled Asp, which also receives a hydrogen bond from the coordinated hydroxide. The fifth and final manganese ligand, a histidine, in front of the manganese plane is not shown. The coordinated hydroxide also receives a hydrogen bond from a conserved glutamine, labelled Gln. The conserved glutamine donates a hydrogen bond to the solvent-access funnel tyrosine, labelled Tyr. The hydrogen of the tyrosine OH protrudes into the solvent-access funnel. The two substrates, superoxide and a proton, are shown in the solvent space, along with a water molecule, all of which will move into the active site during the first half-reaction of catalysis. This diagram is part of a series of related figures that include Figure 7-3, Figure 7-4, Figure 7-5, Figure 7-6 and Figure 7-7.

7.4.2 High-entropy binding of superoxide

The superoxide ion enters into the active site by passing through the solvent-access funnel. At this point the "head" of the superoxide ion initially associates with the metal ion; refer to Figure 7-3. The "tail" of the superoxide ion, which is slightly negatively charged, hydrogen-bonds to the hydrogen of the tyrosine. At this point there is no viable

pathway for a proton to enter the active site to travel to the coordinated hydroxide. This initial binding is a high-entropy state because the superoxide "tail" has conformational freedom. The extremely transitory high-entropy state requires the breaking of a hydrogen bond for transition to the next state to occur. It is unclear whether there is a substantial sharing of electrons between superoxide and the metal centre, that is the formation of a covalent bond, as the dynamics of this process are too fast to be recorded accurately, a bond is shown in Figure 7-3, but this bond may be quite weak.

This transition state of the active-site structure is mimicked by the structures of *Thermus*-MnSOD-N_3^- and *Ec*-Mn-FeSOD-N_3^-. These two azide-inhibited structures are high-entropy analogues to the Mn^{3+}SOD-O_2^- species. The *Thermus*-MnSOD-N_3^- is a high entropy structure as it was solved at ambient temperatures above the point where thermochromic transition occurs. The structure of *Ec*-Fe-MnSOD-N_3^-, with its weak and long Mn-azide bond (2.8 Å), is also a high-entropy structure analogue where metal substitution prevents the "tail" of the azide reaching a free energy minimum.

Figure 7-3 shows the initial high-entropy binding of superoxide to the active-site metal after moving in from the solvent. The labelling of this image is similar to that shown in Figure 7-2. Superoxide association changes the coordination of the active-site from penta-coordinate to hexa-coordinate. The sixth ligand, the "head" of superoxide, makes a bond to cationic centre. The "tail" receives a hydrogen-bond from the solvent-access funnel tyrosine. This binding pattern is a high entropy state where the "tail" of superoxide has conformational freedom. Catalysis does not occur as there is no credible pathway for proton transfer into the active site. This state is followed by the state illustrated in Figure 7-4.

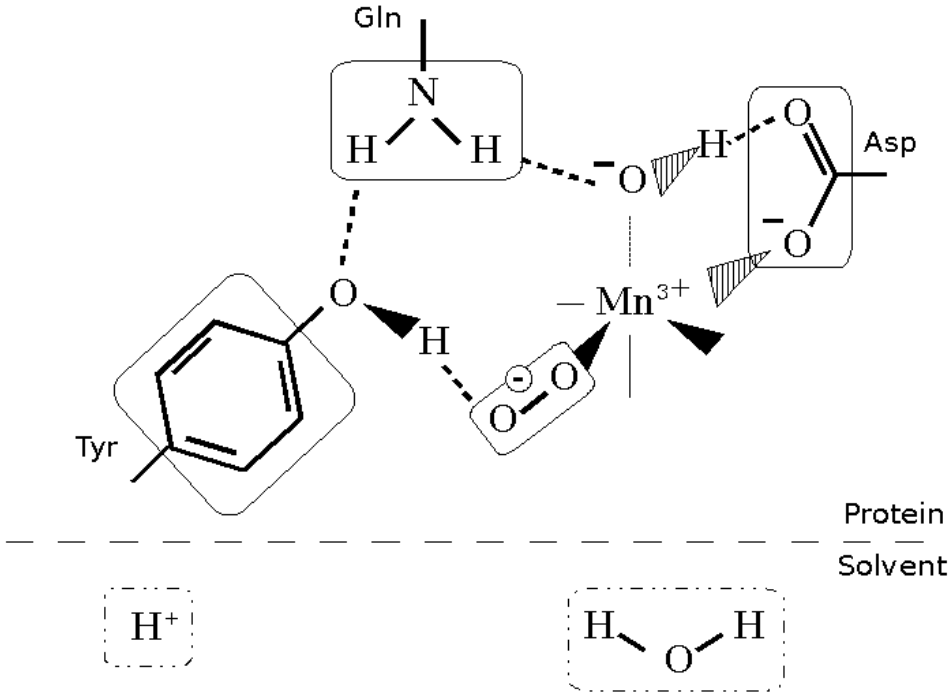

Figure 7-3. The arrival of superoxide at the active site for the first half-reaction of the inner-sphere mechanism.

7.4.3 Low-entropy bound state of superoxide

After initial superoxide interaction with the active site there is a conformational change at the active site and the superoxide then re-orients so that the "tail" of the superoxide falls into a cavity near the active-site metal; refer to Figure 7-4. At this point in the reaction scheme, it is unclear as to whether the interaction between superoxide and the metal centre forms a bond. This conformation is inferred from both the Fe-SOD-N_3^- structures and the structure of *Deino*-MnSOD-N_3^- and Y174F-*Ec*-MnSOD-N_3^-, all of which have azide bound end-on with the tail of the azide ion projecting into a cavity. There is no clear pathway for protons to enter the active site.

The two different modes of azide binding seen in MnSODs may be related to a detected thermal shift in the presence of azide (Whittaker & Whittaker, 1997b). The ambient temperature form of MnSOD-N_3^- is a high-entropy structure and when temperature decreases there is a change in coordination of the sixth ligand at the active-site so that at cryo-conditions the low-entropy form of MnSOD-N_3^- predominates. The thermal shift is due to either the reorientation of the coordinated azide, the associated movement of solvent-access funnel tyrosine and/or the movement of water into the active site.

The energy barrier required for the reorientation of superoxide is likely to be much less than that for the equivalent reorientation of azide, as the substrate analogue is one atom larger than the substrate.

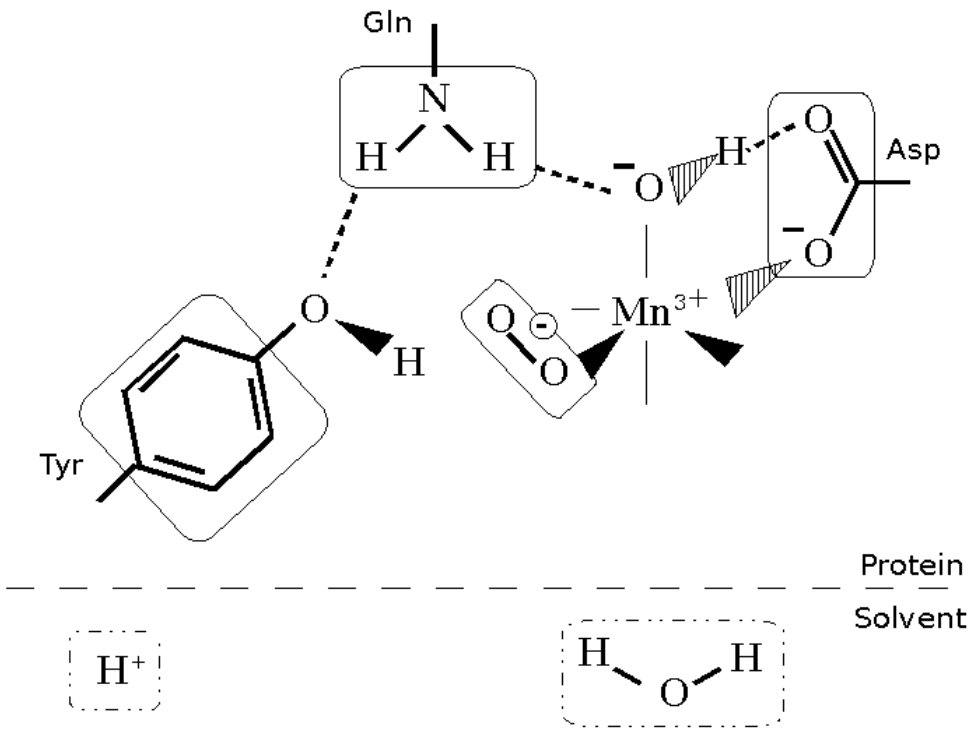

Figure 7-4. Rearrangement of hydrogen bonding after coordination of superoxide in the first half-reaction of the inner-sphere mechanism.

Figure 7-4 shows the low-entropy binding of superoxide. It follows from the events of Figure 7-3 and is labelled in a similar manner to Figure 7-2. This structure occurs after the "tail" of superoxide rotates into a nearby cavity, which limits the conformational freedom of the "tail" of superoxide. The hydrogen of the tyrosine OH and the oxygen of the "head" of the superoxide are potential hydrogen-bonding partners for the accompanying water molecule as shown in the next image in this series, Figure 7-5.

7.4.4 Water moves into the active site

A water molecule moves into the active site and hydrogen-bonds to both the superoxide and the solvent-access funnel tyrosine. The movement of a water molecule into the active site is seen in the structure of *Deino*-MnSOD-N_3^-. This water molecule provides a link between the active site and the solvent space. The "novel" water molecule is a potential pathway for protons to enter the active site.

The equivalent water molecule has been seen in some, but not all, FeSOD-N_3^- structures. In the *Ec*-FeSOD-N_3^- structure there is an equivalent water in the B subunit of the dimer but not in the A subunit (Lah *et al.*, 1995), although azide is only present in ~50% occupancy. An equivalent water molecule is seen at the B subunit of *Psherm*-

cambFeSOD-N_3^- making a 3.14 Å hydrogen bond to the N1 of the bound azide (Schmidt *et al.*, 1998). There may be an equivalent water molecule in the A subunit but the distance between the water and the N1 atom of the azide is 4.37 Å which is too long to be considered a classical hydrogen bond.

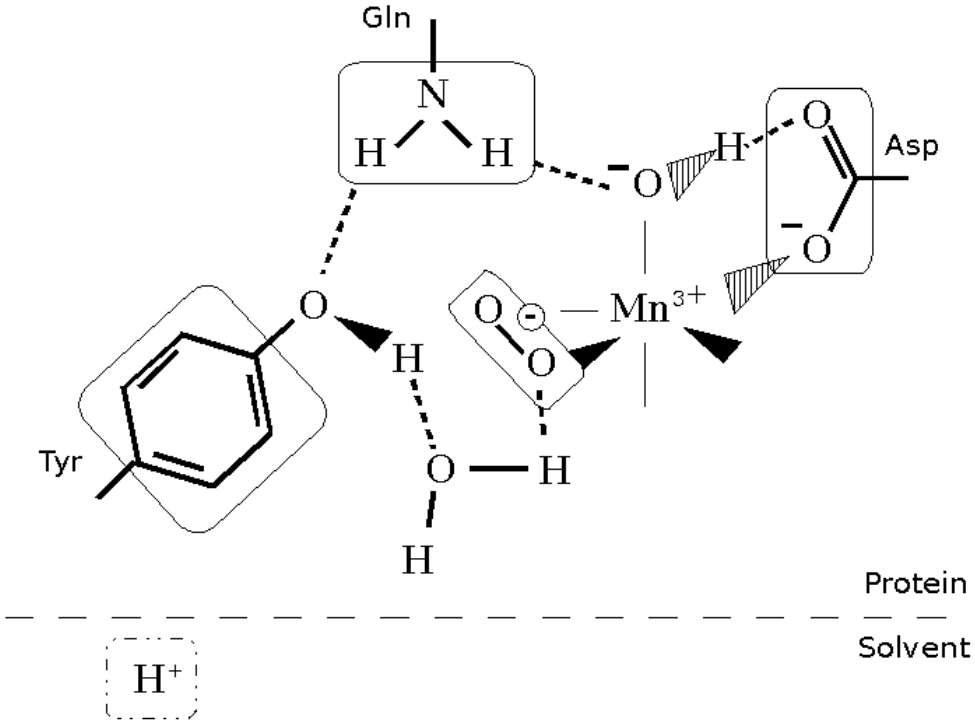

Figure 7-5. Arrival and hydrogen bonding of water to superoxide in the first half-reaction of the inner-sphere mechanism.

Figure 7-5 follows the events depicted in Figure 7-4. A water molecule has moved into the active site, making hydrogen bonds with the "head" of the superoxide and the OH of the tyrosine. Once the water molecule has moved into this hydrogen-bonded position, a possible proton-transfer pathway is formed that links the solvent to the tyrosine, to the glutamine, and finally to the hydroxide.

7.4.5 Electron transfer to Mn^{3+} and coupled proton uptake

At the point of catalysis, refer to Figure 7-6, an electron from superoxide transfers to the active-site metal, reducing it. Almost simultaneously a proton moves from the solvent to the stabilised water, a proton then moves to the tyrosine and from there to the glutamine and to the hydroxide ion via the glutamine, by unknown mechanism. This allows the rapid proton uptake at the hydroxide ion and conversion to a water molecule. Evidence against this proton-transfer mechanism involving glutamine is given in section 7.9.

It is unlikely that the proton uptake occurs before reduction, as proton uptake is unfavourable while reduction of the metal centre is extremely favourable. It is unclear how the reduction of the metal centre changes active-site structure to trigger proton transfer. Associated with the movement of the electron are: the transitory appearance of

a hexa-coordinate state, change of Mn^{3+} to Mn^{2+}, change in length of metal-ligand bonds, and the appearance of a non-polar product (O_2) at the charged active-site. With the reduction of the manganese, to Mn^{2+}, the cation becomes a much poorer Lewis acid and coordinated hydroxide becomes protonated.

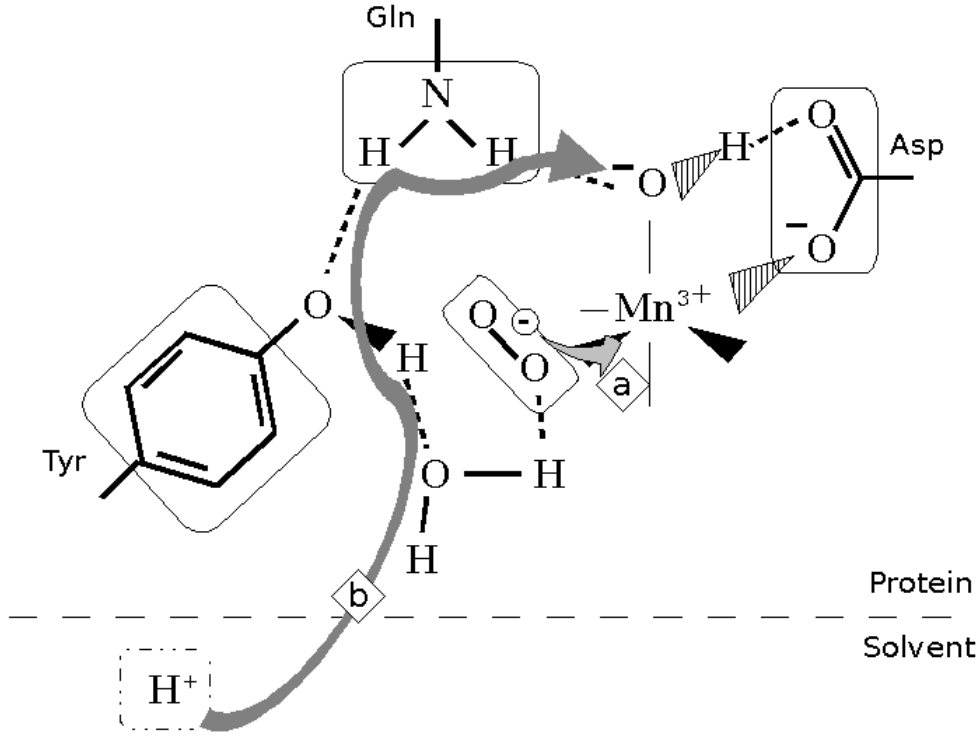

Figure 7-6. Coupled proton and electron transfer in the first half-reaction of the inner-sphere mechanism.

Figure 7-6 shows the catalytic step of the first half-reaction. Through-bond electron transfer from the bound superoxide to the Mn^{3+}, reducing it to Mn^{2+}, indicated by a grey arrow labelled "a", triggers a proton-transfer cascade. Proton transfer from the bulk solvent to the coordinated hydroxide is shown by the arrow labelled "b". Protons travel via the stabilised water to the tyrosine, then to the glutamine. There is a redistribution of protons at the glutamine and a proton is finally transferred to hydroxide.

7.4.6 End of the first half-reaction

At the end of the first half-reaction, non-polar molecular oxygen is located at the reduced active-site; refer to Figure 7-7. The active site remains positively charged, due in part to the uptake of a proton by the coordinated solvent. The interaction between the non-polar substrate and the charged active site drives the movement of oxygen away from the active site.

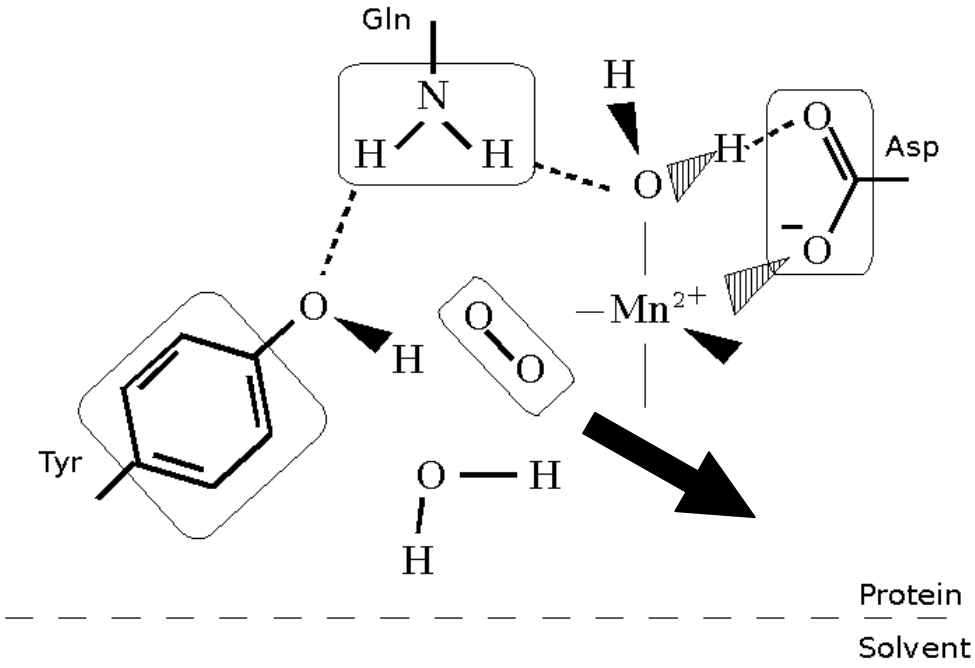

Figure 7-7. Departure of dioxygen and water from the active site in the first half-reaction of the inner-sphere mechanism.

Figure 7-7, shows the structure of the active site after the first catalysis step. Bound superoxide has been converted to an oxygen molecule. The active-site metal is now reduced and again penta-coordinate. The coordinated hydroxide ion has been converted to a water molecule with a hydrogen atom added in front of the manganese plane. There is no bond between the dioxygen and the metal centre. It is likely that the hydrogen bond between the water and the tyrosine is broken to allow oxygen to leave the active site.

7.5 Second half-reaction: reduction of superoxide by Mn^{2+}SOD

7.5.1 Proposed second half-reaction: reduction of superoxide by Mn^{2+}

At the start of the second half-reaction, the active-site manganese cation is in the reduced form, Mn^{2+}. The associated solvent molecule is a water molecule. This water molecule will be the source of one of the protons during the second catalysis step. The principal substrate, superoxide, exists in the solvent space. Also residing in the bulk solvent is the second proton and water molecules. At this point the active-site metal is penta-coordinate, the active site maintaining an overall positive charge.

The solvent molecule, to maintain tetrahedral coordination, is oriented such that one pair of electrons is stabilised by the metal centre and the other pair stabilised by the hydrogen bonding to the glutamine NH2 group. One of the hydrogen atoms is stabilised by the nearby active-site aspartate; the second hydrogen protrudes towards a tryptophan; refer to Figure 7-13, Figure 7-14, Figure 7-15 and Figure 7-16.

There may be a high-entropy superoxide binding state reminiscent of Figure 7-3 but this has not been depicted as catalysis is most likely to occur in the low-entropy form.

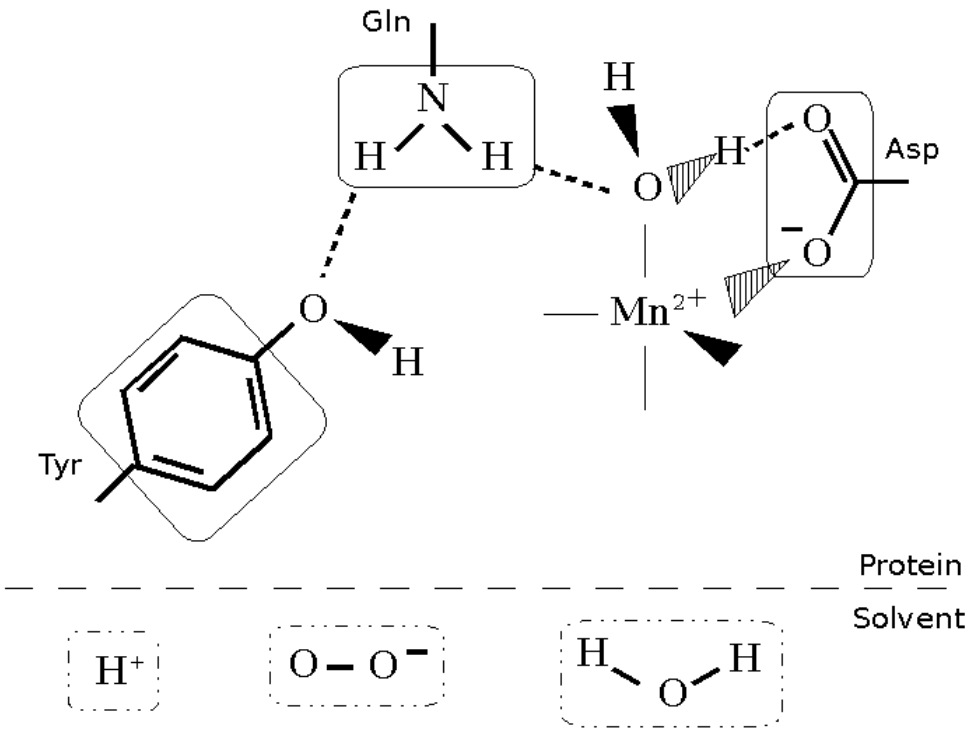

Figure 7-8. Starting state for the second half-reaction of the inner-sphere mechanism.

Figure 7-8 shows a schematic representation of the active site of a generic MnSOD prior to the second half-reaction cycle. The active-site Mn^{2+} is penta-coordinate at the start of the second half-reaction cycle. Description of the active-site is the same as Figure 7-2, except the metal centre is reduced and the coordinated hydroxide has been protonated to give a water molecule. The second hydrogen of the coordinated water is depicted protruding out of plane to maintain a tetrahedral arrangement for the solvent derived molecule. The conserved glutamine donates a hydrogen bond to the solvent-access funnel tyrosine, labelled Tyr. The hydrogen of the tyrosine OH protrudes into the solvent-access funnel. The two substrates, superoxide and a proton are shown in the solvent space, with a water molecule, all of which will move into the active site during the second half-reaction of catalysis. This figure is part of series of related images that includes Figure 7-9, Figure 7-10, Figure 7-11 and Figure 7-12.

7.5.2 Superoxide associates with metal ion

The superoxide anion diffuses into the active site, drawn in by the net positive charge; refer to Figure 7-9. It associates in a similar fashion to that seen in the low-entropy binding in the first half-reaction; refer to Figure 7-4.

At this point it is unclear what is the nature of the interaction between the superoxide anion and the Mn^{2+} and whether a covalent bond is formed. The "tail" of the superoxide molecule is oriented towards two hydrogen atoms, one from the coordinated water and the other from the glutamine. The coordinated water molecule is the more likely proton source for the first proton. The ultimate source of the second proton for catalysis is the bulk solvent, but at this point there is no credible pathway for the proton transport into the active site.

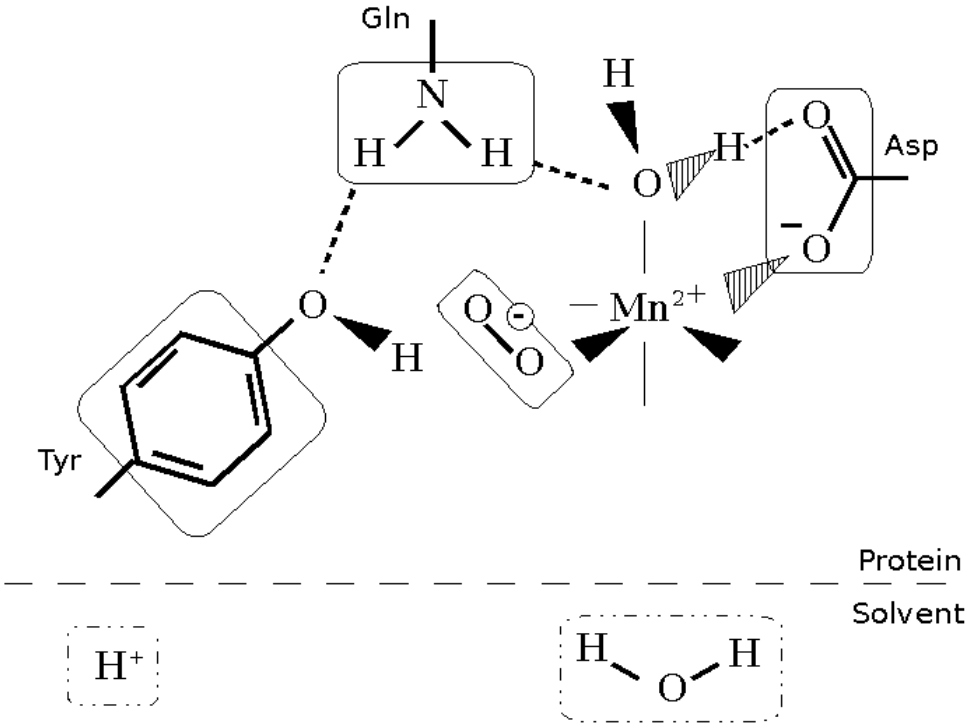

Figure 7-9. Arrival of superoxide at the active site in the second half-reaction of the inner-sphere mechanism.

Figure 7-9 shows superoxide has moved from the solvent space to the active site and become associated with the reduced metal centre in a low-entropy binding state. The nature of the association between the metal centre and the superoxide remains unclear; in the above image it has been shown as a weak bond.

7.5.3 Water associates with superoxide ion

A water molecule follows superoxide into the active site and hydrogen-bonds with both the superoxide and the hydrogen of the conserved solvent-access funnel tyrosine; refer to Figure 7-10. This water molecule provides a pathway for the second proton to enter the active site from the bulk solvent. The negatively charged "head" of the superoxide is now hydrogen-bonded to hydrogen of the stabilised water molecule that has moved into the active site. The "tail" of the superoxide remains buried in a nearby cavity (Miller *et al.*, 1999).

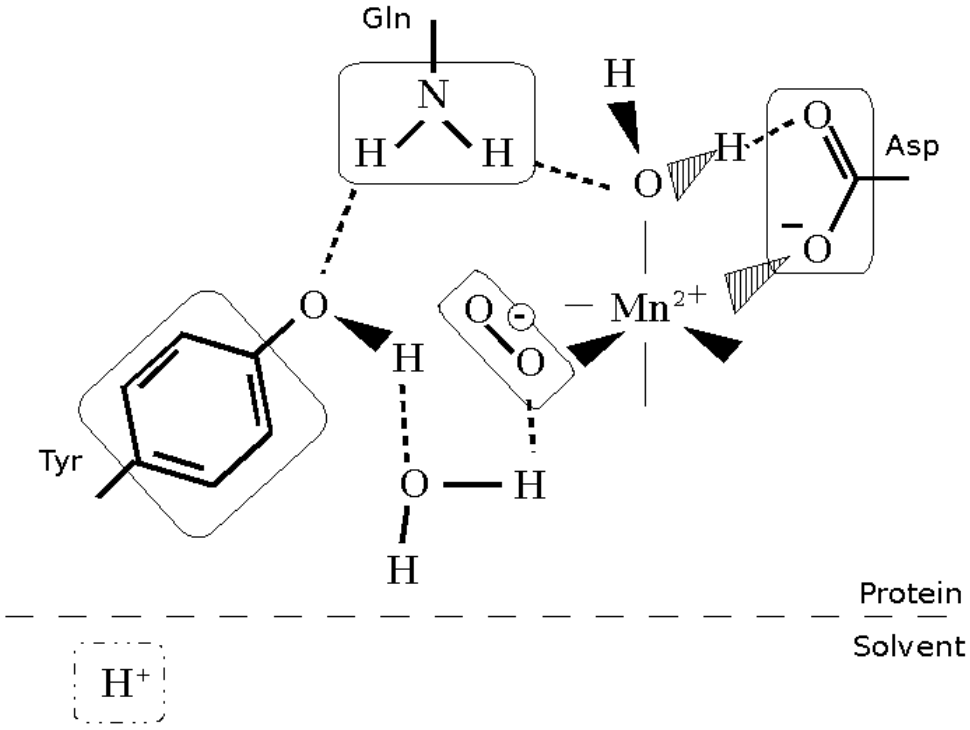

Figure 7-10. Arrival and binding of water to the superoxide ion for the second half-reaction of the inner-sphere mechanism.

Figure 7-10 shows that a water molecule has moved from the solvent space into the active site and formed hydrogen bonds with tyrosine and the "head" of the superoxide. This water molecule now forms part of a proton-transfer pathway that links the solvent to the tyrosine, glutamine and hydroxide.

7.5.4 Electron transfer from Mn^{2+} to superoxide and coupled proton transfer

During the second catalysis step; refer to Figure 7-11, an electron is passed from the metal centre to the superoxide, almost simultaneously a proton moves from the metal-coordinated water molecule onto the nascent peroxo group. This generates a short-lived peroxo species. The peroxo species is converted to hydrogen peroxide by a proton, which is ultimately derived from the solvent.

One possible pathway for the second proton to be transferred to the peroxo species is shown in Figure 7-11, where the proton moves from the solvent to the stabilised water molecule, then onto the nascent peroxo species. Alternately, the peroxo species could diffuse away from the active site and acquire the second proton from the bulk solvent.

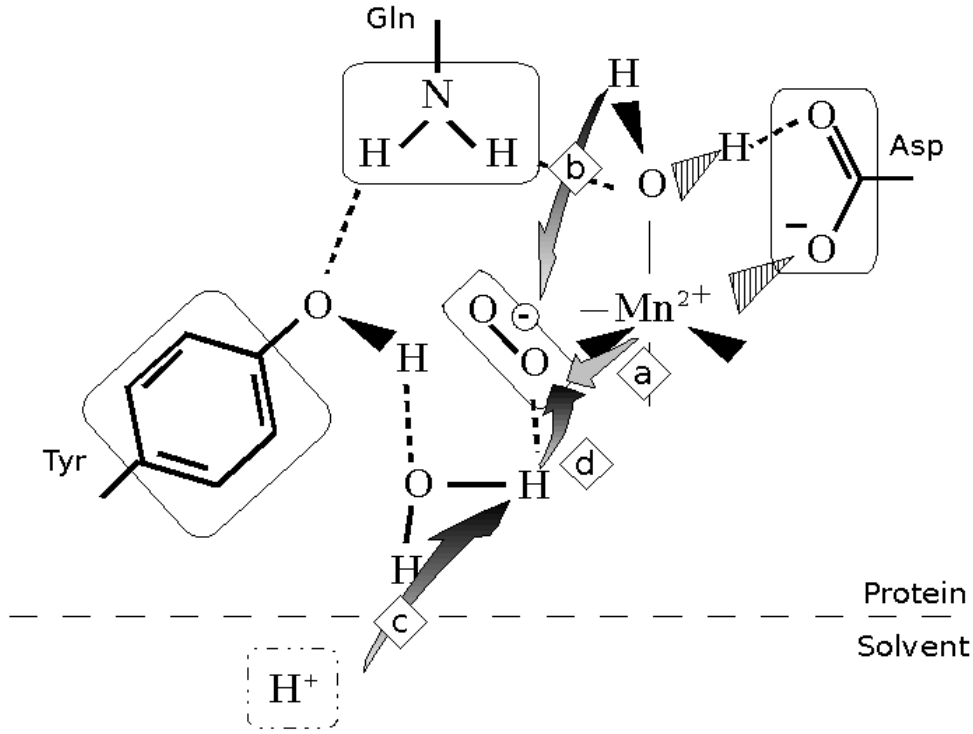

Figure 7-11. Coupled electron and proton transfer in the second half-reaction of the inner-sphere mechanism.

Figure 7-11 shows the second catalytic dismutation of superoxide. Electron transfer from the Mn^{2+} to the superoxide molecule is shown by the grey arrow labelled "a". At the same time a proton is transferred from the coordinated water molecule to the superoxide, arrow labelled "b". These two coupled reactions form a peroxo species at the active site.

A proton is transferred from the bulk solvent to the stabilised water molecule, indicated by the arrow labelled "c". From there a proton is transferred to the peroxo species to form hydrogen peroxide, indicated by the arrow labelled "d".

7.5.5 The end of the second half-reaction

At the end of the second catalysis step the active site will contain a hydrogen peroxide (or a peroxo species); refer to Figure 7-12. The coordinated water must leave the active site for hydrogen peroxide (or peroxo anion) to leave the active site. The reaction product can then diffuse away from the active site.

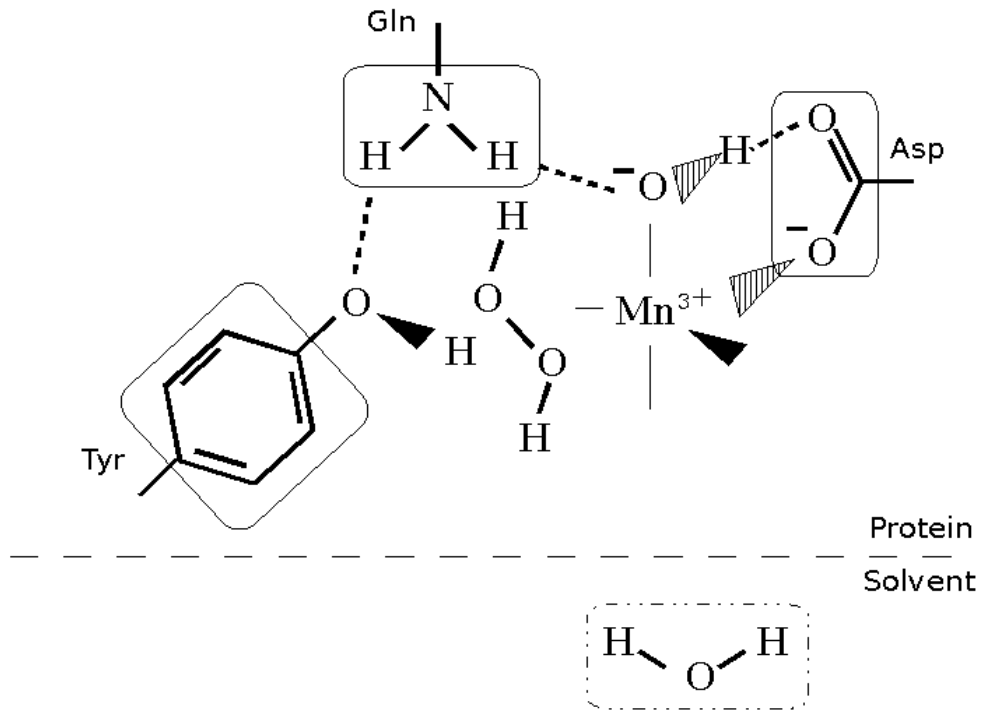

Figure 7-12. Departure of hydrogen peroxide and water in the second half-reaction of the inner-sphere mechanism.

Figure 7-12 shows the active site of MnSOD at the end of the second half-reaction. The active-site manganese cation is oxidised and the coordinated solvent-derived molecule is an hydroxide ion. The hydrogen peroxide at the active site will diffuse away, leaving MnSOD back at the starting point, as seen in Figure 7-2.

At the end of the second half-reaction, the metal centre is in the oxidised state and the coordinated fifth ligand is a hydroxide. At this point the enzyme is back at the starting point, reminiscent of Figure 7-2, predisposed for binding of another superoxide.

7.6 Implications of the inner-sphere mechanism

In FeSODs, both the first and second half-reactions occur by an inner-sphere mechanism (Bull & Fee, 1985). When superoxide reacts with the oxidised manganese centre, electron transfer is by an inner-sphere mechanism where electrons are shared through a fleeting covalent bond (Maliekal *et al.*, 2002). In the second half-reaction superoxide interacts with the reduced manganese to receive an electron, this is likely to be due to an outer-sphere electron transfer, as Mn^{2+} has a low affinity for a sixth anionic ligand. This implies that in the second half-reaction no covalent bond is formed. However there is evidence of association between azide and Mn^{2+}SODs (Tabares *et al.*, 2007).

When the previous mechanism was proposed (Lah *et al.*, 1995) it was called the "5-6-5 mechanism" and proposed to apply to both half-reactions of FeSODs and MnSODs. This is valid for FeSODs; however, for MnSODs only the first half-reaction can accurately be described as a "5-6-5 mechanism". The second half-reaction may be more accurately described as a "5-5-5 mechanism" or possibly a "5-5½-5 mechanism" as the interaction between superoxide and Mn^{2+}, shown in Figure 7-9, may not be a covalent bond.

The proposed scheme is slightly ambiguous at some steps. When superoxide associates with the reduced Mn^{2+}SOD, as shown in Figure 7-9, the distribution of the extra electron is unknown, but the electron probably spends the majority of its time associated with the oxygen atom closest to the metal centre, which is assumed to be positively charged.

The proton transfer to the active-site hydroxide at the end of the first half-reaction is dependent on the conserved glutamine and tyrosine to transfer protons. Other residues located close to the hydroxide ion, for example the conserved tryptophan, are not typically associated with rapid proton transfer. The movement of an electron into the active site at Equation 19 would neutralise the positive local environment of the active-site; the coupled uptake of a proton maintains the active-site net positive charge. There are two possible scenarios for the coupled proton transfer shown in Figure 7-6. In the first scenario the oxidation of superoxide causes a conformational change at the bound hydroxide that "pulls" the proton into the active site. In the "pulls" scenario, upon reduction of the metal centre the nature of the bond between metal and hydroxide alters, a proton jumps from the glutamine onto the hydroxide, this in turn pulls a proton of the conserved tyrosine OH, which in turn is protonated by the stabilised water.

Alternately, the conformational change is transmitted to the solvent, probably in the solvent-access funnel, and the proton is "pushed" into the active site. In the "pushed" scenario the loss of an electron by superoxide alters the nearby solvent structure pushing an extra proton onto the conserved tyrosine OH, which collapses losing a proton onto the conserved glutamine which in turn also loses a proton onto the coordinated hydroxide.

In both half-reactions, a water molecule moves into the active site, hydrogen bonding to both the superoxide and the conserved tyrosine; refer to Figure 7-5 and Figure 7-10. This is based on structural information derived from *Deino*-MnSOD-N_3^-, which had a solvent molecule at the equivalent point. However, the solvent molecule could also be a hydronium ion with the positive charge of the added proton stabilising the negative superoxide.

In the inner-sphere scheme, the solvent-access funnel Tyr_OH fulfils both a structural role and a catalytic role in MnSODs. The structural roles of Tyr_OH are to first act as hydrogen-bond acceptor to the conserved glutamine, and second during turnover to act as a hydrogen bond donor to both the "head" of the superoxide and the oxygen of the stabilised water molecule. The catalytic role of Tyr_OH is to provide a pathway for protons to reach the solvent-derived fifth ligand in the first half-reaction.

7.7 Differences between MnSODs and FeSODs

The inner-sphere proton-transfer scheme proposed above is primarily MnSODs, but a similar mechanism may occur in FeSODs. The functional difference between MnSODs and FeSODs can be explained by minor differences in proton transport, which is probably the result of differences in hydrogen-bonding motifs. Whether differences in hydrogen-bonding patterns are the result or cause of metal specificity remains unclear.

Mutation of the conserved solvent-access funnel tyrosine to a phenylalanine abolishes activity in FeSODs (Sorkin *et al.*, 1997), but only slightly diminishes activity in MnSODs (Whittaker & Whittaker, 1997a). This is seen to indicate that there exists a second proton-uptake pathway between solvent and the coordinated hydroxide in mutant MnSODs, a pathway which does not exist in the equivalent mutant FeSODs. This can be interpreted that the native MnSODs and FeSODs also have different pathways of proton uptake, and hence different hydrogen-bonding networks.

One of the other major differences between MnSODs and FeSODs is that most MnSODs suffer from product inhibition, likely from a peroxo species, and FeSODs do not. This dead-end product persists at the active site, preventing catalysis, but breaks down over time to regenerate active enzyme. The exact nature of this by-product is unknown (Carrasco *et al.*, 2007). In the scheme presented above the most likely point for generation of by-product is in the second half-reaction, which requires four substrates (superoxide, an electron, and two protons) to come together correctly; refer to Figure 7-11. Incorrect proton transfer to a reaction intermediate or coordination of a nascent peroxo species may be sources of the reaction by-product. If FeSODs have a different pattern of supplying protons, then they may be precluded from by-product inhibition.

The third point of difference between FeSODs and MnSODs lies in differences in inhibitor specificity. Generally, the FeSODs are inhibited by azide, resistant to product inhibition by hydrogen peroxide but are prone to inactivating chemical modification by hydrogen peroxide. Meanwhile, the MnSODs are more resistant to azide, susceptible to product inhibition by hydrogen peroxide and resistant to chemical modification by hydrogen peroxide. These differences may be partially explained by differences in hydrogen-bonding patterns between FeSODs and MnSODs.

Thus, the likely difference between FeSODs and MnSODs is in how protons reach substrates and reaction intermediates, manifested as different hydrogen bonding patterns. It is unclear whether this is due to differences in how the two distinct metal cations influence active-site environments or the reciprocal, where minor differences in MnSODs and FeSODs modulate the cations differently.

7.8 Evidence in support of inner-sphere proton transfer

The advantages of this proposed reaction scheme is that superoxide binds in a similar fashion in both half-reactions, rather than binding differently in both half-reactions. This is in despite of the vast differences between the chemistry of Mn^{3+} and Mn^{2+}, and Fe^{3+} and Fe^{2+} ions. The binding of superoxide is also reminiscent of the binding of azide to FeSODs, suggesting that the binding pattern of superoxide is the same across the entire Fe/MnSOD family. This is contrast to previously proposed 5-6-5 mechanism (Lah *et al.*, 1995) which had implied a different mode of superoxide binding between the FeSODs and MnSODs based on different modes of azide binding.

The original 5-6-5 mechanism was based on structural information derived from *Thermus*-MnSOD-N_3^-. Here, the structural information from *Thermus*-MnSOD-N_3^- is pertinent, perhaps as a high-entropy state that requires a minor conformational change to reach a low-entropy state, reminiscent of *Deino*-MnSOD-N_3^-. The first half-reaction is inferred to happen when superoxide is bound in the low-entropy state, hydrogen-bonded to a water molecule to provide an intact proton-uptake pathway.

Proton uptake at the bound hydroxide favours the second half-reaction as a proton is located close to the bound superoxide. So that for the second half-reaction, none of the substrates has to travel any great distance to the nascent peroxo species.

The second half-reaction is believed to occur with a similar overall structural arrangement, with superoxide binding/interacting with the metal ion in a similar position in both half-reactions. The net difference between the two half-reactions is the presence/absence of an electron and a proton at the active site, providing an overall positively charged active site for both half-reactions. There is no requirement for the breaking/formation of hydrogen bonds and there is little movement of amino-acid side chains, except for the solvent-access funnel tyrosine, which is required to shift between the high-entropy and low-entropy states.

Efficient catalysis is not favoured by the high-entropy state because there is no proton pathway into the active site. In the high-entropy state, the “tail” of the superoxide is hydrogen bonded to the solvent-access funnel tyrosine, effectively blocking access to the active site. This would require a decoupling between Equation 19 and Equation 20 as molecular oxygen would have to leave the active site before proton transfer to the coordinated hydroxide could occur.

The existence of a high-entropy state, at least in the *Ec*-Mn-FeSOD-N_3^- and *Thermus*-MnSOD-N_3^- structures, can explain why azide is an inhibitor of MnSODs at ambient temperatures without directly coordinating to the active site Mn. The transition from a high-entropy state to a low-entropy state also explains the second mode of azide binding seen in N_3^--*Deino*-MnSOD. The transition between high-entropy and low-entropy states could also explain the temperature-dependent spectroscopic changes in *Ec*-MnSOD-N_3^- (Whittaker & Whittaker, 1996) and *Thermus*-MnSOD-N_3^- (Whittaker & Whittaker, 1997b).

Proton uptake at the active-site coordinated hydroxide must circumvent the positive charge at the cation which lies between the hydroxide and the solvent. The proposed proton uptake pathway here skirts around the cation.

To be classed as an inner-sphere mechanism of proton transfer, the site of proton uptake must be in the immediate vicinity of the metal centre or of the first or second shell of residues. In the past, other sites had been proposed as the site of inner-sphere proton uptake, most notably the conserved solvent-access funnel tyrosine, but this has been largely discredited due to NMR studies (Miller *et al.*, 2003).

7.9 Evidence against inner-sphere proton transfer

There is no X-ray structure of a reduced Mn^{2+}SOD complex with azide. This means that the structure of the Mn^{2+}SOD complex with superoxide is inferred from Mn^{3+} complexes with azide. This may introduce errors, as the binding of mode of azide (and by inference superoxide) may be different between oxidised and reduced MnSODs.

The inner-sphere scheme of proton transfer relies on the commonly held assumption that the coordinated solvent-derived molecule is the site of reduction-coupled proton uptake. While there is space to accommodate a coordinated hydroxide, a coordinated water molecule would introduce a steric clash between the added hydrogen atom and the surrounding peptide. The distance between the hydroxide/water and the Gln_NE2 is about 3 Å, indicative of a hydrogen bond between one of the hydrogen atoms of Gln_NE2 and the oxygen atom of the hydroxide. The hydrogen of the hydroxide makes a hydrogen bond to the active-site aspartate ligand and the third interaction is with the metal ion itself. This leaves one vacant site for a hydrogen atom to sit if hydroxide is converted to a water molecule. Close inspection of SOD structures reveals that there is little space for an additional atom due to steric clash with a highly conserved tryptophan; refer to Figure 7-13, Figure 7-14, Figure 7-15 and Figure 7-16. In the 0.9 Å-resolution structure of Y174F-*Ec*-Mn^{3+}SOD (PDB code 1IX9), the distance between the solvent-derived molecule and atom Trp169_CD1 is 3.20 Å in the A subunit and 3.16 Å in the B subunit, making little space for the acquisition of a proton. Upon reduction to Y174F-*Ec*-Mn^{2+}SOD (PDB code 1IXB), this distance decreases by 0.10 Å to 3.10 Å in the A subunit and decreases by 0.06 Å to 3.10 Å in the B subunit

If, upon reduction, the hydroxide is converted to a water molecule, then an additional proton is added into the system and existing hydrogen bonds should be disrupted and/or side chains would move to accommodate it. Comparison of the ultra-high resolution

structures of Y174F-*Ec*-Mn^{3+}SOD and Y174F-*Ec*-Mn^{2+}SOD, (1IX9 and 1IXB in the PDB respectively) reveals that the changes in these hydroxide/water to Trp distances are small and in the wrong direction to accommodate an added proton on a coordinated water molecule. Inspection of electron density maps at 0.9 Å resolution, derived from submitted structure factors, also reveals no density for the second hydrogen atom of a coordinated water molecule; refer to Figure 7-17 and Figure 7-18. There is also no movement of peptide side chains around the coordinated hydroxide that would allow a water molecule to fit. There is, however, ample evidence from small-molecule crystallography to support the existence of a penta-coordinate Mn^{2+} species with a water molecule as one of the coordinating ligands, but very little to support an Mn^{2+}-OH^- species. On the other hand, as the reduction potential for Mn^{3+} in MnSODs is unusually low (Vance & Miller, 1998b) the Mn^{2+} in MnSODs must be more readily oxidised than similar pentacoordinate small-molecule Mn^{2+} complexes. This is more consistent with a Mn^{2+}-OH^- species than a Mn^{2+}-H_2O species at the active site of MnSODs.

The other assumption that is made in the scheme presented is that there is efficient proton transfer from the conserved solvent-access funnel tyrosine to the solvent-derived molecule via the conserved glutamine. This may be unfavourable, as there are several energy barriers for efficient proton transfer, as protons have to "jump" across two hydrogen-bonding linkages before reaching the hydroxide. Proton transfer within proteins remains a poorly understood phenomenon (Wraight, 2006).

In several cambialistic SODs such as that from *Propionibacterium shermanii* (*Psherm*-camb-FeSOD), the glutamine is replaced by a histidine residue; refer to Figure 2-5. For camibialistic SODs to function with an inner-sphere proton transfer mechanism, this histidine must also be able to act as a proton donor and acceptor. In the structure of *Psherm*-camb-FeSOD (Schmidt *et al.*, 1996) the rotamer of histidine is likely incorrect; refer to Figure 5-6. In the likely correct rotamer, Figure 5-7, the active-site hydroxide is stabilised by a hydrogen bond from the CE1 atom (and associated proton) of the histidine. If this is the case, then the likelihood of proton trasfer to or from this histidine is low.

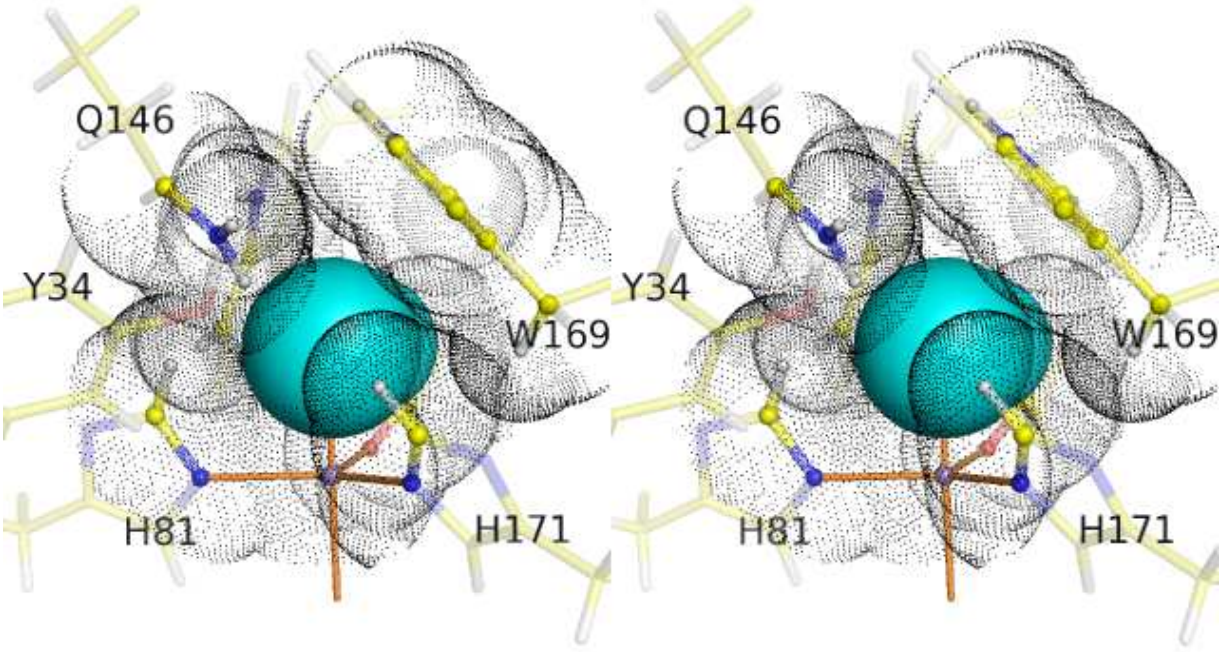

Figure 7-13. Wall-eyed stereo-image, looking down the solvent-access funnel, showing the potential steric clashes if the solvent-derived molecule is an hydroxide ion.

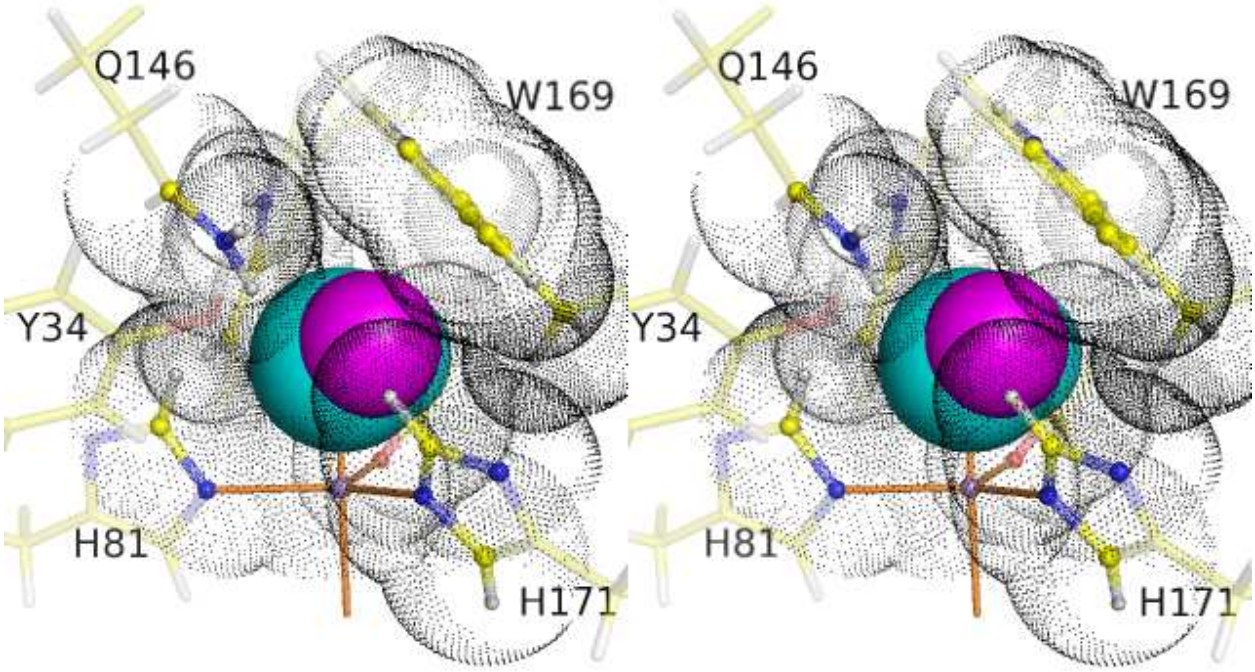

Figure 7-14. Wall-eyed stereo-image, looking down the solvent-access funnel, showing the potential steric clashes if the solvent-derived molecule is a water.

In Figure 7-13 and Figure 7-14, the solvent-derived hydroxide ion is shown as two space-filling spheres (the sphere corresponding to the hydrogen is partially obscured by the sphere corresponding to oxygen). Both spheres are coloured cyan, showing van der Waals radii. In this orientation the hydroxide hydrogen atom is partially obscured. Upon reduction of the enzyme the bound hydroxide in the inner-sphere mechanism for proton transfer is believed to take up a proton to become a water molecule. In the lower stereo-image, Figure 7-14, the fifth ligand,

a water molecule, is depicted as space-filling spheres of van der Waals radii coloured cyan with the added modelled hydrogen atom represented as a magenta sphere. In both images the metallo-enzyme, excluding the solvent derived molecule, is shown as a ball-and-stick representation in which carbon, nitrogen, oxygen, hydrogen and manganese have been coloured yellow, blue, red, white and magenta respectively. Ball-and-stick atoms within 4 Å of the coordinated fifth ligand are fully visible, those greater than 4 Å distant are rendered with partial transparency. The van der Waals spheres of atoms within 4 Å of the fifth ligand are shown as a black dot representation. The bonds between the metal ion and the five ligands, four protein and the solvent molecule, are shown as orange lines. Both images are based on the coordinates of 1VEW, to which hydrogen atoms have been modelled in their riding position using the CCP4 program HGEN. The orientation of hydroxide and water molecules has been modelled manually to make acceptable hydrogen bonding contacts.

The location of hydroxide binding is extremely constrained by van der Waal contacts, as well as limited number of hydrogen-bonding partners. The hydroxide in the top image is constrained by three interactions. The hydrogen of the hydroxide interacts with active-site aspartate (obscured), one pair of electrons interacts with the active-site cation and the other pair interacts with the glutamine leaving one plausible site for proton uptake. If a water molecule is modelled into the location of the hydroxide, maintaining these three interactions leads to a potential steric clash of the added proton with a nearby tryptophan as indicated by the overlapping spheres in Figure 7-14.

Figure 7-15 and Figure 7-16 show modelled potential steric clashes of the solvent-derived ligand, viewed from “behind” the active-site. In the top stereo-image, Figure 7-15, and the lower stereo-image, Figure 7-16, atoms are depicted using the same scheme as Figure 7-14 and Figure 7-15. In the top image the fifth ligand, is modelled as a space-filling hydroxide and in the lower image the fifth ligand is modelled as a space-filling water molecule with the additional hydrogen coloured magenta.

In this view, the active-site metal, which interacts with one pair of electrons on the solvent-derived molecule, is obscured by the space-filling representation. The aspartate clearly is clearly a hydrogen-bond acceptor to either the hydroxide or the bound water. In a similar fashion, the glutamine is a hydrogen-bond donor to a pair of electrons. In the lower image an additional hydrogen atom has been added at the only vacant site of the hydroxide. The additional hydrogen, coloured magenta, is located uncomfortably close to a tryptophan, labelled W169, with no nearby hydrogen bond acceptors to stabilise this added proton.

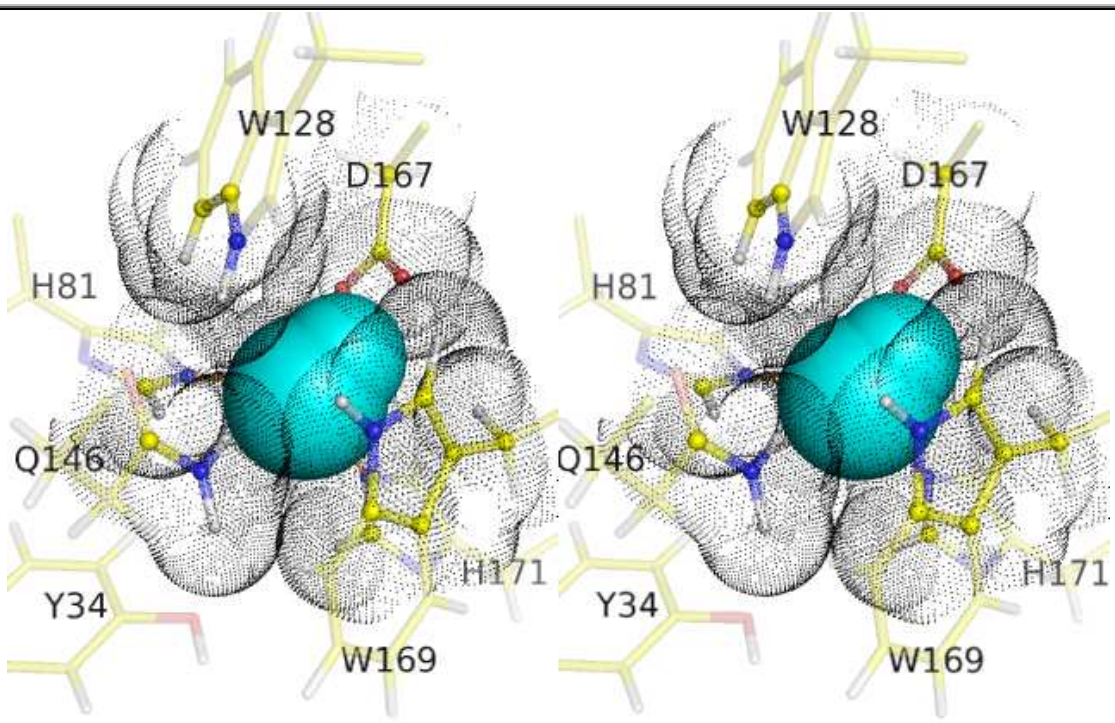

Figure 7-15. Wall-eyed stereo-image, looking down the bond between active-site Mn and the solvent-derived molecule, here modelled as an hydroxide ion.

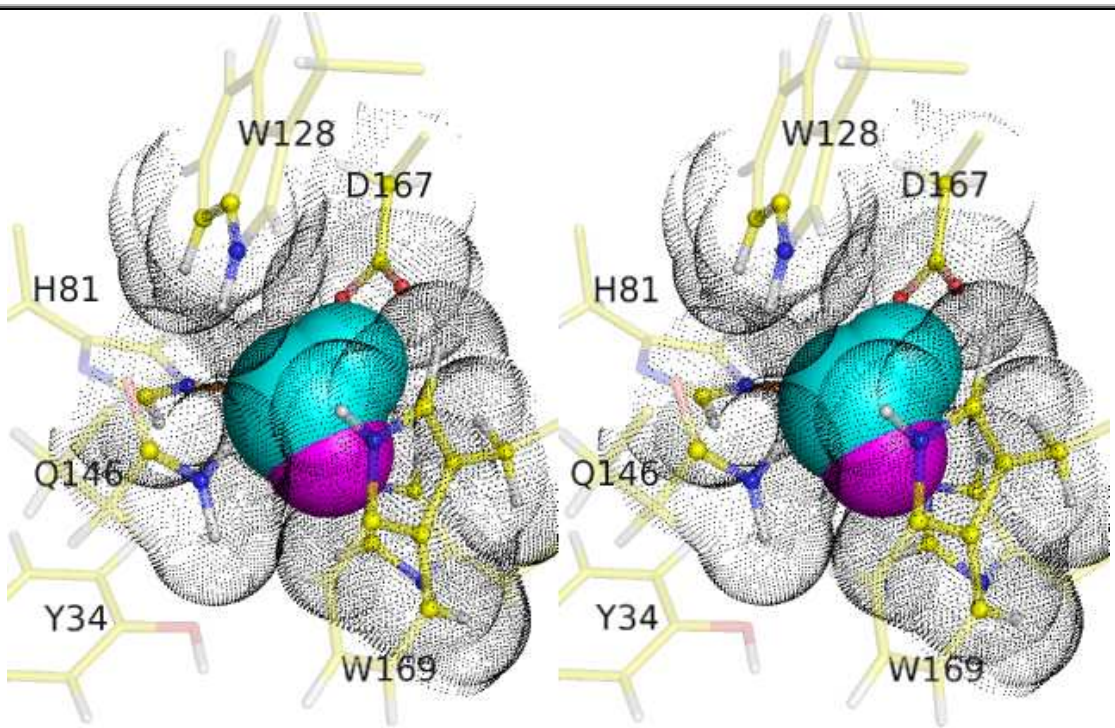

Figure 7-16. Wall-eyed stereo-image, looking down the bond between active-site Mn and the solvent-derived molecule, here modelled as a water.

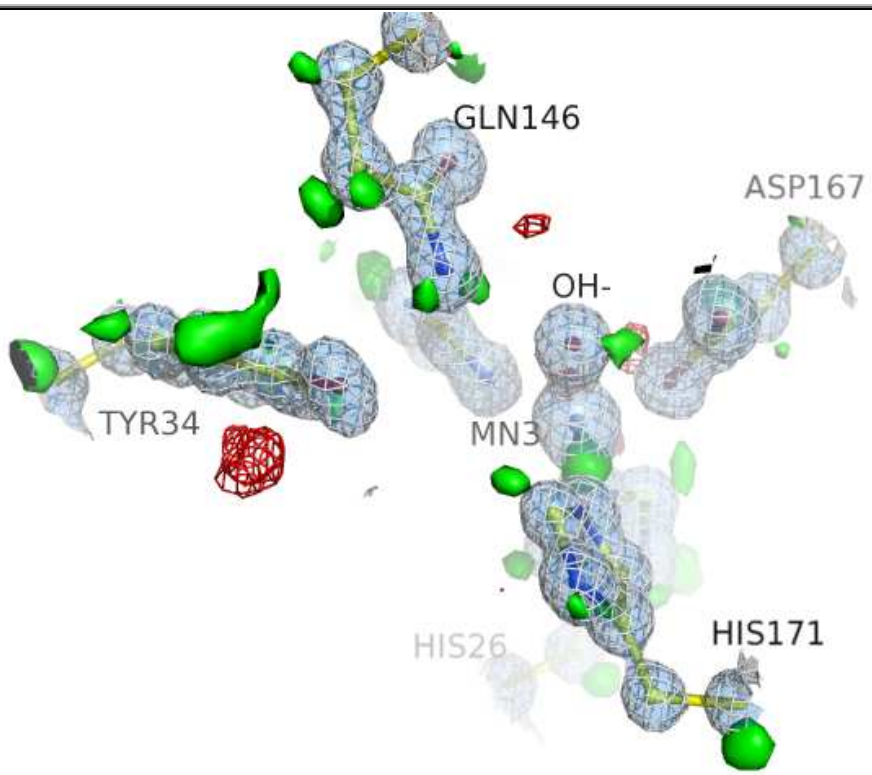

Figure 7-17. Ultra-high-resolution electron-density maps of the active-site of the A subunit of the oxidised form of Y174F-*Ec*-MnSOD where positive peaks in difference maps may be hydrogen atoms.

Figure 7-17**.** The electron density maps were calculated from submitted coordinates, PDB code 1IX9, and from the deposited structure factors using the PHENIX programming suite. Atoms of side chains are shown as a ball-and-stick representation where carbon, nitrogen and oxygen atoms are coloured yellow, blue and red respectively. The active-site manganese is shown as a magenta sphere and the coordinated hydroxide is shown as a red sphere. The weighted $2|F_O|-|F_C|$ map is shown as a transparent blue surface contoured at the 2 σ level. Positive peaks, above 2.2 σ in the $|F_O|-|F_C|$ maps are shown as a green surface while negative peaks below -3.0 σ are shown as a red mesh.

The resolution of the X-ray data is 0.90 Å, at which resolution it may be possible to detect hydrogen atoms. There are a number of positive density peaks in the difference map that are located near the expected riding positions of hydrogen atoms, most notably around Gln146 and the coordinated hydroxide. The coordinated hydroxide ion has a positive density peak oriented towards the active-site aspartate, its expected hydrogen bonding partner.

The image shown here is derived from the A subunit, the electron density at B subunit is similar, especially with regard to the single peak of positive electron density associated with the solvent-derived ligand.

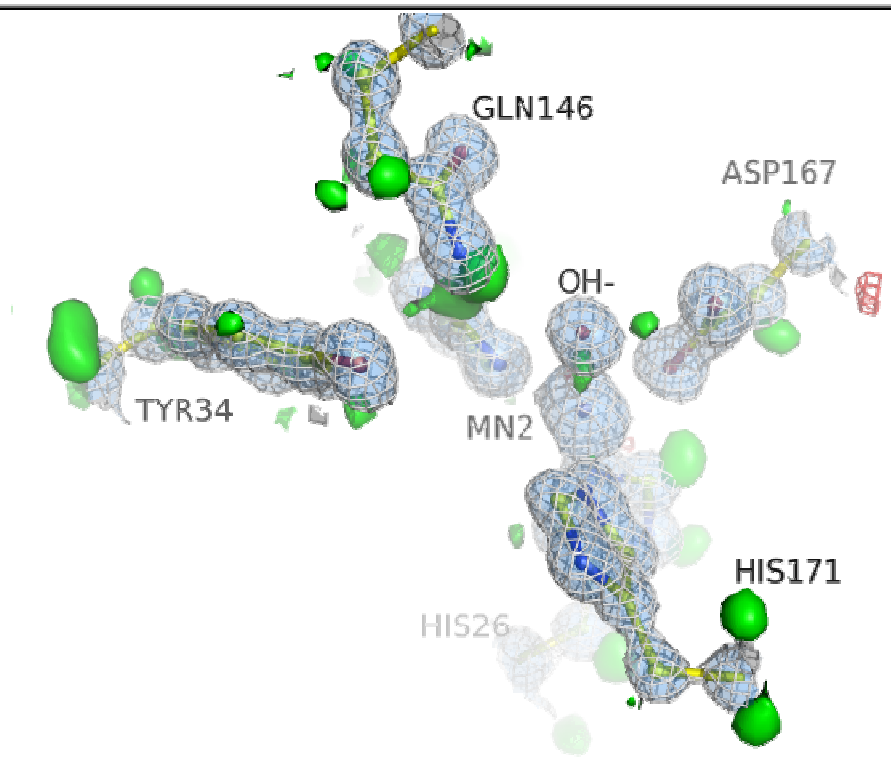

Figure 7-18. Ultra-high-resolution electron-density maps of the active-site of the A subunit of the reduced form of Y174F-*Ec*-MnSOD where positive peaks in difference maps may be hydrogen atoms.

Figure 7-18**.** The electron density maps were calculated from submitted coordinates, PDB code 1IXB, and from the deposited structure factors using the PHENIX programming suite to refine temperature factors. The structural representations here are the same as in Figure 7-17. As detailed in the atomic coordinate file, reduction was achieved using dilute hydrogen peroxide. The maps shown are also rendered with the same contour levels as in Figure 7-17, for X-ray data to 0.90 Å. There are several positive density peaks in the difference map located near the expected riding positions of hydrogen atoms. The solvent-derived fifth ligand has a single positive density peak oriented towards the active-site aspartate, an expected hydrogen-bonding partner. A second nearby peak is located between the metal ion and the solvent-derived molecule. There is no density peak in the expected position that a hydrogen atom would occupy if the solvent-derived molecule were a water molecule. Similar density peaks are seen in the corresponding difference maps in the B subunit.

8 An alternate, outer-sphere mechanism for proton transfer in MnSODs, that is independent of coordinated hydroxide

Described below is the alternate reaction scheme. The major difference compared to the scheme presented above is the location of proton uptake. In the inner-sphere scheme proton uptake occurs at the coordinated hydroxide; refer to Figure 7-6. However, in the outer-sphere scheme detailed below, proton uptake occurs at an as yet unidentified side chain that is probably in the solvent-access funnel, possibly the absolutely conserved glutamate of the dimer interface. From the remote site of reduction-coupled proton uptake, the proton shuffles through water molecules to the active site via a Grötthus mechanism (for an historical overview, plus modern interpretation refer to (Cukierman, 2006)).

8.1 "Outer-sphere" scheme

During the first half-reaction, one superoxide is converted to molecular oxygen while the active-site metal is reduced. Coupled to this is the uptake of a proton. However, the location of proton uptake is unknown. The site of proton uptake is likely an amino-acid side-chain that can readily accept protons at physiological pH ranges. The other requirement for the site of proton uptake is that it be located close to the solvent. In this outer-sphere scheme, Equation 17 can be further expanded, with the site of proton uptake being "SOD" not an hydroxide as shown in Equation 20 for the outer-sphere mechanism.

$$Mn^{3+} + O_2^- \rightarrow Mn^{2+} + O_2$$

Equation 27

$$H^+ + SOD \rightarrow H^+SOD$$

Equation 28

There is coupling between Equation 27 and Equation 28. The second half-reaction, Equation 18, can be expanded to show the individual pathways for three reaction substrates: a proton, an electron and superoxide. For further reactions to proceed a superoxide anion moves into the active site.

$$Mn^{2+} \rightarrow Mn^{3+} + e^-$$

Equation 29

$$H^+SOD \rightarrow H^+ + SOD$$

Equation 30

The released proton is distant to the active site, but since proton transfer is rapid through water (Williams, 2002), there is little energy penalty for it to "diffuse" rapidly to the active site.

$$O_2^- + H^+ + e^- \rightarrow HOO^-$$

Equation 31

Before the procession of products from Equation 30 and Equation 29 can be utilised as substrates in Equation 31, the second superoxide anion must move into the active site. Equation 31 yields a peroxo species, which then diffuses away from the active site, to pick up a second proton from the solvent, to generate hydrogen peroxide.

$$HOO^- + H^+ \rightarrow H_2O_2$$

Equation 32

The final step, Equation 32, does not occur at the active site as there is no clear pathway for a proton to reach the peroxo species. It is feasible that the final step occurs in the solvent-access funnel.

8.2 Sequence of events in the outer-sphere mechanism of proton transfer

The early stages of the outer-sphere scheme are almost identical to those of the inner-sphere scheme, so are not depicted as individual images. The initial association of superoxide to Mn^{3+} occurs in a manner similar to that depicted in Figure 7-2 and Figure 7-3, and is likely to be a high-entropy state reminiscent of that seen in *Thermus*-MnSOD-N_3^- and *Ec*-Mn-FeSOD-N_3^-. In this reaction scheme the site of proton uptake is unknown but it is distant from the active-site metal. Importantly, it is not the coordinated hydroxide, the glutamine or the solvent-access funnel tyrosine.

8.2.1 Divergence from the inner-sphere mechanism

Just prior to the first catalysis step in the outer-sphere proton-transfer scheme, refer to Figure 8-1 (similar to that seen in the inner-sphere mechanism in Figure 7-4), superoxide moves close to the active-site metal and binds in a low-entropy state with the tail of the superoxide located in a small cavity. In the outer-sphere mechanism the conserved tyrosine and glutamine have structural roles but do not have roles in catalysis. During catalysis the coordinated hydroxide also does not participate directly, but it is likely that bond distance to the metal changes during catalysis.

This structure is inferred from *Deino*-MnSOD-N_3^- and FeSODs complexed with azide.

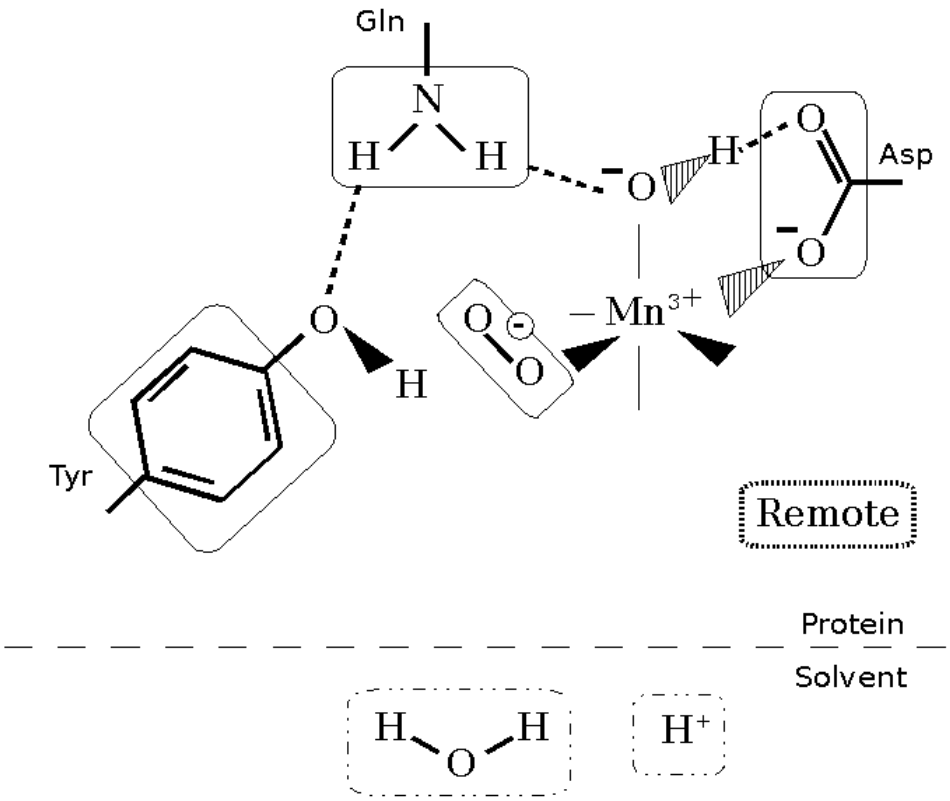

Figure 8-1. Binding of superoxide in the low-entropy state for the first half-reaction of the outer-sphere mechanism.

Figure 8-1 is a schematic representation of the active site of an MnSOD. In this representation the point of view is looking down the solvent-access funnel. The substrate superoxide has bound in a low-entropy state, similar to that seen in Figure 7-4. The distant site where proton uptake will occur is labelled “remote”. The other substrate for the first half-reaction, a proton, exists in the bulk solvent as does a structurally important water. Figure 8-1 is the first in a series detailing a proposed outer-sphere proton-transfer mechanism.

8.2.2 Water moves into the active site

Concurrent with the binding of superoxide in the low-entropy state, a water molecule moves into the active site; refer to Figure 8-2. This active-site structure is reminiscent of the binding pattern seen in *Deino*-MnSOD-N_3^-. The water molecule acts to stabilise the position of superoxide close to the metal centre. The movement of the water molecule into the active site will alter the hydrogen-bonding structure of the nearby water molecules.

Changes in the structure of the water molecules in the solvent-access funnel could act as the necessary communication pathway between the active site and remote site of reduction-coupled proton uptake.

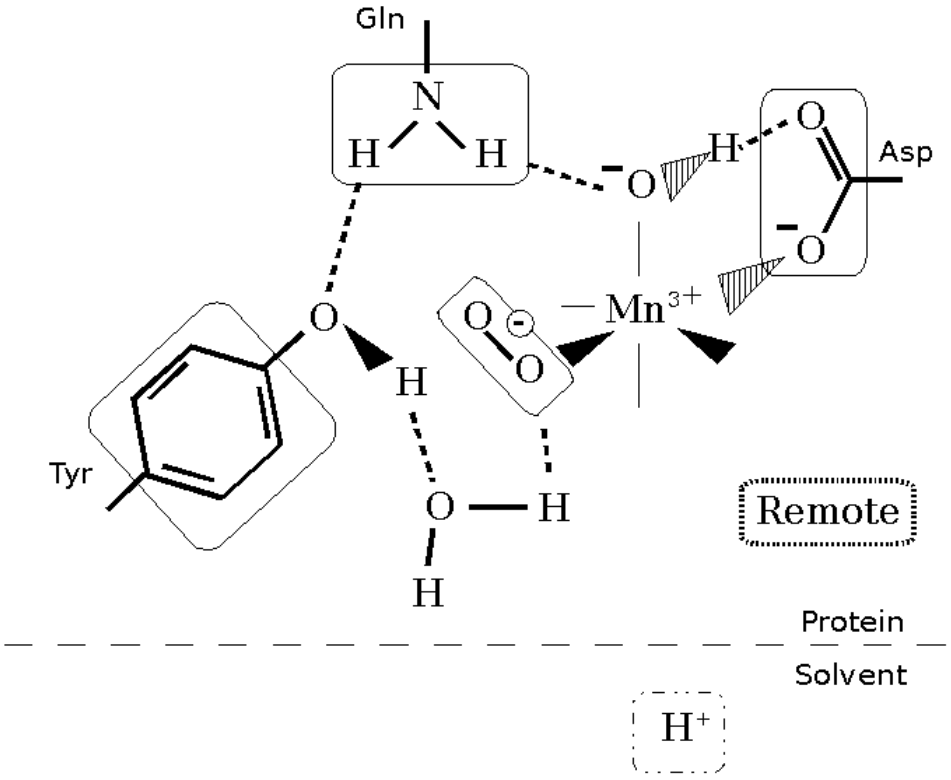

Figure 8-2. Arrival and binding of water to the superoxide ion for the first half-reaction of the outer-sphere mechanism.

Figure 8-2 shows a water molecule that has moved into the active site from the solvent to form hydrogen bonds to both the "head" of the superoxide ion and the hydrogen of the solvent-access funnel tyrosine. In the outer-sphere proton-transfer mechanism this water molecule provides the link from the bulk solvent to the active site, as well as to the remote site via other water molecules.

8.2.3 First catalysis step in the outer-sphere mechanism

Catalysis occurs when an electron is passed from the superoxide anion, leaving molecular oxygen, to the cation reducing it, refer to Figure 8-3. Distant from the active site, a proton is taken up at a remote site. The exact nature of communication between the active site and the site of proton uptake is not known. There are two strong possibilities.

The loss of a negative charge at the "head" of polar superoxide converts it to a non-polar diatomic oxygen. This will disrupt the hydrogen bond to the nearby water molecule, and in turn disrupt the hydrogen bonding of the solvent-access funnel and the remote site of proton uptake. The reduction at the active-site cation changes the charge density at the metal and surrounding ligands, which alters bond angles and lengths of coordinated ligands. This will, in turn, alter the hydrogen bonds in the first coordination shell. This change is transferred through the peptide and/or through a chain of water molecules to the remote site of proton uptake.

Diatomic oxygen then diffuses away from the active-site, leaving the enzyme reduced and the remote site protonated, ready for the second catalysis.

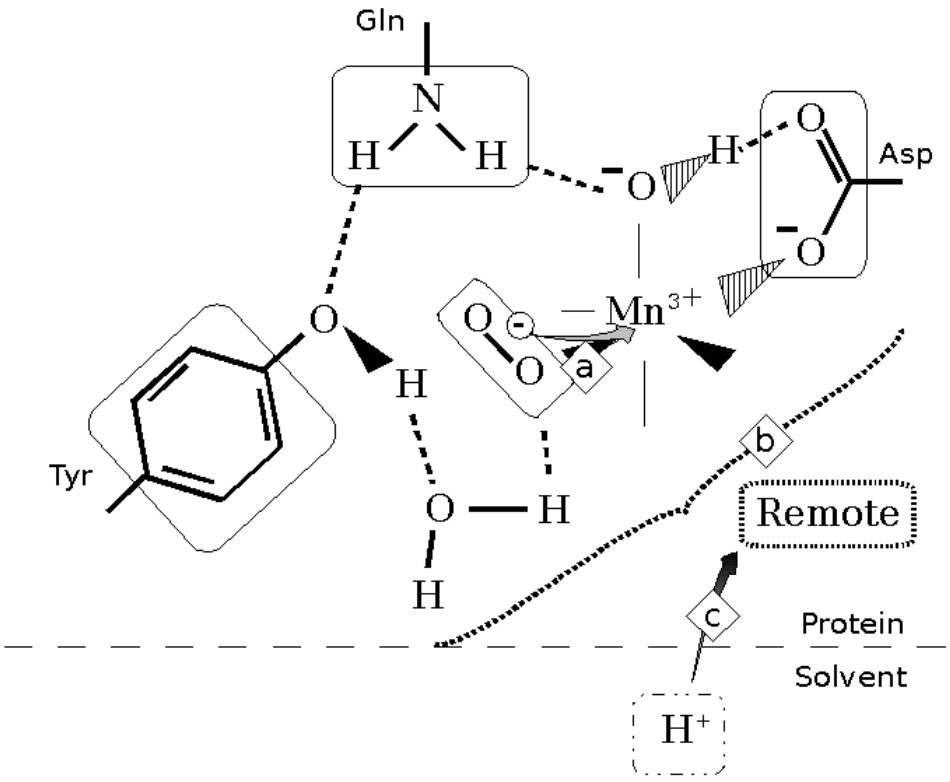

Figure 8-3. Coupled electron and proton transfer in the first half-reaction of the outer-sphere mechanism.

Figure 8-3 shows the catalytic step for the first half-reaction in the outer-sphere mechanism. An electron is transferred through a bond from superoxide to Mn^{3+}, shown by the grey arrow labelled "a", reducing it to Mn^{2+}. This perturbs the active site; this information is transferred to the remote site, indicated here by the angled bracket labelled "b". At the remote site a proton moves from the bulk solvent onto the protein, indicated by the arrow labelled "c". After reduction the diatomic oxygen and "associated" water can move away from the active-site.

8.2.4 Outer-sphere mechanism, prior to association of second superoxide

Prior to the second catalysis step the metal centre is reduced and the remote site is protonated; refer to Figure 8-4. The substrates for the second half-reaction, superoxide and a proton, are present in the solvent. A water molecule will also move into the active site during the second catalysis step.

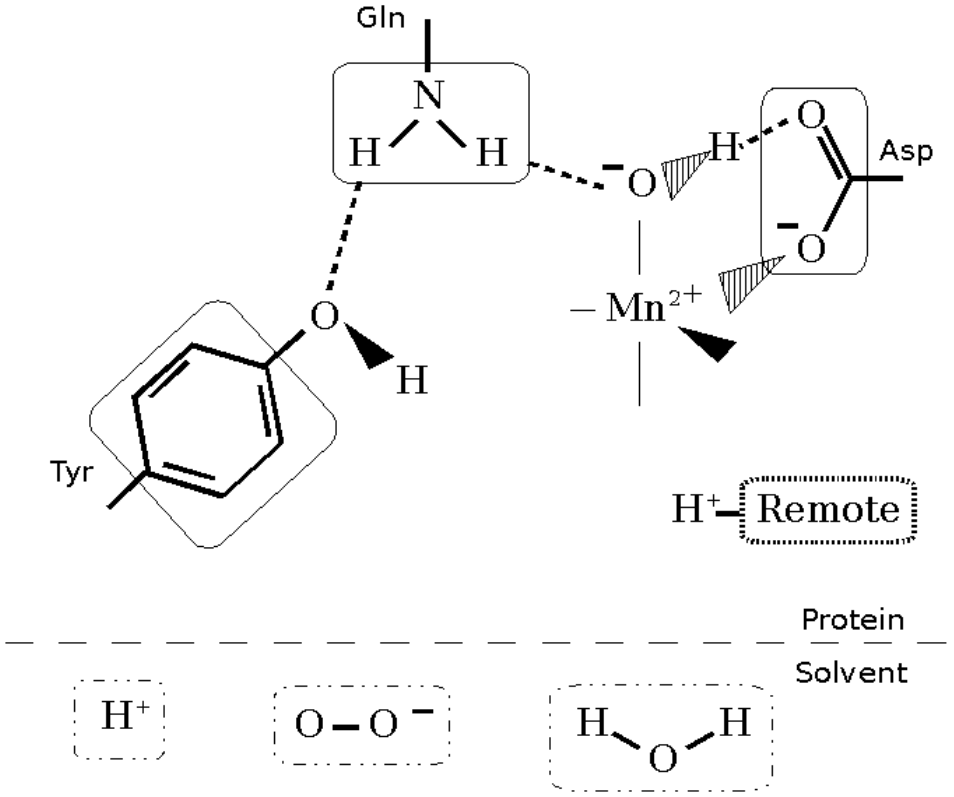

Figure 8-4. Starting state for the second half-reaction of the outer-sphere mechanism.

Figure 8-4 shows the penta-coordinate active site of Mn^{2+}SOD prior to the second half-reaction in the outer-sphere mechanism. The remote site is protonated. This is in contrast to the inner-sphere mechanism where the coordinated solvent-derived molecule is the site of proton uptake; refer to Figure 7-8. Two substrates, superoxide and a proton, are depicted as being located in the bulk solvent. Also shown is a water molecule that will move into the active site during the reaction cycle.

8.2.5 Superoxide and water associate prior to second catalysis step

Negatively charged superoxide is drawn into the active site towards the positive microenvironment located near the bound cation. The initial binding may be a high-entropy state. The remote proton uptake site, now more positively charged with a proton, may also help to attract the anion. The superoxide then rotates into the low-entropy binding mode. A water molecule moves into the active site and forms hydrogen bonds with both the nearby tyrosine and the "head" of the bound superoxide; refer to Figure 8-5. This water molecule completes a path for the movement of the proton bound at the remote site to the stabilised "head" of the bound superoxide. It is also unclear whether the interaction between the superoxide and the reduced manganese cation is a covalent bond rather than close interaction, as explained in section 7.6. In Figure 8-5 a weak bond has been depicted.

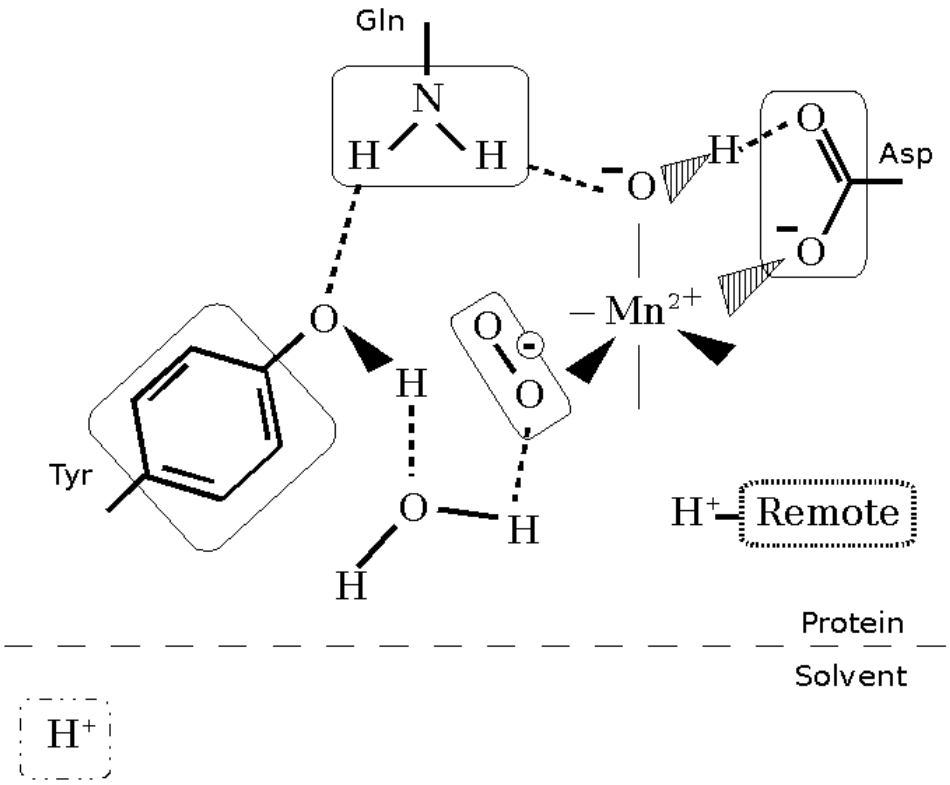

Figure 8-5. Binding of water and superoxide in the second half-reaction of the outer-sphere mechanism.

Figure 8-5 shows the association of the substrate, superoxide, with the metal centre in a low-entropy binding state. A water molecule has also moved into the active site to make a hydrogen bond to both the "head" of the superoxide. One set unpaired electrons of the oxygen atom of the water molecule also receive a hydrogen bond from the tyrosine of the solvent-access funnel. The other set of unpaired electrons is predisposed to receive a hydrogen bond from water molecules as shown in Figure 8-6.

The structure of the active site with superoxide and associated water molecule is inferred from the structure of *Deino*-MnSOD-N_3^-. The water molecules of the solvent access funnel are also well ordered, as shown in Figure 4-19; this means that a Grötthus pathway can form, shown in Figure 8-6, that links the superoxide ion to the remote site of proton uptake.

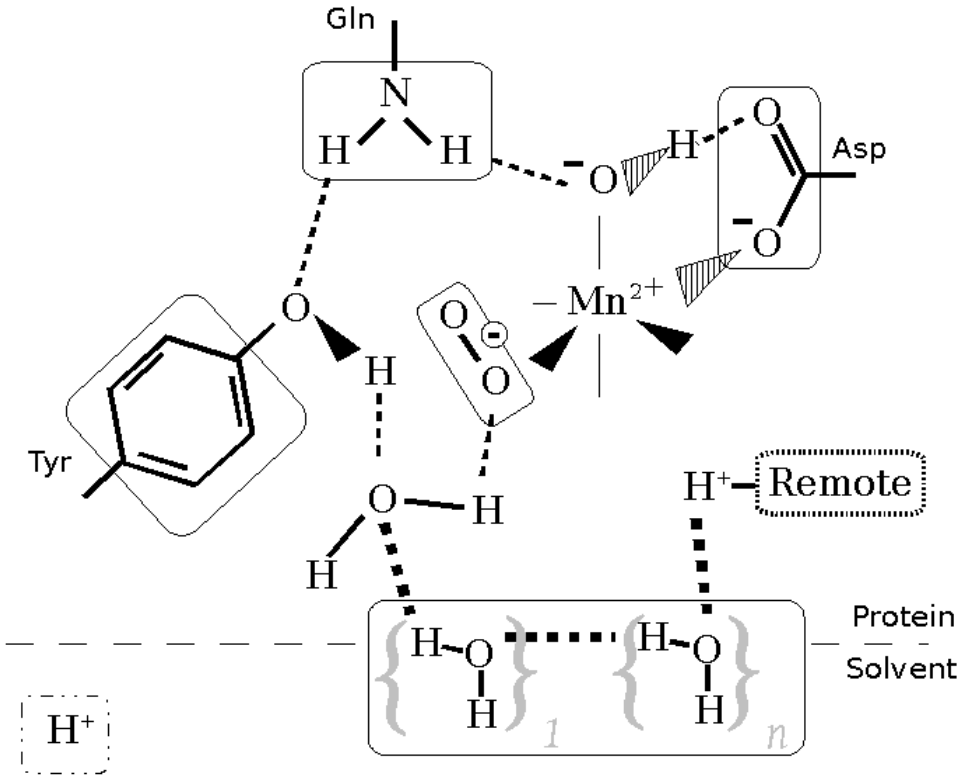

Figure 8-6. Ordered water linking the superoxide ion to the remote site of proton uptake.

Figure 8-6. After fhe binding of superoxide and the tyrosine-stabilised water molecule, a chain of ordered water molecules now links the remote site of protonation to the superoxide ion. The superoxide-associated water is unlabelled, the next water molecule of the proton transfer pathway is labelled *1* and the water molecule closest to the site of proton uptake is labelled *n.* It is unclear how many water molecules are involved in the Grötthus mechanism. This conformation represents the active site just prior to electron transfer.

8.2.6 Second catalysis in the outer-sphere mechanism

When the second catalysis occurs, refer to Figure 8-7, an electron passes from the metal centre to the bound superoxide. Almost simultaneously this change is transmitted to the remote site and the proton is rapidly transferred to the stabilised water, via the Grötthus mechanism (Cukierman, 2006). A proton then passes from the tyrosine-stabilised water, or rather a transitory H_3O^+, to the bound superoxide generating a peroxo species.

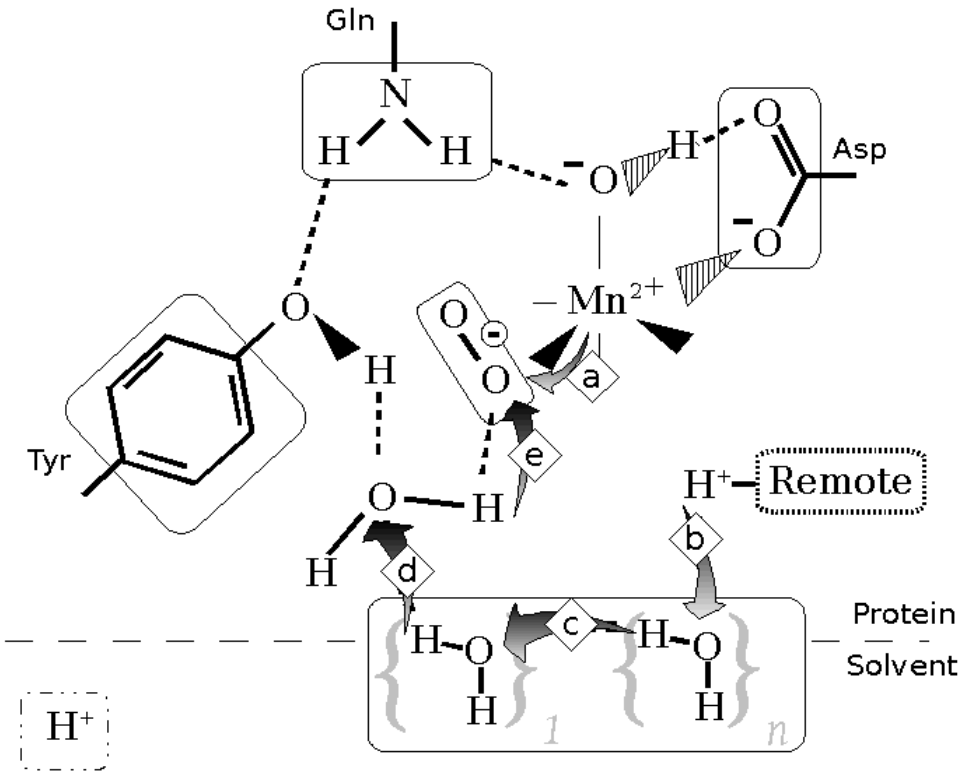

Figure 8-7. Coupled electron and proton transfer in the second half-reaction of the outer-sphere mechanism.

Figure 8-7 shows the second catalytic step in the proposed outer-sphere mechanism. Electron transfer from the reduced cation to the nearby superoxide is shown by the grey arrow labelled "a". This triggers the release of a proton from the remote-site into the ordered solvent (labelled *n*), indicated by an arrow labelled "b". This proton moves through the solvent to the nearby water (labelled *1*) by a Grötthus mechanism, shown as an arrow labelled "c". At the end of the chain of ordered water molecules a proton is passed onto the tyrosine-stabilised water forming a transitory H_3O^+, shown by arrow labelled "d". A proton then passes from the tyrosine-stabilised H_3O^+ onto the "head" of the bound superoxide, indicated by the arrow labelled "e". Once the superoxide has acquired a proton and an electron a peroxo species is formed.

In the second catalysis step there is a "domino effect" that results in the movement of a proton which propagates from one water molecule to the next. Thus, as the proton moves, hydrogen bonds are converted into covalent bonds while previous covalent linkages are coverted into hydrogen bonds. The ultimate proton source for this pathway is the remote site of proton uptake and the ultimate proton sink is the nascent peroxo species. The proton environment after the second catalysis is shown in Figure 8-8, which shows that individual protons have moved very little distance, relative to Figure 8-6, but the bonding arrangement has changed.

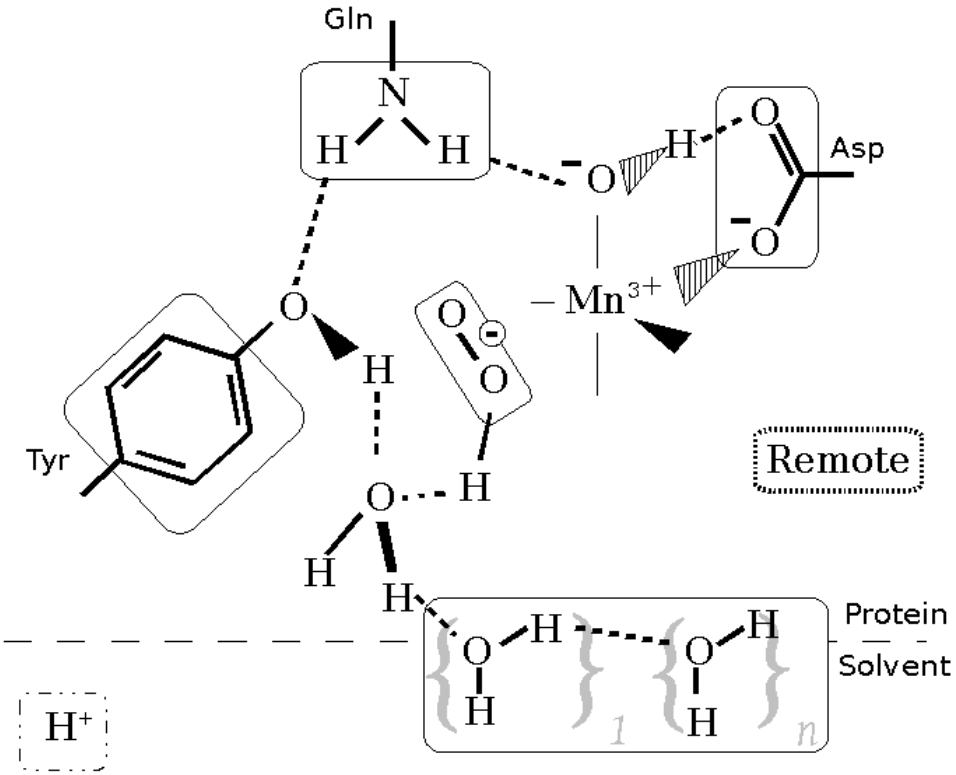

Figure 8-8. Arrangement of protons after the second catalysis step of the outer-sphere mechanism.

Figure 8-8 shows the active site with the product of the second catalysis, a peroxo ion, at the active site instead of superoxide. There has been a clockwise movement of protons relative to those shown in Figure 8-6.

8.2.7 Elimination of the peroxo species

Once the peroxo species has moved into the solvent, a second proton is able to react to form hydrogen peroxide; refer to Figure 8-9. In the outer-sphere mechanism, it is unlikely that a second proton can reach the nascent peroxo molecule when it is bound to the active-site metal with its “tail” buried in a cavity. The departure of the peroxo species from the active site leaves the enzyme oxidised and deprotonated.

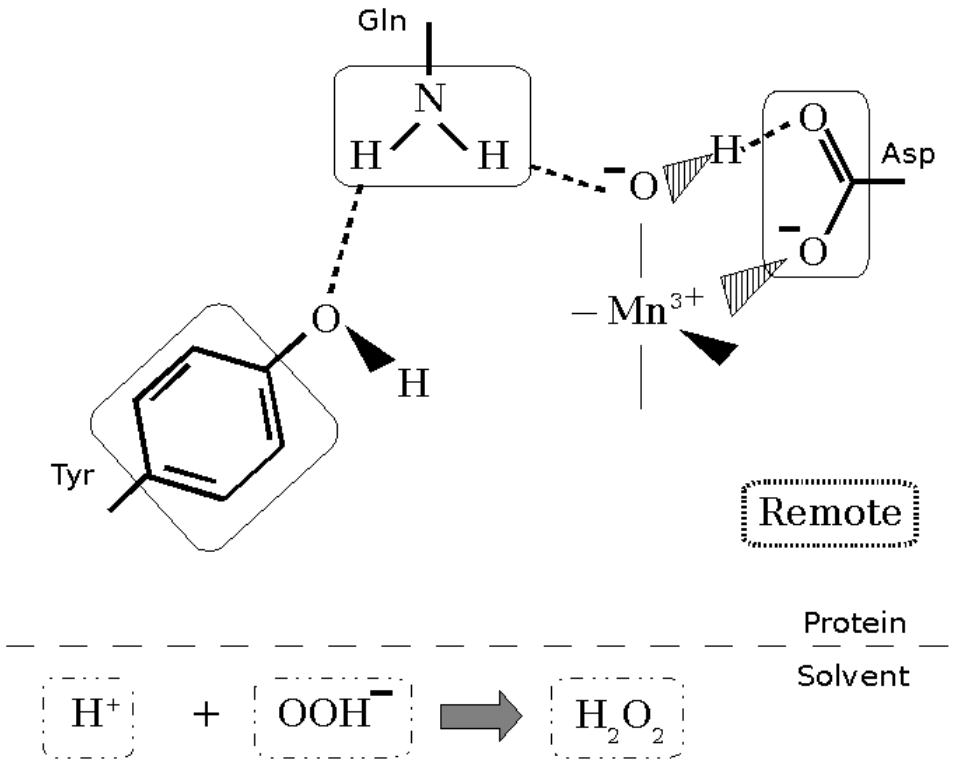

Figure 8-9. Final protonation of the peroxo species in the second half-reaction of the outer-sphere mechanism.

Figure 8-9 shows the final stages of the second half-reaction, where the elimination of the peroxo species occurs in the solvent and not at the active site. This is indicated by the reaction between peroxo species and a proton to give hydrogen peroxide. The rest of the active site has returned to the starting state, the cation is oxidised and the remote site lacks a proton.

8.3 Potential ambiguities in the outer-sphere mechanism

The outer-sphere mechanism proposed is potentially ambiguous at some points. Potential ambiguities may be difficult to resolve experimentally as they involve extremely transitory states.

In the second half-reaction it is implied that proton transfer to the superoxide occurs only after superoxide is bound to the metal. This may not be the case, as when the negatively charged superoxide passes by the bound positive proton it could pull the proton off the peptide side chain, in particular, if the site of proton uptake is located in the solvent-access funnel. If this occurs, then the superoxide-proton conjunct, a powerful oxidant, would move into the active site, and pull an electron off the Mn^{2+}.

In the outer-sphere mechanism the site of proton uptake is not the active site and may be quite distant from the cation. Active-site reduction may predispose MnSOD to uptake a proton rather than absolutely require proton uptake as in the inner-sphere mechanism. Therefore the stoichiometry of proton uptake to active-site reduction does not have to be

strictly one to one. Different side chains may be the site of proton uptake at different pH ranges. At low pH, there may be no site of proton uptake at all, with protons being supplied from the solvent directly.

As MnSODs are dimers so the site of proton uptake is likely duplicated. It is unclear if the site of proton uptake is in the same monomer as the active site that is reduced. This may be particularly true of tetramers, which could potentially have double the sites of proton uptake respective to dimers. This potential cooperativity across monomers may be responsible for the high catalytic activity in Mn/FeSODs.

8.3.1 Location of the remote site of proton uptake

There are many candidate locations for the site of proton uptake. The ultra-high resolution structures of oxidised and reduced Y174F-*Ec*-MnSOD (1IX9 and 1IXB respectively) show minor redox-dependent structural changes. Close to the active site there are minor differences in the structure of the solvent molecules and there are also more remote differences that indicate a rearrangement of hydrogen-bonding networks associated with proton uptake; refer to Figure 8-10. Each of these are potential candidates for the site of proton uptake.

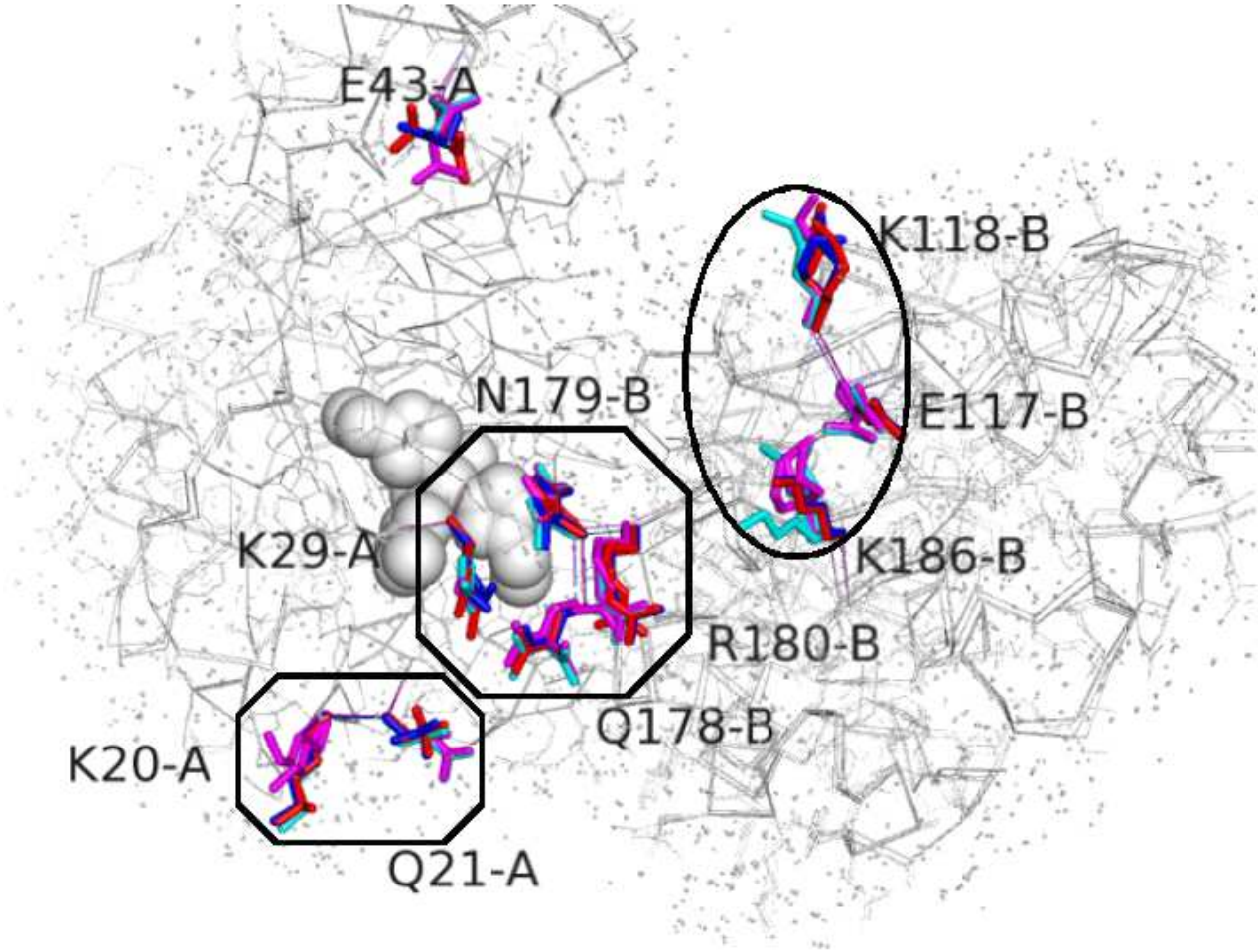

Figure 8-10. Reduction/oxidation linked changes in selected side chains of Y174F-*Ec*-MnSOD.

Figure 8-10 shows an overlay of four subunits from an ultra-high resolution study of the oxidised (1IX9) and reduced (1IXB) forms of Y174F-*Ec*-MnSOD. The overlay was performed using the CA atoms of one half of the obligate dimer (the left side of the image) while atoms from the other half of the dimer were not overlaid (the right side of the image). Hence the overlay in the left-side of the image appears more tightly overlaid. The backbone of each protein is shown as a grey C-alpha trace while irrelevant side-chains are shown as grey sticks. The metal ion and five metal-binding ligands are shown as space-filling spheres. Water molecules are shown as very small grey spheres. There was generally high agreement between water molecules and side chains of each monomer with those of other monomers. Where there were substantial and interesting differences; these residues have been shown as coloured sticks. The numbering scheme assumes that the monomer on the left is the A chain and the monomer on the right is a B chain. The red sticks represent side-chain orientations derived from chain A of Y174F-*Ec*-Mn^{3+}-SOD. The magenta-coloured sticks represent side-chain orientations derived chain B of Y174F-*Ec*-Mn^{3+}-SOD. The blue-coloured sticks represent side-chain orientations derived chain A of Y174F-*Ec*-Mn^{2+}-SOD. The cyan-coloured sticks represent side-chain orientations derived chain B of Y174F-*Ec*-Mn^{2+}-SOD. Comparing red to magenta will show differences between the A chain and B chain of the oxidised state. In a similar fashion comparing blue to

cyan will show differences between the A chain and B chain in the reduced form. Comparing red to blue and magenta to cyan coloured will highlight effects which are dependent on reduction state.

Four regions of high variability are shown. The closest to the active-site is shown bound by an octagon including *A*_K29, *B*_Q178, *B*_N179 and *B*_R180. The second region of interest is bound by a smaller octagon that includes residues *A*_K20 and *A*_Q21. The third region of interest is found on the adjacent monomer and is bound by an ellipse that includes *B*_E117, *B*_K118 and *B*_K186. There are also remote consequences of changes in redox state, as shown by *A*_E43.

Another candidate for the site of proton uptake is the asymmetric hydrogen environment at the dimer interface: refer to Figure 6-15. There is a narrow channel that links the solvent molecules close to the active site to the buried solvent molecules of the dimer interface; refer to Figure 8-11, and in turn to the solvent molecules of the other monomer subunit. One of the residues that gate this narrow channel is a conserved glutamate, number 170 in *Ec*-MnSOD, which protrudes from one of the monomer units into the active site of the other. This glutamate may play a role in proton transfer between the bulk solvent, buried waters and the active site. Glutamate readily accepts and donates protons at physiological pH ranges.

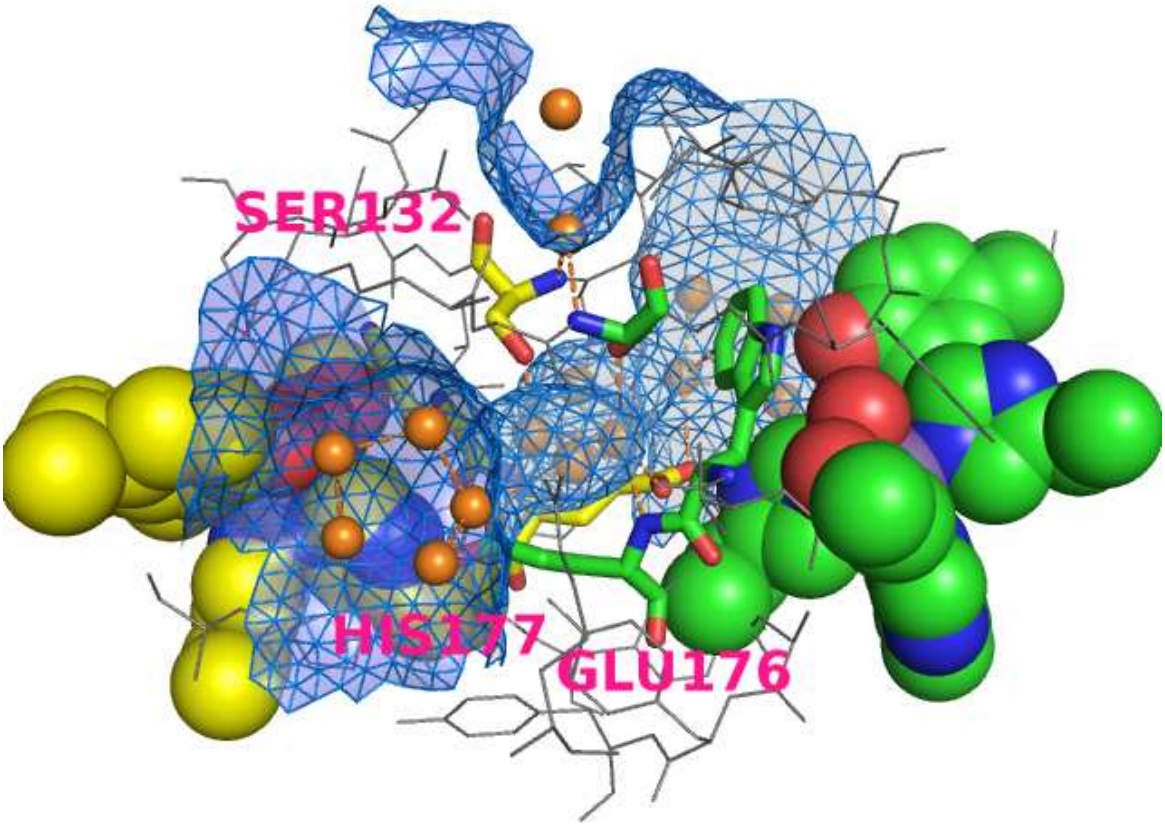

Figure 8-11. The active sites of the dimer of *Deino*-MnSOD and the waters that line the dimer interface.

Figure 8-11. The solvent-access funnel tyrosine, four active-site residues, coordinated hydroxide and the active-site manganese are depicted as large space-filling spheres. The residues of the dimer interface that create an inherently asymmetric environment, as shown in Figure 6-15, are shown as thick sticks. Other residues are shown as thin black sticks. Water molecules that line the dimer interface are shown orange spheres. The blue mesh and transparent surface show a narrow tunnel between the solvent-access funnel of one active site to the other via the asymmetric dimer interface.

8.4 Implications of an outer-sphere mechanism

In the inner-sphere mechanism, active-site reduction changes the nature of the bond between the cation and the hydroxide, implying direct coupling of electron transfer to protonation of the hydroxide ligand. In contrast, in the outer-sphere mechanism the site of proton uptake is located distant to the site of catalysis. This implies there may not be direct coupling of electron uptake at the metal centre with a remote proton uptake; rather there may be an indirect coupling or weak coupling. The outer-sphere mechanism is therefore more disordered than the stringent inner-sphere mechanism.

Weak coupling of proton uptake to reduction implies that proton uptake could occur at any point: before the first superoxide associates, before reduction, during reduction, after reduction, after oxygen leaves, or even just before the second superoxide associates. This may have favourable consequences for the temporal coordination of reaction processes, as the arrival of substrates and departure of products are less regimented.

8.5 Potential differences between FeSODs and MnSODs in the outer-sphere mechanism

The outer-sphere mechanism presented above is intended primarily to explain MnSODs, but it could also be extended to FeSODs. In the outer-sphere mechanism the potential differences between FeSODs and MnSODs are similar to those presented above in section 7.7, in which the differences between the two families of SODs manifest as differences in hydrogen-bonding networks. Whether this is due to the bound metal ion modifying hydrogen bonds, or to inherent differences in the hydrogen-bonding network derived from the different amino-acid sequences, and water structure, is not clear.

This is evident in the different role that the solvent-access funnel tyrosine plays between FeSODs and MnSODs. In addition to its structural roles, in the outer-sphere mechanism presented above the solvent-access funnel tyrosine stabilises the proton-transfer

pathway in the second half-reaction by hydrogen-bonding to a water. Mutation of this tyrosine to a phenylalanine severely decreases activity in FeSODs but only slightly diminishes activity in MnSODs. In MnSODs the solvent-access funnel tyrosine is not absolutely required for structural and stabilising roles. However, it is hard to say whether the equivalent mutation in FeSODs affects structural roles or disrupts a proton-transfer network. Other chief differences between FeSODs and MnSODs are differences in inhibitor specificity and product inhibition. These differences are likely due to differences in the environment around the active-site metal, which will be determined by both the metal bound and the amino-acids surrounding the active site.

8.6 Evidence in support of the outer-sphere proton-transfer mechanism

The advantage of the outer-sphere scheme is that the three members of the hydrogen-bonding network (tyrosine, glutamine, and solvent-derived hydroxide) that link the solvent to the hydroxide have a structural role and not a catalytic role. This may explain why mutants of the solvent-access tyrosine and glutamine in MnSODs have diminished but not abolished activity (Edwards *et al.*, 2001a), as they are not absolutely required for proton transfer.

Proton transfer through water is an extremely fast process, whereas proton transfer through proteins is largely dependent on local protein structure and is inherently much slower. This is particularly true of the glutamine which provides a substantial energy barrier for proton transfer, as it lacks capacity to accept or donate a proton. The outer-sphere mechanism is independent of through-protein proton transfer. The outer-sphere mechanism does not introduce a potential steric clash with a neighbouring tryptophan when converting the bound hydroxide to a water molecule; refer to Figure 7-14 and Figure 7-16. Hydroxide does not have a direct catalytic role in outer-sphere mechanism, rather it has a structural role and a role in controlling the reduction potential of the manganese ion.

As noted earlier the outer-sphere mechanism is less rigid than the inner-sphere mechanism as the coupling between the active-site reduction and proton uptake is implied to be weaker. This may be better suited for fast turnover of superoxide as the association of superoxide anions and protons with the enzyme may become virtually independent processes with little crosstalk.

8.7 Evidence against the outer-sphere proton transfer

There is much evidence, mostly inferred from spectroscopic disciplines, that the solvent-derived molecule is an hydroxide that takes up a proton to form a coordinated water molecule when the metallo-enzyme is reduced (Miller *et al.*, 2003). So the outer-sphere scheme does not conform to this accepted dogma as the coordinated solvent molecule remains an hydroxide throughout both half-reactions.

The site of proton uptake is unknown in the outer-sphere scheme, but it is located away from the active-site metal. This means that at the end of the first half-reaction the active-site is less positively charged as it has acquired an electron during the first catalysis step, lessening the attraction between the active-site and an incoming superoxide during the second half-reaction. This is in contrast to the inner-sphere mechanism where a positive charge, in the form of a proton, is also taken up with the electron during first half-reaction maintaining a positive charge in the vicinity of the active site. On the other hand, if the site of remote proton uptake is in the solvent-access funnel, then upon reduction the subsequent proton uptake at the solvent-access funnel will act to make the solvent-access funnel more positive, attracting the superoxide.

9 Conclusions and future directions

Broad research targets were given in section 2.21 and specific research targets were given in section 2.22. In this final chapter I comment on the results obtained with respect to those targets and finally make suggestions for further research

9.1 Conclusions

The active-site residues of *Deino*-MnSOD are almost identical to those of *Ec*-MnSOD and *mito*-MnSOD despite major differences in by-product inhibition. There are, however, detectable differences in the size of the substrate-binding cavity that may preclude the formation of by-product at the active site and allow *Deino*-MnSOD to function in concentrations of superoxide that would saturate other MnSODs.

There are at least two azide-binding motifs seen in the Fe/MnSODs. The most commonly detected motif, seen in *Psherm*-FeSOD-N_3^-, *Ec*-FeSOD-N_3^-, Y174F-*Ec*-MnSOD-N_3^- and *Deino*-MnSOD-N_3^-, possibly represents a low-entropy state which is likely analogous to a transition state for superoxide binding to oxidised enzyme, the other motif seen in *Thermus*-MnSOD-N_3^- and *Ec*-Fe-MnSOD-N_3^- represents a high-entropy state that is analogous to initial superoxide association or a by-product inhibited species. A major difference between the structures of *Deino*-MnSOD-N_3^- and *Thermus*-MnSOD-N_3^- is the temperature of data collection. This supports spectral studies described in sections 2.14 and 6.4.8 that show temperature-dependent changes in active-site structure in azide-inhibited MnSODs, but not in azide-inhibited FeSODs. However, a likely interpretative bias in the structure determination of *Thermus*-MnSOD-N_3^- may affect any conclusions derived from this structure.

The binding of azide occurs in a high-entropy state in *Ec*-Fe-MnSOD-N_3^-, not in the low-entropy state, even though the temperature of data collection was at cryogenic temperatures. This indicates that the *Ec*-Fe-MnSOD may be thermodynamically perturbed from both *Ec*-MnSOD and *Ec*-FeSOD and precluded from forming a low-entropy state of azide, and by inference superoxide. The basis for this thermodynamic fine tuning in FeSODs and MnSODs is likely due to differences in primary amino acid sequence, though which residues are responsible remains unknown. Incorrect thermodynamic tuning in metal-substituted Fe/MnSODs relative to correct metal forms may also explain observed differences in reduction potentials, coordination number and inhibitor specificity.

At first glance the structure of the obligate dimer of Fe/MnSODs appears to be symmetrical. However, there is an inherent asymmetry at the dimer interface. This is caused by an asymmetrical hydrogen bond across the dimer interface between the OH group of two pseudo-symmetry equivalent serines. This asymmetry appears highly conserved which may, in part, explain why a large number of solved Fe/MnSODs structures have slight asymmetries across dimer partners and all crystallise as dimers.

A previously proposed inner-sphere mechanism for proton transfer may not apply to MnSODs as it relies on an unfavourable through-protein proton pathway to an unfavourable proton uptake site to form an Mn^{2+} species. An outer-sphere mechanism, which relies on through solvent proton transfer, lacks these hindrances and is potentially much faster. The other advantage of an inner-sphere mechanism is that there is negligible rearrangement of the active-site during catalysis; this is one of the hallmarks of kinetically-perfect enzymes. During normal turnover, active-site atoms move very little when one active-site cation changes oxidation state. Most of the structural rearrangement occurs in solvent structure with proton uptake occuring distant to the active site.

Exhaustive, but unsuccessful, efforts have been made to collect a room temperature *Deino*-MnSOD-N_3^- structure; this may be difficult to achieve using this crystal system.

9.2 Future directions and experiments

9.2.1 Specific to results presented in this thesis

The four mutants of *Ec*-MnSOD need to be further refined structurally. They also need to be biochemically characterised in terms of pH dependence, specific activity, inhibitor specificity, metal specificity and product inhibition.

9.2.2 The entire Fe/MnSOD field

In the future it may be possible to design a SOD *de novo*. However, despite an abundance of structural information there is still no cohesive theory as to how the Fe/MnSODs actually function. The definitive test of this will be to create a rationally-designed gain-of-function mutant through minimal number of mutations. There are many possible gain-of-functions, such as converting an MnSOD into an FeSOD or reducing product inhibition in an inhibition-prone MnSOD such as *mito*-MnSOD. There have been many studies that have produced loss-of-function Fe/MnSODs. But, by analogy, it is easier to break a wrist-watch than to mend a broken one, or to improve the basic design.

The temperature dependence of azide binding in MnSODs needs to be further investigated using crystallographic techniques. It would be desirable to have a high resolution structure at ambient temperature of MnSOD with azide at the active site and the same MnSOD with azide at cryogenic temperatures so that temperature-dependent differences can be detected. The lack of a structure of *Ec*-MnSOD with azide is also problematic as this is the best characterised MnSOD.

The asymmetric environment of the dimer interface needs to be further investigated, as it is a potential communication pathway. This could be done by generating point mutants of contributing residues, such as the strongly conserved serine, hopefully to disrupt the solvent structure. Alternately Fe/MnSOD members from the *Halobacterium* family could be solved as they have a unique dimer interface that lacks the conserved serine.

The positions of hydrogen atoms within the Fe/MnSODs and associated solvent-derived molecules need to be accurately determined and how they change with pH, oxidation/reduction, metal substitution and inhibitors. The best current technique for this is neutron crystallography. Another approach would be to use NMR to elucidate the position of hydrogen atoms within the peptide, but this would not provide any information on solvent molecules or active-site metals.

10 References

Abreu, I. A., Hearn, A., An, H., Nick, H. S., Silverman, D. N. & Cabelli, D. E. (2008). The Kinetic Mechanism of Manganese-Containing Superoxide Dismutase from *Deinococcus radiodurans*: A Specialized Enzyme for the Elimination of High Superoxide Concentrations,
Biochemistry Vol. 47, (8) 2350-2356.

Adams, P. D., Grosse-Kunstleve, R. W., Hung, L. W., Ioerger, T. R., McCoy, A. J., Moriarty, N. W., Read, R. J., Sacchettini, J. C., Sauter, N. K. & Terwilliger, T. C. (2002). *PHENIX:* building new software for automated crystallographic structure determination,
Acta Crystallographica Section D-Biological Crystallography Vol. 58, 1948-1954.

Anderson, A. W., Nordan, H. C., Cain, R. F., Parrish, G. & Duggan, D. (1956). Studies on a Radio-Resistant Micrococcus .1. Isolation, Morphology, Cultural Characteristics, and Resistance to Gamma Radiation,
Food Technology Vol. 10, (12) 575-578.

Antoniou, D., Caratzoulas, S., Kalyanaraman, C., Mincer, J. S. & Schwartz, S. D. (2002). Barrier passage and protein dynamics in enzymatically catalyzed reactions,
European Journal of Biochemistry Vol. 269, (13) 3103-3112.

Asada, K., Yoshikawa, K., Takahashi, M. A., Maeda, Y. & Enmanji, K. (1975). Superoxide Dismutases from a Blue-Green-Alga, *Plectonema-Boryanum*,
Journal of Biological Chemistry Vol. 250, (8) 2801-2807.

Baas, A. S. & Berk, B. C. (1995). Differential Activation of Mitogen-Activated Protein-Kinases by H_2O_2 and $O_2^{(-)}$ in Vascular Smooth-Muscle Cells,
Circulation Research Vol. 77, (1) 29-36.

Bailey, S. (1994). The *CCP4* Suite: Programs for Protein Crystallography,
Acta Crystallographica Section D-Biological Crystallography Vol. 50, 760-763.

Baker, N. A., Sept, D., Joseph, S., Holst, M. J. & McCammon, J. A. (2001). Electrostatics of nanosystems: Application to microtubules and the ribosome,
Proceedings of the National Academy of Sciences of the United States of America Vol. 98, (18) 10037-10041.

Barondeau, D. P., Kassmann, C. J., Bruns, C. K., Tainer, J. A. & Getzoff, E. D. (2004). Nickel Superoxide Dismutase Structure and Mechanism,
Biochemistry Vol. 43, (25) 8038-8047.

Barrett, A. J. & Rawlings, N. D. (2001). Evolutionary lines of cysteine peptidases,
Biological Chemistry Vol. 382, (5) 727-733.

Barrette, W. C., Sawyer, D. T., Fee, J. A. & Asada, K. (1983). Potentiometric Titrations and Oxidation-Reduction Potentials of Several Iron Superoxide Dismutases,
Biochemistry Vol. 22, (3) 624-627.

Benovic, J., Tillman, T., Cudd, A. & Fridovich, I. (1983). Electrostatic Facilitation of the Reaction Catalyzed by the Manganese-Containing and the Iron-Containing Superoxide Dismutases,
Archives of Biochemistry and Biophysics Vol. 221, (2) 329-332.

Berman, H. M., Westbrook, J., Feng, Z., Gilliland, G., Bhat, T. N., Weissig, H., Shindyalov, I. N. & Bourne, P. E. (2000). The Protein Data Bank,
Nucleic Acids Res Vol. 28, (1) 235-242.

Bert, P. (1878). La pression barométrique. Recherches de physiologie expérimentale,
G. Masson Paris,.

Beyer, W. F., Jr. & Fridovich, I. (1988). An Ultrasensitive Colorimetric Assay for Manganese,
Analytical Biochemistry Vol. 170, (2) 512-519.

Beyer, W. F., Jr. & Fridovich, I. (1990). Superoxide dismutase mimic prepared from desferrioxamine and manganese dioxide,
Methods in Enzymology Vol. 186, 242-249.

Beyer, W. F., Jr. & Fridovich, I. (1991). *In vivo* competition between iron and manganese for occupancy of the active site region of the manganese-superoxide dismutase of *Escherichia coli*,
Journal of Biological Chemistry Vol. 266, (1) 303-308.

Bhat, T. N. (1989). Correlation between occupancy and temperature factors of solvent molecules in crystal structures of proteins,
Acta Crystallographica Section A Vol. 45, 145-146.

Birney, E., Stamatoyannopoulos, J. A., Dutta, A., Guigo, R., Gingeras, T. R., Margulies, E. H., Weng, Z. P., Snyder, M., Dermitzakis, E. T., Stamatoyannopoulos, J. A., et al. (2007). Identification and analysis of functional elements in 1% of the human genome by the ENCODE pilot project,
Nature Vol. 447, (7146) 799-816.

Borgstahl, G. E., Parge, H. E., Hickey, M. J., Beyer, W. F., Jr., Hallewell, R. A. & Tainer, J. A. (1992). The structure of human mitochondrial manganese superoxide dismutase reveals a novel tetrameric interface of two 4-helix bundles.,
Cell Vol. 71, (1) 107-118.

Borgstahl, G. E., Parge, H. E., Hickey, M. J., Johnson, M. J., Boissinot, M., Hallewell, R. A., Lepock, J. R., Cabelli, D. E. & Tainer, J. A. (1996). Human Mitochondrial Manganese Superoxide Dismutase Polymorphic Variant Ile58Thr Reduces Activity by Destabilizing the Tetrameric Interface,
Biochemistry Vol. 35, (14) 4287-4297.

Borgstahl, G. E., Pokross, M., Chehab, R., Sekher, A. & Snell, E. H. (2000). Cryo-trapping the Six-coordinate, Distorted-octahedral Active Site of Manganese Superoxide Dismutase,
Journal of Molecular Biology Vol. 296, (4) 951-959.

Brent, M. R. (2008). Steady progress and recent breakthroughs in the accuracy of automated genome annotation,

Nature Reviews Genetics Vol. 9, (1) 62-73.

Brown, E. N. & Ramaswamy, S. (2007). Quality of protein crystal structures, **Acta Crystallographica Section D-Biological Crystallography** Vol. 63, 941-950.

Brünger, A. T. (1992a). X-PLOR, Version 3.1 : a system for X-ray crystallography and NMR, **Yale University Press** New Haven.

Brünger, A. T. (1992b). Free R-Value - a Novel Statistical Quantity for Assessing the Accuracy of Crystal-Structures, **Nature** Vol. 355, (6359) 472-475.

Brünger, A. T., Adams, P. D., Clore, G. M., DeLano, W. L., Gros, P., Grosse-Kunstleve, R. W., Jiang, J. S., Kuszewski, J., Nilges, M., Pannu, N. S., et al. (1998). *Crystallography & NMR system:* A New Software Suite for Macromolecular Structure Determination, **Acta Crystallogr D Biol Crystallogr** Vol. 54 (Pt 5), 905-921.

Buerger, M. J. (1942). X-ray crystallography; an introduction to the investigation of crystals by their diffraction of monochromatic X-radiation, **J. Wiley & Sons, Chapman & Hall, limited** New York, London.

Buerger, M. J. (1964). The precession method in X-ray crystallography, **Wiley** New York.

Bull, C. & Fee, J. A. (1985). Steady-State Kinetic-Studies of Superoxide Dismutases - Properties of the Iron Containing Protein from *Escherichia coli*, **Journal of the American Chemical Society** Vol. 107, (11) 3295-3304.

Bull, C., Niederhoffer, E. C., Yoshida, T. & Fee, J. A. (1991). Kinetic-Studies of Superoxide Dismutases: Properties of the Manganese-Containing Protein from *Thermus-Thermophilus*, **Journal of the American Chemical Society** Vol. 113, (11) 4069-4076.

Cabelli, D. E., Guan, Y., Leveque, V., Hearn, A. S., Tainer, J. A., Nick, H. S. & Silverman, D. N. (1999). Role of Tryptophan 161 in Catalysis by Human Manganese Superoxide Dismutase, **Biochemistry** Vol. 38, (36) 11686-11692.

Carlioz, A., Ludwig, M. L., Stallings, W. C., Fee, J. A., Steinman, H. M. & Touati, D. (1988). Iron superoxide dismutase NUCLEOTIDE SEQUENCE OF THE GENE FROM *ESCHERICHIA COLI* K12 AND CORRELATIONS WITH CRYSTAL STRUCTURES, **Journal of Biological Chemistry** Vol. 263, (3) 1555-1562.

Carlioz, A. & Touati, D. (1986). Isolation of superoxide dismutase mutants in *Escherichia coli*: is superoxide-dismutase necessary for aerobic life?, **EMBO Journal** Vol. 5, (3) 623-630.

Carrasco, R., Morgenstern-Badarau, I. & Cano, J. (2007). Two proton-one electron coupled transfer in iron and manganese superoxide dismutases: A density functional study,

Inorganica Chimica Acta Vol. 360, (1) 91-101.

Chance, B., Sies, H. & Boveris, A. (1979). Hydroperoxide Metabolism in Mammalian Organs,
Physiological Reviews Vol. 59, (3) 527-605.

Christianson, D. W. (1997). STRUCTURAL CHEMISTRY AND BIOLOGY OF MANGANESE METALLOENZYMES,
Progress in Biophysics & Molecular Biology Vol. 67, (2-3) 217-252.

Clare, D. A., Blum, J. & Fridovich, I. (1984). A Hybrid Superoxide-Dismutase Containing Both Functional Iron and Manganese,
Journal of Biological Chemistry Vol. 259, (9) 5932-5936.

Cornish-Bowden, A. (1984). Nomenclature and Symbolism for Amino-Acids and Peptides - Recommendations 1983,
European Journal of Biochemistry Vol. 138, (1) 9-37.

Cukierman, S. (2006). Et tu, Grotthuss! and other unfinished stories,
Biochimica Et Biophysica Acta-Bioenergetics Vol. 1757, (8) 876-885.

Curnutte, J. T. & Babior, B. M. (1974). Biological Defense-Mechanisms - THE EFFECT OF BACTERIA AND SERUM ON SUPEROXIDE PRODUCTION BY GRANULOCYTES,
Journal of Clinical Investigation Vol. 53, (6) 1662-1672.

Dahl, M., Bowler, R. P., Juul, K., Crapo, J. D., Levy, S. & Nordestgaard, B. G. (2008). Superoxide Dismutase 3 Polymorphism Associated with Reduced Lung Function in Two Large Populations,
American Journal of Respiratory and Critical Care Medicine Vol. 178, (9) 906-912.

de Aguilar, J. L. G., Echaniz-Laguna, A., Fergani, A., René, F., Meininger, V., Loeffler, J. P. & Dupuis, L. (2007). Amyotrophic lateral sclerosis: all roads lead to Rome,
Journal of Neurochemistry Vol. 101, (5) 1153-1160.

Dennis, R. J., Micossi, E., McCarthy, J., Moe, E., Gordon, E. J., Kozielski-Stuhrmann, S., Leonard, G. A. & McSweeney, S. (2006). Structure of the manganese superoxide dismutase from *Deinococcus radiodurans* in two crystal forms,
Acta Crystallographica Section F-Structural Biology and Crystallization Communications Vol. 62, 325-329.

Diederichs, K. & Karplus, P. A. (1997). Improved *R*-factors for diffraction data analysis in macromolecular crystallography,
Nature Structural Biology Vol. 4, (4) 269-275.

Dougherty, H. W., Sadowski, S. J. & Baker, E. E. (1978). New Iron-Containing Superoxide-Dismutase from *Escherichia coli*,
Journal of Biological Chemistry Vol. 253, (14) 5220-5223.

Dupont, C. L., Neupane, K., Shearer, J. & Palenik, B. (2008). Diversity, function and evolution of genes coding for putative Ni-containing superoxide dismutases,
Environmental Microbiology Vol. 10, (7) 1831-1843.

Dyall, S. D., Brown, M. T. & Johnson, P. J. (2004). Ancient invasions: From endosymbionts to organelles,
Science Vol. 304, (5668) 253-257.

Edwards, R. A., Baker, H. M., Whittaker, M. M., Whittaker, J. W., Jameson, G. B. & Baker, E. N. (1998). Crystal structure of *Escherichia coli* manganese superoxide dismutase at 2.1-Å resolution,
Journal of Biological Inorganic Chemistry Vol. 3, (2) 161-171.

Edwards, R. A., Whittaker, M. M., Whittaker, J. W., Baker, E. N. & Jameson, G. B. (2001a). Outer sphere mutations perturb metal reactivity in manganese superoxide dismutase,
Biochemistry Vol. 40, (1) 15-27.

Edwards, R. A., Whittaker, M. M., Whittaker, J. W., Baker, E. N. & Jameson, G. B. (2001b). Removing a hydrogen bond in the dimer interface of *Escherichia coli* manganese superoxide dismutase alters structure and reactivity,
Biochemistry Vol. 40, (15) 4622-4632.

Edwards, R. A., Whittaker, M. M., Whittaker, J. W., Jameson, G. B. & Baker, E. N. (1998). Distinct Metal Environment in Fe-substituted Manganese Superoxide Dismutase Provides a Structural Basis of Metal Specificity,
Journal of the American Chemical Society Vol. 120, (37) 9684-9685.

Emsley, P. & Cowtan, K. (2004). *COOT*: model-building tools for molecular graphics,
Acta Crystallographica Section D-Biological Crystallography Vol. 60, 2126-2132.

Evans, P. (2006). Scaling and assessment of data quality,
Acta Crystallographica Section D-Biological Crystallography Vol. 62, 72-82.

Fabiola, F., Korostelev, A. & Chapman, M. S. (2006). Bias in cross-validated free *R* factors: mitigation of the effects of non-crystallographic symmetry,
Acta Crystallographica Section D-Biological Crystallography Vol. 62, 227-238.

Ferraroni, M., Rypniewski, W. R., Bruni, B., Orioli, P. & Mangani, S. (1998). Crystallographic determination of reduced bovine superoxide dismutase at pH 5.0 and of anion binding to its active site,
Journal of Biological Inorganic Chemistry Vol. 3, (4) 411-422.

Fink, R. C. & Scandalios, J. G. (2002). Molecular Evolution and Structure--Function Relationships of the Superoxide Dismutase Gene Families in Angiosperms and Their Relationship to Other Eukaryotic and Prokaryotic Superoxide Dismutases,
Archives of Biochemistry & Biophysics Vol. 399, (1) 19-36.

French, S. & Wilson, K. (1978). On the Treatment of Negative Intensity Observations,
Acta Crystallographica Section A Vol. 34, (JUL) 517-525.

Fridovich, I. (1978). The Biology of Oxygen Radicals,
Science Vol. 201, (4359) 875-880.

Fry, I. (2006). The origins of research into the origins of life,

Endeavour Vol. 30, (1) 24-28.

Gabbianelli, R., Battistoni, A., Polticelli, F., Meier, B., Schmidt, M., Rotilio, G. & Desideri, A. (1997). Effect of Lys175 mutation on structure function properties of *Propionibacterium shermanii* superoxide dismutase,
Protein Engineering Vol. 10, (9) 1067-1070.

Gilbert, W. (1986). Origin of Life: the RNA World,
Nature Vol. 319, (6055) 618-618.

Griffin, M. D. W., Dobson, R. C. J., Pearce, F. G., Antonio, L., Whitten, A. E., Liew, K., Mackay, J. P., Trewhella, J., Jameson, G. B., Perugini, M. A., et al. (2008). Evolution of Quaternary Structure in a Homotetrameric Enzyme,
Journal of Molecular Biology Vol. 380, (4) 691-703.

Guan, Y., Hickey, M. J., Borgstahl, G. E., Hallewell, R. A., Lepock, J. R., O'Connor, D., Hsieh, Y., Nick, H. S., Silverman, D. N. & Tainer, J. A. (1998). Crystal Structure of Y34F Mutant Human Mitochondrial Manganese Superoxide Dismutase and the Functional Role of Tyrosine 34,
Biochemistry Vol. 37, (14) 4722-4730.

Hammes-Schiffer, S. & Benkovic, S. J. (2006). Relating Protein Motion to Catalysis,
Annual Review of Biochemistry Vol. 75, 519-541.

Hampel, A., Labanaus.M, Connors, P. G., Kirkegar.L, Rajbhand.Ul, Sigler, P. B. & Bock, R. M. (1968). Single Crystals of Transfer RNA from Formylmethionine and Phenylalanine Transfer RNAs,
Science Vol. 162, (3860) 1384-1387.

Hart, P. J., Balbirnie, M. M., Ogihara, N. L., Nersissian, A. M., Weiss, M. S., Valentine, J. S. & Eisenberg, D. (1999). A Structure-Based Mechanism for Copper-Zinc Superoxide Dismutase,
Biochemistry Vol. 38, (7) 2167-2178.

Haugaard, N. (1968). Cellular Mechanisms of Oxygen Toxicity,
Physiological Reviews Vol. 48, (2) 311-373.

Hearn, A. S., Fan, L., Lepock, J. R., Luba, J. P., Greenleaf, W. B., Cabelli, D. E., Tainer, J. A., Nick, H. S. & Silverman, D. N. (2004). Amino Acid Substitution at the Dimeric Interface of Human Manganese Superoxide Dismutase,
Journal of Biological Chemistry Vol. 279, (7) 5861-5866.

Hearn, A. S., Stroupe, M. E., Cabelli, D. E., Ramilo, C. A., Luba, J. P., Tainer, J. A., Nick, H. S. & Silverman, D. N. (2003). Catalytic and Structural Effects of Amino Acid Substitution at Histidine 30 in Human Manganese Superoxide Dismutase: Insertion of Valine Cγ into the Substrate Access Channel,
Biochemistry Vol. 42, (10) 2781-2789.

Hendrickson, W. A. (1985). Stereochemically Restrained Refinement of Macromolecular Structures,
Methods in Enzymology Vol. 115, 252-270.

Hodel, A., Kim, S. H. & Brünger, A. T. (1992). Model Bias in Macromolecular Crystal Structures,

Acta Crystallographica Section A Vol. 48, 851-858.

Hsieh, Y., Guan, Y., Tu, C., Bratt, P. J., Angerhofer, A., Lepock, J. R., Hickey, M. J., Tainer, J. A., Nick, H. S. & Silverman, D. N. (1998). Probing the Active Site of Human Manganese Superoxide Dismutase: The Role of Glutamine 143, **Biochemistry** Vol. 37, (14) 4731-4739.

Huang, Y. S., Su, W. J., Huang, Y. H., Chen, C. Y., Chang, F. Y., Lin, H. C. & Lee, S. D. (2007). Genetic polymorphisms of manganese superoxide dismutase, NAD(P)H:quinone oxidoreductase, glutathione *S*-transferase M1 and T1, and the susceptibility to drug-induced liver injury, **Journal of Hepatology** Vol. 47, (1) 128-134.

Hunter, T., Ikebukuro, K., Bannister, W. H., Bannister, J. V. & Hunter, G. J. (1997). The Conserved Residue Tyrosine 34 Is Essential for Maximal Activity of Iron-Superoxide Dismutase from *Escherichia coli*, **Biochemistry** Vol. 36, (16) 4925-4933.

Jackson, T. A., Karapetian, A., Miller, A. F. & Brunold, T. C. (2004). Spectroscopic and Computational Studies of the Azide-Adduct of Manganese Superoxide Dismutase: Definitive Assignment of the Ligand Responsible for the Low-Temperature Thermochromism, **Journal of the American Chemical Society** Vol. 126, (39) 12477-12491.

Jackson, T. A., Xie, J., Yikilmaz, E., Miller, A. F. & Brunold, T. C. (2002). Spectroscopic and Computational Studies on Iron and Manganese Superoxide Dismutases: Nature of the Chemical Events Associated with Active-Site pKs, **Journal of the American Chemical Society** Vol. 124, (36) 10833-10845.

Jackson, T. A., Yikilmaz, E., Miller, A. F. & Brunold, T. C. (2003). Spectroscopic and Computational Study of a Non-Heme Iron $\{Fe\text{-}NO\}^7$ System: Exploring the Geometric and Electronic Structures of the Nitrosyl Adduct of Iron Superoxide Dismutase, **Journal of the American Chemical Society** Vol. 125, (27) 8348-8363.

Jaenicke, R. (1991). Protein stability and molecular adaptation to extreme conditions, **European Journal of Biochemistry** Vol. 202, (3) 715-728.

Jencks, W. P. (1975). Binding-Energy, Specificity, and Enzymic Catalysis - Circe Effect, **Advances in Enzymology and Related Areas of Molecular Biology** Vol. 43, 219-410.

Jensen, L. H. (1990). Solvent Model for Protein Crystals: on Occupancy Parameters for Discrete Solvent Sites and the Solvent Continuum, **Acta Crystallographica Section B-Structural Science** Vol. 46, 650-653.

Johari, G. P., Hallbrucker, A. & Mayer, E. (1987). The glass-liquid transition of hyperquenched water, **Nature** Vol. 330, (6148) 552-553.

Joshi, P. & Dennis, P. P. (1993). Characterization of Paralogous and Orthologous Members of the Superoxide Dismutase Gene Family from Genera of the Halophilic Archaebacteria,

Journal of Bacteriology Vol. 175, (6) 1561-1571.

Juan, J. Y., Keeney, S. N. & Gregory, E. M. (1991). Reconstitution of the *Deinococcus radiodurans* Aposuperoxide Dismutase,
Archives of Biochemistry and Biophysics Vol. 286, (1) 257-263.

Kasting, J. F. (1993). Earth's Early Atmosphere,
Science Vol. 259, (5097) 920-926.

Keele, B. B., Jr., McCord, J. M. & Fridovich, I. (1970). Superoxide Dismutase from *Escherichia coli* B. A NEW MANGANESE-CONTAINING ENZYME,
Journal of Biological Chemistry Vol. 245, (22) 6176-6181.

Keele, B. B., Jr., McCord, J. M. & Fridovich, I. (1971). Further Characterization of Bovine Superoxide Dismutase and Its Isolation from Bovine Heart,
Journal of Biological Chemistry Vol. 246, (9) 2875-2880.

Kirby, T., Blum, J., Kahane, I. & Fridovich, I. (1980). Distinguishing between Mn-Containing and Fe-Containing Superoxide Dismutases in Crude Extracts of Cells,
Archives of Biochemistry & Biophysics Vol. 201, (2) 551-555.

Kirschvink, J. L., Gaidos, E. J., Bertani, L. E., Beukes, N. J., Gutzmer, J., Maepa, L. N. & Steinberger, R. E. (2000). Paleoproterozoic snowball Earth: Extreme climatic and geochemical global change and its biological consequences,
Proceedings of the National Academy of Sciences of the United States of America Vol. 97, (4) 1400-1405.

Kleywegt, G. J. (2000). Validation of protein crystal structures,
Acta Crystallographica Section D-Biological Crystallography Vol. 56, 249-265.

Kleywegt, G. J., Henrick, K., Dodson, E. J. & van Aalten, D. M. F. (2003). Pound-Wise but Penny-Foolish: How Well Do Micromolecules Fare in Macromolecular Refinement?,
Structure Vol. 11, (9) 1051-1059.

Kleywegt, G. J. & Jones, T. A. (1994). Detection, Delineation, Measurement and Display of Cavities in Macromolecular Structures,
Acta Crystallographica Section D-Biological Crystallography Vol. 50, 178-185.

Kleywegt, G. J. & Jones, T. A. (1995). Where freedom Is given, liberties are taken,
Structure Vol. 3, (6) 535-540.

Kleywegt, G. J. & Jones, T. A. (1996). *xdlMAPMAN* and *xdlDATAMAN* - Programs for Reformatting, Analysis and Manipulation of Biomacromolecular Electron-Density Maps and Reflection Data Sets,
Acta Crystallographica Section D-Biological Crystallography Vol. 52, 826-828.

Kleywegt, G. J. & Jones, T. A. (2002). Homo Crystallographicus - Quo Vadis?,
Structure Vol. 10, (4) 465-472.

Kukavica, B., Vučinić, Ž. & Vuletić, M. (2005). Superoxide dismutase, peroxidase, and germin-like protein activity in plasma membranes and apoplast of maize roots, **Protoplasma** Vol. 226, (3-4) 191-197.

Kundrot, C. E. & Richards, F. M. (1987). Use of the Occupancy Factor in the Refinement of Solvent Molecules in Protein Crystal Structures, **Acta Crystallographica Section B-Structural Science** Vol. 43, 544-547.

Lah, M. S., Dixon, M. M., Pattridge, K. A., Stallings, W. C., Fee, J. A. & Ludwig, M. L. (1995). Structure-Function in *Escherichia coli* Iron Superoxide Dismutase: Comparisons with the Manganese Enzyme from *Thermus thermophilus*, **Biochemistry** Vol. 34, (5) 1646-1660.

Landis, G. N. & Tower, J. (2005). Superoxide dismutase evolution and life span regulation, **Mechanisms of Ageing and Development** Vol. 126, (3) 365-379.

Larkin, M. A., Blackshields, G., Brown, N. P., Chenna, R., McGettigan, P. A., McWilliam, H., Valentin, F., Wallace, I. M., Wilm, A., Lopez, R., et al. (2007). Clustal W and Clustal X version 2.0, **Bioinformatics** Vol. 23, (21) 2947-2948.

Laskowski, R. A., Macarthur, M. W., Moss, D. S. & Thornton, J. M. (1993). *PROCHECK*: a program to check the stereochemical quality of protein structures, **Journal of Applied Crystallography** Vol. 26, 283-291.

Lau, E. Y. & Bruice, T. C. (1998). Importance of Correlated Motions in Forming Highly Reactive Near Attack Conformations in Catechol *O*-Methyltransferase, **Journal of the American Chemical Society** Vol. 120, (48) 12387-12394.

Lavoisier, A. L. & Lavoisier, M. A. P. (1789). Traité élémentaire de chimie, présenté dans un ordre nouveau et d'après les découvertes modernes; avec figures, **Cuchet** Paris,.

Lawrence, G. D. & Sawyer, D. T. (1979). Potentiometric Titrations and Oxidation-Reduction Potentials of Manganese and Copper-Zinc Superoxide Dismutases, **Biochemistry** Vol. 18, (14) 3045-3050.

Lévêque, V. J., Stroupe, M. E., Lepock, J. R., Cabelli, D. E., Tainer, J. A., Nick, H. S. & Silverman, D. N. (2000). Multiple Replacements of Glutamine 143 in Human Manganese Superoxide Dismutase: Effects on Structure, Stability, and Catalysis, **Biochemistry** Vol. 39, (24) 7131-7137.

Li, J. M. & Shah, A. M. (2004). Endothelial cell superoxide generation: regulation and relevance for cardiovascular pathophysiology, **American Journal of Physiology-Regulatory Integrative and Comparative Physiology** Vol. 287, (5) R1014-R1030.

Lin, J., Qi, R., Aston, C., Jing, J., Anantharaman, T. S., Mishra, B., White, O., Daly, M. J., Minton, K. W., Venter, J. C., et al. (1999). Whole-Genome Shotgun Optical Mapping of *Deinococcus radiodurans*, **Science** Vol. 285, (5433) 1558-1562.

Lipton, M. S., Paša-Tolić, L., Anderson, G. A., Anderson, D. J., Auberry, D. L., Battista, J. R., Daly, M. J., Fredrickson, J., Hixson, K. K., Kostandarithes, H., et al. (2002). Global analysis of the *Deinococcus radiodurans* proteome by using accurate mass tags.,
Proceedings of the National Academy of Sciences of the United States of America Vol. 99, (17) 11049-11054.

Liu, Y., Zhou, J., Omelchenko, M. V., Beliaev, A. S., Venkateswaran, A., Stair, J., Wu, L., Thompson, D. K., Xu, D., Rogozin, I. B., et al. (2003). Transcriptome dynamics of *Deinococcus radiodurans* recovering from ionizing radiation,
Proceedings of the National Academy of Sciences of the United States of America Vol. 100, (7) 4191-4196.

Livesay, D. R., Jambeck, P., Rojnuckarin, A. & Subramaniam, S. (2003). Conservation of Electrostatic Properties within Enzyme Families and Superfamilies,
Biochemistry Vol. 42, (12) 3464-3473.

Ludwig, M. L., Metzger, A. L., Pattridge, K. A. & Stallings, W. C. (1991). Manganese Superoxide Dismutase from *Thermus thermophilus* A Structural Model Refined at 1.8 Å Resolution,
Journal of Molecular Biology Vol. 219, (2) 335-358.

Maliekal, J., Karapetian, A., Vance, C., Yikilmaz, E., Wu, Q., Jackson, T., Brunold, T. C., Spiro, T. G. & Miller, A. F. (2002). Comparison and Contrasts between the Active Site PKs of Mn-Superoxide Dismutase and Those of Fe-Superoxide Dismutase,
Journal of the American Chemical Society Vol. 124, (50) 15064-15075.

Markillie, L. M., Varnum, S. M., Hradecky, P. & Wong, K. K. (1999). Targeted Mutagenesis by Duplication Insertion in the Radioresistant Bacterium *Deinococcus radiodurans*: Radiation Sensitivities of Catalase (*katA*) and Superoxide Dismutase (*sodA*) Mutants,
Journal of Bacteriology Vol. 181, (2) 666-669.

Matthews, B. W. (1968). Solvent Content of Protein Crystals,
Journal of Molecular Biology Vol. 33, (2) 491-497.

McCord, J. M. & Fridovich, I. (1969). Superoxide Dismutase AN ENZYMIC FUNCTION FOR ERYTHROCUPREIN (HEMOCUPREIN),
Journal of Biological Chemistry Vol. 244, (22) 6049-6055.

McCord, J. M., Keele, B. B., Jr. & Fridovich, I. (1971). An Enzyme-Based Theory of Obligate Anaerobiosis: The Physiological Function of Superoxide Dismutase,
Proceedings of the National Academy of Sciences of the United States of America Vol. 68, (5) 1024-1027.

Meier, B., Barra, D., Bossa, F., Calabrese, L. & Rotilio, G. (1982). Synthesis of Either Fe- or Mn-Superoxide Dismutase with an Apparently Identical Protein Moiety by an Anaerobic Bacterium Dependent on the Metal Supplied,
Journal of Biological Chemistry Vol. 257, (23) 13977-13980.

Meier, B., Scherk, C., Schmidt, M. & Parak, F. (1998). pH-dependent inhibition by azide and fluoride of the iron superoxide dismutase from *Propionibacterium shermanii*,

Biochemical Journal Vol. 331, (Pt 2) 403-407.

Miller, A. F., Padmakumar, K., Sorkin, D. L., Karapetian, A. & Vance, C. K. (2003). Proton-coupled electron transfer in Fe-superoxide dismutase and Mn-superoxide dismutase,
Journal of Inorganic Biochemistry Vol. 93, (1-2) 71-83.

Miller, A. F., Schwartz, A. L. & Vance, C. K. (1999). Mechanisms of redox tuning in Fe- and Mn-superoxide dismutases,
Journal of Inorganic Biochemistry Vol. 74, (1-4) 41-41.

Miller, A. F., Sorkin, D. L. & Padmakumar, K. (2005). Anion Binding Properties of Reduced and Oxidized Iron-Containing Superoxide Dismutase Reveal No Requirement for Tyrosine 34,
Biochemistry Vol. 44, (16) 5969-5981.

Mizuno, K., Whittaker, M. M., Bächinger, H. P. & Whittaker, J. W. (2004). Calorimetric Studies on the Tight Binding Metal Interactions of *Escherichia coli* Manganese Superoxide Dismutase,
Journal of Biological Chemistry Vol. 279, (26) 27339-27344.

Murshudov, G. N., Vagin, A. A. & Dodson, E. J. (1997). Refinement of Macromolecular Structures by the Maximum-Likelihood Method,
Acta Crystallographica Section D-Biological Crystallography Vol. 53, 240-255.

Murshudov, G. N., Vagin, A. A., Lebedev, A., Wilson, K. S. & Dodson, E. J. (1999). Efficient anisotropic refinement of macromolecular structures using FFT,
Acta Crystallographica Section D-Biological Crystallography Vol. 55, 247-255.

Navaza, J. (1994). *AMoRe*:an Automated Package for Molecular Replacement,
Acta Crystallographica Section A Vol. 50, 157-163.

Navaza, J. (2001). Implementation of molecular replacement in *AMoRe*,
Acta Crystallographica Section D-Biological Crystallography Vol. 57, (Pt 10) 1367-1372.

Nosaka, Y., Ishizuka, Y., Norimatsu, K. & Miyama, H. (1984). Photocatalytic Reactions of Azide Ions on Platinized Titanium-Dioxide Powders in Solutions,
Bulletin of the Chemical Society of Japan Vol. 57, (11) 3066-3069.

Oberley, L. W. & Buettner, G. R. (1979). Role of Superoxide-Dismutase in Cancer: A Review,
Cancer Research Vol. 39, (4) 1141-1149.

Orrell, R. W. (2006). Aeol-10150 Aeolus,
Current Opinion in Investigational Drugs Vol. 7, (1) 70-80.

Ose, D. E. & Fridovich, I. (1979). Manganese-Containing Superoxide-Dismutase from Escherichia-Coli - Reversible Resolution and Metal Replacements,
Archives of Biochemistry and Biophysics Vol. 194, (2) 360-364.

Oshima, T. & Imahori, K. (1971). ISOLATION OF AN EXTREME THERMOPHILE AND THERMOSTABILITY OF ITS TRANSFER RIBONUCLEIC ACID AND RIBOSOMES,
Journal of General and Applied Microbiology Vol. 17, (6) 513-517.

Oury, T. D., Crapo, J. D., Valnickova, Z. & Enghild, J. J. (1996). Human extracellular superoxide dismutase is a tetramer composed of two disulphide-linked dimers: a simplified, high-yield purification of extracellular superoxide dismutase,
Biochemical Journal Vol. 317, 51-57.

Pannu, N. S. & Read, R. J. (1996). Improved Structure Refinement Through Maximum Likelihood,
Acta Crystallographica Section A Vol. 52, 659-668.

Parker, M. W. & Blake, C. C. (1988). Crystal Structure of Manganese Superoxide Dismutase from *Bacillus stearothermophilus* at 2.4 Å Resolution,
Journal of Molecular Biology Vol. 199, (4) 649-661.

Pauling, L. (1948). Nature of Forces between Large Molecules of Biological Interest,
Nature Vol. 161, (4097) 707-709.

Ramachandran, G. N., Ramakrishnan, C. & Sasisekharan, V. (1963). Stereochemistry of Polypeptide Chain Configurations,
Journal of Molecular Biology Vol. 7, (1) 95-99.

Raup, D. M. (1986). Biological Extinction in Earth History,
Science Vol. 231, (4745) 1528-1533.

Read, R. J. & Schierbeek, A. J. (1988). A phased translation function,
Journal of Applied Crystallography Vol. 21, 490-495.

Reddan, J. R., Giblin, F. J., Sevilla, M., Padgaonkar, V., Dziedzic, D. C., Leverenz, V. R., Misra, I. C., Chang, J. S. & Pena, J. T. (2003). Propyl gallate is a superoxide dismutase mimic and protects cultured lens epithelial cells from H_2O_2 insult,
Experimental Eye Research Vol. 76, (1) 49-59.

Richardson, D. C., Richardson, J. S. & Bier, C. J. (1972). Two Crystal Forms of Bovine Superoxide Dismutase,
Journal of Biological Chemistry Vol. 247, (19) 6368-6369.

Richardson, J. S., Richardson, D. C., Thomas, K. A., Silverton, E. W. & Davies, D. R. (1976). Similarity of 3-Dimensional Structure between Immunoglobulin Domain and Copper, Zinc Superoxide Dismutase Subunit,
Journal of Molecular Biology Vol. 102, (2) 221-235.

Rigel, N. W. & Braunstein, M. (2008). A new twist on an old pathway - accessory secretion systems,
Molecular Microbiology Vol. 69, (2) 291-302.

Ringe, D., Petsko, G. A., Yamakura, F., Suzuki, K. & Ohmori, D. (1983). Structure of iron superoxide dismutase from *Pseudomonas ovalis* at 2.9-Å resolution,
Proceedings of the National Academy of Sciences of the United States of America Vol. 80, (13) 3879-3883.

Rodríguez-Serrano, M., Romero-Puertas, M. C., Pastori, G. M., Corpas, F. J., Sandalio, L. M., del Rio, L. A. & Palma, J. M. (2007). Peroxisomal membrane manganese superoxide dismutase: characterization of the isozyme from watermelon (*Citrullus lanatus* Schrad.) cotyledons,
Journal of Experimental Botany Vol. 58, (10) 2417-2427.

Rossmann, M. G. (2001). Molecular replacement - historical background,
Acta Crystallographica Section D-Biological Crystallography Vol. 57, (Pt 10) 1360-1366.

Rulíšek, L., Jensen, K. P., Lundgren, K. & Ryde, U. (2006). The Reaction Mechanism of Iron and Manganese Superoxide Dismutases Studied by Theoretical Calculations,
Journal of Computational Chemistry Vol. 27, (12) 1398-1414.

Rulíšek, L. & Ryde, U. (2006). Structure of Reduced and Oxidized Manganese Superoxide Dismutase: A Combined Computational and Experimental Approach,
Journal of Physical Chemistry B Vol. 110, (23) 11511-11518.

Salvemini, D., Wang, Z. Q., Zweier, J. L., Samouilov, A., Macarthur, H., Misko, T. P., Currie, M. G., Cuzzocrea, S., Sikorski, J. A. & Riley, D. P. (1999). A Nonpeptidyl Mimic of Superoxide Dismutase with Therapeutic Activity in Rats.,
Science Vol. 286, (5438) 304-306.

Sambrook, J., Russell, D. W. & Sambrook, J. (2006). The condensed protocols from Molecular cloning : a laboratory manual,
Cold Spring Harbor Laboratory Press Cold Spring Harbor, N.Y.

Schäfer, G. & Kardinahl, S. (2003). Iron superoxide dismutases: structure and function of an archaic enzyme,
Biochemical Society Transactions Vol. 31, 1330-1334.

Schiavone, J. R. & Hassan, H. M. (1988). The Role of Redox in the Regulation of Manganese-containing Superoxide Dismutase Biosynthesis in *Escherichia coli*,
Journal of Biological Chemistry Vol. 263, (9) 4269-4273.

Schmidt, M. (1999). Manipulating the coordination number of the ferric iron within the cambialistic superoxide dismutase of *Propionibacterium shermanii* by changing the pH-value A crystallographic analysis,
European Journal of Biochemistry Vol. 262, (1) 117-127.

Schmidt, M., Meier, B. & Parak, F. (1996). X-ray structure of the cambialistic superoxide dismutase from *Propionibacterium shermanii* active with Fe or Mn,
Journal of Biological Inorganic Chemistry Vol. 1, (6) 532-541.

Schmidt, M., Scherk, C., Iakovleva, O., Nolting, H. F., Meier, B. & Parak, F. (1998). The structure of the azide coordinated superoxide dismutase of *Propionibacterium shermanii* investigated by X-ray structure analysis, extended X-ray absorption fine structure, Mössbauer and electron paramagnetic resonance spectroscopy,
Inorganica Chimica Acta Vol. 276, (1-2) 65-72.

Shao, J., Chen, L. S., Marrs, B., Lee, L., Huang, H., Manton, K. G., Martin, G. M. & Oshima, J. (2007). *SOD2* polymorphisms: unmasking the effect of polymorphism on splicing,
Bmc Medical Genetics Vol. 8, 7.

Slykhouse, T. O. & Fee, J. A. (1976). Physical and Chemical Studies on Bacterial Superoxide Dismutases - PURIFICATION AND SOME ANION BINDING PROPERTIES OF IRON-CONTAINING PROTEIN OF *ESCHERICHIA COLI* B,
Journal of Biological Chemistry Vol. 251, (18) 5472-5477.

Smith, J. L. (1899). THE PATHOLOGICAL EFFECTS DUE TO INCREASE OF OXYGEN TENSION IN THE AIR BREATHED.,
The Journal of Physiology Vol. 24, (1) 19-35.

Smith, M. W. & Doolittle, R. F. (1992). A Comparison of Evolutionary Rates of the 2 Major Kinds of Superoxide-Dismutase,
Journal of Molecular Evolution Vol. 34, (2) 175-184.

Smith, M. W., Feng, D. F. & Doolittle, R. F. (1992). Evolution by acquisition - the case for horizontal gene transfers,
Trends in Biochemical Sciences Vol. 17, (12) 489-493.

Sorkin, D. L., Duong, D. K. & Miller, A. F. (1997). Mutation of Tyrosine 34 to Phenylalanine Eliminates the Active Site p*K* of Reduced Iron-Containing Superoxide Dismutase,
Biochemistry Vol. 36, (27) 8202-8208.

Sorkin, D. L. & Miller, A. F. (1997). Spectroscopic Measurement of a Long-Predicted Active Site p*K* in Iron-Superoxide Dismutase from *Escherichia coli*,
Biochemistry Vol. 36, (16) 4916-4924.

Stallings, W. C., Pattridge, K. A., Powers, T. B., Fee, J. A. & Ludwig, M. L. (1981). Characterization of Crystals of Tetrameric Manganese Superoxide Dismutase from *Thermus thermophilus* HB8,
Journal of Biological Chemistry Vol. 256, (11) 5857-5859.

Stallings, W. C., Pattridge, K. A., Strong, R. K. & Ludwig, M. L. (1984). Manganese and Iron Superoxide Dismutases Are Structural Homologs,
Journal of Biological Chemistry Vol. 259, (17) 10695-10699.

Stallings, W. C., Pattridge, K. A., Strong, R. K. & Ludwig, M. L. (1985). The Structure of Manganese Superoxide Dismutase from *Thermus thermophilus HB8* at 2.4-Å Resolution,
Journal of Biological Chemistry Vol. 260, (30) 16424-16432.

Stallings, W. C., Powers, T. B., Pattridge, K. A., Fee, J. A. & Ludwig, M. L. (1983). Iron superoxide dismutase from *Escherichia coli* at 3.1-Å resolution: A structure unlike that of copper/zinc protein at both monomer and dimer levels,
Proceedings of the National Academy of Sciences of the United States of America Vol. 80, (13) 3884-3888.

Stein, J., Fackler, J. P., Mcclune, G. J., Fee, J. A. & Chan, L. T. (1979). Superoxide and Manganese(III). Reactions of Mn-EDTA and Mn-CyDTA Complexes with O_2^-. X-ray structure of KMnEDTA.$2H_2O$,
Inorganic Chemistry Vol. 18, (12) 3511-3519.

Steller, I., Bolotovsky, R. & Rossmann, M. G. (1997). An Algorithm for Automatic Indexing of Oscillation Images using Fourier Analysis,
Journal of Applied Crystallography Vol. 30, 1036-1040.

Stoddard, B. L., Howell, P. L., Ringe, D. & Petsko, G. A. (1990). The 2.1-Å Resolution Structure of Iron Superoxide Dismutase from *Pseudomonas ovalis*,
Biochemistry Vol. 29, (38) 8885-8893.

Stoddard, B. L., Ringe, D. & Petsko, G. A. (1990). The structure of iron superoxide dismutase from *Pseudomonas ovalis* complexed with the inhibitor azide,
Protein Engineering Vol. 4, (2) 113-119.

Stothard, P. & Wishart, D. S. (2006). Automated bacterial genome analysis and annotation,
Current Opinion in Microbiology Vol. 9, (5) 505-510.

Tabares, L. C., Bittel, C., Carrillo, N., Bortolotti, A. & Cortez, N. (2003). The Single Superoxide Dismutase of *Rhodobacter capsulatus* Is a Cambialistic, Manganese-Containing Enzyme,
Journal of Bacteriology Vol. 185, (10) 3223-3227.

Tabares, L. C., Cortez, N., Agalidis, I. & Un, S. (2005). Temperature-Dependent Coordination in *E. coli* Manganese Superoxide Dismutase,
Journal of the American Chemical Society Vol. 127, (16) 6039-6047.

Tabares, L. C., Cortez, N., Hiraoka, B. Y., Yamakura, F. & Un, S. (2006). Effects of Substrate Analogues and pH on Manganese Superoxide Dismutases,
Biochemistry Vol. 45, (6) 1919-1929.

Tabares, L. C., Cortez, N. & Un, S. (2007). Role of Tyrosine-34 in the Anion Binding Equilibria in Manganese(II) Superoxide Dismutases,
Biochemistry Vol. 46, (32) 9320-9327.

Takao, M., Yasui, A. & Oikawa, A. (1991). Unique Characteristics of Superoxide Dismutase of a Strictly Anaerobic Archaebacterium *Methanobacterium thermoautotrophicum*,
Journal of Biological Chemistry Vol. 266, (22) 14151-14154.

Tardat, B. & Touati, D. (1991). Two global regulators repress the anaerobic expression of MnSOD in *Escherichia coli*::Fur (ferric uptake regulation) and Arc (aerobic respiration control),
Molecular Microbiology Vol. 5, (2) 455-465.

Thomas, K. A., Rubin, B. H., Bier, C. J., Richardson, J. S. & Richardson, D. C. (1974). The Crystal-Structure of Bovine Cu^{2+} ,Zn^{2+} Superoxide Dismutase at 5.5-Å Resolution,
Journal of Biological Chemistry Vol. 249, (17) 5677-5683.

Tierney, D. L., Fee, J. A., Ludwig, M. L. & Penner-Hahn, J. E. (1995). X-ray Absorption Spectroscopy of the Iron Site in *Escherichia coli* Fe(III) Superoxide Dismutase,
Biochemistry Vol. 34, (5) 1661-1668.

Tottey, S., Waldron, K. J., Firbank, S. J., Reale, B., Bessant, C., Sato, K., Cheek, T. R., Gray, J., Banfield, M. J., Dennison, C., et al. (2008). Protein-folding location can regulate manganese-binding versus copper- or zinc-binding,
Nature Vol. 455, (7216) 1138-1142.

Touati, D. (1983). Cloning and Mapping of the Manganese Superoxide Dismutase Gene (*sodA*) of *Escherichia coli* K-12,
Journal of Bacteriology Vol. 155, (3) 1078-1087.

Un, S., Tabares, L. C., Cortez, N., Hiraoka, B. Y. & Yamakura, F. (2004). Manganese(II) Zero-Field Interaction in Cambialistic and Manganese Superoxide Dismutases and Its Relationship to the Structure of the metal Binding Site,
Journal of the American Chemical Society Vol. 126, (9) 2720-2726.

Vagin, A. & Teplyakov, A. (1997). *MOLREP:* an Automated Program for Molecular Replacement,
Journal of Applied Crystallography Vol. 30, 1022-1025.

Vaguine, A. A., Richelle, J. & Wodak, S. J. (1999). SFCHECK: a unified set of procedures for evaluating the quality of macromolecular structure-factor data and their agreement with the atomic model,
Acta Crystallographica Section D-Biological Crystallography Vol. 55, (Pt 1) 191-205.

Vance, C. K. & Miller, A. F. (1998a). Spectroscopic Comparisons of the pH Dependencies of Fe-Substituted (Mn)Superoxide Dismutase and Fe-Superoxide Dismutase,
Biochemistry Vol. 37, (16) 5518-5527.

Vance, C. K. & Miller, A. F. (1998b). A Simple Proposal That Can Explain the Inactivity of Metal-Substituted Superoxide Dismutases,
Journal of the American Chemical Society Vol. 120, (3) 461-467.

Vance, C. K. & Miller, A. F. (2001). Novel Insights into the Basis for *Escherichia coli* Superoxide Dismutase's Metal Ion Specificity from Mn-Substituted FeSOD and Its Very High E_m,
Biochemistry Vol. 40, (43) 13079-13087.

Wagner, U. G., Pattridge, K. A., Ludwig, M. L., Stallings, W. C., Werber, M. M., Oefner, C., Frolow, F. & Sussman, J. L. (1993). Comparison of the crystal structures of genetically engineered human manganese superoxide dismutase and manganese superoxide dismutase from *Thermus thermophilus*: differences in dimer-dimer interaction,
Protein Science Vol. 2, (5) 814-825.

Warshel, A. (1978). Energetics of enzyme catalysis,
Proceedings of the National Academy of Sciences of the United States of America Vol. 75, (11) 5250-5254.

Whittaker, J. W. & Whittaker, M. M. (1991). Active Site Spectral Studies on Manganese Superoxide-Dismutase,
Journal of the American Chemical Society Vol. 113, (15) 5528-5540.

Whittaker, M. M. & Whittaker, J. W. (1996). Low-Temperature Thermochromism Marks a Change in Coordination for the Metal Ion in Manganese Superoxide Dismutase,
Biochemistry Vol. 35, (21) 6762-6770.

Whittaker, M. M. & Whittaker, J. W. (1997a). Mutagenesis of a proton linkage pathway in Escherichia coli manganese superoxide dismutase,
Biochemistry Vol. 36, (29) 8923-8931.

Whittaker, M. M. & Whittaker, J. W. (1997b). A "thermophilic shift" in ligand interactions for *Thermus thermophilus* manganese superoxide dismutase,
Journal of Biological Inorganic Chemistry Vol. 2, (5) 667-671.

Whittaker, M. M. & Whittaker, J. W. (1998). A Glutamate Bridge Is Essential for Dimer Stability and Metal Selectivity in Manganese Superoxide Dismutase,
Journal of Biological Chemistry Vol. 273, (35) 22188-22193.

Williams, R. J. P. (2002). The Problem of Proton Transfer in Membranes,
Journal of Theoretical Biology Vol. 219, (3) 389-396.

Wilson, A. J. C. (1949). The Probability Distribution of X-Ray Intensities,
Acta Crystallographica Vol. 2, (5) 318-321.

Wilson, C. J., Apiyo, D. & Wittung-Stafshede, P. (2004). Role of cofactors in metalloprotein folding,
Quarterly Reviews of Biophysics Vol. 37, (3-4) 285-314.

Wintjens, R., Gilis, D. & Rooman, M. (2008). Mn/Fe superoxide dismutase interaction fingerprints and prediction of oligomerization and metal cofactor from sequence,
Proteins-Structure Function and Bioinformatics Vol. 70, (4) 1564-1577.

Wraight, C. A. (2006). Chance and design - Proton transfer in water, channels and bioenergetic proteins,
Biochimica Et Biophysica Acta-Bioenergetics Vol. 1757, (8) 886-912.

Wuerges, J., Lee, J. W., Yim, Y. I., Yim, H. S., Kang, S. O. & Carugo, K. D. (2004). Crystal structure of nickel-containing superoxide dismutase reveals another type of active site,
Proceedings of the National Academy of Sciences of the United States of America Vol. 101, (23) 8569-8574.

Xuong, N. H., Sullivan, D., Nielsen, C. & Hamlin, R. (1985). Use of the Multiwire Area Detector Diffractometer as a National Resource for Protein Crystallography,
Acta Crystallographica Section B-Structural Science Vol. 41, (Aug) 267-269.

Yamakura, F., Kobayashi, K., Ue, H. & Konno, M. (1995). The pH-dependent changes of the enzymic activity and spectroscopic properties of iron-substituted

manganese superoxide dismutase. A study on the metal-specific activity of Mn-containing superoxide dismutase,
European Journal of Biochemistry Vol. 227, (3) 700-706.

Yamakura, F., Sugio, S., Hiraoka, B. Y., Ohmori, D. & Yokota, T. (2003). Pronounced Conversion of the Metal-Specific Activity of Superoxide Dismutase from *Porphyromonas gingivalis* by the Mutation of a Single Amino Acid (Gly155Thr) Located Apart from the Active Site,
Biochemistry Vol. 42, (36) 10790-10799.

Yamakura, F. & Suzuki, K. (1980). Cadmium, Chromium, and Manganese Replacement for Iron in Iron-Superoxide Dismutase from *Pseudomonas ovalis*,
Journal of Biochemistry Vol. 88, (1) 191-196.

Yamakura, F., Suzuki, K. & Mitsui, Y. (1976). Crystallization and Preliminary Crystal Data of Iron-Containing Superoxide Dismutase from *Pseudomonas ovalis*,
Journal of Biological Chemistry Vol. 251, (15) 4792-4793.

Yikilmaz, E., Porta, J., Grove, L. E., Vahedi-Faridi, A., Bronshteyn, Y., Brunold, T. C., Borgstahl, G. E. & Miller, A. F. (2007). How Can a Single Second Sphere Amino Acid Substitution Cause Reduction Midpoint Potential Changes of Hundreds of Millivolts?,
Journal of the American Chemical Society Vol. 129, (32) 9927-9940.

Yikilmaz, E., Rodgers, D. W. & Miller, A. F. (2006). The Crucial Importance of Chemistry in the Structure-Function Link: Manipulating Hydrogen Bonding in Iron-Containing Superoxide Dismutase,
Biochemistry Vol. 45, (4) 1151-1161.

Yost, F. J. & Fridovich, I. (1973). An Iron-Containing Superoxide Dismutase from *Escherichia coli*,
Journal of Biological Chemistry Vol. 248, (14) 4905-4908.

Youn, H. D., Kim, E. J., Roe, J. H., Hah, Y. C. & Kang, S. O. (1996). A novel nickel-containing superoxide dismutase from *Streptomyces* spp.,
Biochemical Journal Vol. 318, 889-896.

Zelko, I. N., Mariani, T. J. & Folz, R. J. (2002). SUPEROXIDE DISMUTASE MULTIGENE FAMILY: A COMPARISON OF THE CuZn-SOD (SOD1), Mn-SOD (SOD2), AND EC-SOD (SOD3) GENE STRUCTURES, EVOLUTION, AND EXPRESSION,
Free Radical Biology and Medicine Vol. 33, (3) 337-349.

Zhu, D. H. & Scandalios, J. G. (1993). Maize mitochondrial manganese superoxide dismutases are encoded by a differentially expressed multigene family,
Proceedings of the National Academy of Sciences of the United States of America Vol. 90, (20) 9310-9314.

Appendix-Programs Used

A variety of programs and web resources have been used during the preparation of this thesis. Where relevant they have been specifically mentioned in the text. However a lot of utility programs were also used.

General

Firefox	web-browser, Mozilla Corporation. http://www.firefox.com/
Netscape	web-browser, http://netscape.aol.com/
ImageMagick	image manipulation, http://imagemagick.org
Open office	word processing, image creation, spreadsheet http://www.openoffice.org/
GIMP	graphics utilities, http://www.gimp.org/
EndNote	citation manager, http://www.endnote.com/

Microsoft®

Homepage http://www.microsoft.com

Word	word processing/ Text editor,
Microsoft Office Excel	spreadsheet application
PowerPoint	presentation
Paint	graphics utility

Bioinformatics

World Wide Web

CLUSTAL	sequence alignment, http://www.clustal.org/
EXPASY	general proteomics, http://au.expasy.org/

PDB	database of solved macro molecular structures, http://www.pdb.org

Macromolecular crystallography

CCP4

Homepage, http://www.ccp4.ac.uk

AMoRe	molecular replacement
ARP_WATERS	automated water picking
BEAST	Molecular replacement
CCP4MG	image generation
CIF2MTZ	file conversion for reflections
COOT	interactive building program with internal validation tools
CONTACT	protein contact
DISTANG	distance/angles calculation
DM	density modification
FFT	fast fourier transform, map generation
F2MTZ	file conversion for reflections
HKLVIEW	reciprocal space viewer
LSQKAB	coordinate translation, rotation
MAPDUMP	map information
MAPMASK	map manipulation
MOLREP	molecular replacement
MOSFLM	identification/integration of raw data from diffractometer

MTZDMP	data utility
MTZUTILS	dataset utilities
MTZ2VARIOUS	reflection data file conversion tool
OMIT	omit map calculation
PDBSET	coordinate manipulation
PHASER	molecular replacement
PROCHECK	coordinate validation
RASMOL	molecular visualisation
SCALA	scaling and merging
SFCHECK	test agreement between coordinates and data
SOLOMON	density modification
REFMAC	Macromolecular refinement
SFALL	structure factor calculation
SFTOOLS	dataset utilities
TRUNCATE	structure factor calculation
WATPEAK	peak search
WATERTIDY	organising solvent structure
XLOGGRAPH	data analysis

CNS

Homepage http://cns-online.org/

Temperature factor refinement, position refinement, simulated annealing, energy minimisation, map generation based on distributed input files.

USSF

Homepage http://xray.bmc.uu.se/usf/

DATAMAN	dataset manipulation
VOIDOO	cavity detection in PDB files
MAPMAN	map manipulation
MOLEMAN2	coordinate manipulation

Stand alone/Independent

ARP/WARP	Automated building program, http://www.embl-hamburg.de/ARP/
GRASP	molecular surface calculation
Pymol	molecular visualisation/ graphic generation. http://pymol.sourceforge.net/
APBS	electrostatic calculation, http://apbs.sourceforge.net/
MOLSCRIPT	graphics, http://www.avatar.se/molscript/
PHENIX	macromolecular refinement, http://www.phenix-online.org/
TURBO-FRODO	structure building, http://afmb.cnrs-mrs.fr/
RASTER3D	graphics rendering, http://skuld.bmsc.washington.edu/raster3d/b